12-14-2015

Approaching Aromatic Interactions with Small Molecule Model Systems: Assessing N-Heteroarene in ∏ -Stacking and CH-∏ Interactions, Crystal Engineering of Atropisomeric Rotors, and Developing Responsive Organic Charge-Transfer Complex

Ping Li
University of South Carolina - Columbia

APPROACHING AROMATIC INTERACTIONS WITH SMALL MOLECULE MODEL SYSTEMS: ASSESSING *N*-HETEROARENE IN Π-STACKING AND CH-Π INTERACTIONS, CRYSTAL ENGINEERING OF ATROPISOMERIC ROTORS, AND DEVELOPING RESPONSIVE ORGANIC CHARGE-TRANSFER COMPLEX

Ping Li

Bachelor of Science
East China University of Science and Technology, 2006

Submitted in Partial Fulfillment of the Requirements

For the Degree of Doctor of Philosophy in

Chemistry

College of Arts and Sciences

University of South Carolina

2015

Accepted by:

Ken D. Shimizu, Major Professor

Linda S. Shimizu, Committee Member

Daniel L. Reger, Committee Member

Andreas Heyden, Committee Member

Lacy Ford, Senior Vice Provost and Dean of Graduate Studies

DEDICATION

To my dad, Zhongyuan Li

ACKNOWLEDGEMENTS

First and foremost, I would like to thank my advisor Dr. Ken D. Shimizu for his years of guidance and support. I am truly grateful not only for the knowledge and skills he passed on to me but, more importantly, the habit of thinking critically and the rigorous and meticulous professionalism. All of these will surely benefit my career and life in future. Next, I would like express me wholehearted appreciation to the Shimizu group members, both current and former. Without the help and encouragements from theirs, I perhaps could not have accomplished even half what I have now. I am also so honored to meet and work with a highly talented group of fellow students, postdoc researchers, faculty, and staffs at the chemistry department. I shall give special thanks to our personnel at the NMR, X-ray crystallography, and MS facilities for their kind and patient help on various research problems.

At last, I would like express my deepest gratitude to my dad, Zhongyuan Li, my cousin Amanda Ling, my mentor Dr. Wei Wang, my best buddies Xinyue Wei and Zimu Liu, and countless friends who have helped and supported me along the way. My pursuit in chemistry took some unexpected turns at the beginning. Without their caring and help, I would have never come out that miserable period of life. I owe this dissertation to them much more than to myself. In the end, I want to close with a dedication to my dad: "Dad, thank you for being so supportive over these years! I hope what I have accomplished make you proud. I love you!"

ABSTRACT

Non-covalent interactions involving aromatic species are important in many areas in chemistry, biochemistry, and materials sciences. During the past two decades, small molecule model systems have emerged as a powerful tool to advance our knowledge of the stability trends for aromatic interactions in the condensed phase. Among these, the C-shape *N*-arylimide molecular balances developed by our laboratory have proven to be one most successful and versatile model systems that can be readily adapted to investigate various types of aromatic interactions. These molecular balances are particularly apt at isolating and accurately measuring the targeted weak aromatic interaction energies for different geometries. In this dissertation, our experimental efforts in utilizing the *N*-arylimide molecular balance to examine the impacts of nitrogen-containing aromatic surfaces (*N*-heteroarenes) on π-stacking and CH-π interactions are detailed. Polar *N*-heteroarenes displayed pronounced electrostatic character in these interactions which influenced both their stability trends and geometric preferences. Introducing a formal positive charge at the heterocyclic nitrogen greatly enhanced these electrostatic effects. Next, this versatile molecular model system was applied to the study of the relationship between the solution and solid-state conformational preferences for rapid interconverting conformers. Close examination of a library of atropisomeric *O*-tolyl succinimide rotors revealed that the solution conformational preferences were generally excellent predictors of the conformational preferences in crystal structures. Interestingly, the correlation function between the solid-state and solution mole fraction of *syn*- conformer (χ_{syn}) were

not linear but fit to a step-function trend where the solid-state χ_{syn} was either 0 or 1 for most rotors except for those with a solution χ_{syn} of 0.50 ± 0.06. Finally, we examined the behavior of a dynamic intramolecular aromatic stacking donor-acceptor-donor complex. This system displayed interesting reversible color changes in the solid-state when treated with different organic solvents. The unique responsive behavior was attributed to solvent-induced changes in the intramolecular stacking geometry of the D-A-D complex.

TABLE OF CONTENTS

DEDICATION iii

ACKNOWLEDGEMENTS iv

ABSTRACT v

LIST OF TABLES viii

LIST OF FIGURES x

CHAPTER 1: MOLECULAR BALANCES AND THEIR APPLICATIONS IN EXPERIMENTAL STUDIES OF NON-COVALENT AROMATIC INTERACTIONS 1

CHAPTER 2: A COMPREHENSIVE EXPERIMENTAL STUDY OF *N*-HETEROCYCLIC Π-STACKING INTERACTIONS OF NEUTRAL AND CATIONIC PYRIDINES 37

CHAPTER 3: THE CH-Π INTERACTION OF METHYL ETHERS AS A MODEL FOR CARBOHYDRATE-*N*-HETEROARENE INTERACTIONS 82

CHAPTER 4: CORRELATION BETWEEN SOLID-STATE AND SOLUTION CONFORMATIONAL RATIOS IN A SERIES OF *N*-(*O*-TOLYL)SUCCINIMIDE MOLECULAR ROTORS. 123

CHAPTER 5: SOLVENT-INDUCED REVERSIBLE SOLID-STATE COLOR CHANGE OF AN INTRAMOLECULAR CHARGE-TRANSFER COMPLEX. 165

CHAPTER 6: FUTURE WORK. 189

APPENDIX A− COPYRIGHT PERMISSIONS. 195

LIST OF TABLES

Table 2.1 Measured plane-to-plane angle (**α**), centroid-to-plane distance (**D**) and horizontal centroid-to-centroid off-set (**H**) between the two π-stacking six-membered rings in the crystal structures of balances **1'**, **2**, **3'**, **4**, **6**, and **7**. 48

Table 2.2 Measured conformational equilibrium energies (ΔG, kcal/mol) for balances **1**-**7** in DMSO-d_6 at 23 °C and relative energies (ΔΔG, kcal/mol) of the *N*-heterocyclic balances **2**-**7** relative to the non-heterocyclic balance **1**.....53

Table 2.3 Measured relative energies (ΔΔG, kcal/mol) of the *N*-heterocyclic balances **2**-**7** relative to the non-heterocyclic balance **1**.....58

Table 2.4 The measured ΔG's [kcal/mol] in deutrated solvents at rt. 74

Table 2.5 Tabulated data for the correlation plot in the text.....74

Table 2.6 Measured geometric parameters (***r*** and ***h***) defined for characterizing the O-π interactions in crystal structure **1'**, **2**, **3'**, **4**, **6** and **7**. 75

Table 2.7 The measured relative amounts of added MsOH, *folded/unfolded* ratios and calculated ΔG's in the titration experiment of |**2** + MsOH → **4**| in DMSO-d_6. 77

Table 2.8 The measured relative amounts of added MsOH, *folded/unfolded* ratios and calculated ΔG's in the titration experiment of |**3** + MsOH → **5**|in DMSO-d_6 77

Table 2.9 The measured relative amounts of added MsOH, *folded/unfolded* ratios and calculated ΔG's in the titration experiment of |**2** + MsOH → **4**|in CD_3CN 78

Table 2.10 The measured relative amounts of added MsOH, *folded/unfolded* ratios and calculated ΔG's in the titration experiment of |**3** + MsOH → **5**|in CD_3CN 78

Table 2.11 The measured relative amounts of added MsOH, *folded/unfolded* ratios and calculated ΔG's in the titration experiment of |**2** + MsOH → **4**| in $CDCl_3$.....79

Table 2.12 The measured relative amounts of added MsOH, *folded/unfolded* ratios and calculated ΔG's in the titration experiment of |**3** + MsOH → **5**| in $CDCl_3$.....79

Table 3.1 ^1H NMR solution measurements of balances **1**-**6** in CD_2Cl_2 at 25 °C.....86

Table 3.2 Measured geometric parameters for characterizing CH-π interactions in crystal structures **1'-3'** and **6'**: the atom-to-plane distance (***D***), CH-to-plane accessing angle (**α**) and the hydrogen projection-to-centroid displacement (***d*$_1$**), the closest annular sp^2 atom (***X***), and the hydrogen projection-to-X displacement (***d*$_2$**). 110

Table 3.3 Measured folding energies (ΔG, kcal/mol) for balances **1**, **2**, **3** and **6** in six common organic solvents at 25 ˚C.....121

Table 3.4 Measured [*folded*]/[*unfolded*] ratios using two different sets of peaks, i.e., the arm OCH_3 protons (H_{arm}) and the succinimide methide protons (H_S) in six solvents at 25 ˚C. 122

Table 3.5 Measured ΔG's (kcal/mol)^a for balances **4** and **5** in C_6D_6, CD_2Cl_2 and DMSO-d_6 at 25 ˚C. 122

Table 4.1 Measured mole fraction of *syn*-conformer (χ_{syn}) in solution and in solid-state crystals and relevant information of crystal structure. 135

Table 4.2 Measured bite angle (θ) for 30 rotors in their crystal structures.....137

Table 4.3 The measured in-solution χ_{syn} for 30 rotors in this study.....139

Table 5.1 Measured geometric parameters in crystal structures of **1** and **2**.....187

LIST OF FIGURES

Figure 1.1 Schematic demonstration of the versatile *N*-arylimide molecular balance model system developed to quantitatively assess various aromatic interactions of different strengths in solution. 3

Figure 1.2 **(A)** ChemDraw representation of the *syn-anti* conformational equilibrium for our first generation molecular balance **1**, highlighting the formation of different number of intramolecular aromatic π-stacking interactions in the *syn* and *anti*-conformers; **(B)** The plot of measured equilibrium energies (ΔG's in TCE) of our generation balances versus calculated polarizability of the arm arenes (B3LYP, 6-31G*), highlighting the systematic change in ΔG as the arm arene varied; **(C)** Partial side-view of X-ray crystal structure of *anti*-**1**, highlighting the formation of two intramolecular aromatic π-stacking interactions. 4

Figure 1.3 **(A)** ChemDraw representation of the *folded-unfolded* equilibrium of π-stacking balance **2**, highlighting the formation of intramolecular aromatic stacking interaction as well as the oxygen-pi repulsion in the *folded* conformer; **(B)** The region for quantifying *folded/unfolded* ratio of **2** in the ^{1}H NMR spectrum (in chloroform). (5 **Figure 1.4** Partial side- and top-views of the X-ray crystal structure of the "two-arm" balance **2'** (left) together with their ChemDraw representations (right), highlighting the formation of a well-defined intramolecular aromatic off-set stacking interaction. The bridgehead phenyl groups are omitted for visual clarity.....7

Figure 1.4 Partial side- and top-views of the X-ray crystal structure of the "two-arm" balance **2'** (left) together with their ChemDraw representations (right), highlighting the formation of a well-defined intramolecular aromatic off-set stacking interaction. The bridgehead phenyl groups are omitted for visual clarity.....9

Figure 1.5 Measured folding ratios for our second generation π-stacking balance (**2**) and two control balances with smaller benzene (**3**) and alkene (**4**) shelves, highlighting the impact of secondary repulsive oxygen-pi interaction on the *folded-unfolded* equilibrium 10

Figure 1.6 Folding energies of π-stacking (red dots) and control balances (blue dots) and their difference (ΔΔG) used to estimate the strength of intramolecular aromatic stacking interaction (black dots) 12

Figure 1.7 Schematic representation of the two modular synthetic routes to assemble the *N*-arylimide molecular balances.....13

Figure 1.8 **(A)** Schematic representation of the heterocyclic π-stacking molecular balances developed to experimentally examine the influences of heterocyclic nitrogen in aromatic stacking interactions; **(B)** Measured ΔG's of non-heterocyclic (**2**) and heterocyclic π-stacking balances (**5**-**11**) in DMSO-d_6, highlighting the impacts of presence, charge, positioning, and substituent of heterocyclic nitrogen over the strength of aromatic stacking interactions in solution.....15

Figure 1.9 Partial top-views of the *folded* conformational regions in the X-ray crystal structures of heterocyclic π-stacking balances **5**, **7'**(two-armed), and **8**-**11**, highlighting the distinct *distal* and *proximal* orientations of *N*-heterocyclic ring in aromatic stacking interactions.....16

Figure 1.10 **(A)** Schematic representation of the substituted π-stacking balances developed to experimentally examine the electrostatic substituent effects (ESEs) in aromatic stacking interaction; **(B)** Correlation between the calculated and measured ESEs in multi-substituent stacking systems, highlighting the additive ESEs; **(C)** Measured ESEs of mono-substituent aromatic stacking systems, highlighting the distinctly different trends of *meta*- (blue dots) and *para*-ESEs (red dots).....18

Figure 1.11 **(A)** Schematic representation of the *unfolded-folded* equilibrium of dispersion balances developed to assess the dispersion contributions to aromatic stacking interactions in solution; **(B)** Plot of the estimated aromatic stacking strengths (in $CDCl_3$) *versus* the polarizabilities (Spartan 10, B3LYP, 6-31G*) of arm aromatic surfaces, highlighting the lacking of correlation in-between. 20

Figure 1.12 **(A)** Schematic representation for the CH-π and control balances developed to quantitatively study the CH-π interactions in solution; **(B)** Folding enthalpy (ΔH), entropy (-TΔS) and free energy (ΔG) values for the CH-π and control balances with OMe and OEt arms.....22

Figure 1.13 **(A)** ChemDraw representations of CH-π balances developed to examine the affinity trend of the OCH_3 with *N*-heterocyclic and non-heterocyclic arenes (top), and partial top-views of the CH-π interaction regions in the crystal structures of corresponding two-armed CH-π balance analogues (bottom), highlighting the dipole alignments between the O-C bond and *N*-heterocyclic unit; **(B)** Folding energies (in CD_2Cl_2) for the *N*-heterocyclic and non-heterocyclic CH-π balances and two control models with the non-polar CH_2CH_3 arm. ChemDraw representations of the CH-π interaction in each balance were provided 23

Figure 1.14 Schematic representations of the CH-π and control balances developed to experimentally examine the cooperativity in CH-π interactions, and measured folding energy (in chloroform) for these redesigned molecular balances, highlighting a positive cooperativity in the CH-π interaction of isopropyl group.....25

Figure 1.15 Measured ΔG's (in chloroform) for a series of deuterated and protic methyl arm balances developed to investigate D/H isotope effects in CH-π interactions ...27

Figure 1.16 **(A)** Schematic representation of the silver-bound *N*-pyridyl rotor balances and partial side-views of their crystal structures, highlighting the formation of intramolecular Ag-π interactions; **(B)** Double mutant cycle analysis of silver-bound and unbound N-pyridyl rotor molecular balances to quantify the strength of individual Ag-π interaction in solution. 29

Figure 1.17 Schematic representation of the dihedral angle (***θ***) between the succinimide and arene residing planes (top), and the histogram of ***θ*** angle (bottome) observed in the crystal structures of various methyl arm balances containing various backbridge functionalities (**Y**): 1,2-arylene, carbonyl, ether, and methylene. 31

Figure 1.18 Schematic representation of DMC analysis on the CH_2 linker molecular balances and control balances. 32

Figure 2.1 A general depiction of the molecular balance model system utilized in this study to measure the intramolecular *N*-heterocyclic π-stacking interactions formed in the *folded* conformer between an *N*-heterocyclic and a non-heterocyclic aromatic ring. 39

Figure 2.2 Comparison highlighting the greater structural and geometric diversity of the π-stacking complexes of (A) non-substituted *N*-heterocycles *versus* (B) non-substituted benzene rings.....40

Figure 2.3 The *folded* conformers of molecular balances **1-7** that form intramolecular Ph–Ph, Py–Ph, PyH^+–Ph and $PyMe^+$–Ph stacking interactions. The two interacting rings are highlighted in red (*N*-heterocycle) and blue (non-heterocycle). Balances **1'** and **3'** are two-armed analogues used in the crystallographic analysis and balance **1"** is a control used to examine influence of the difference in bridgehead Z group over the *folded/unfolded* ratios in solution. 43

Figure 2.4 Maleimide **15** and diene **16** precursors used in the syntheses of the control balances **3'** and **1"**.....46

Figure 2.5 X-ray crystal structures of balances **2** and **3'** (the bridgehead phenyl and methyl functional groups are omitted for viewing clarity). The intramolecular *N*-heterocyclic π-stacking interactions are highlighted: *N*-heterocycle in red and non-heterocycle in blue 48

Figure 2.6 Top views of the crystal structures of balances **1'**, **2**, **3'**, **4**, **6**, and **7** highlighting the intramolecular π-stacking interactions in the *folded* conformers. The corresponding ChemDraw representations are also provided for viewing clarity. ..49

Figure 2.7 Top and front views of the overlaid crystal structures for balances **1'**, **2**, **3'**, **4**, **6**, and **7** highlighting the relative geometries of the oxygen linkers on the arm over the arene shelf. Only the arene shelves and arm ether oxygens are shown, and the overlapping center six-membered aromatic ring of the shelves is highlighted in yellow. 50

Figure 2.8 ^{1}H NMR measured ΔG's (kcal/mol) for balances **1-7** at 23 °C in DMSO-d_6 at 23 °C. The ChemDraw representation of the π-stacking interaction in each balance is shown. The uncertainty in ^{1}H NMR integration measurements gives an error of less than ± 0.03 kcal/mol. 52

Figure 2.9 Schematic representations comparing the neutral Py–Ph π-stacking interactions in the *proximal* and *distal* geometries using Hunter and Sander's electrostatic quadruple model. 55

Figure 2.10 Truncated side-view (left) of the crystal structure of *folded*-**7** highlighting the presence of a CH–π interaction between the *proximal N*-methylated heterocycle on the shelf and the phenyl ring on the arm. A ChemDraw representation is also provided (right). The short distance contacts between *N*-methyl proton and phenyl carbon are highlighted with red dotted lines. 57

Figure 2.11 Correlation plot between the calculated energies from the benchmark quality computations in literature and the experimentally observed relative energies (ΔΔG's) in DMSO-d_6 for the π-stacking interactions in balances **1-7**. The computational data were from ref. 27 (open diamonds), ref. 29 (open squares) and ref. 56 (open triangles) 59

Figure 2.12 **(a)** Front-view of the crystal structure overlapping for **1'**, **2**, **3'**, **4**, **6** and **7** (the six atoms for overlapping operation are highlighted with yellow threads). The bridgehead groups are omitted for visual clarity; **(b)** Truncated back-view of the arm aromatic unit and shelf aromatic motifs; **(c)** Truncated top-view of the arm oxygen (with connected aromatic carbon) and the shelf aromatic motif. 73

Figure 2.13 Geometric parameters defined for the characterizing the intramolecular π-stacking interactions in the *folded* conformers. (**α**: plane-to-plane angle, **D**: centroid-to-plane vertical distance, and **H**: centroid-to-centroid horizontal off-set). The top ring is aromatic ring of the arm, and the bottom is ring the outer ring of the arene shelf. 73

Figure 2.14 Geometric parameters defined for characterizing the O-π interaction. (**r**: the atom-to-plain distance; **h**: atom-to-centroid horizontal displacement) 75

Figure 2.15 The compiled integration areas on ^{1}H-NMR spectra in the experiment process of |**2** + MsOH →**4**|. 77

Figure 2.16 The plot of ΔG's against the relative amount of added MsOH in the titration experiment of |**2** + MsOH → **4**| in DMSO-d_6 78

Figure 2.17 The plot of ΔG's against the relative amount of added MsOH in the titration experiment of |**3** + MsOH → **5**| in DMSO-d_6 78

Figure 2.18 The plot of ΔG's against the relative amount of added MsOH in the titration experiment of |**2** + MsOH → **4**| in CD_3CN 79

Figure 2.19 The plot of ΔG's against the relative amount of added MsOH in the titration experiment of |**3** + MsOH → **5**| in CD_3CN 79

Figure 2.20 The plot of ΔG's against the relative amount of added MsOH in the titration experiment of |**2** + MsOH → **4**| in $CDCl_3$ 80

Figure 2.21 The plot of ΔG's against the relative amount of added MsOH in the titration experiment of |**3** + MsOH → **5**| in $CDCl_3$ 80

Figure 3.1 **(A)** Crystal structure of the active site of the *Urtica dioica* agglutinin with a bound tri-*N*-acetylchitotriose (NAG3).[9] The heterocyclic residues that form CH-π interactions (Trp69, Trp23, His67 and Trp21) are highlighted (PDB entry 1EHH); **(B)** Schematic representation of the CH-π interactions of a methyl ether group with an *N*-heterocyclic and non-heterocyclic aromatic ring.....84

Figure 3.2 **(A)** Schematic representation of the *unfolded–folded* conformational equilibrium of molecular balances **1-3** for measuring the CH-π interactions of the methyl ether group; **(B)** Structures of the *folded* conformers of molecular balances

with methyl ether (**1, 2, 3,** and **6**) and with ethyl arms (**4** and **5**) and their two-armed analogues (**1'**, **2'**, **3'** and **6'**) for X-crystallographic analysis.....85

Figure 3.3 Truncated front views of the X-ray crystal structures of balances **1' (A)**, **2' (B)**, **3' (C)** and **6' (D)**, highlighting the intramolecular CH-π interactions. In the structure for **3'**, both the **3'** major and **3'** minor configurations were observed with a ratio of 62:38. The atom-to-plane distances for the intramolecular CH-π interactions are highlighted as red lines.....87

Figure 3.4 **(A)** Calculated CCSD(T)/CBS [i.e., MP2/CBS from aug-cc-pVQZ/aug-cc-pV5Z extrapolation + (CCSD(T)/aug-cc-pVTZ – MP2/aug-cc-pVTZ)] interaction energy differences (**ΔE**) between the heterocyclic and non-heterocyclic CH-π complexes [ΔE = E (CH_3**X**/Py) - E (CH_3**X**/Bz); **X** = H or OMe] at four different orientations of the dipoles (□ = 180˚, 120˚, 60˚ and 0˚); **(B)** Partial top-views of the CH-π interaction regions in crystal structures **1'** (top) and **6'** (bottom) highlighting the orientations of the C-O bond and heterocycle dipoles. 90

Figure 3.5 List of molecular balances **1-6** (shown in their *folded* conformers) and precursors used in this study and the general synthetic route 96

Figure 3.6 (a) Side views (top row) and truncated top views (bottom row) of the X-ray crystal structures **1'-3'** and **6'** highlighting the relative position between the interacting arm OCH_3 and shelf arene. The bridgehead functional groups are omitted for viewing clarity. The major structure observed in **3'** is shown here. (b) Definition of the geometric parameters for characterizing the intramolecular CH-π interactions in these crystal structures: the hydrogen-to-plane distance (***H***); the C-H-plane accessing angle (***α***); the hydrogen projection-to-centroid displacement (***d*$_1$**), the closet annular sp^2 atom of the interacting CH projection (**X**), the hydrogen projection-to-X displacement (***d*$_2$**).....110

Figure 3.7 Front views of the optimized geometry (DFT-M06/6-31G**, *in vacuum*) for the *folded* balances **1** (**A**), **2** (**B**), **3** (**D** and **E**) and **6** (**C**). To lower the computational cost, the bridgehead groups were eliminated. The interacting methyl groups and six-membered aromatic units are highlighted in green. 111

Figure 3.8 Assignment of the ^{1}H NMR spectrum for balance **1** in CD_2Cl_2. The indexing of protons in balances is provided. The *unfolded* and *folded* conformers are indicated in parenthesis......112

Figure 3.9 Assignment of the ^{1}H NMR spectrum for balance **1'** in CD_2Cl_2. The indexing of protons in balances is provided.....113

Figure 3.10 Assignment of the ^{1}H NMR spectrum for balance **2** in CD_2Cl_2. The indexing of protons in balances is provided. The *unfolded* and *folded* conformers are indicated in parenthesis. 113

Figure 3.11 Assignment of the ^{1}H NMR spectrum for balance **3** in CD_2Cl_2. The indexing of protons in balances is provided. The *unfolded* and *folded* conformers are indicated in parenthesis 114

Figure 3.12 Assignment of the ^{1}H NMR spectrum for balance **3'** in CD_2Cl_2. The indexing of protons in balances is provided. 114

Figure 3.13 Assignment of the ^{1}H NMR spectrum for balance **4** in CD_2Cl_2. The indexing of protons in balances is provided. The *unfolded* and *folded* conformers are indicated in parenthesis 115

Figure 3.14 Assignment of the ^{1}H NMR spectrum for balance **5** in CD_2Cl_2. The indexing of protons in balances is provided. The *unfolded* and *folded* conformers are indicated in parenthesis 115

Figure 3.15 Assignment of the ^{1}H NMR spectrum for balance **6** in CD_2Cl_2. The indexing of protons in balances is provided. The *unfolded* and *folded* conformers are indicated in parenthesis 116

Figure 3.16 Assignment of the ^{1}H NMR spectrum for balance **6'** in CD_2Cl_2. The indexing of protons in balances is provided. 116

Figure 3.17 Partial ^{1}H-^{1}H NOESY spectrum of balance **1** highlighting the spatial proximity between the arm OCH_3 with the shelf aromatic surface in the *folded* conformer..117

Figure 3.18 Partial ^{1}H-^{1}H NOESY spectrum of balance **2** highlighting the spatial proximity between the arm OCH_3 with the shelf aromatic surface in the *folded* conformer..117

Figure 3.19 Partial ^{1}H-^{1}H NOESY spectrum of balance **3** highlighting the spatial proximity between the arm OCH_3 with the shelf aromatic surface in the *folded* conformer..118

Figure 3.20 Partial ^{1}H-^{1}H NOESY spectrum of balance **6** highlighting the spatial proximity between the arm OCH_3 with the shelf aromatic surface in the *folded* conformer..118

Figure 3.21 Partial ^{1}H-^{1}H NOESY spectrum of balance **1'** highlighting the spatial proximity between the arm OCH_3 with the shelf aromatic surface in the *folded* conformer. 119

Figure 3.22 Partial ^{1}H-^{1}H NOESY spectrum of balance **3'** highlighting the spatial proximity between the arm OCH_3 with the shelf aromatic surface in the *folded* conformer 119

Figure 3.23 Partial ^{1}H-^{1}H NOESY spectrum of balance **6'** highlighting the spatial proximity between the arm OCH_3 with the shelf aromatic surface in the *folded* conformer 120

Figure 3.24 The *unfolded* ⇌ *folded* conformational equilibrium of balance **1** highlighting the protons ($\mathbf{H}_{arm}$ and $\mathbf{H}_{s}$) for quantifying the two conformers in solution on the ^{1}H-NMR spectra.. 121

Figure 4.1 Schematic representation of the *anti*-*syn* conformational equilibrium of a bicyclic *N*-(*o*-tolyl)succinimide molecular rotor. 124

Figure 4.2 Structures of molecular rotors **1**-**30** used in the solid-state versus solution correlation study. The *o*-tolyl rotor is highlighted in red, and the shelf surface is highlighted in blue.....125

Figure 4.3 **(a)** Schematic representation for the *anti*- and *syn*-conformers of *o*-tolyl rotor 7 occupying the same crystallographic site in crystal. **(b)** Partial side-view of crystal structures **7** highlighting the partial disorder at the *o*-tolyl rotor motif; the *syn*-conformer is highlighted in red and the *anti*-conformer is highlighted in blue. 128

Figure 4.4 A correlation plot of the measured solution and crystal χ_{syn} values for a library of 30 *o*-tolyl molecular rotors.....129

Figure 4.5 Schematic representation for the bite angle (**θ**) in the bicyclic framework: the green and purple planes were defined using the eight carbon atoms highlighted in color.....137

Figure 4.6 Correlation between the measure χ_{syn} in $CHCl_3$ and in *four* other common solvents: CH_2Cl_2(A), C_6H_6(B), CH_3CN(C), and CH_3COCH_3(D), highlighting the minimal solvent impact over χ_{syn} in solution. Numerical data are tabulated in Table 4.3.....138

Figure 4.7 Two modular synthetic routes for assembling the *o*-tolyl rotors: (left) Diels-Alder reaction between a diene derivative containing the aromatic shelf and a maleimide derivative containing the *o*-tolyl rotor and thermal imide formation (right) between a bicyclic anhydride bearing the aromatic shelf and an *o*-methyl aniline derivative. 141

Figure 4.8 The anhydride and diene derivatives (with arbitrary indexes) used in the syntheses. 141

Figure 5.1 **(a)** Molecular CT platform **1** highlighting the intramolecular donor-acceptor-donor sandwich complex; and **(b)** a schematic representation of the solvation-desolvation induced complexation change in color and geometry in **1** 167

Figure 5.2 Normalized diffuse reflectance UV-vis spectra of the purple CH_2Cl_2-solvate solid of **1** (purple line), the orange non-solvate solid of **1** (orange line), and the white solid of control **2** (dotted black line). 169

Figure 5.3 **(a)** The reversible color switching of solid **1** between purple CH_2Cl_2-solvate and orange non-solvate solid forms by precipitation from dichloromethane and acetone, respectively. **(b)** The CH_2Cl_2-solvate (left) and non-solvate (right) crystals of **1**, highlighting the distinct difference in color.. 171

Figure 5.4 Side views of the X-ray structures of **(a)** the dark purple **1**•$(CH_2Cl_2)_2$ and **(b)** the orange non-solvate **1** crystals. Insets are top views of the PYR and NDI surfaces (with linkers, frameworks, and bottom PYR surface omitted for viewing clarity). The pyrene surfaces in both crystals were disordered and only the major conformers (76% and 72%) are shown. 172

Figure 5.5 UV-vis spectra of molecular CT model **1** (red trace) and control **2** (black trace) at 0.25 mM in chloroform and the intermolecular **2**•PYR complex (green trace) at 6.55 mM in chloroform. 177

Figure 5.6 Partial UV/vis spectra of **1** in chloroform from 0.1 to 0.5 mM highlighting the charge-transfer absorption band (left), and the linear fitting of absorption (**A**) at λ_{max} = 505 nm against the concentration of **1** (right) 177

Figure 5.7 Partial UV/vis spectra of **2**·PYR in chloroform from 4.2 to 20 mM highlighting the charge-transfer absorption band (left), and the polynomial fitting of absorption (A) at λ_{max} = 511 nm against the concentration of **[2]** (right). 178

Figure 5.8 (a) Normalized solid-state diffuse reflectance UV-vis spectra for purple and red solid of **1** (inlet) and white solid of control **2**; (b) TGA traces of the purple (black) and orange (red) powders of **1**.....178

Figure 5.9 (a) Solid-state diffuse reflectance UV-vis spectra of purple and orange solids (colored solid traces) and dichloromethane-solvate and non-solvate crystals (colored dashed traces) of **1**, highlighting the similarity in color between the solid and crystal samples. (b) Soaking **1** in a minimum amount of dichloromethane and acetone, highlighting the sensitivity of color change.. 179

Figure 5.10 Powder X-ray diffraction data for the orange and purple solids of **1** together with the simulated powder patterns from the crystal structures **1** and **1**•$(CH_2Cl_2)_2$.....179

Figure 5.11 Scatter plot of the CT band λ_{max} against the rotational angle (**θ**) between PYR and NDI units of the intramolecular CT complexes in the six crystal structures of **1**, highlighting the **θ** angle difference between the solvate (■) and non-solvate structures (▲) 180

Figure 5.12 (a) Scatter plot of the CT band λ_{max} against the PYR-NDI interplanar distance (**h**) of the intramolecular CT complexes in the six crystal structures of **1**, highlighting their insignificant correlation due to the small difference in **h** (~0.05 Å) between the solvate and non-solvate structures. (b) Double-Y plot of the linker-to-NDI dihedral angle (**α**) and PYR-NDI interplanar distance (**h**) of the intramolecular CT complexes in the six crystal structures, highlighting that variations in the PYR-NDI interplanar distance were tightly related to the linker rotation. All observed conformations were included. Definitions of geometric parameters **α** and **h** are illustrated in Figure 5.13.....180

Figure 5.13 Geometric parameters defined to characterize the intramolecular PYR-NDI CT complex in **1**: (a) Chemdraw representation of **1** in side view; (b) the C-to-CN bond distance (**l**) for characterizing linker length; (c) the dihedral angle (**α**) between the N-Ph and NDI residing planes for characterizing the conformational flexibility of linker motif; (d) the twist angle (**θ**) defined by the long axes of PYR and NDI units; (e) the interplanar distance (**h**) between the PYR and NDI residing planes, the horizontal off-set (**d**) between the centroids of PYR and NDI units, and PYR-NDI stacking angle (**β**) for characterizing the intramolecular aromatic stacking interaction.....186

Figure 5.14 Solid-state diffuse reflectance UV-vis spectra of six-single crystals of **1** highlighting the λ_{max}, $\lambda_{half\text{-}height}$, and $\lambda_{on\text{-}set}$ of the CT absorption band 188

Figure 6.1 Schematic representation of three synthetic strategies to develop water-soluble molecular balances together with their corresponding starting materials. The solubilizing groups or their precursors are highlighted in yellow.....191

Figure 6.2 (A) Front view of the X-ray crystal structure of a two-arm fluorine-heteroarene balance (top) together with the ChemDraw representation (bottom), highlighting the orthogonal alignment between the C-F bond dipole and opposing pyridine ring dipole; (B) Measured folding energies for a series of F-arm balances with zero, one, and two heterocyclic nitrogens on the tricyclic shelf arene, highlighting the stabilizing orthogonal C-F···pyridine interaction. 193

CHAPTER 1

MOLECULAR BALANCES AND THEIR APPLICATIONS IN EXPERIMENTAL STUDIES OF NON-COVALENT AROMATIC INTERACTIONS[i]

[i] Shimizu, K. D.; Li, P.; Hwang, J.; Maier, J. M. To be submitted to *Acc. Chem. Res.*

1. Introduction

In this account, we briefly described our efforts to provide a refined experimental knowledge of aromatic interactions, such π-stacking,[1-4] heterocycle-π,[5] cation-π,[5] CH-π,[6-9] and Ag-π interactions,[10] through the developments and analyses of small molecular balances. These non-covalent interactions of aromatic species have been found of great importance in modern chemistry and biology and materials science.[11-14] However, the weak nature (usually several kilocalories per mole) of these aromatic interactions together with their high sensitivity to changes in the interaction geometry, participant structure, and solvent environments renders them rather elusive to experimental quantitative assessments. One successful strategy for experimentally analyzing aromatic interactions is to develop and analyze small molecular balances, a class of synthetic unimolecular model systems.[15] These molecular balances often feature one or more easily trackable conformational events that were craftily associated with the forming and breaking of one or more intramolecular aromatic interactions of interest. Energy information of the aromatic interactions under study thus could be easily accessed via conformational analyses of corresponding molecular models. The strategy allows researchers to bypass the problematic entropic penalty associated with intermolecular processes when assessing weak non-covalent interactions. Moreover, the deliberately designed molecular models often provide a means to control and interrogate the aromatic interaction geometry under study. Such character is of crucial importance to quantitative assessments of weak aromatic interactions whose geometric dependence matters but is hard to capture (*vide infra*)In the following sections, we summarized our contribution of developing molecular balances to experimentally study various aromatic interactions in solutions (Figure 1.1).

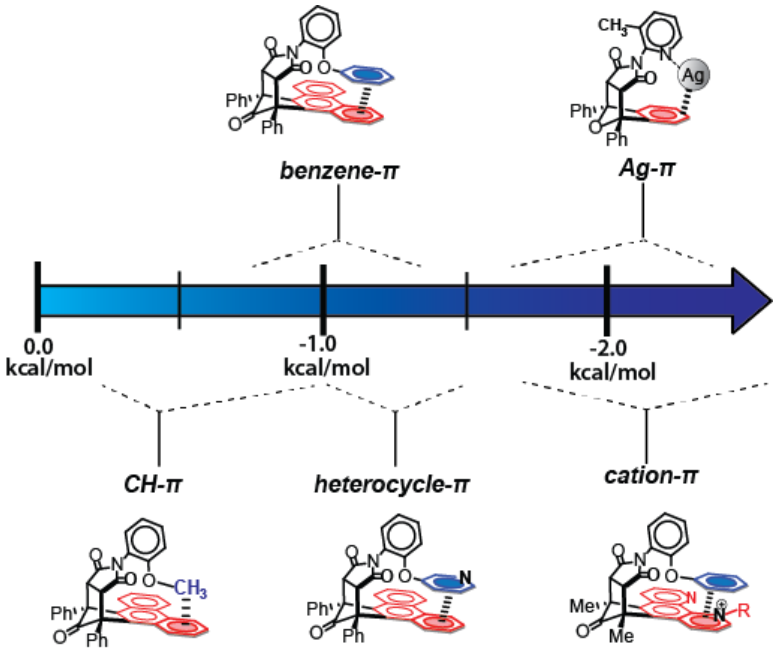

Figure 1.1 Schematic demonstration of the versatile *N*-arylimide molecular balance model system developed to quantitatively assess various aromatic interactions of different strengths in solution.

2. Molecular balances for studying aromatic π-stacking interactions

2.1 First generation *N,N'*-diphenyl naphthalenediimide molecular balances

Our journey of developing molecular balances started serendipitously from an unsuccessful attempt to develop pyrene-based fluorescent molecular switches.[1] We synthesized an atropisomeric *N,N'*-diphenyl naphthalenediimde compound (**1**) in which two pyrene fluorophores could be held at distinctly different distances in the *syn*- and *anti*-conformers (Figure 1.2A). While we failed to observe any associated change in the emission properties, we were surprised and puzzled by a significantly imbalance in the equilibrium *syn-/anti*- ratio favoring the *anti*-conformer (20:80). A clue later surfaced from the X-ray crystal structure of *anti*-conformer of **1** where the two pyrene arms each formed an intramolecular stacking interaction on both sides of NDI core (Figure 1.2C). The formation of two such interactions obviously was not possible in the *syn*-conformer as the

NDI core could only accommodate one pyrene unit to form intramolecular π-stacking interaction per face. The skewed *syn-/anti-* ratio thus might reflect the *net* stabilizing aromatic stacking interaction in the *anti*-conformer. This was indeed the case! As we strategically varied the arm arene to biphenyl, naphthalene, and eventually benzene, the *syn-anti* equilibrium energy gradually shrunk. This stability trend consisted with the expected weakening of aromatic stacking interaction due to the reduced size and polarizability of participant arene (Figure 1.2B). To our fascination, these simple atropisomeric molecules, much resembling the renowned Wilcox torsional balances,[16] demonstrated an excellent ability in accurately quantifying weak non-covalent aromatic interactions in solution. For example, a change in equilibrium ratio of 50/50 to 45/55 corresponds to a change in equilibrium energy as small as 0.12 kcal/mol. However, we also realized there were some drawbacks with these first generation balances. First, these model did not provide rigorous control over the aromatic interaction geometry as the alternative edge-to-face interaction mode could also occur in certain cases. Second, structural diversity was rather limited with these first generation balances as one aromatic surface, the NDI core, had to be fixed as part of the framework. Lastly, the excessively high rotational barrier (~27 kcal/mol) in the *N*-arylimide rotor resulted in a slow equilibration process that would require elevated temperatures to accomplish (10 h at 80 °C), limiting their applications in exploring aromatic interaction at rt.

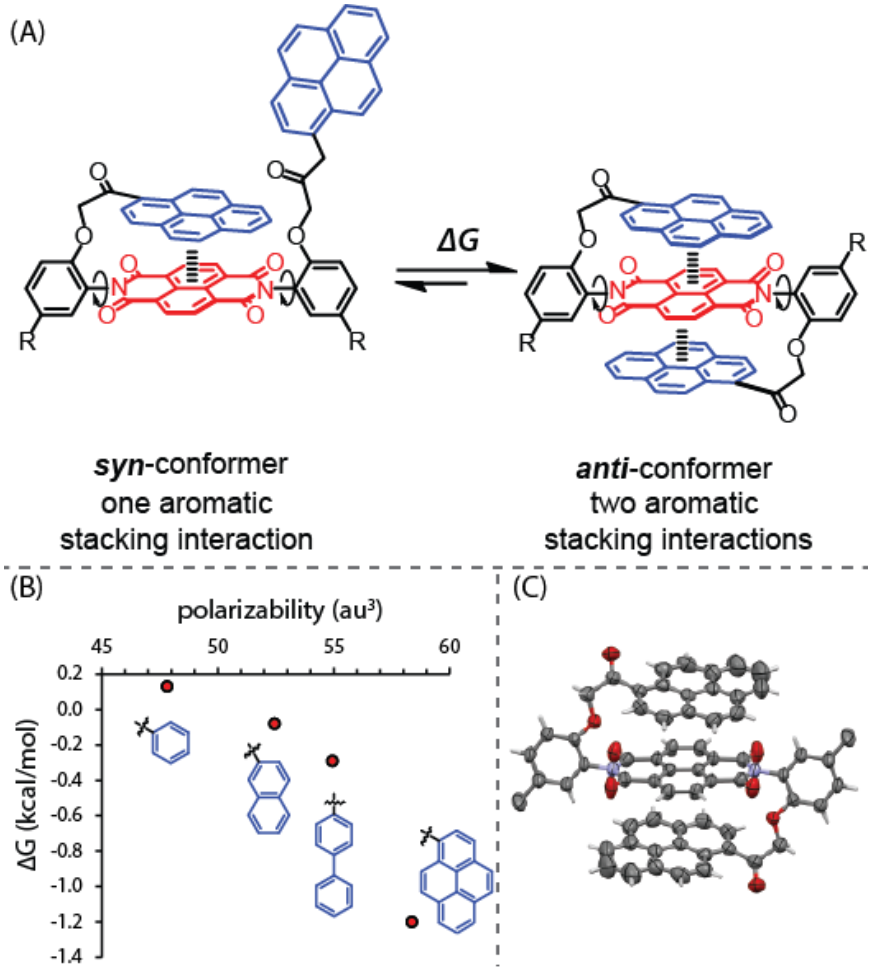

Figure 1.2 (A) ChemDraw representation of the *syn-anti* conformational equilibrium for our first generation molecular balance **1**, highlighting the formation of different number of intramolecular aromatic π-stacking interactions in the *syn* and *anti*-conformers; **(B)** The plot of measured equilibrium energies (ΔG's in TCE) of our generation balances versus calculated polarizability of the arm arenes (B3LYP, 6-31G*), highlighting the systematic change in ΔG as the arm arene varied; **(C)** Partial side-view of X-ray crystal structure of *anti*-**1**, highlighting the formation of two intramolecular aromatic π-stacking interactions.

2.2 Second generation bicyclic C-shape N-arylimide molecular balances.

We then developed our second generation molecular balances for quantitatively assessing aromatic stacking interactions. These molecular balances were built on a rigid C-shape bicyclic framework with an asymmetrically fused *N*-arylsuccinimide rotor (Figure

1.3A).[2] Two aromatic surfaces of interest could be incorporated respectively into the *ortho* substituent in the *N*-aryl rotor, referred to as the "arm", and the base region of the C-shape bicyclic framework, referred to as the "shelf". Rotation around the C_{aryl}-N_{imide} single bond led to distinct *folded* and *unfolded* atropisomers in which the arm arene was positioned differently toward the aromatic shelf. In the *folded* conformer, the two surfaces were held close to each other forming an intramolecular aromatic stacking interaction. More importantly, owing to the rigid molecular framework, the arm and shelf aromatic surfaces were forced to adopt exclusively the face-to-face off-set stacking geometry upon interaction. Such excellent control over interaction geometry was predicted by simple molecular modeling and later on confirmed by X-ray crystal structure (*vide infra*). In the *unfolded* conformer, in contrast, the arm and shelf were held far apart and the intramolecular aromatic interaction was broken. The *folded/unfolded* ratios of these molecular balances therefore provided an accurate measure for the strength of the corresponding intramolecular aromatic π-stacking interactions in solution. Restricted rotation of the *N*-arylimide rotor caused the two conformers to undergo slow exchange in solution at rt giving distinct sets of peaks in ^{1}H NMR spectrum. The *folded/unfolded* ratios thus were easily and accurately (less 5.1% error) obtained through comparing integration of the corresponding peaks in ^{1}H NMR spectra (Figure 3B). Unlike with their *N,N'*-diphenyl naphthalenediimde predecessors, the moderate rotational barrier (~21 kcal/mol) in atropisomerization of these π-stacking balances allowed the *folded-unfolded* equilibrium to be reached in 30 min (~10 half-lives) at rt in solution.

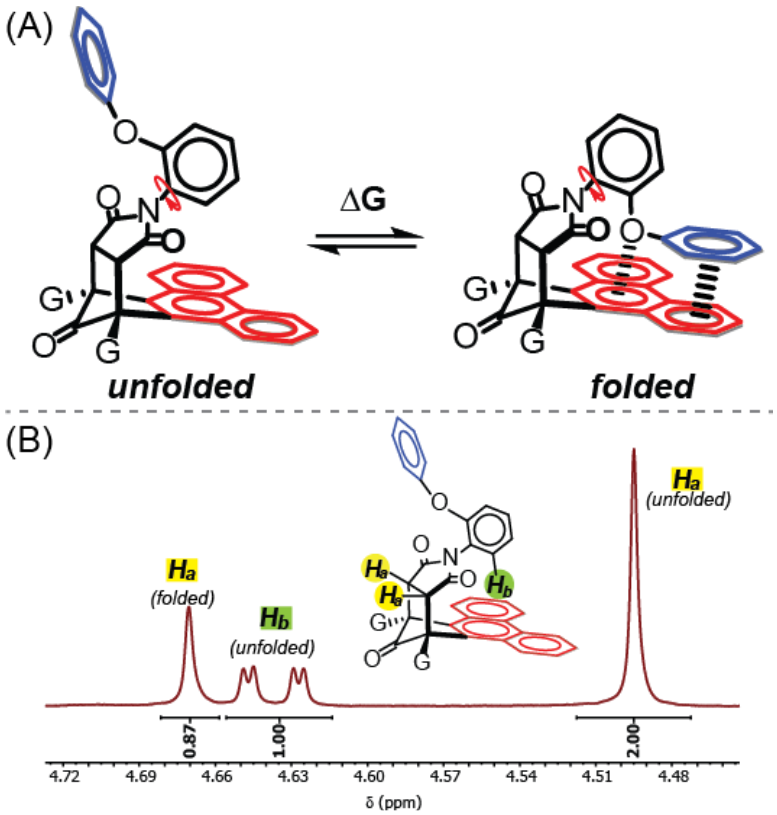

Figure 1.3 (A) ChemDraw representation of the *folded-unfolded* equilibrium of π-stacking balance **2**, highlighting the formation of intramolecular aromatic stacking interaction as well as the oxygen-pi repulsion in the *folded* conformer; **(B)** The region for quantifying *folded/unfolded* ratio of **2** in the ^{1}H NMR spectrum (in chloroform).

Formation of intramolecular aromatic stacking interactions in these second generation π-stacking balances was confirmed both in solution by ^{1}H NMR and in the solid-state through X-ray crystallography. First, distinct anisotropic effects were observed for the protons on the aromatic arm and shelf in the *folded* conformer in ^{1}H NMR spectra, suggesting the formation of aromatic stacking interaction in solution. In the *folded* **2**, for instance, clear upfield shifts were observed for the protons at the *ortho* positions on the arm phenyl group (Δδ up to -0.6 ppm) and the central bay region on the phenanthrene shelf (Δδ up to at least -1.2 ppm) due to the shielding effect upon assuming the face-to-face aromatic stacking geometry. However, the presence of multiple aromatic motifs in these

molecules complicated the further conformational analyses in solution. Fortunately, these second generation molecular balances readily crystallized in the solid-state, providing an easy access to their X-ray crystal structures to study the intramolecular aromatic stacking interactions formed therein. To ensure one arm arene always stayed in the *folded* conformation with the shelf arene in the crystallization process, "two-armed" balance analogues in which two identical aromatic arms are attached to both *ortho*-positions in the *N*-phenyl rotor were often invoked (Figure 1.4). These two-armed balances otherwise inherited all the structural properties of their one-armed relatives and thus served as an ideal surrogate in X-ray crystallographic studies. As expected, the intramolecular aromatic offset stacking interaction was unequivocally observed in the *folded* conformational region in the resolved crystal structures of these molecular balances. For example, the *folded* arm benzene ring in **2'** stacked on top of one outer benzene ring on the shelf; the two aromatic rings adopted an approximate parallel geometry (with the dihedral angle of 7.8°) and the vertical (centroid-to-plane) distance of 3.75 Å. Moreover, the top benzene ring was positioned to extend beyond the bottom shelf benzene ring with a horizontal off-set of 0.82 Å. This unique geometric constraint clearly differentiated the *ortho*-, *meta*-, and *para*-positions on the arm benzene ring upon forming π-stacking interaction, laying the foundation for many later investigations (*vide infra*).

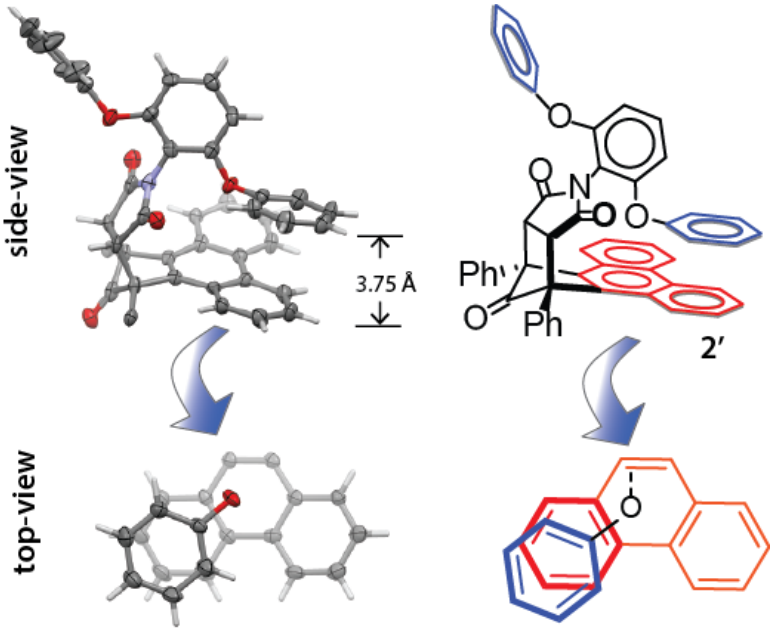

Figure 1.4 Partial side- and top-views of the X-ray crystal structure of the "two-arm" balance **2'** (left) together with their ChemDraw representations (right), highlighting the formation of a well-defined intramolecular aromatic off-set stacking interaction. The bridgehead phenyl groups are omitted for visual clarity.

2.3 Quantitative measurements of aromatic π-stacking interactions in solution

We then moved on to assess the strength of aromatic π-stacking interactions using our second generation π-stacking molecular balances. To our surprise, even with such relative simple molecular model systems as ours, quantifying weak aromatic interactions under experimental settings was not an easy job due to the inevitable interferences from secondary interactions and factors. For instance, we were initially rather bewildered that the *folded* conformers with stabilizing intramolecular aromatic interactions often existed as the minor conformers. It was only after we carefully examined two control balances with smaller benzene (**3**) and alkene shelves (**4**) did we realize the problem was caused by a concurrent repulsive secondary interaction between the linker oxygen and aromatic shelf in the *folded* conformers (Figure 1.5). This repulsive oxygen-pi interaction often

outweighed the stabilizing aromatic stacking interaction, tipping the conformational equilibrium to the *unfolded* conformer side. We became alerted that other secondary interactions, changes in dipole, and solvophobics might exit and influence the *folded-unfolded* equilibrium of these seemingly simple model systems (*vide infra*). Therefore, single measurements of the *folded/unfolded* ratio in solution provided little useful even misleading information regarding the strength of aromatic interactions under study. To address this problem, we began to invoke appropriate control models to help assess the aromatic interactions in these second generation balances.

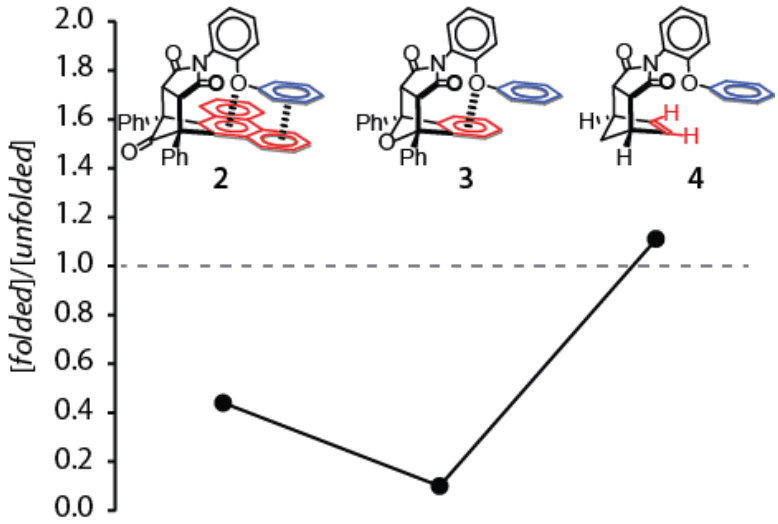

Figure 1.5 Measured folding ratios for our second generation π-stacking balance (**2**) and two control balances with smaller benzene (**3**) and alkene (**4**) shelves, highlighting the impact of secondary repulsive oxygen-pi interaction on the *folded-unfolded* equilibrium.

When quantitatively analyzing the intramolecular π-stacking interactions, we utilized the benzene shelf balances as control models to help isolate the impacts of secondary O-π repulsive interactions as well as other structural effects and solvation interferences (*vide infra*) over the *folded/unfolded* ratios. These benzene control balances could not form the intramolecular aromatic π-stacking interaction, due to its truncated

aromatic shelf, and thus *mostly* reflected the impacts from secondary interactions and factors over the *folded-unfolded* equilibrium. Therefore, the difference in folding energies ($\Delta\Delta G$) between the π-stacking and control balances provided a good estimate for the strength of intramolecular π-stacking interactions in solution. For example, the measured folding energies (ΔG) in chloroform were found to be 0.48 kcal/mol for the π-stacking balance **2** and 1.39 kcal/mol for the control balance **3**. The intramolecular aromatic interactions in π-stacking balance **2** were thus estimated to be -0.91 kcal/mol in chloroform.

Admittedly, these benzene shelf balances were not supposed to, and possibly could not, *accurately* quantify the O-π repulsion in corresponding π-stacking and CH-π balances. Instead, these control balances were designate to quantitatively estimate the influences of linker oxygen, such O-π repulsion, solvent effects (*vide infra*), possible dipole change, and other unknown intramolecular force of bias, over the equilibrium *folded/unfolded* ratios. For instance, the measured ΔG for π-stacking balance **2** was found to become more negative as the solvent polarity rises, suggesting the *folded* former became more stabilized in polar environment (Figure 1.6). However, this trend was found to rise from the interaction between the linker oxygen and solvent since the control benzene shelf balance **3** displayed the same ΔG trend. The strength of aromatic π-stacking interactions, which was estimated as $\Delta\Delta G$ between balances **2** and **3**, appeared to stay relatively constant across these non-polar and polar organic solvents. Such observed solvent trend agreed with the dispersion dominant nature of aromatic stacking interactions.

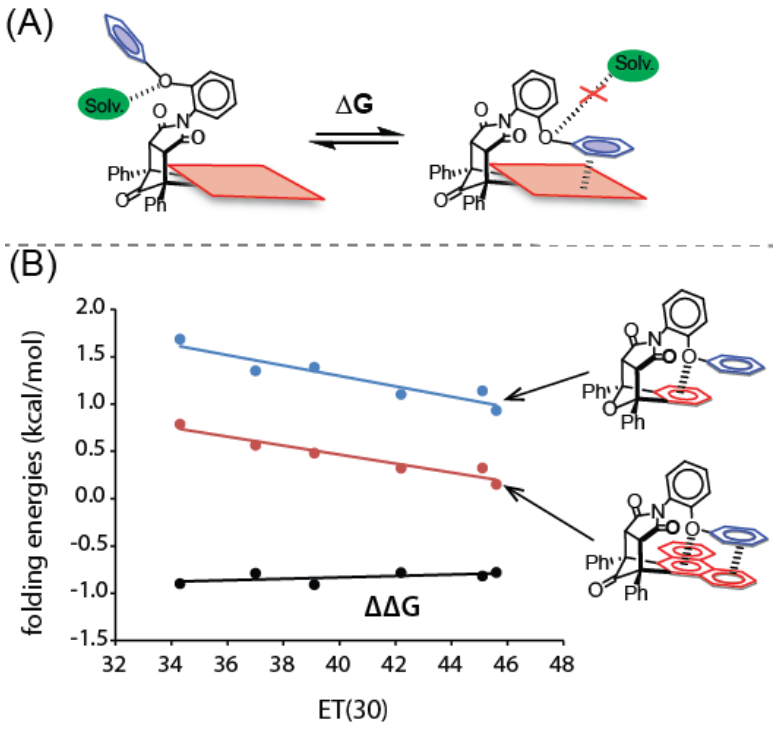

Figure 1.6 Folding energies of π-stacking (red dots) and control balances (blue dots) and their difference (ΔΔG) used to estimate the strength of intramolecular aromatic stacking interaction (black dots).

2.4 Versatile molecular balance system

Another attractive feature of our C-shape bicyclic *N*-arylimide molecular balances was their high synthetic versatility. These molecular balances could be readily assembled via one of the two modular synthetic routes from readily accessible building blocks bearing the arm and shelf motifs (Figure 1.7). For instance, a Diels-Alder reaction between maleic anhydride and a cyclic diene bearing the aromatic shelf yielded the *endo*-bicyclic anhydride. Next, the thermal imide formation between the anhydride and an aniline derivative bearing the aromatic arm gave the desired molecular balance. Alternatively, an *N*-phenyl maleimide derivative bearing the aromatic arm could be used to react with the shelf-containing diene in a thermal Diel-Alder reaction to give the C-shape molecular balance. Both synthetic routes were, simple, robust, and applicable to building blocks with

varying functionalities. This high versatility allowed us to stick with one molecular model system to systematically examine many aspects of aromatic π-stacking interactions in solution, such as the influences of heteroatom and formal charge, substituent effects, and dispersion contribution (*vide infra*), but also investigate other aromatic interactions, such as CH-π and metal-π interactions (Figure 1.1). Such unifying approach is particularly valuable in experimentally exploring weak aromatic interactions because it effectively lowers problematic inter-system bias.

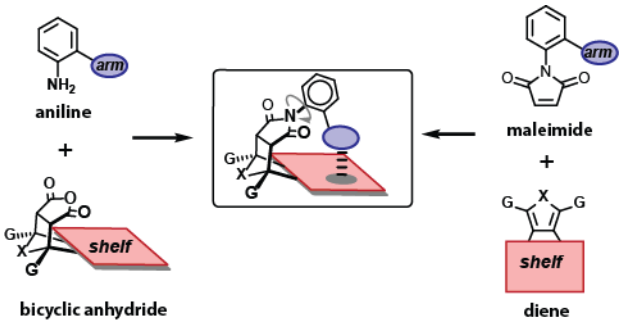

Figure 1.7 Schematic representation of the two modular synthetic routes to assemble the *N*-arylimide molecular balances.

4. In-depth experimental studies of aromatic π-stacking interactions

4.1 Impact of N-heterocycles in aromatic π-stacking interactions

Next, we experimentally examined the impacts of presence, positioning, charge, and substituent effects of heterocyclic nitrogen in aromatic stacking interactions with a series of heterocyclic π-stacking balances.[5] Aromatic *N*-heterocycles are ubiquitous in both synthetic and biological systems, and their aromatic interactions are frequently found vital to various important chemical and physical processes. However, our knowledge on *N*-heterocyclic aromatic stacking interactions had been largely relying on theoretical computations[17-19] due to the difficulty in appropriately handling the geometric variables in *N*-heterocyclic π-stacking interactions with molecular model systems (*vide infra*). The

excellent ability of π-stacking balance **2** to effectively enforce a well-defined intramolecular off-set π-stacking interaction (Figure 1.4) presented us an opportunity to solve this problem. Incorporating one or more neutral or charged pyridine unit(s) into the arm or shelf arene of the *N*-arylimide balance model provided a series of heterocyclic π-stacking balances that formed intramolecular aromatic π-stacking interactions much resembling those of a neutral or charged pyridine-benzene off-set stacking complex at various geometries (Figure 1.8A). Their ΔG's thus offered a measure for the influences of heterocyclic nitrogen in aromatic stacking interactions in solution. Examination of the measured ΔG's for these heterocyclic π-stacking balances revealed that the presence of nitrogen in aromatic surface in general stabilized the aromatic stacking interaction (Figure 1.8B) possibly due to an enhanced electrostatic interaction.[18] For example, introducing a neutral nitrogen was found to bring an additional stabilization of -0.4 to -0.7 kcal/mol to the measured ΔG for π-stacking balances **5**-**7** in comparison to their non-heterocyclic analogue **2**. The stabilizing effect was expected to become even more pronounced when a positive charge was introduced to the heterocyclic nitrogen.[19] Indeed, the cationic heterocyclic π-stacking balances **8**-**11** were more stabilizing than their neutral counterparts by up to -1.4 kcal/mol.

We also experimentally examined the influence of the positioning of nitrogen in *N*-heterocyclic aromatic stacking interactions. Built upon the same rigid C-shape bicyclic framework, these heterocyclic π-stacking balances possessed a unique ability to isolate varying orientations within *N*-heterocyclic π-stacking interactions. Strategic incorporation of pyridine units into the arm or shelf arene allowed the *N*-heterocyclic ring in intramolecular π-stacking interactions to position its nitrogen far way, referred to as the

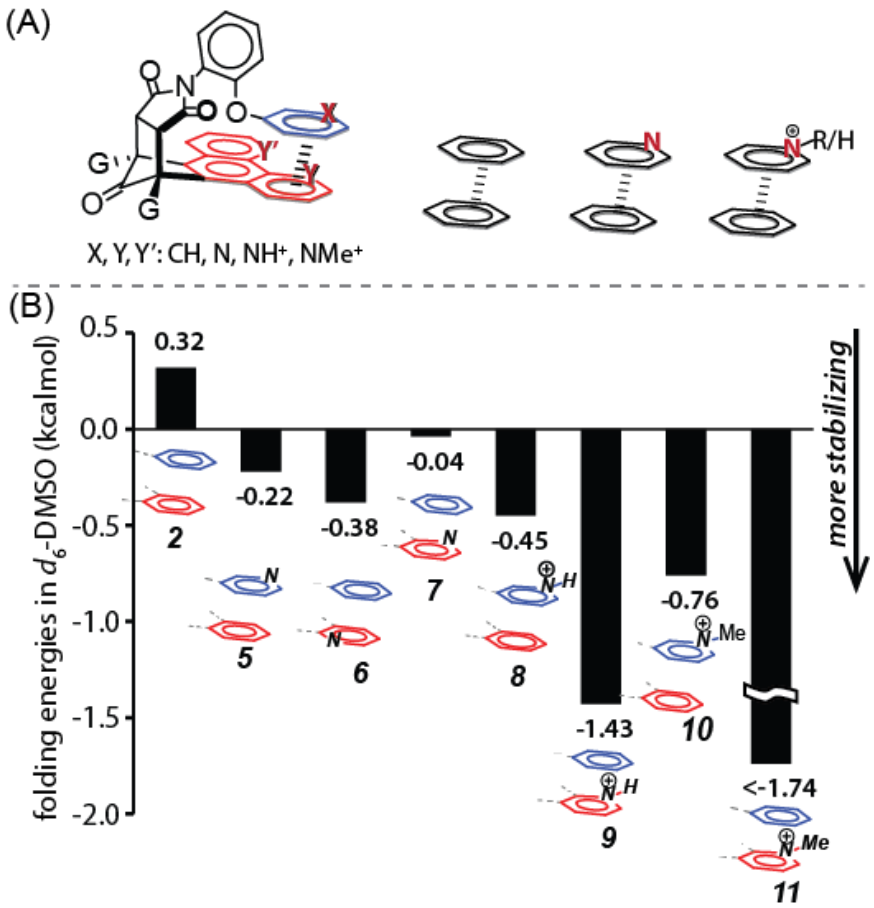

Figure 1.8 (A) Schematic representation of the heterocyclic π-stacking molecular balances developed to experimentally examine the influences of heterocyclic nitrogen in aromatic stacking interactions; **(B)** Measured ΔG's of non-heterocyclic (**2**) and heterocyclic π-stacking balances (**5-11**) in DMSO-d_6, highlighting the impacts of presence, charge, positioning, and substituent of heterocyclic nitrogen over the strength of aromatic stacking interactions in solution.

"*distal*" orientation, or closely approaching, referred to as the "*proximal*" orientation, against the opposing aromatic surface as later confirmed by X-ray crystal structures (Figure 1.9). ΔG analyses revealed clear orientational dependences in the strength of *N*-heterocyclic π-stacking interactions. For example, the *distal* orientation was favored (by -0.3 to -0.7 kcal/mol) in neutral heterocyclic π-stacking interactions, while the proximal orientation was much more preferred (by at least -1.0 kcal/mol) among the charged ones.

Such observed orientational trend in *N*-heterocyclic π-stacking interactions reaffirmed the significant electrostatic nature of these aromatic interactions.[17] Besides, good overall correlations were found between these experimentally measured ΔG's and literature benchmark theoretical predictions,[17-19] demonstrating the excellent performance of molecular balances in reporting aromatic stacking interactions.

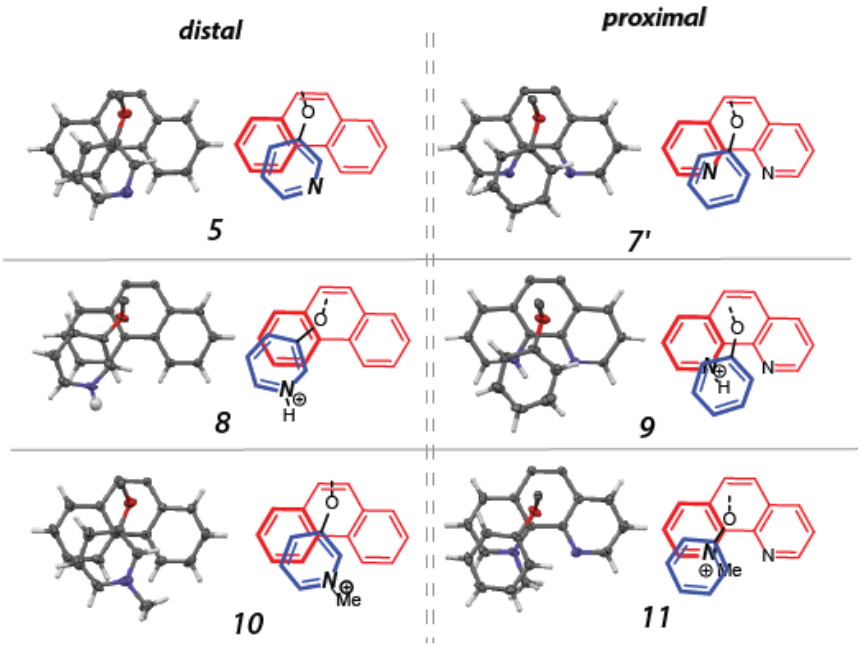

Figure 1.9 Partial top-views of the *folded* conformational regions in the X-ray crystal structures of heterocyclic π-stacking balances **5**, **7'**(two-armed), and **8**-**11**, highlighting the distinct *distal* and *proximal* orientations of *N*-heterocyclic ring in aromatic stacking interactions.

4.2 Additive electrostatic substituent effects (ESEs) in aromatic π-stacking interactions.

Greatly encouraged by the success with *N*-heterocyclic π-stacking interactions, we took on another challenge to experimentally probe the additivity (or the lack thereof) in the electrostatic substituent effects (ESEs).[3] Introducing substituents has been one of the most commonly used methods to modulate the electrostatic nature of aromatic surfaces and thus their π-stacking strengths. Recent theories had predicted additive ESEs in aromatic

stacking system with multiple substituents.[20,21] In addition, a "direct substituent-pi interaction theory" had emerged to challenge our conventional perception of aromatic stacking interactions.[22] However, a complimenting experimental investigation was still yet to be seen, presumably a consequence of the difficulty in experimentally dissecting the substituent effects in multi-substituent aromatic stacking systems. As demonstrated earlier, our *N*-arylimide π-stacking balance system had a unique ability to distinguish the *ortho*-, *meta*-, and *para*-positions in the arm phenyl group upon forming the intramolecular off-set π-stacking interactions. Such geometric feature presented an opportunity to experimentally parse the substituent effects in multi-substituent aromatic systems (Figure 1.10A). Five substituents (CH_3, OCH_3, Cl, CN, and NO_2) of varying electronic nature in various substitution patterns (mono-, di-, and tri-substituted) were introduced to the arm phenyl group to produce a library of 21 substituted π-stacking balances. The strengths of these substituted aromatic stacking interactions in solution were then quantitatively evaluated in a similar fashion as before with the aid of corresponding control balances. Additive ESEs were clearly observed for these substituted aromatic stacking interactions; experimental ESEs of di- and tri-substituents system could be accurately (within 0.01 to 0.02 kcal/mol) predicted by adding up the ESEs in mono-substituent systems (Figure 1.10B). Furthermore, the *para*- and *meta*-substituents were found to exert distinctly different ESEs (Figure 1.10C), suggesting a distance dependence in ESEs. *meta*-ESEs were consistently stronger than the *para*-ESEs, and the energy gap clearly widened as the ESEs increased. These observations pointed to a distinct electrostatic nature of ESEs in aromatic stacking interactions, lending an experimental support to the recent direct substituent-pi interaction theory.[23]

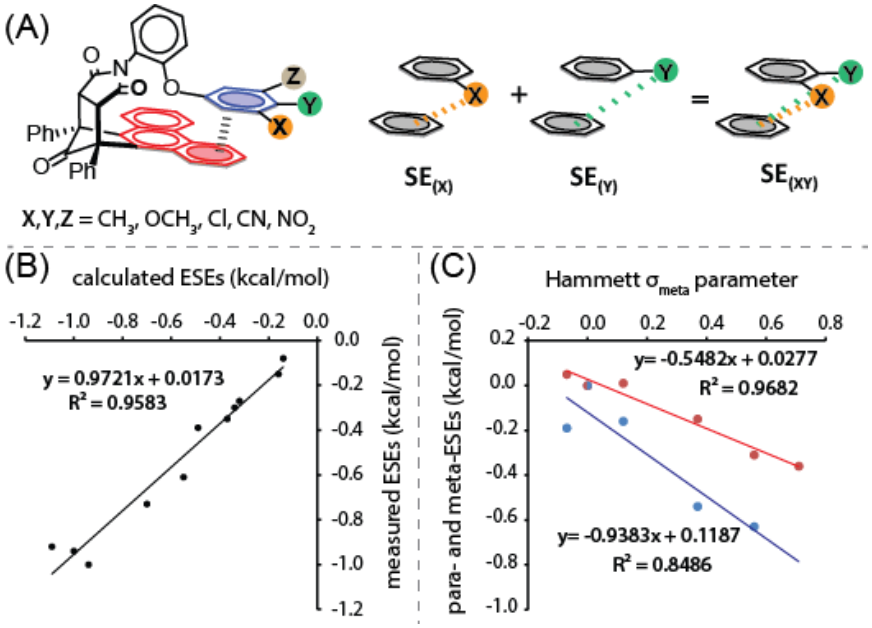

Figure 1.10 (A) Schematic representation of the substituted π-stacking balances developed to experimentally examine the electrostatic substituent effects (ESEs) in aromatic stacking interaction; **(B)** Correlation between the calculated and measured ESEs in multi-substituent stacking systems, highlighting the additive ESEs; **(C)** Measured ESEs of mono-substituent aromatic stacking systems, highlighting the distinctly different trends of *meta*- (blue dots) and *para*-ESEs (red dots).

4.3 Dispersion contribution in aromatic π-stacking interactions in solution

Very recently, we further innovated our *N*-arylimide π-stacking balances and examined contributions of dispersion forces to the strength of aromatic stacking interactions in solution (Figure 1.11A).[4] Dispersion forces have been deemed as the dominant source of attraction in aromatic stacking interactions in *vacuum* or the gas phase,[24-26] whereas their role in solution has been controversial. Specifically, the dispersion contributions were proposed to be much weakened in solution[27] presumable due to the competing solvent-solute interactions.[28] Assessments of the dispersion contributions in solution were often complicated by the solvophobic effects (the solvent dispersion effects),[29] which also scale with the size of aromatic surfaces. One strategy to circumvent

the interference from solvophobic effects was to fix the contact area of aromatic stacking interactions in analysis. Our *N*-arylimide balances in turn offered a suitable venue for such analyses of dispersion contribution (*vide infra*). The arm aromatic surface was thus systematically varied in the size and conjugation length (benzene, naphthalene, phenanthrene, biphenyl, diphenylethene, and diphenylacetylene) to yield a series of dispersion balances. Like their parent **2**, these dispersion balances enforced the well-defined off-set π-stacking geometry regardless the variations in the arm arene and thus essentially fixed a relative constant area of direct contact across various intramolecular π-stacking interactions. Examination of these aromatic stacking interactions involving large size arenes revealed that increase in size of the aromatic surface did result in increasing stabilization in solution, but the extent was much smaller than predicted by theory (Figure 11B). For instance, increasing the arene from benzene to naphthalene only increased the strength of corresponding aromatic interaction by 26% in solution as opposed to a 230% increase predicted by theory. Extending the conjugation length, like changing from biphenyl to diphenylethene, brought a destabilizing effect to aromatic stacking interactions, conflicting the positive correlation with polarizability predicted by theory. Further analyses revealed that a large portion (up to 50%) of the apparent stabilizing effects associated with the arenes of larger size and conjugation might in fact rise from the corresponding ESE's. Overall, our results suggested that dispersion contributions in aromatic stacking interactions were rather weakened in solution, pointing the significant competing solvent dispersion effects.

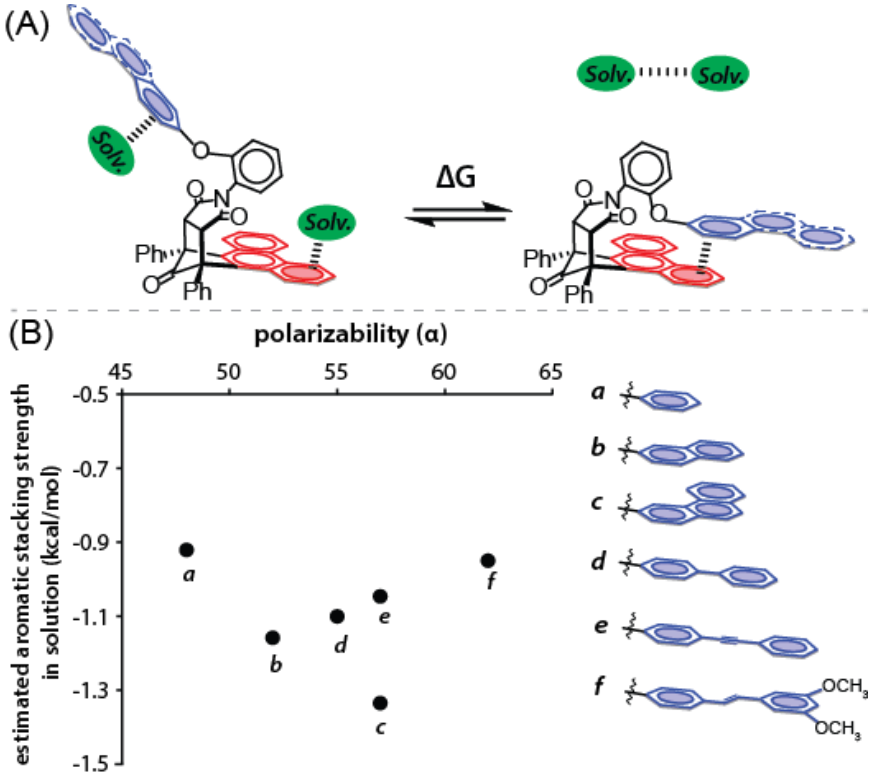

Figure 1.11 (A) Schematic representation of the *unfolded-folded* equilibrium of dispersion balances developed to assess the dispersion contributions to aromatic stacking interactions in solution; **(B)** Plot of the estimated aromatic stacking strengths (in $CDCl_3$) *versus* the polarizabilities (Spartan 10, B3LYP, 6-31G*) of arm aromatic surfaces, highlighting the lacking of correlation in-between.

5. Molecular balances for studying aliphatic CH-π interactions

Another important family in aromatic interactions is the ubiquitous weak attractions between alkyl and arene groups, that is, the aliphatic CH-π interactions.[30] These CH-π interactions had been primarily studied in solid-state crystal structures[31,32] and computational models,[33-35] but remained elusive to direct quantitative assessments in solution due to their weak and non-directional nature. We reckoned that the C-shape framework of our *N*-arylimide molecular balances should well accommodate the typical CH-π interaction geometry (the H-to-C distance cutoff of 3.05 Å),[36,37] providing us an opportunity to study weak CH-π interactions in solution. In this section, we briefly

described our efforts in developing various CH-π balances to assess the strength, *N*-heterocycle effects, cooperativity, and deuteratium isotope effects in CH-π interactions in solution.

5.1 Quantitative measurements of CH-π interactions in solution

Incorporating alkoxyl groups of varying size and shape (OR: R=Me, Et, *i*-Pr, *n*-Bu, and *c*-Hex) as the arm motif of the C-shape *N*-arylimide bicyclic platform yielded a series of CH-π balances for quantitatively studying CH-π interactions in solution (Figure 1.12A).[6] The formation of intramolecular CH-π interactions in these balances was confirmed both in solution by ^{1}H NMR and in the solid-state by X-ray crystal structures. Corresponding benzene shelf balances were utilized as control models to help isolate the interferences of the repulsive O-π interaction and solvent dispersion in quantitative analyses of CH-π interactions. The CH-π interaction between the methoxyl arm and aromatic shelf was found to be weakly attractive (-0.95 kcal/mol) in solution. Increasing the alkyl group size from methyl to ethyl, however, only slightly enhanced the CH-π interaction (by -0.15 kcal/mol or 16%) in contrast to the expected nearly two-fold enhancement. Such lower-than-expected increase in strength was attributed to the additional CH_3 group extending beyond the aromatic shelf and thus unable to form a strong CH-π interaction. This explanation was supported by the small enthalpic difference between the OEt and OMe arm CH-π balances ($\Delta\Delta H$ = -0.14 kcal/mol) observed in the van't Hoff analyses (Figure 1.12B). Furthermore, we spotted an increased entropic penalty ($-T\Delta\Delta S$ = ~0.6 kcal/mol) in the *folded* OEt arm balances, which was likely associated with the loss of rotational freedom around the C-O bond.[38] This unfavorable entropic change might also contribute in part to the weak CH-π interaction observed in the OEt arm balance. Similar entropic

penalties were also suspected to occur but to a greater degree in the OR arms with larger alkyl groups (*i*-Pr, *n*-Bu, and *c*-Hex), which would significantly attenuate the CH-π interactions. However, these CH-π interactions could not be accurately measured with our molecular balances due to the *folding* ratios exceeding the lower limit (1/20) for accurate quantitative analysis (± 0.03 kcal/mol).

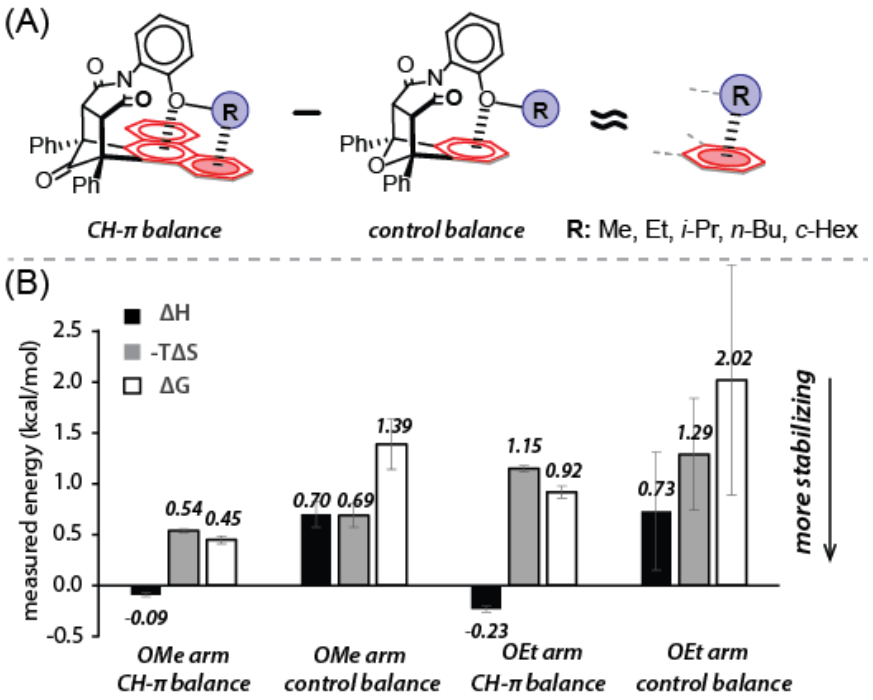

Figure 1.12 (A) Schematic representation for the CH-π and control balances developed to quantitatively study the CH-π interactions in solution; **(B)** Folding enthalpy (ΔH), entropy (-TΔS) and free energy (ΔG) values for the CH-π and control balances with OMe and OEt arms.

5.2 Impacts of *N*-heterocyclic arene in CH-π interactions

We next to investigate the impacts of nitrogen-containing heterocycles (*N*-heterocycles) in CH-π interactions (Figure 1.13). *N*-heteroarenes had been found in a higher percentage of the carbohydrate-aromatic interactions in Nature.[39,40] However, *N*-heteroarenes were *not* considered to form stronger CH-π interactions than their isosteric

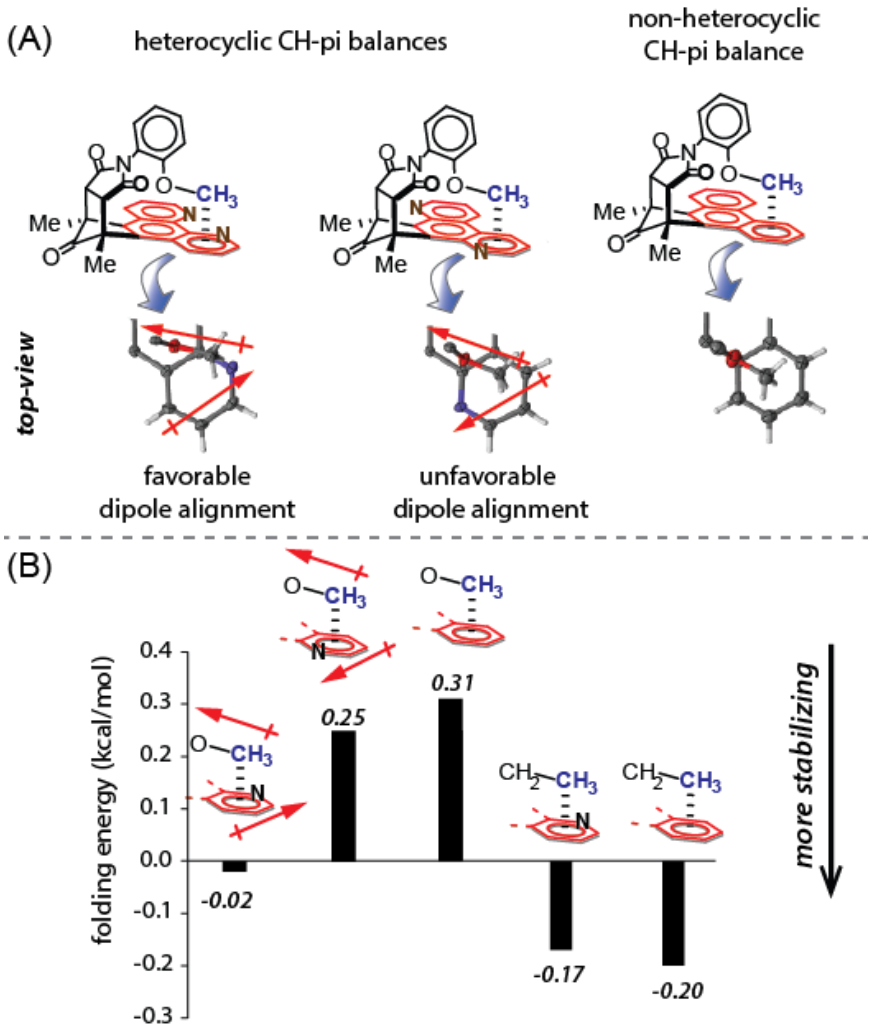

Figure 1.13 (A) ChemDraw representations of CH-π balances developed to examine the affinity trend of the OCH_3 with *N*-heterocyclic and non-heterocyclic arenes (top), and partial top-views of the CH-π interaction regions in the crystal structures of corresponding two-armed CH-π balance analogues (bottom), highlighting the dipole alignments between the O-C bond and *N*-heterocyclic unit; **(B)** Folding energies (in CD_2Cl_2) for the *N*-heterocyclic and non-heterocyclic CH-π balances and two control models with the non-polar CH_2CH_3 arm. ChemDraw representations of the CH-π interaction in each balance were provided.

non-heterocyclic analogues. Thus, whether this phenomenon was a statistical consequence of the greater abundance of *N*-heteroarenes in Nature or due to a greater affinity actually occurred between *N*-heteroarenes and carbohydrates remained unclear. Our OCH_3 arm CH-π balances offered a means to investigate this issue: 1) the arm OCH_3 structurally

resembled the polarized CH units in carbohydrates and thus served as a minimalistic model in probing the corresponding aromatic interactions, and 2) the tricyclic aromatic shelf could be easily mutated into isosteric *N*-heteroaromatic surfaces allowing easy assessments of the *N*-heterocycle effects (Figure 1.13A). Examination of ΔG's of these OCH_3 arm CH-π balances revealed that presence of heterocyclic nitrogen did significantly increase the affinity (by -0.3 kcal/mol) between the OCH_3 and aromatic surface (Figure 1.13B). The stabilizing effect, however, was not due to an enhanced CH-π interaction itself but the favorable dipole-dipole interaction between the C-O bond and *N*-heterocyclic ring. Structurally implementing an unfavorable dipole alignment in the *N*-heterocyclic CH-π region effectively decimated the stabilizing effect. Analysis of control models that had the polar C-O bond mutated to a non-polar C-C bond confirmed the CH-π interactions stayed little changed between non-heteroarene and isoteric *N*-heteroarene (Figure 1.13B).

5.3 Experimental assessments of cooperativity in CH-π interactions

We then redesigned our CH-π balances and experimentally examined the cooperativity of CH-π interactions. Cooperative CH-π interactions had been widely observed in various applications but still remained less understood. Theory suggested a decrease in interaction energy per carbon as the alkyl group increased in size, that is, a negative cooperativity.[41,42] However, a complement experimental investigation on this matter was still in void. To effectively examine cooperative CH-π interactions, the C-shape *N*-arylimide CH-π balances were redesigned to have the arm alkyl group directly attached to the *N*-succinimide rotor so that large alkyl groups, such as ethyl and isopropyl could access the shelf arene to form strong CH-π interactions (Figure 1.14). This improved design also conveniently eliminated the repulsive O-π secondary interaction. Measured

ΔG's of these CH-π balances therefore directly reflected the strength of intramolecular CH-π interactions in solution. This method was confirmed by the near-zero ΔG's observed for

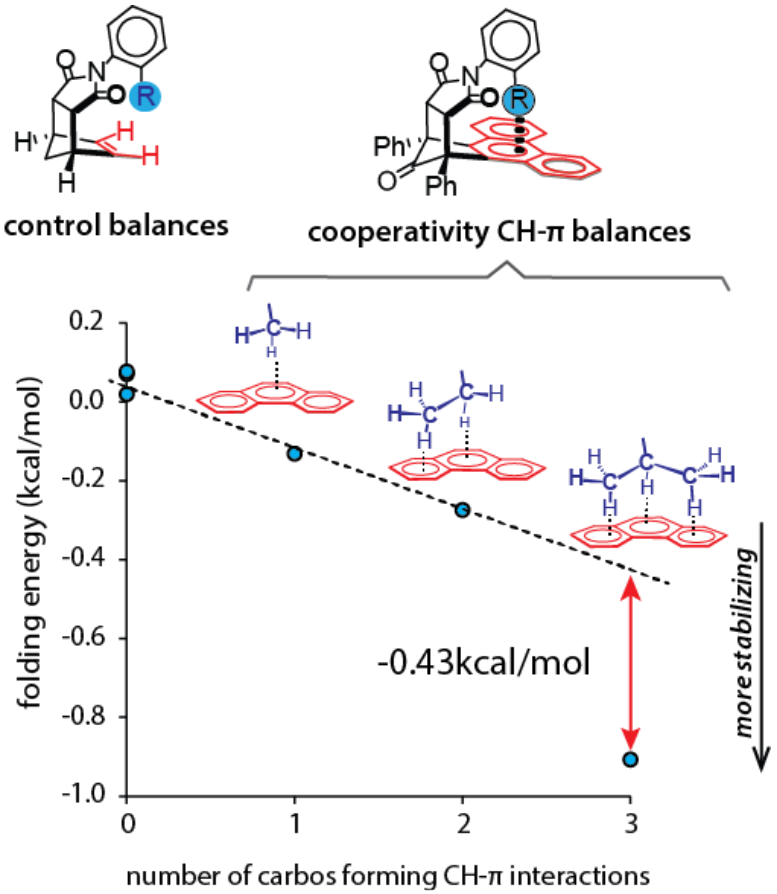

Figure 1.14 Schematic representations of the CH-π and control balances developed to experimentally examine the cooperativity in CH-π interactions, and measured folding energy (in chloroform) for these redesigned molecular balances, highlighting a positive cooperativity in the CH-π interaction of isopropyl group.

the control balances with a truncated alkene shelf. The CH-π interactions of methyl and ethyl groups were found to linearly correlate with the number of participating alkyl carbons rather than the observed CH-π short contacts, agreeing well with the dispersion dominated nature of CH-π interactions.[43] In contrast, the large *iso*-propyl group was found to form much stronger CH-π interactions than predicted by the additive trend, suggesting a positive

cooperativity in CH-π interactions. The discrepancy with the precedented computational studies was likely attributed to the difference in aromatic surfaces of choice. The literature computations utilized relative small surfaces to accommodate large alkyl groups, which might cause weakened CH-π interactions and thus an apparent negative cooperativity.[41]

5.4 Deuterium isotope effects in CH-π interactions

We also experimentally investigated the D/H isotope effects in CH-π interactions with a series of methyl arm CH-π balances.[9] D/H isotope effects had been a powerful tool for studying non-covalent interactions in terms of verifying the formation of interactions of interest, probing their stability trends, and their corresponding isotope labeling in various occasions.[44] However, whether the CH-π interactions showed any D/H isotope effect remained controversial due to conflicting reports in literature.[45-47] The methyl arm CH-π balances had demonstrated an excellent performance in directly reporting the CH-π interaction strengths in solution with high accuracy (±0.03 kcal/mol), offering us a venue to experimentally investigate the D/H isotope effects (or the lack thereof) in CH-π interactions. Thus a series of deuterated and protic methyl arm balances that contained various aromatic shelves and molecular frameworks were assembled to thoroughly examine the CH-π and CD-π interactions in solution (Figure 1.15). Analyzing ΔG's of these deuterated and protic balances found the very small even insignificant difference in strength (within the error of ±0.03 kcal/mol in quantitative analysis) between CH-π and CD-π interactions. Further van't Hoff analyses and dispersion-corrected DFT calculation (PDE-D2/6-31+G*) confirmed the very small or non-existent D/H isotope effect in the CH-π interactions. Reevaluating the literature cases that reported D/H isotope effects in CH-π interactions suggested that the isotope effects observed therein might actually rise from the

attenuated sterics rather than enhanced CH-π interactions.[45,46] The slightly shorter vibrationally averaged bond length of C-D bonds than C-H bond (by ~0.005A) would ensue a noticeable steric-driven D/H isotope effect if deuterated alkyl group of interest was confined to a crowded environment. Such steric-driven D/H isotope effect was rather minimal in our molecular balance as the methyl arm had sufficient conformational freedom in the *folded* conformers to avoid severe steric clashing with other functional groups.

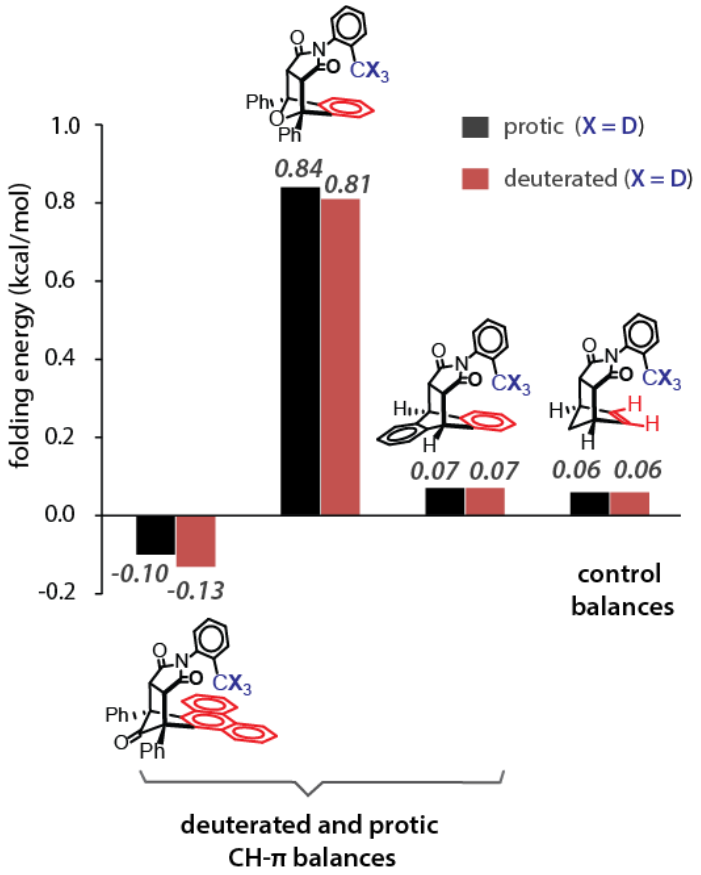

Figure 1.15 Measured ΔG's (in chloroform) for a series of deuterated and protic methyl arm balances developed to investigate D/H isotope effects in CH-π interactions

6. Molecular balances for studying the silver-π interactions in solution

We recently reengineered a series of *N*-(3-methylpyridin-2-yl) succinimide balances to experimentally study the silver-π interactions in solution.[10] The weak

attractions between silver atoms and aromatic surfaces, often referred to as the silver-π interactions, had been widely utilized in many chemical processes and applications.[48,49] However, individual silver-π interactions had been weak and difficult to capture and measure experimentally. Relevant experimental studies had been mostly focus on systems having multiple Ag-π interactions,[50-54] and the strength of individual silver-π interactions in solution remained unclear. Incorporating an *ortho*-nitrogen in the *N*-aryl rotor enabled the *N*-arylimide balances to accommodate intramolecular Ag-π interactions as later confirmed in the solid-state by X-ray crystal structures (Figure 1.16A). In solution, these reengineered balances stoichemically bound silver ions (1:1) and thus displayed distinct changes in folding energy. The strength of individual intramolecular Ag-π interactions in solution was quantified via double mutant cycle (DMC) analyses on the measured ΔG's for the silver-bound and unbound balances (Figure 1.16B). We found that an individual intramolecular Ag-π interaction was stabilizing in nature and quantified to be -1.34 to 2.63 kcal/mol in dichloromethane. Increase in solvent polarity brought a detrimental influence on the Ag-π interaction, presumable due to the competing binding between the silver ions and solvent molecules. Through tweaking the C-shape molecular framework, we also investigated the impact of interaction geometry in Ag-π interactions. These weak silver-π interactions were found to be highly sensitive to changes in interaction geometry. A decrease in the N-Ag-π angle from 161° to 145°, for instance, ensued approximately 1.3 kcal/mol or 50% drop in the Ag-π interaction strength (Figure 1.16A).

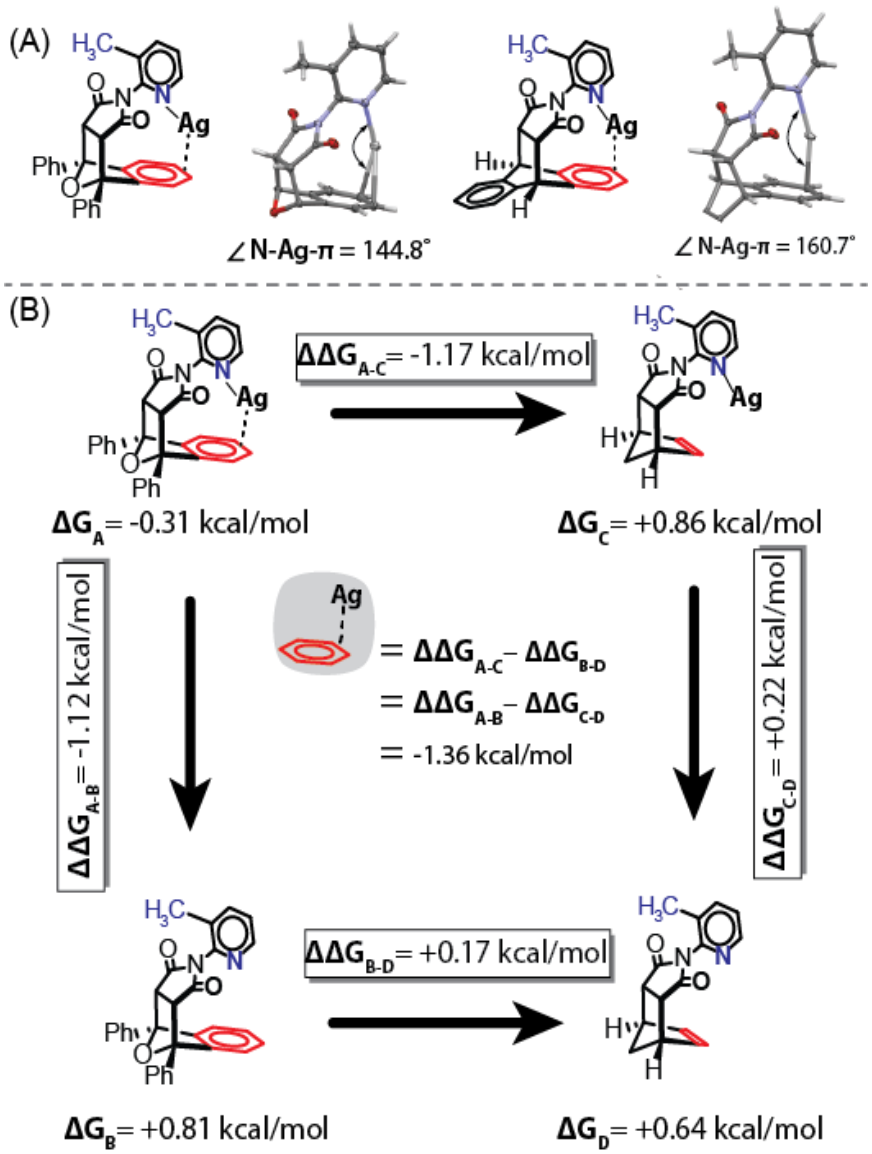

Figure 1.16 (A) Schematic representation of the silver-bound *N*-pyridyl rotor balances and partial side-views of their crystal structures, highlighting the formation of intramolecular Ag-π interactions; **(B)** Double mutant cycle analysis of silver-bound and unbound N-pyridyl rotor molecular balances to quantify the strength of individual Ag-π interaction in solution.

7. Re-evaluation of the C-shape *N*-arylimide molecular balance system

Another fascinating aspect of continuously and intensely working on these *N*-arylimide molecular balances is that we could gain a tremendous amount of knowledge regarding the model system itself. This knowledge helps avoid false interpretations of

experimental data and aids to the development of future models. In this section, we further elaborated our C-shape *N*-arylimide molecular balance system through discussions of the framework and linker effects. We hoped such close-up examinations would help readers better apprehend the capability of our molecular balances in experimentally studying aromatic interactions as well as the potential directions for future innovation.

7.1 Framework effects

One unparalleled character of small molecular balances in studying non-covalent interactions is the excellent control over interaction geometry. Not only do they provide a higher certainty in the non-covalent interactions under study, but they offer a unique opportunity to interrogate the geometry of non-covalent interactions experimentally. An example in this regard was from Ams and co-workers on the Wilcox balance.[55] Our C-shape *N*-arylimide balances turned out to be particularly apt in modulating the aromatic interaction geometry. For instance, we had demonstrated with a series of methyl arm balances that the dihedral angle ($\boldsymbol{\theta}$) between the succinimide and aromatic shelf could be gradually altered up to 10° simply by varying the backbridge functionality (Figure 1.17).[56] These variations in $\boldsymbol{\theta}$ angle translated into pronounced changes in the relative positioning of the methyl arm and shelf arene upon forming the CH-π interactions (up to 0.7 Å in the C-to-arene distance). This structural versatility pointed to the possibility of experimentally probing the Lennard-Jones type of potential for various aromatic interactions. Indeed, we had briefly demonstrated such research strategy in our Ag-π interaction study in which different backbridge functionalities ensued different Ag-π interaction geometries and stability profiles.[10]

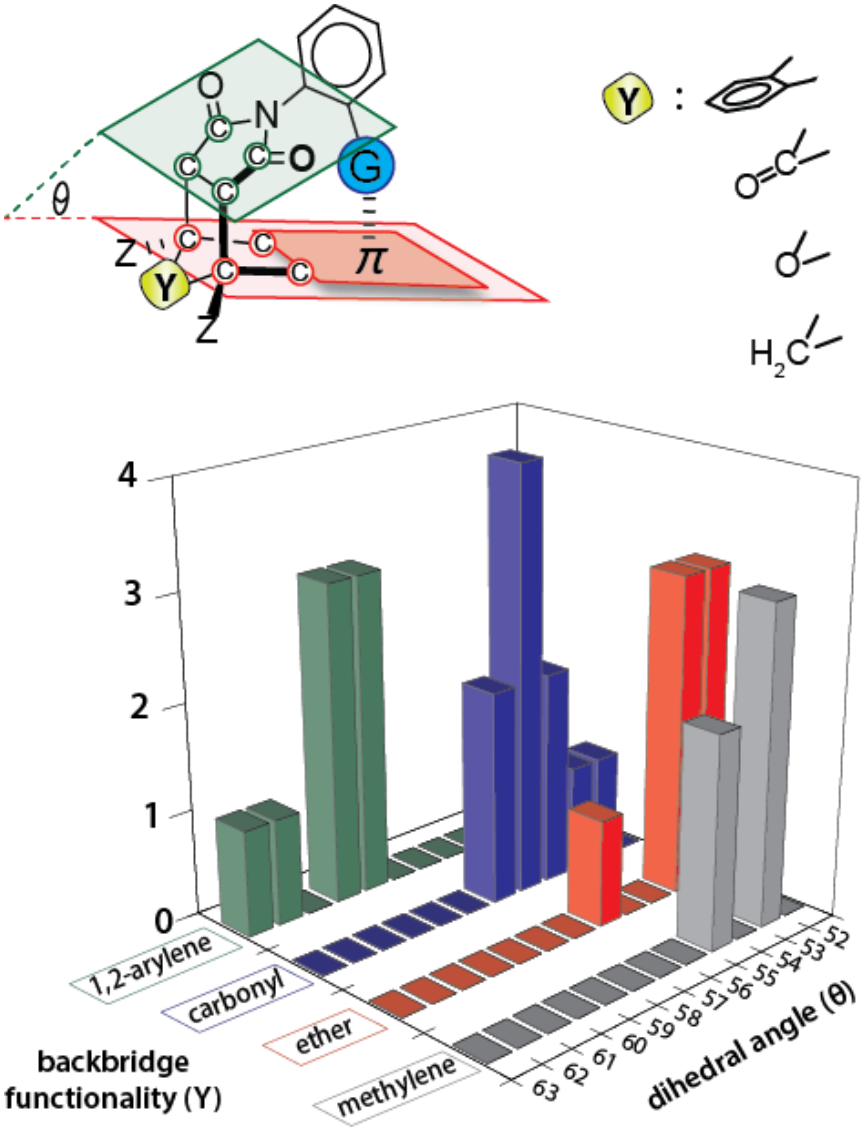

Figure 1.17. Schematic representation of the dihedral angle (***θ***) between the succinimide and arene residing planes (top), and the histogram of ***θ*** angle (bottome) observed in the crystal structures of various methyl arm balances containing various backbridge functionalities (**Y**): 1,2-arylene, carbonyl, ether, and methylene.

7.2 Arm linker effects

Secondary interactions are a persistent problem associated with experimental models in quantitative assessments of non-covalent interactions. One such interaction in our molecular balances is the repulsive O-π interaction between the linker oxygen and shelf

arene in the *folded* conformers. In our OAr and OR arm balances, the repulsive O-π interaction shifted the *folded-unfolded* equilibrium significantly towards the *unfolded* side. Moreover, the oxygen linker was found to strongly interact with solvents causing the balances to display a solvophobic behavior in polar solvents. Quantitative analyses of aromatic π-stacking and CH-π interactions in these molecular balances therefore required using control balances with a smaller benzene shelf to help remove the impacts of repulsive secondary interaction and solvent effects caused by the oxygen linker.

Another strategy to resolve the arm linker effects is to modify the molecular balances to contain a CH_2 linker and invoke DMC analyses to quantify the non-covalent interaction under study (Figure 1.18). The CH_2 linker formed a stabilizing CH-π interaction

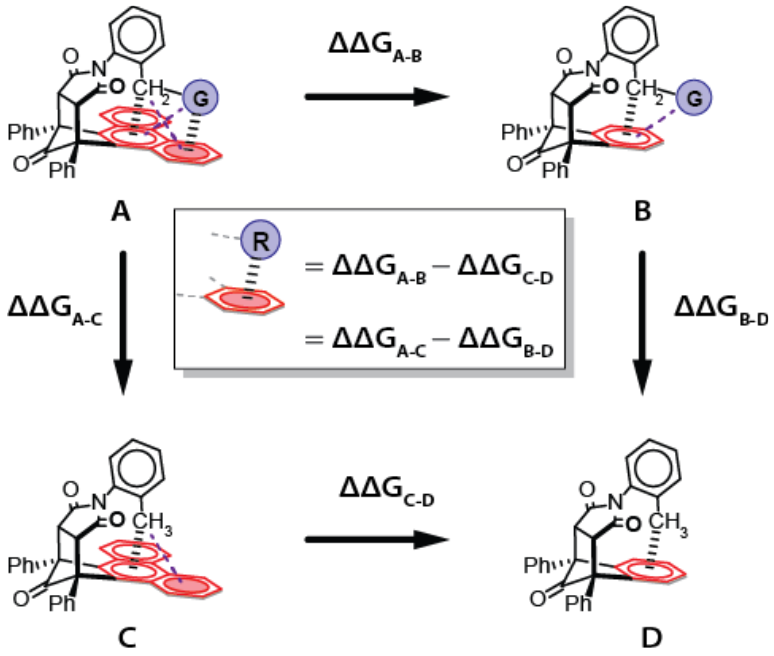

Figure 1.18 Schematic representation of DMC analysis on the CH_2 linker molecular balances and control balances.

resulting in much higher equilibrium *folded/unfolded* ratios.[7,8] Both the linker effects and aromatic interaction of interest could be accurately isolated through DMC analyses with

appropriate control balances. Such analyses, however, might not be applicable to the oxygen linker molecular balances as the OH arms in the corresponding control balances would experience significantly different H-bond interactions than the oxygen linkers did in the OAr and OR arm balances. Moreover, the OH arm might fail to effectively slow down the rotation of *N*-phenyl rotor due to a "proton grease" phenomenon.[57]

8. Conclusion and outlook

Molecular balances have emerged as one quintessential tool in the experimental studies of weak non-covalent aromatic interactions in condensed phase media. These unimolecular model systems capture the weak interactions of interest intramolecularly in one or more readily measurable conformational events, nicely bypassing problematic entropic penalties encountered otherwise. Their ability to precisely control interaction geometry is particularly desirable in the studies of weak or non-directional aromatic interactions, such as π-stacking and CH-π interactions. Our C-shape *N*-arylimide molecular balances and other model systems in literature have showcased the viability and advantages of such molecular balance strategy to study aromatic interactions in solution. Results from these molecular balances not only provided a more realistic understanding of aromatic interactions but also helped corroborate and revise theory. Future research on small molecule model systems are expected to address several challenging aspects: 1) "how to experimentally facilitate accurate crossover comparison among non-covalent interactions of various types?"; 2) "how to access to the non-deuterated solvent environments?"; 3) "how to quantitatively examine geometric aspect of various non-covalent interactions in solution?", 4)"how to effectively evaluate weak van de Waal forces to provide a conciliating view between the steric repulsion and stabilizing dispersion" and

5) "how to access to the gas phase and solid state?" We hope this account will help fellow researchers gain a clear picture of our efforts in pursuing an improved experimental knowledge on aromatic interactions, and also inspire peer experimentalists to develop more efficient model systems in future.

Reference

[1]. Chong, Y. S.; Carroll, W. R.; Burns, W. G.; Smith, M. D.; Shimizu, K. D. *Chem.-Eur. J.* **2009**, *15*, 9117.

[2]. Carroll, W. R.; Pellechia, P.; Shimizu, K. D. *Org. Lett.* **2008**, *10*, *3547*.

[3].Hwang, J.; Li, P.; Carroll, W. R.; Smith, M. D.; Pellechia, P. J.; Shimizu, K. D. *J. Am. Chem. Soc.* **2014**, *136*, 14060.

[4]. Hwang, J. W.; Dial, B. E.; Li, P.; Kozik, M. E.; Smith, M. D.; Shimizu, K. D. *Chem. Sci.* **2015**, *6*, 4358.

[5]. Li, P.; Zhao, C.; Smith, M. D.; Shimizu, K. D. *J. Org. Chem.* **2013**, *78*, 5303.

[6]. Carroll, W. R.; Zhao, C.; Smith, M. D.; Pellechia, P. J.; Shimizu, K. D. *Org. Lett.* **2011**, *13*, 4320.

[7]. Li, P.; Parker, T. M.; Hwang, J.; Deng, F.; Smith, M. D.; Pellechia, P. J.; Sherrill, C. D.; Shimizu, K. D. *Org. Lett.* **2014**, *16*, 5064.

[8]. Zhao, C.; Li, P.; Smith, M. D.; Pellechia, P. J.; Shimizu, K. D. *Org. Lett.* **2014**, *16*, 3520.

[9]. Zhao, C.; Parrish, R. M.; Smith, M. D.; Pellechia, P. J.; Sherrill, C. D.; Shimizu, K. D. *J. Am. Chem. Soc.* **2012**, *134*, 14306.

[10]. Maier, J. M.; Li, P.; Hwang, J.; Smith, M. D.; Shimizu, K. D. *J. Am. Chem. Soc.* **2015**, *137*, 8014.

[11]. Meyer, E. A.; Castellano, R. K.; Diederich, F. *Angew. Chem., Int. Ed.* **2003**, *42*, 1210.

[12]. Salonen, L. M.; Ellermann, M.; Diederich, F. *Angew. Chem., Int. Ed.* **2011**, *50*, 4808.

[13]. Takahashi, O.; Kohno, Y.; Nishio, M. *Chem. Rev.* **2010**, *110*, 6049

[14]. Ma, J. C.; Dougherty, D. A. *Chem. Rev.* **1997**, *97*, 1303.

[15]. Mati, I. K.; Cockroft, S. L. *Chem. Soc. Rev.* **2010**, *39*, 4195.

[16]. Paliwal, S.; Geib, S.; Wilcox, C. S. *J. Am. Chem. Soc.* **1994**, *116*, 4497.

[17]. Tsuzuki, S.; Mikami, M.; Yamada, S. *J. Am. Chem. Soc.* **2007**, *129*, 8656.

[18]. Hohenstein, E. G.; Sherrill, C. D. *J. Phys. Chem. A* **2009**, *113*, 878.

[19]. Singh, N. J.; Min, S. K.; Kim, D. Y.; Kim, K. S. *J. Chem. Theory Comput.* **2009**, *5*, 515.

[20]. Ringer, A. L.; Sinnokrot, M. O.; Lively, R. P.; Sherrill, C. D. *Chem.--Eur. J.* **2006**, *12*, 3821.

[21]. Wheeler, S. E. *J. Am. Chem. Soc.* **2011**, *133*, 10262.

[22]. Wheeler, S. E.; Houk, K. N. *J. Am. Chem. Soc.* **2008**, *130*, 10854.

[23]. Parrish, R. M.; Sherrill, C. D. *J. Am. Chem. Soc.* **2014**, *136*, 17386.

[24]. Tsuzuki, S.; Uchimaru, T.; Sugawara, K.; Mikami, M. *J. Chem. Phys.* **2002**, *117*, 11216.

[25]. Sinnokrot, M. O.; Sherrill, C. D. *J. Phys. Chem. A* **2004**, *108*, 10200.

[26]. Sherrill, C. D. *Acc. Chem. Res.* **2013**, *46*, 1020.

[27]. Yang, L. X.; Adam, C.; Nichol, G. S.; Cockroft, S. L. *Nat. Chem.* **2013**, *5*, 1006.

[28]. Hunter, C. A. *Angew. Chem., Int. Ed.* **2004**, *43*, 5310.
[29]. Chen, Z.; Lohr, A.; Saha-Moller, C. R.; Wurthner, F. *Chem. Soc. Rev.* **2009**, *38*, 564.
[30]. Nishio, M.; Hirota, M.; Umezawa, Y. The CH/pi interaction evidence, nature, and consequences Wiley-VCH: New York, **1998**.**[31]**. Takahashi, H.; Tsuboyama, S.; Umezawa, Y.; Honda, K.; Nishio, M. *Tetrahedron* **2000**, *56*, 6185.
[32]. Suezawa, H.; Yoshida, T.; Umezawa, Y.; Tsuboyama, S.; Nishio, M. *Eur. J. Inorg. Chem.* **2002**, 3148.
[33]. Tsuzuki, S.; Honda, K.; Uchimaru, T.; Mikami, M.; Tanabe, K. *J. Am. Chem. Soc.* **2000**, *122*, 3746.
[34]. Tsuzuki, S.; Honda, K.; Uchimaru, T.; Mikami, M.; Fujii, A. *J. Phys. Chem. A* **2006**, *110*, 10163.
[35]. Tsuzuki, S.; Honda, K.; Fujii, A.; Uchimaru, T.; Mikami, M. *Phys. Chem. Chem. Phys.* **2008**, *10*, 2860.
[36]. Nishio, M. *CrystEngComm* **2004**, *6*, 130.
[37]. Nishio, M.; Umezawa, Y.; Honda, K.; Tsuboyama, S.; Suezawa, H. *CrystEngComm* **2009**, *11*, 1757.
[38]. Mammen, M; Shakhnovich, E. I.; Whitesides, G. M. *J. Org. Chem.* **1998**, *63*, 3168
[39]. Asensio, J. L.; Arda, A.; Canada, F. J.; Jimenez-Barbero, J. *Acc. Chem. Res.* **2013**, *46*, 946.
[40]. Nishio, M.; Umezawa, Y.; Fantini, J.; Weiss, M. S.; Chakrabarti, P. *Phys. Chem. Chem. Phys.* **2014**, *16*, 12648.
[41]. Ran, J.; Wong, M. W. *J. Phys. Chem. A* **2006**, *110*, 9702.
[42]. Kozmon, S.; Matuska, R.; Spiwok, V.; Koca, J. *Phys. Chem. Chem. Phys.* **2011**, *13*, 14215.
[43]. Fujii, A.; Hayashi, H.; Park, J. W.; Kazama, T.; Mikami, N.; Tsuzuki, S. *Phys. Chem. Chem. Phys.* **2011**, *13*, 14131.
[44]. Wade, D. *Chem-Biol. Interact.* **1999**, *117*, 191.
[45]. Rechavi, D.; Scarso, A.; Rebek, J. *J. Am. Chem. Soc.* **2004**, *126*, 7738.
[46]. Zhao, Y.-L.; Houk, K. N.; Rechavi, D.; Scarso, A.; Rebek, J. *J. Am. Chem. Soc.* **2004**, *126*, 11428.
[47]. Mugridge, J. S.; Bergman, R. G.; Raymond, K. N. *J. Am. Chem. Soc.* **2010**, *132*, 1182.
[48]. Dias, H. V. R.; Wang, Z.; Jin, W. *Inorg. Chem.* **1997**, *36*, 6205.
[49]. Munakata, M.; Wu, L. P.; Ning, G. L. *Coord. Chem. Rev.* **2000**, *198*, 171.
[50]. Rathore, R.; Chebny, V. J.; Abdelwahed, S. H. *J. Am. Chem. Soc.* **2005**, *127*, 8012.
[51]. Emond, S. J.; Debroy, P.; Rathore, R. *Org.Lett.* **2008**, *10*, 389.
[52]. Habata, Y.; Ikeda, M.; Yamada, S.; Takahashi, H.; Ueno, S.; Suzuki, T.; Kuwahara, S. *Org. Lett.* **2012**, *14*, 4576.
[53]. Habata, Y.; Taniguchi, A.; Ikeda, M.; Hiraoka, T.;Matsuyama, N.; Otsuka, S.; Kuwahara, S. *Inorg. Chem.* **2013**, *52*, 2542
[54]. Gogoll, A.; Polavarapu, P.; Grennberg, H. *Inorg. Chem.* **2007**,*46*, 5271.
[55]. Bhayana, B.; Ams, M. R. *J. Org. Chem.* **2011**, *76*, 3594.
[56]. Li, P.; Hwang, J.; Maier, J. M.; Zhao, C.; Kaborda, D. V.; Smith, M. D.; Pellechia, P. J.; Shimizu, K. D. *Cryst. Growth Des.* **2015**, *15*, 3561.
[57]. Dial, B. E.; Pellechia, P. J.; Smith, M. D.; Shimizu, K. D. *J. Am. Chem. Soc.* **2012**, *134*, 3675.

CHAPTER 2

A COMPREHENSIVE EXPERIMENTAL STUDY OF *N*-HETEROCYCLIC π-STACKING INTERACTIONS OF NEUTRAL AND CATIONIC PYRIDINES[i]

[i] Reproduced with permission from Li, P.; Zhao, C.; Smith, M. D.; Shimizu, K. D. *J. Org. Chem.* **2013**, *78*, 5303. Copyright 2013 American Chemical Society.

1. Introduction

Attractive non-covalent interactions between aromatic surfaces play an important role in many key molecular recognition processes.[1,2] The majority of π-stacking interaction studies, to date, have focused on the interactions of non-heterocycles such as benzene[3-7] and substituted benzene dimers.[8-19] Yet, *N*-heterocycles are ubiquitous in synthetic[20,21] and biological systems[22] and their π-stacking interactions are often key to their function and utility.[23,24] The fewer experimental studies with *N*-heterocycles can be attributed to the greater synthetic challenge and the greater number of possible π-stacking geometries. Consequently, the majority of *N*-heterocyclic π-stacking studies have been theoretical computational studies.[25-30]

In this paper, we describe the development of a versatile and rigid molecular model system that can fix an *N*-heterocyclic and a non-heterocyclic ring into specific π-stacking geometries. The model system also provides a quantitative measure of the strengths of these interactions via their conformational equilibrium ratios (Figure 2.1). These "molecular balances" are in conformational equilibrium between *unfolded* and *folded* conformations due to restricted rotation around the C_{aryl}-N_{imide} single bond. In the *folded* conformation, the rigid bicyclic framework forces the aromatic surfaces of the arm and shelf into an off-set parallel π-stacking geometry. In the *unfolded* conformation, these two surfaces are held apart. Therefore, the *folded/unfolded* ratio provides a sensitive measure of the relative strengths of the intramolecular π-stacking interactions in solution.

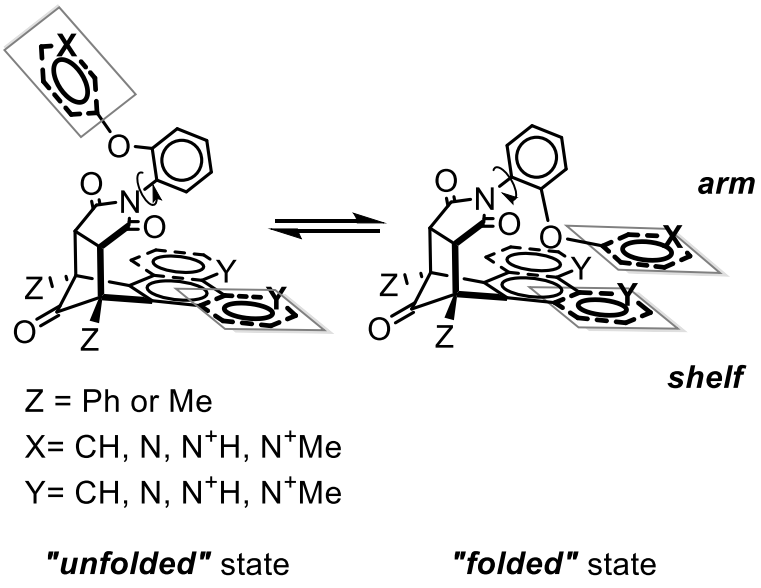

Figure 2.1 A general depiction of the molecular balance model system utilized in this study to measure the intramolecular *N*-heterocyclic π-stacking interactions formed in the *folded* conformer between an *N*-heterocyclic and a non-heterocyclic aromatic ring.

The structural rigidity and synthetic versatility of our molecular balance model system enabled the systematic study of the influences of position of the nitrogen atom, charge, and substituent on the nitrogen atom within a single molecular framework. This is important, as much greater structural and geometric diversity of π-stacking complexes can form with *N*-heterocycles (Figure 2.2A) than with simple benzenes (Figure 2.2B). First, the nitrogen atom disrupts the symmetry of the π-stacking complexes giving rise to multiple geometries. These can be grouped into two distinct classes: the ***distal*** geometry where the pyridine nitrogen is far from the π-face of the opposing benzene ring, and the ***proximal*** geometry where the pyridine nitrogen is close to the π-face of the opposing benzene ring. Second, *N*-heterocyclic complexes can be neutral or charged via the absence or presence of a substituent on the nitrogen. Finally, the cationic *N*-heterocyclic complexes can have a proton or alkyl *N*-substituent.

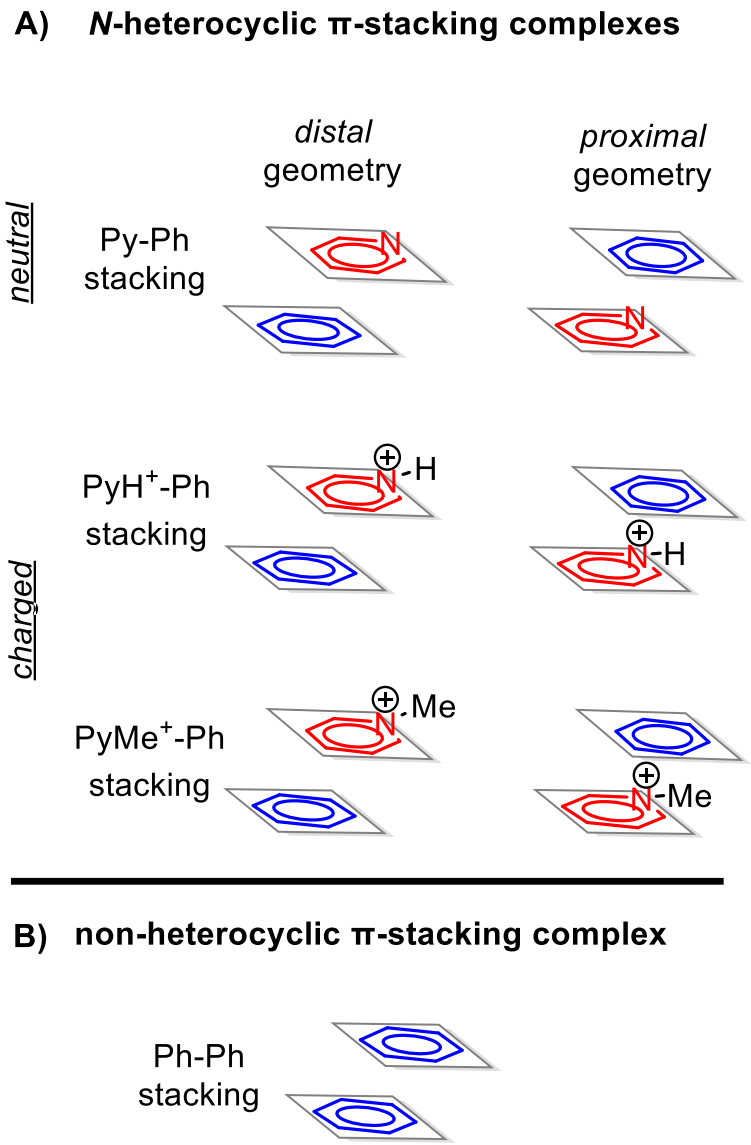

Figure 2.2 Comparison highlighting the greater structural and geometric diversity of the π-stacking complexes of (A) non-substituted *N*-heterocycles *versus* (B) non-substituted benzene rings.

Similar small molecule model systems that use conformational equilibriums to study non-covalent interactions have been widely employed with great success.[31] This includes the studies of the π-stacking interactions of *N*-heterocycles. However, these studies have not been comprehensive and have only focused on specific pairwise comparisons. For example, Gellman and co-workers used a flexible secondary amide-

based model system to demonstrate the enhanced affinity of a neutral six-membered heterocycle versus a phenyl ring.[32] Gung and co-workers also observed the stronger π-stacking interactions of an *N*-heterocyclic versus non-heterocyclic aromatic rings using a three-state triptycene-based model system.[33] Dougherty and co-workers used an electron-rich cyclophane aromatic host to measure the enhanced affinities of cationic versus neutral quinoline guests.[34] Waters and co-workers used a flexible rotamer model system to demonstrate that the position of the nitrogen atom in cationic π-stacking interactions had a profound influence on the interaction energies.[35] However, the results from these pioneering studies cannot be combined to produce an accurate comprehensive quantitative comparison of all of the *N*-heterocyclic π-stacking complexes shown in Figure 2.2.

To simplify the discussions, the following abbreviations will be used to describe the different complexes shown in Figure 2.2. The aromatic groups are abbreviated as follows: phenyl (Ph), pyridine (Py), pyridinium (PyH^+), *N*-methylpyridinium ($PyMe^+$). Thus, the interactions and complexes shown in Figure 2.2 (from top to bottom) are Py–Ph, PyH^+–Ph, $PyMe^+$–Ph and Ph–Ph. In addition, we will use the term, "π-stacking", to describe the interactions shown in Figure 2.2 in order to maintain consistency with the literature. However, we realize this term is somewhat misleading as the π-π interaction is repulsive.[36-39] The attractive components of π-stacking interactions are generally attributed to dispersion interactions of molecular surfaces and electrostatic attraction between dipoles and/or quadrupoles of aromatic rings.

2 Results and discussion

2.1 Molecular balance design

The molecular balance model system developed in this study has the same rigid bicyclic *N*-arylimide framework that we have successfully used to study face-to-face aromatic π-stacking (balance **1**)[40] and aliphatic CH–π[41] interactions (not shown). This similarity provided a number of advantages for the present study. First, the *N*-heterocyclic and non-heterocyclic aromatic surfaces could be predictably and precisely positioned relative to each other. We have previously demonstrated that the bicyclic framework fixes the arm and shelf aromatic surfaces into an off-set parallel π-stacking geometry in the *folded* conformer.[40] The proximity of the two interacting surfaces in the *folded* conformers also prevents the formation of the other commonly observed edge-to-face, perpendicular geometry. Second, a series of molecular balances with *N*-heterocyclic units incorporated into either the arm or shelf surfaces can be rapidly assembled owing to the highly modular syntheses of this framework. Third, the *folded*/*unfolded* ratios can be easily and accurately measured via the integration of the ^{1}H NMR spectra. The two conformers are in slow exchange at room temperature (23 ˚C), and differences as small as ±0.03 kcal/mol can be accurately measured. Fourth, the crystallinity of these molecular balances provided a unique opportunity to simultaneously characterize and study the geometry of *N*-heterocyclic π-stacking interactions in the solid-state.

For this study, six new molecular balances (**2-7**) were developed (Figure 2.3). The intramolecular interactions in **2-7** mirror the different types of the *N*-heterocyclic π-stacking complexes shown in Figure 2.2A. The relative position of the nitrogen atom in the complexes was controlled by placing the *N*-heterocyclic ring into either the arm or shelf.

Incorporation of a pyridine ring into the aromatic arm of **2** yielded a molecular balance that adopts a *distal* geometry. The pyridine ring of the arm extends beyond the edge of the aromatic shelf so the pyridine nitrogen is away from the π-face of the aromatic shelf. Conversely, incorporating pyridine rings into the arene shelf in **3** yielded a molecular balance that adopts a *proximal* geometry. In this case, the benzene arm extends out and over one of the nitrogens in the aromatic shelf. Similarly, cationic *N*-protonated and *N*-methylated balances with the *N*-heterocycles in the arm (**4** and **6**) adopt *distal* geometries and with the *N*-heterocycles in the shelf (**5** and **7**) adopt *proximal* geometries.

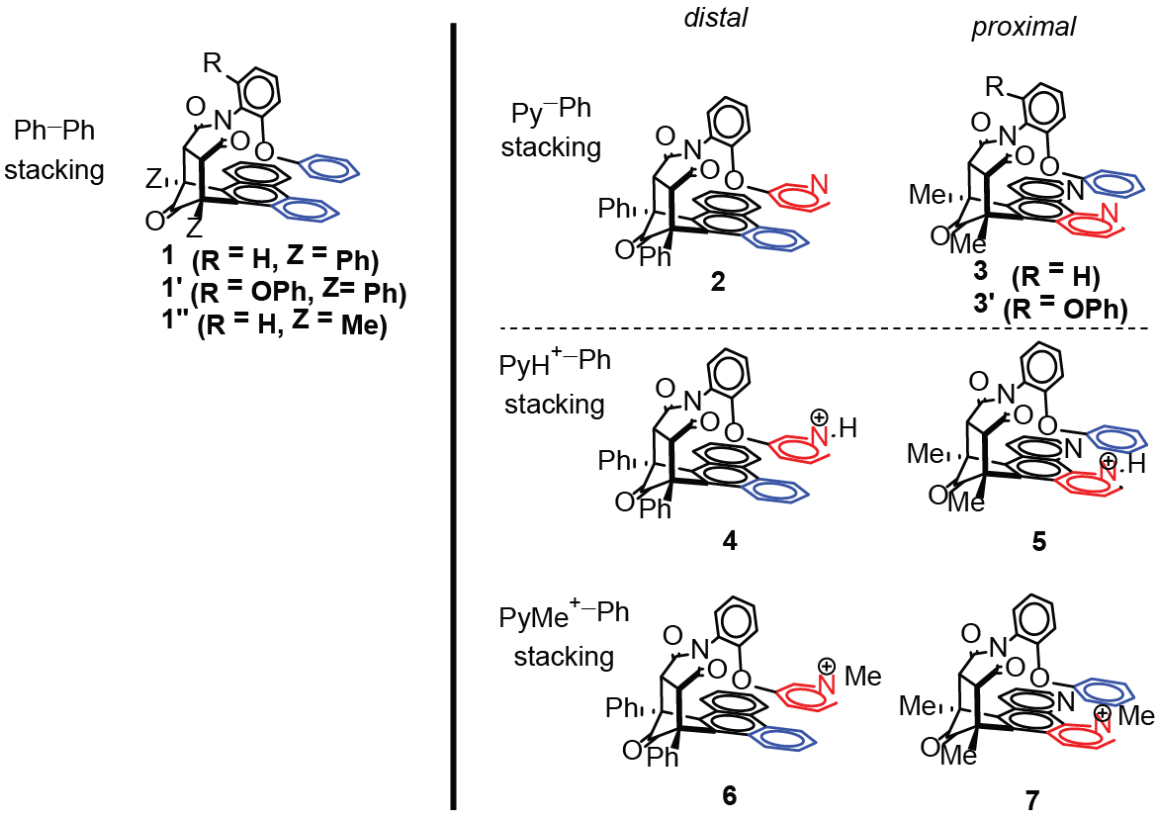

Figure 2.3 The *folded* conformers of molecular balances **1-7** that form intramolecular Ph–Ph, Py–Ph, PyH^+–Ph and $PyMe^+$–Ph stacking interactions. The two interacting rings are highlighted in red (*N*-heterocycle) and blue (non-heterocycle). Balances **1'** and **3'** are two-armed analogues used in the crystallographic analysis and balance **1"** is a control used to examine influence of the difference in bridgehead Z group over the *folded/unfolded* ratios in solution.

2.1 Synthesis

The syntheses of balances with the *N*-heterocyclic ring in the arm (**2**, **4** and **6**) followed the previously reported the two-step convergent route.[40,41] A representative synthesis of **2** is shown in Scheme 2.1. First, the S_NAr reaction between 3-hydroxypyridine (**8**) and 2-fluoronitrobenzene (**9**) followed by Pd/C catalyzed reduction of the nitro group yielded aniline **10**.[42] The thermal condensation of aniline **10** with the *endo*-bicyclic anhydride **11** yielded the *endo*-bicyclic balance **2**. Pyridyl arms with the nitrogen in the *meta*-position were prepared because the S_NAr reaction with the *para*-pyridyl precursor, 4-hydroxypyridine, was not successful due to preferential *N- versus* O-arylation.[43] Despite its lack of symmetry, the *meta*-pyridyl arm was able to adopt the desired *distal* geometry, as was later confirmed in the X-ray crystallographic study and the solution ^{1}H NMR study.

Scheme 2.1 Syntheses of balances **2** and **6** [a]

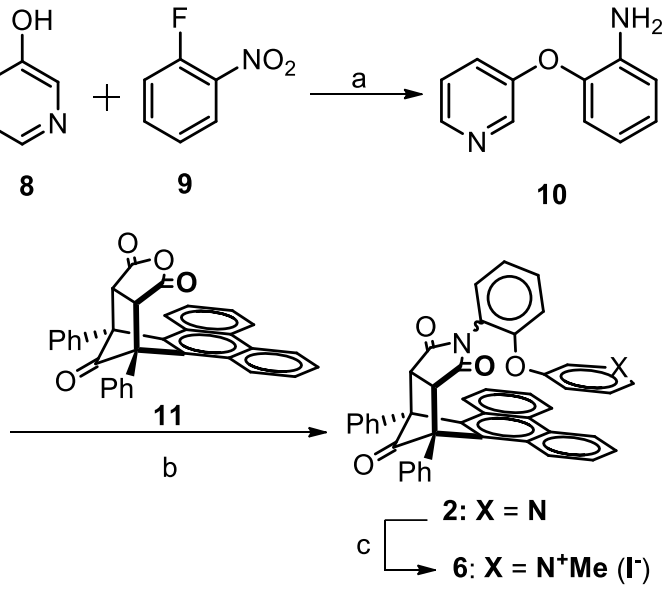

[a]Key: (a) i. Cs_2CO_3, 23 °C; ii. H_2, Pd/C, MeOH, 23 °C, 76% for two steps (b) HOAc, reflux, 81% (c) MeI, acetone, reflux, quantitative.

Incorporation of the *N*-heterocyclic rings into the shelf of balances (**3**, **5** and **7**) required the synthesis of a new diene building block (**13**) that contained an *N*-heterocyclic phenanthroline shelf. Diene **13** was formed in two-steps from the Knovenagel cyclization reaction of dione **12** and 2-pentanone.[44] The Diels-Alder reaction between diene **13** and maleimide **14** gave the *endo*-bicyclic balance **3** (Scheme 2.2). The choice of 1,10-phenanthroline with two heterocyclic nitrogens as the shelf motif was intended to ensure the symmetry of the arene shelf, as the arene of arm can form π-stacking interactions with either of the two outer rings of the shelf.

Scheme 2.2. Syntheses of balances **3** and **7** [a]

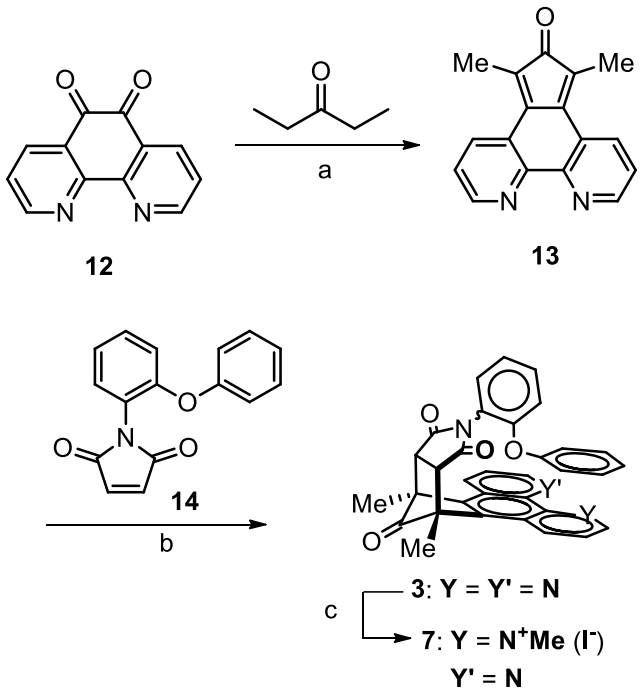

[a]Key: (a) i. K_2CO_3, MeOH, 23 °C; ii. py-$SOCl_2$, 23 °C 37% for two steps (b) CH_2Cl_2, pressure tube, 90 °C, 45% (c) MeI, acetone, reflux, quantitative.

In addition, two new control balances **3'** and **1''** were prepared. Balance **3'** is a "two-armed" analogue of **3**, which was synthesized from diene **11** and two-armed *N*-phenylmaleimide **15** following the previously reported method.[40] Balance **1''** is a

structural analogue of **1** with methyl groups instead of phenyl groups attached to the bridgeheads (Figure 2.4). Balance **1''** was prepared by a similar route as **3** via the Diels-Alder reaction between maleimide **14** and the known diene **16.**[45]

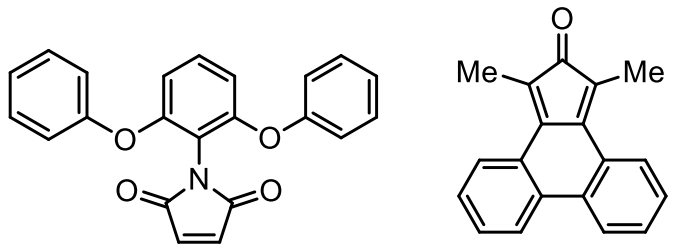

15 **16**

Figure 2.4 Maleimide **15** and diene **16** precursors used in the syntheses of the control balances **3'** and **1"**.

The cationic balances (**4-7**) were formed by methylation or protonation of the *N*-heterocycles in the arms or shelves. The *N*-methylated balances **6** and **7** were obtained through methylation of the neutral balances **2** and **3** using methyl iodide in acetone (Scheme 2.1 and 2.2). The protonated balances **4** and **5**, on the other hand, were obtained by *in situ* treatment of balances **2** and **3** with methanesulfonic acid.

2.2 X-Ray crystal structure analysis

To confirm the formation and correct geometry of the intramolecular *N*-heterocyclic π-stacking interactions in our model systems, the molecular balances were characterized using X-ray crystallography. X-ray quality single crystals of balances **2**, **3**, **4**, **6**, and **7** were successfully obtained from chloroform-acetonitrile mixtures; only balance **5** did not form X-ray quality crystals. All but one of the molecular balances crystalized in the *folded* conformation. This observation provided the first indication of the greater strength of the *N*-heterocyclic π-stacking interactions. In contrast, the non-heterocyclic π-

stacking balance **1** consistently crystalized in the *unfolded* conformation.[40] The only *N*-heterocyclic balance that crystalized in the *unfolded* conformation was balance **3** that contains the weakest *N*-heterocyclic π-stacking interaction, as was later confirmed by the solution study. To characterize the intramolecular π-stacking interaction in balance **3**, a two-armed version **3'** was synthesized and crystalized. The presence of two identical phenyl ether arms attached to both *ortho*-position of the *N*-aryl rotor ensured that one arm would always adopt the *folded* conformation.

The crystal structures of **2**, **3'**, **4**, **6**, and **7** all showed intramolecular parallel π-stacking interactions between the aromatic arm and shelf surfaces. Representative crystal structures of balances **2** and **3'** are shown in Figure 2.5. The rigid C-shaped *endo*-bicyclic framework brings the aromatic arm surface in close proximity to the aromatic shelf in the *folded* conformation. Examination of the geometries of the interacting six-membered rings confirmed the formation of the expected off-set face-to-face π-stacking interactions in balances **2**, **3'**, **4**, **6** and **7**. The center-to-plane distance distances (**D**) were 3.31–3.63 Å, which were well within the typical range of 3.3–3.8 Å for face-to-face aromatic stacking interactions.[46] The two rings were roughly parallel as shown by the relatively small dihedral angles (**α**) (4.81°–17.04°) between the planes of the interacting rings, which were below the cutoff (< 20°) for the face-to-face π-stacking geometry.[47] Finally, the centroid-to-centroid horizontal off-set (**H**) of the two interacting rings (0.82–1.98 Å) compared favorably with the reported average value (1.30 Å) for the off-set geometry in the literature.[46] (Definition for these geometric parameters is provided in Figure 2.13 in Supporting Information)

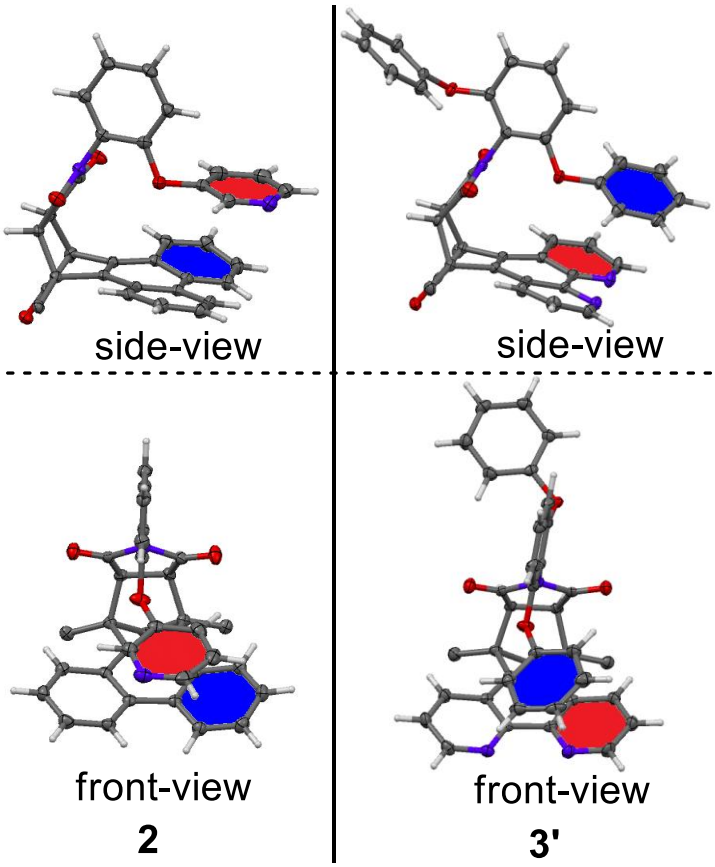

Figure 2.5 X-ray crystal structures of balances **2** and **3'** (the bridgehead phenyl and methyl functional groups are omitted for viewing clarity). The intramolecular *N*-heterocyclic π-stacking interactions are highlighted: *N*-heterocycle in red and non-heterocycle in blue.

Table 2.1. Measured plane-to-plane angle (**α**), centroid-to-plane distance (**D**) and horizontal centroid-to-centroid off-set (**H**) between the two π-stacking six-membered rings in the crystal structures of balances **1'**, **2**, **3'**, **4**, **6**, and **7**.

Balance.	π-stacking interaction	geometry	**α**	**D** [Å]	**H** [Å]
1'	Ph–Ph	–	7.8°[a]	3.75[a]	0.82[a]
2	Py–Ph	*distal*	9.3°	3.63	1.67
3'	Py–Ph	*proximal*	15.3°	3.60	1.82
4	PyH^+–Ph	*distal*	17.0°	3.37	1.27
6	$PyMe^+$–Ph	*distal*	4.8°, 6.4°[b]	3.29, 3.36[b]	1.78, 1.98[b]
7	$PyMe^+$–Ph	*proximal*	10.3°	3.31	1.65

[a]Ref. 40 [b]The crystal structure of **6** contains two crystallographically independent molecules.

Analysis of the crystal structures also provided verification of the formation of the predicted *proximal* and *distal* π-stacking geometries. To better visualize the geometries, top views of the interacting rings in the crystal structures were examined (Figure 2.6). In particular, we were concerned that the mobility of the arene arm in the plane of the arene shelf might lead to alternative geometries. However, examination of each structure in Figure 2.7 shows the expected *distal* geometries in the *folded* conformers **2**, **4** and **6**, and the *proximal* geometries in the *folded* conformers **3'** and **7**. We were also concerned with the ability of balances **3'**, **4** and **6** to adopt the less favorable geometries (*proximal*, *distal* and *distal*) for their respective *N*-heterocyclic π-stacking interactions. However, examination of these structures shows the *N*-heterocyclic nitrogen has been positioned into the designed geometry. This study confirmed the ability of the rigid framework to control the intramolecular interaction geometries.

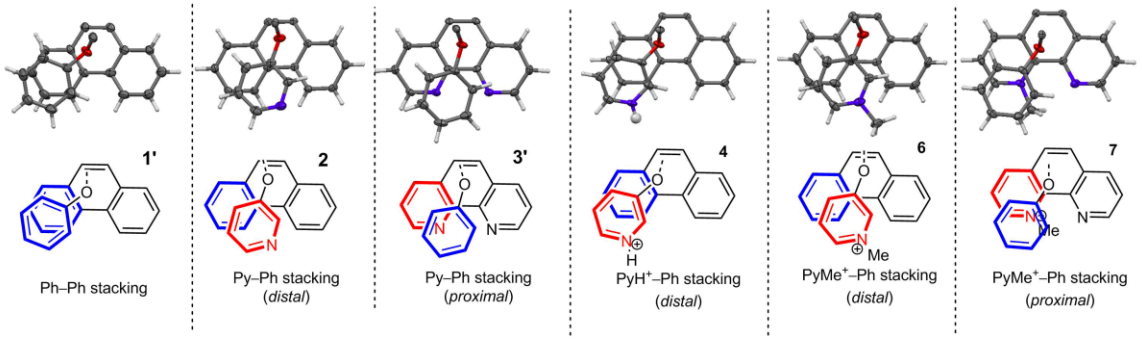

Figure 2.6 Top views of the crystal structures of balances **1'**, **2**, **3'**, **4**, **6**, and **7** highlighting the intramolecular π-stacking interactions in the *folded* conformers. The corresponding ChemDraw representations are also provided for viewing clarity.

Third, analysis of the crystal structures for balances **1'**, **2**, **3'**, **4**, **6** and **7** confirmed the structural continuity of the intramolecular π-stacking interactions providing supports for the ability to compare the energies of the respective interactions. These new heterocyclic balances contained a much wider diversity of functional groups, charges, and

geometries which, we were concerned, might lead to different secondary interactions and steric effects and thus mask the π-stacking interactions of interest. The similarity in the structures of the balances was demonstrated by the conformity of the positions of the ether oxygen linkers to the arene shelves. Figure 2.7 shows the overlaid structures of the ether oxygen linkers and the arene shelves of the *folded* conformers **1'**, **2**, **3'**, **4**, **6**, and **7**. The position of the oxygen linkers was remarkably consistent among the seven crystal structures, confirming that the geometric and steric constraints in the *folded* conformers were very similar.

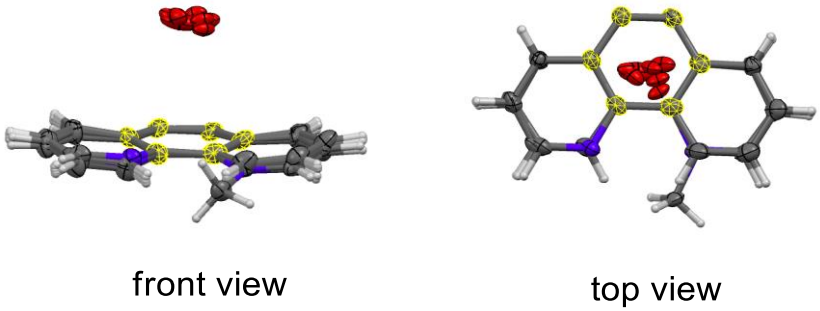

Figure 2.7 Top and front views of the overlaid crystal structures for balances **1'**, **2**, **3'**, **4**, **6**, and **7** highlighting the relative geometries of the oxygen linkers on the arm over the arene shelf. Only the arene shelves and arm ether oxygens are shown, and the overlapping center six-membered aromatic ring of the shelves is highlighted in yellow.

2.3 Characterization in solution

The relative strengths of the intramolecular π-stacking interactions in the *N*-heterocyclic molecular balances were assessed by their *folded/unfolded* equilibrium ratios. These were measured for balances **1-7** in solution via integration of their ^{1}H NMR spectra at 23 °C. The polar solvent DMSO-d_6 was chosen for these studies due to its ability to dissolve both the neutral and cationic balances. The equilibrium ratios were measured from the areas of the separate peaks for the *unfolded* and *folded* succinimide methylene protons,

which were singlets at ~4.9 ppm. The assignment of the *unfolded* succinimide peak was made by matching its area to the distinct doublet of doublet for the *unfolded* conformer's *ortho*-proton of the *N*-aryl rotor, which is shifted drastically upfield (~ 4.5 ppm) due to its proximity over the aromatic shelf. The *folded*/*unfolded* equilibrium ratios were converted to energies using the equation: $\Delta G = -RT\ln([folded]/[unfolded])$. The *folded/unfolded* ratio for balance **7** was estimated to be greater than 19:1 because only the *folded* conformer was observed.

For some of the cationic balances, the *folded/unfolded* ratios were measured indirectly. The cationic *N*-protonated balances **4** and **5** were formed by adding MsOH to solutions of balances **2** and **3**, respectively. Unfortunately, in the presence of 1 equiv. of MsOH, the broad water peak obscured the key succinimide singlets that were used to measure the *folded/unfolded* ratios (See SI Figure 2.15). The *folded/unfolded* ratios, however, could be accurately measured at lower equiv. (< 1.0) of MsOH and the equilibrium energies (ΔG's) were observed to change linearly with the amount of added MsOH (See SI Figure 2.16 and 2.17). Therefore, ΔG's for balances **4** and **5** were obtained from the linear extrapolation to 1 equiv. of added MsOH.

Another concern was that the differences in the substituents at the bridgehead carbons of the balances might not allow accurate comparison. Balances **1**, **2**, **4**, and **6** have bridgehead phenyl rings and balances **3**, **4**, and **7** had bridgehead methyl groups. Thus balance **1"** with a bridgehead methyl group was prepared and compared with balance **1** with a bridgehead phenyl group. Balances **1** and **1"** had idential *unfolded/folded* ratios in DMSO-d_6 (0.58 verus 0.53), suggesting that the bridgehead group did not influence the *folded/unfolded* equilibrium ratio.

2.4 Quantitative analysis of the stability trends

Comparison of the measured ΔG's for balances **1-7** is shown in Figure 2.8. Stronger π-stacking interactions in the *folded* conformer led to higher *folded/unfolded* ratios and more negative ΔG values. In general, the ΔG values were consistent with the expected *N*-heterocyclic π-stacking trends, confirming the ability of the balances to accurately compare these π-stacking interactions. For example, neutral *N*-heterocyclic balances **2-3** showed stronger π-stacking interactions than the non-heterocyclic balance **1**.[29] Cationic *N*-heterocyclic balances **4-7** also showed stronger π-stacking interactions than the neutral *N*-heterocyclic balances **2-3**.[27]

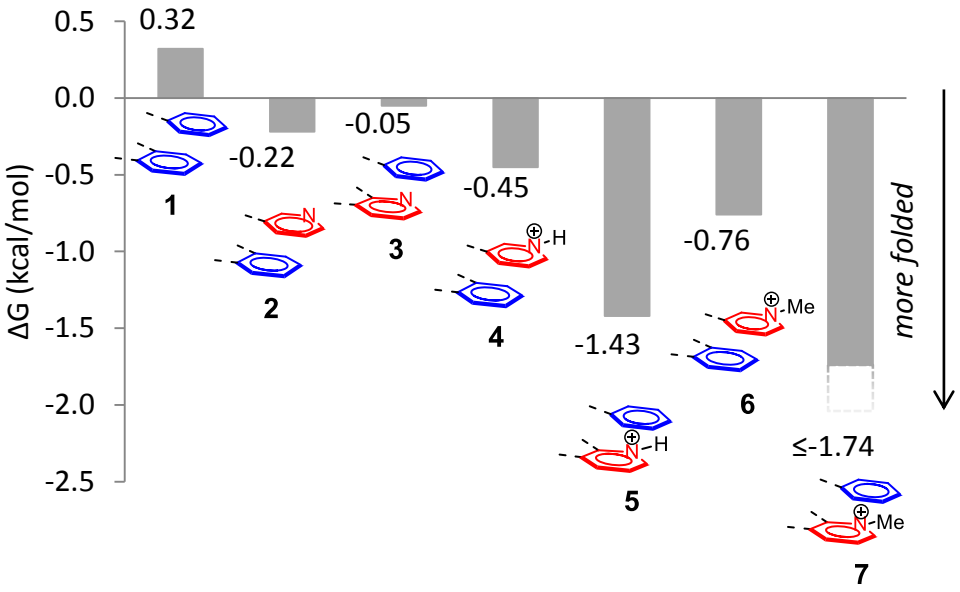

Figure 2.8 ^{1}H NMR measured ΔG's (kcal/mol) for balances **1-7** at 23 °C in DMSO-d_6 at 23 °C. The ChemDraw representation of the π-stacking interaction in each balance is shown. The uncertainty in ^{1}H NMR integration measurements gives an error of less than ± 0.03 kcal/mol.

To facilitate the comparison of the respective π-stacking interactions, ΔΔG's were calculated for the *N*-heterocyclic balances **2-7** relative to the non-heterocyclic balance **1**, which contained the weakest π-stacking interaction (Table 2.2).

Table 2.2 Measured conformational equilibrium energies (ΔG, kcal/mol) for balances **1**-**7** in DMSO-d_6 at 23 °C and relative energies (ΔΔG, kcal/mol) of the *N*-heterocyclic balances **2**-**7** relative to the non-heterocyclic balance **1**.

Balance	π-stacking interaction	geometry	ΔG[a]	ΔΔG[b]
1	Ph–Ph	–	0.32	0.00
2	Py–Ph	*distal*	-0.22	-0.54
3		*proximal*	-0.05	-0.37
4	PyH^+–Ph	*distal*	-0.45	-0.77
5		*proximal*	-1.43	-1.75
6	$PyMe^+$–Ph	*distal*	-0.76	-1.08
7		*proximal*	≤-1.74[c]	≤-2.06

[a] DMSO-d_6, 23 °C; uncertainty less than ± 0.03 kcal/mol [b] ΔΔG = (ΔG[**x**] – ΔG[**1**]); **x** = **2-7**; uncertainty less than ± 0.06 kcal/mol [c] Only the *folded* conformer of balance **7** was observed on the ^{1}H NMR spectrum, and thus ΔG[**7**] was estimated to be ≤ -1.74 kcal/mol.

The neutral *N*-heterocyclic (Py–Ph) π-stacking interactions in balances **2** and **3** were found to be modestly stronger (ΔΔG = -0.4 to -0.5 kcal/mol) than the non-heterocyclic (Ph–Ph) π-stacking interaction in balance **1**. This was consistent with the influence of the electronegative heterocyclic nitrogen that enhances the electrostatic attraction between rings due to the formation of a permanent dipole.[29] The magnitude of this trend compared favorably with the values measured by Gung and co-workers using their triptycene-based molecular model system.[33]

The cationic *N*-heterocyclic π-stacking interactions (PyH^+–Ph and $PyMe^+$–Ph) in balances **4-6** were found to be much stronger than the non-heterocyclic (Ph–Ph) π-stacking interaction in balance **1** (ΔΔG = -0.8 to ≤-2.1 kcal/mol), and also stronger than the neutral Py–Ph π-stacking interactions in balances **2-3** (ΔΔG = -0.2 to ≤-1.7 kcal/mol). This significant increase in strength is consistent with the greater electrostatic attraction arising from cationic nitrogen ring and the π-cloud of the opposing aromatic surface.[27] This observation helps explain the prevalence of cationic *N*-heterocyclic π-stacking interactions

in applications that rely on π-stacking interactions such as biomimetic catalysis of S_N2 reactions,[48] conformational molecular switches,[49] diastereotopic control of stereoselective reactions,[50] and the threading of rotaxanes and catanenes.[51]

2.5 Influence of the position of *N*-heterocyclic nitrogen

The rigidity of the bicyclic framework of this model system provided the unique opportunity to investigate how the relative position of the *N*-heterocyclic nitrogen atom influenced the stabilities of the π-stacking interaction. However, the ability of the molecular balances to maintain the *distal* and *proximal* geometries in solution was first verified. Balances **2-7** adopted the expected *distal* and *proximal* geometries in the solid-state. However, these geometries are more dynamic in solution. Computational studies of our model system have shown that the arene arm can sweep back and forth over the arene shelf.[52] Thus, the conformational equilibrium energies in solution of the *proximal* (**2**, **4** and **6**) and *distal* (**3**, **5** and **7**) balances were compared. Specifically, for each type of *N*-heterocyclic π-stacking interaction (Py–Ph, PyH^+–Ph and $PyMe^+$–Ph), the energies of balances designed to adopt *distal* and *proximal* geometries were compared. In each case, the *distal* and *proximal* balances had distinctly different ΔG values. More importantly, the *distal* versus *proximal* stability trends for each type of interaction matched well the predictions of Hunter and Sander's electrostatic model.[53] This suggests that the balances were adopting the expected geometries in solution.

For the Py–Ph stacking interaction, the *distal* geometry (balance **2**) was found to be slightly stronger than the *proximal* geometry (balance **3**) by $\Delta\Delta G$ = -0.17 kcal/mol. Figure 2.9 shows the electrostatic origins of this geometric preference. The electronegative nitrogen of the pyridine ring bears a partial negative charge ($\boldsymbol{\delta^-}$) and creates a partial

positive charge (δ^+) on the opposite end of the ring. Thus, the *distal* geometry provides better electrostatic complementarity to the quadrupole of the opposing phenyl ring. The *proximal* geometry, on the other hand, lacks an electropositive hydrogen on the pyridine nitrogen which eliminates one of the attractive electrostatic interactions. In addition, the *proximal* geometry contains an additional repulsive interaction between the electronegative pyridine nitrogen and the π-surface of the opposing phenyl ring. The weaker *proximal* Py–Ph stacking interaction in balance **3** was also evident in the solid-state studies, as balance **3** was the only balance that did not crystalize in the *folded* conformation.

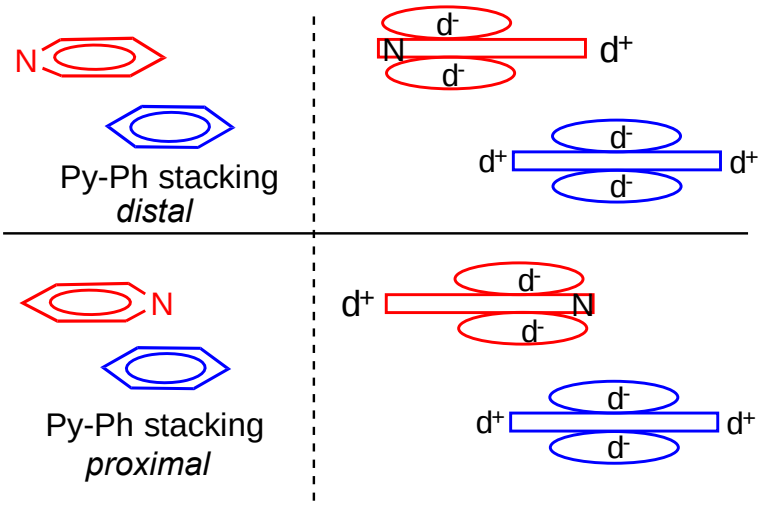

Figure 2.9 Schematic representations comparing the neutral Py–Ph π-stacking interactions in the *proximal* and *distal* geometries using Hunter and Sander's electrostatic quadruple model.

For the cationic *N*-heterocyclic (PyH^+–Ph and $PyMe^+$–Ph) π-stacking interactions, the opposite geometric preference was observed. The *proximal* geometry (balances **5** and **7**) were considerably more stable than the *distal* geometry (balances **4** and **6**) by $\Delta\Delta G = \leq$-0.98 kcal/mol. The preference for the *proximal* geometry in the cationic *N*-heterocyclic π-stacking interactions can also be explained using Hunter's electrostatic model. The

positive charge caused by protonation or alkylation of the pyridine is electrostatically attracted to the π-cloud of the opposing phenyl ring. This attractive force is stronger in the *proximal* geometry as the positively charged nitrogen is closer to the face of opposing phenyl ring. The observed preference for the *proximal* geometry in PyH^+–Ph stacking interactions is also consistent with the "orientation effect" of cationic π-stacking interactions observed by Waters and co-workers in their flexible folding model system.[35] Furthermore, the larger difference in energy between the *proximal* and *distal* geometries for the cationic ($|\Delta\Delta G| \geq 0.98$ kcal/mol) versus neutral ($|\Delta\Delta G| = 0.17$ kcal/mol) π-stacking interactions reinforced the electrostatic origins of these geometrical preferences.

2.6 Influence of the *N*-Substituent

Next the influence of different *N*-substituents (methyl versus proton) in the cationic balances was analyzed. To isolate this variable from the geometric preference noted above, the *proximal* (**5** and **7**) and *distal* (**4** and **6**) balances were compared separately. For the *proximal* balances, the *N*-methylated balance **7** had a stronger π-stacking interaction than the *N*-protonated balance **5** by $\Delta\Delta G \leq -0.31$ kcal/mol. The greater stability of the *proximal* *N*-methylated heterocycle complex was attributed to the ability of the *N*-methyl group to form an additional stabilizing CH–π interaction. Evidence for the additional CH–π interaction was provided by the crystal structure of balance **7**. As shown in Figure 2.10, a proton of the *N*-methyl group points towards the opposing phenyl ring with two short H to C distances (atom-to-atom distance) of 3.02 Å and 3.03 Å, respectively, which falls within the common cut-off distance (3.05 Å) for a CH–π interaction.[54] We have also observed that similar intramolecular CH–π interactions can stabilize the *folded* conformer of our *N*-arylimide bicyclic balances by up to -1.0 kcal/mol in organic solvents.[41] The similar

supporting role of CH–π interactions in the cation–π interactions of alkylated ammonium has been mentioned in several studies, such as the folding of a β-hairpin peptide and the *in vitro* binding of trimethyllysine to the HP1 chromodomain.[55]

A similar analysis was performed on the *distal* cationic balances (**4** and **6**). However, the equilibrium ratios of these *distal* balances were much more susceptible to solvent effects which made the *N*-methyl versus *N*-proton preference solvent dependent. These solvent effects are explained in the next section.

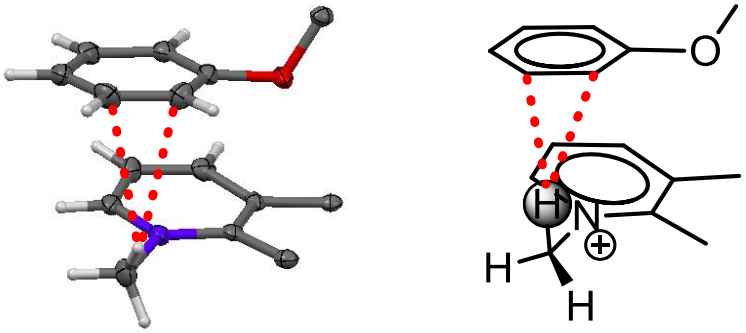

Figure 2.10. Truncated side-view (left) of the crystal structure of *folded*-**7** highlighting the presence of a CH–π interaction between the *proximal N*-methylated heterocycle on the shelf and the phenyl ring on the arm. A ChemDraw representation is also provided (right). The short distance contacts between *N*-methyl proton and phenyl carbon are highlighted with red dotted lines.

2.7 Solvent effects

The ability to measure the *folded/unfolded* ratios in different solvents provided an additional method of probing the origins of the stability trends. Thus, the above analyses were also carried out in two additional organic solvents: $CDCl_3$ and CD_3CN. The measured relative energies are shown in Table 2.3. Overall, the similar stability trends were observed in all three solvents, providing further confirmation of the observed *N*-heterocyclic stability trends.

Table 2.3 Measured relative energies (ΔΔG, kcal/mol) [a] of the *N*-heterocyclic balances **2-7** relative to the non-heterocyclic balance **1**.

Balance	π-stacking interaction	geometry	ΔΔG[a]		
			$CDCl_3$	CD_3CN	DMSO-d_6
1	Ph–Ph	–	0.00	0.00	0.00
2	Py–Ph	*distal*	-0.60	-0.54	-0.54
3		*proximal*	-0.19	-0.21	-0.37
4	PyH^+–Ph	*distal*	-0.89	-1.06	-0.77
5		*proximal*	-1.43	-1.66	-1.75
6	$PyMe^+$–Ph	*distal*	-0.40	-0.98	-1.08
7		*proximal*	≤-2.23	≤-1.89	≤-2.06

[a] The relative energy were quantified as ΔΔG = (ΔG[**x**] – ΔG[**1**]); **x** = **2-7**; propagated uncertainty less than ± 0.06 kcal/mol. The measured ΔG's for balances **1-7** in $CDCl_3$ and CD_3CN were included in Table 2.4 in SI

The only inconsistency was in the trends for the *distal N*-protonated and *N*-methylated cationic balances **4** and **6**, as noted in the last section. In $CDCl_3$, the *N*-protonated balance **4** had a stronger interaction, whereas in DMSO-d_6, the *N*-methylated balance **6** had a stronger interaction. In CD_3CN, the two balances had very similar interaction energies. The greater solvent effects for these *distal* balances may be due to the greater interaction of the solvents with the charged cationic surfaces in **4** and **6**. This may be due to the more solvent exposed positive charge of the *distal* geometry. By comparison, the more shielded positive charge of the *proximal* balances (**5** and **7**) show much smaller solvent effects and consistent *N*-methyl versus *N*-proton trends in each solvent. These differences could also be due to differences in solvation of the different counter-ions (I^- and MsO^-) for the *N*-methylated and *N*-protonated *distal* balances (**4** and **6**), respectively.

2.8 Correlation with benchmark-quality computational calculations

Finally, the experimentally measured values in this study provided an opportunity to test the accuracy of current computational methods as well as the performance of our model system in accurately assessing *N*-heterocyclic π-stacking interactions. Benchmark

quality calculations (CCSD(T) or SCS–MP2 methods) from the literature for π-stacking interactions were used in the correlation analysis (Figure 2.11).[27,29,56] The geometries of the calculations were matched to the geometries of the π-stacking interactions observed in the crystal structures of the balances, and the calculated interaction energies were matched to the experimentally measured relative energies (ΔΔG) in DMSO-d_6 from Table 2.2.

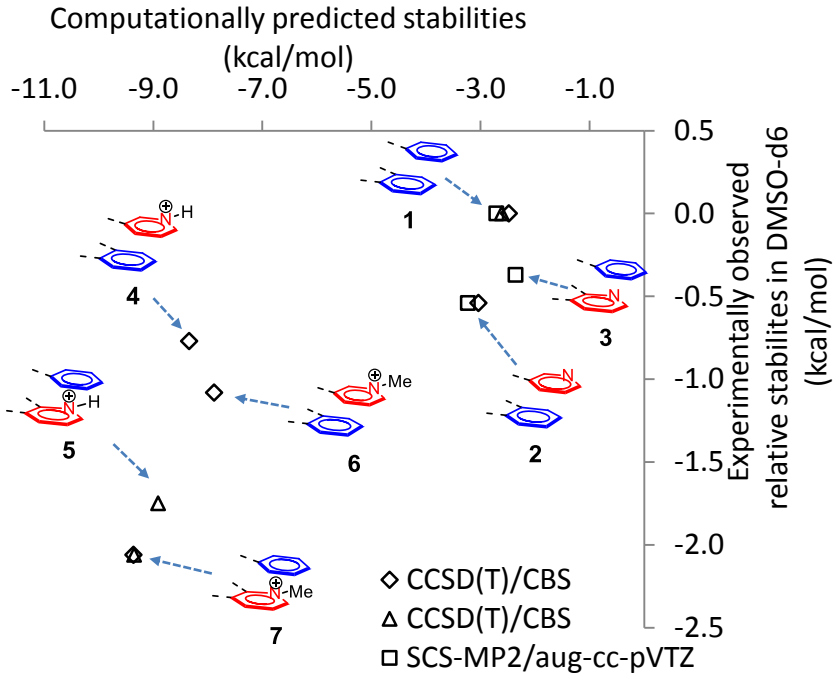

Figure 2.11 Correlation plot between the calculated energies from the benchmark quality computations in literature and the experimentally observed relative energies (ΔΔG's) in DMSO-d_6 for the π-stacking interactions in balances **1-7**. The computational data were from ref. 27 (open diamonds), ref. 29 (open squares) and ref. 56 (open triangles).

The correlation plot showed a good general agreement between the computational and experimentally measured energies. For example, both methods provide similar stability trends: Ph–Ph < Py–Ph < (PyH^+–Ph and $PyMe^+$–Ph). There was also good agreement for the geometry-related stability trends (*distal* versus *proximal*) for the both neutral and cationic *N*-heterocyclic π-stacking interactions. For example, both methods

found that the *distal* geometry was more stabilizing for the neutral Py–Ph stacking interaction; whereas the *proximal* geometry was more stabilizing for the cationic PyH^+–Ph and $PyMe^+$–Ph stacking interactions.

Two minor deviations in the experimental and calculated trends were observed. The first deviation was that the neutral and cationic *N*-heterocyclic π-stacking interactions appeared to form separate trend lines on the correlation plot. This may be explained by the different environments (vacuum versus solvent) of the two methods. The solvent in the experimental studies screen the electrostatic interactions of charged groups, which reduces their interaction strengths as compared to the *in vacuo* computational studies.

The second inconsistency was that the experimental study found that the *proximal* Py–Ph interaction in **3** was slightly stronger than the Ph–Ph stacking interaction in **1**. This trend is in opposition to the computational studies that predicted that positioning an electronegative nitrogen over an opposing aromatic π-surface in the *proximal* geometry should be a destabilizing interaction. We attribute this deviation to the mobility of the phenyl arm in solution, which allows the balance to also adopt geometries that avoid this destabilizing interaction. This minimizes the contribution of the destabilizing interaction to the *folded/unfolded* ratio and leads to an overestimation of the strength of the *proximal* Py–Ph stacking interaction in balance **3**. It should be pointed out that the mobility of the arene arm will have less of an impact on balances that only contain attractive stabilizing interactions, as the arm will preferentially seek out and adopt these more stabilizing geometries.

2.8 Evaluation of the Design of the Molecular Balances

Overall, our *N*-arylimide bicyclic balance model system appeared to provide an effective platform to systematically and quantitatively study many aspects of the *N*-heterocyclic π-stacking interaction. However, as with all model systems, we had a number of concerns. In this section, we re-analyzed the data to check whether each concern was warranted.

The first concern was that the repulsive O-π interaction from the oxygen linker of the arm with the arene shelf might obscure or prevent accurate comparisons of the intramolecular π-stacking interactions of interest. However, this repulsive interaction was actually advantageous feature, which enabled more accurate measurement of the stronger *N*-heterocyclic π-stacking interaction. The strength of the intramolecular interactions that can be measured by our balances is limited by the highest *folded/unfolded* ratio that can be accurately measured. Based on a conservative detection limit of 5% of ^{1}H NMR spectra,[57,58] the highest *folded*/*unfolded* ratio that can be measured is 19:1. If the *folded*/*unfolded* ratio in the absence of the interaction was 1:1, this would correspond to a maximum measureable interaction energy of only -1.74 kcal/mol. This low limit is particularly important for this study because the cationic *N*-heterocyclic π-stacking interactions were all stronger than -2.0 kcal/mol. However, the repulsive interactions of the oxygen linkers in our balances acts like a "spring", which shifts the resting state of the balance toward the *unfolded* conformer to give a *folded*/*unfolded* ratios of approximately 1:7 in DMSO-d_6.[40] This spring effect allows for a larger change in *folded*/*unfolded* ratio from 1:7 to 19:1, which corresponds to a maximum measurable interaction of up to -2.88 kcal/mol.

A second design concern was whether we could compare balances with *N*-heterocycles in the arm against those with *N*-heterocycles in the shelf. These two surfaces are not identical and possess different degrees of π-conjugation. However, analysis of the ΔG's for balances **1**-**7** suggested that this concern was unwarranted or was very minor, as the expected stability trends; Ph–Ph < Py–Ph < (PyH^+–Ph and $PyMe^+$–Ph), were clearly observed. More importantly, the expected and more subtle geometry-related stability trends (*proximal* versus *distal*) were accurately reproduced by the molecular balances. These geometry-related trends relied on directly comparing balances with *N*-heterocycles in the arm and shelf.

A third design concern was whether the mobility of the arm arene in the *folded* conformer balances would compromise their ability to distinguish the *distal* and *proximal* geometries of the *N*-heterocyclic π-stacking interaction. Generally, the expected *distal* versus *proximal* stability trends were observed. However, the ability of the arene arm to slide back and forth across the arene shelf could lead to underestimations of the difference in energy of *proximal* and *distal* geometries when destabilizing repulsive interactions are involved. To address this problem, we are currently utilizing advanced NMR methods such as through-space coupling and nuclear Overhauser effects to investigate the mobility of the arene arm and measuring the population of various sub-conformations to refine the energy calculations.

The last design concern was the asymmetry of the cationic aromatic shelves in balances **5** and **7**. Ideally, both heterocyclic nitrogens would be charged so that the arm arene could form the same π-stacking interactions with either outer ring of the arene shelf, but this was not synthetically feasible. Clearly, these singly charged balances are still able

to form the expected cation-π interactions, as these balances had significantly stronger π-stacking interactions than their neutral counterparts. This highlights one advantage of arm mobility in the study of attractive interactions, as the arms will preferentially form the more stabilizing π-stacking interaction with the cationic versus neutral outer ring. However, we cannot eliminate the possibility that the ability of these balances to also form the neutral π-stacking interaction may lead to an underestimation of the energies of the cationic π-stacking interactions in balances **5** and **7**. Again, advanced NMR techniques will be applied in future studies to quantify the contribution of these less stable geometries.

3. Conclusion

A new series of molecular balance model systems (**2-7**) were designed and used to perform a comprehensive study of the influences of position, charge, and substitution of the nitrogen atom on *N*-heterocyclic π-stacking interactions in the solid-state and in solution. The formation and geometry of the intramolecular *N*-heterocyclic π-stacking interactions in the *folded* conformation models were verified via X-ray crystallographic analysis in the solid-state. The relative stabilities of these *N*-heterocyclic π-stacking interactions in solution were systematically studied by comparing the *folded/unfolded* ratios of the corresponding molecular balances that were measured via integration of the ^{1}H NMR spectra. The stability trend: Ph–Ph < Py–Ph < (PyH^+–Ph and $PyMe^+$–Ph) was quantitatively measured for the first time within a single model system. The position of the heterocyclic nitrogen was found to influence the strengths of both the neutral and cationic *N*-heterocyclic π-stacking interactions leading to opposite stability trends. For the neutral Py–Ph stacking interaction, the *distal* geometry was found to be slightly more favorable. For the cationic PyH^+–Ph and $PyMe^+$–Ph stacking interactions, the *proximal*

geometry was found to be significantly more favorable. The influence of *N*-methylation and *N*-protonation was also compared. For the *proximal* complex, the $PyMe^+$–Ph interaction was found to be significantly stronger than the PyH^+–Ph stacking interaction. This was attributed to the formation of additional CH–π interaction between the *N*-methyl proton and the opposing phenyl ring. The measured trends were consistently observed in three common organic solvents (chloroform, acetonitrile and DMSO) confirming the generality of these trends. The experimentally measured stabilities for the *N*-heterocyclic π-stacking interactions in balances **1-7** were found to generally agree with the corresponding benchmark quality computational values in literature. Discrepancies were mainly attributed to the presence of solvent in the experimental studies and the difficulties in experimentally measuring interactions strength of unfavorable geometries.

The quantitatively measured stability trends for the *N*-heterocyclic π-stacking interactions provide guidance in the design and optimization of applications that rely on these molecular recognition processes. For example, insertion of *N*-heterocycles will strengthen attractive aromatic π-stacking interactions but only if the nitrogen atoms are appropriately positioned away from the π-face of the opposing aromatic surface. The insertion of positively charged *N*-heterocycles also provide a simple means to significantly strengthen the π-stacking interaction, but these charged heteroarenes also impose an even stronger directional preference. Finally, to study the stability trends for the non-covalent interactions of aromatic surfaces in more biologically relevant aqueous environments, we have developed a water-soluble version of these molecular balances and will be reporting these results in future studies.

Reference

[1]. Meyer, E. A.; Castellano, R. K.; Diederich, F. *Angew. Chem., Int. Ed.* **2003**, *42*, 1210.
[2]. Salonen, L. M.; Ellermann, M.; Diederich, F. *Angew. Chem., Int. Ed.* **2011**, *50*, 4808.
[3]. Jaffe, R. L.; Smith, G. D. *J. Chem. Phys.* **1996**, *105*, 2780.
[4]. Hobza, P.; Selzle, H. L.; Schlag, E. W. *J. Phys. Chem.* **1996**, *100*, 18790.
[5]. Tsuzuki, S.; Honda, K.; Uchimaru, T.; Mikami, M.; Tanabe, K. *J. Am. Chem. Soc.* **2002**, *124*, 104.
[6]. Sinnokrot, M. O.; Valeev, E. F.; Sherrill, C. D. *J. Am. Chem. Soc.* **2002**, *124*, 10887.
[7]. Sinnokrot, M. O.; Sherrill, C. D. *J. Phys. Chem. A* **2004**, *108*, 10200.
[8]. Sinnokrot, M. O.; Sherrill, C. D. *J. Am. Chem. Soc.* **2004**, *126*, 7690.
[9]. Tsuzuki, S.; Uchimaru, T.; Mikami, M. *J. Phys. Chem. A* **2006**, *110*, 2027.
[10]. Ringer, A. L.; Sherrill, C. D. *J. Am. Chem. Soc.* **2009**, *131*, 4574.
[11]. Cozzi, F.; Cinquini, M.; Annunziata, R.; Dwyer, T.; Siegel, J. S. *J. Am. Chem. Soc.* **1992**, *114*, 5729.
[12]. Cozzi, F.; Ponzini, F.; Annunziata, R.; Cinquini, M.; Siegel, J. S. *Angew. Chem., Int. Ed. Engl.* **1995**, *34*, 1019.
[13]. Rashkin, M. J.; Waters, M. L. *J. Am. Chem. Soc.* **2002**, *124*, 1860.
[14]. Gung, B. W.; Patel, M.; Xue, X. W. *J. Org. Chem.* **2005**, *70*, 10532.
[15]. Gung, B. W.; Xue, X. W.; Reich, H. J. *J. Org. Chem.* **2005**, *70*, 3641.
[16]. Cockroft, S. L.; Hunter, C. A.; Lawson, K. R.; Perkins, J.; Urch, C. J. *J. Am. Chem. Soc.* **2005**, *127*, 8594.
[17]. Gung, B. W.; Amicangelo, J. C. *J. Org. Chem.* **2006**, *71*, 9261.
[18]. Cockroft, S. L.; Perkins, J.; Zonta, C.; Adams, H.; Spey, S. E.; Low, C. M. R.; Vinter, J. G.; Lawson, K. R.; Urch, C. J.; Hunter, C. A. *Org. Biomol. Chem.* **2007**, *5*, 1062.
[19]. Gung, B. W.; Emenike, B. U.; Alverez, C. N.; Rakovan, J.; Kirschbaum, K.; Jain, N. *Tetrahedron Lett.* **2010**, *51*, 1648.
[20]. Yamada, S. *Org. Biomol. Chem.* **2007**, *5*, 2903.
[21]. Yamada, S.; Fossey, J. S. *Org. Biomol. Chem.* **2011**, *9*, 7275.
[22]. Saenger, W. *Principles of nucleic acid structure*; Springer-Verlag: New York, 1984.
[23]. Li, X. M.; Liu, P.; Houk, K. N.; Birman, V. B. *J. Am. Chem. Soc.* **2008**, *130*, 13836.
[24]. Hunter, C. A. *J. Mol. Biol.* **1993**, *230*, 1025.
[25]. Geerlings, P.; Mignon, P.; Loverix, S.; De Proft, F. *J. Phys. Chem. A* **2004**, *108*, 6038.
[26]. Mishra, B. K.; Sathyamurthy, N. *J. Phys. Chem. A* **2005**, *109*, 6.
[27]. Tsuzuki, S.; Mikami, M.; Yamada, S. *J. Am. Chem. Soc.* **2007**, *129*, 8656.
[28]. Wang, W. Z.; Hobza, P. *ChemPhysChem* **2008**, *9*, 1003.
[29]. Hohenstein, E. G.; Sherrill, C. D. *J. Phys. Chem. A* **2009**, *113*, 878.
[30]. Smith, Q. A.; Gordon, M. S.; Slipchenko, L. V. *J. Phys. Chem. A* **2011**, *115*, 4598.
[31]. Mati, I. K.; Cockroft, S. L. *Chem. Soc. Rev.* **2010**, *39*, 4195.
[32]. Mckay, S. L.; Haptonstall, B.; Gellman, S. H. *J. Am. Chem. Soc.* **2001**, *123*, 1244.
[33]. Gung, B. W.; Wekesa, F.; Barnes, C. L. *J. Org. Chem.* **2008**, *73*, 1803.

[34]. Kearney, P. C.; Mizoue, L. S.; Kumpf, R. A.; Forman, J. E.; Mccurdy, A.; Dougherty, D. A. *J. Am. Chem. Soc.* **1993**, *115*, 9907.
[35]. Rashkin, M. J.; Hughes, R. M.; Calloway, N. T.; Waters, M. L. *J. Am. Chem. Soc.* **2004**, *126*, 13320.
[36]. Grimme, S. *Angew. Chem., Int. Ed.* **2008**, *47*, 3430.
[37]. Wheeler, S. E.; Houk, K. N. *J. Am. Chem. Soc.* **2008**, *130*, 10854.
[38]. Wheeler, S. E. *J. Am. Chem. Soc.* **2011**, *133*, 10262.
[39]. Martinez, C. R.; Iverson, B. L. *Chem. Sci.* **2012**, *3*, 2191.
[40]. Carroll, W. R.; Pellechia, P.; Shimizu, K. D. *Org. Lett.* **2008**, *10*, 3547.
[41]. Carroll, W. R.; Zhao, C.; Smith, M. D.; Pellechia, P. J.; Shimizu, K. D. *Org. Lett.* **2011**, *13*, 4320.
[42]. Huang, D. H.; Poon, S. F.; Chapman, D. F.; Chung, J.; Cramer, M.; Reger, T. S.; Roppe, J. R.; Tehrani, L.; Cosford, N. D. P.; Smith, N. D. *Bioorg. Med. Chem. Lett.* **2004**, *14*, 5473.
[43]. You, F. X.; Twieg, R. J. *Tetrahedron Lett.* **1999**, *40*, 8759.
[44]. Warrener, R. N.; Schultz, A. C.; Houghton, M. A.; Butler, D. N. *Tetrahedron* **1997**, *53*, 3991.
[45]. Fuchs, B.; Pasternak, M. *Tetrahedron* **1981**, *37*, 2501.
[46]. Janiak, C. *J. Chem. Soc. Dalton Trans.* **2000**, 3885.
[47]. Chelli, R.; Gervasio, F. L.; Procacci, P.; Schettino, V. *J. Am. Chem. Soc.* **2002**, *124*, 6133.
[48]. Mccurdy, A.; Jimenez, L.; Stauffer, D. A.; Dougherty, D. A. *J. Am. Chem. Soc.* **1992**, *114*, 10314.
[49]. Yamada, S. J.; Uematsu, N.; Yamashita, K. *J. Am. Chem. Soc.* **2007**, *129*, 12100.
[50]. Yamada, S.; Morita, C. *J. Am. Chem. Soc.* **2002**, *124*, 8184.
[51]. Barin, G.; Coskun, A.; Fouda, M. M. G.; Stoddart, J. F. *Chempluschem* **2012**, *77*, 159.
[52]. Nijamudheen, A.; Jose, D.; Shine, A.; Datta, A. *J. Phys. Chem. Lett.* **2012**, *3*, 1493.
[53]. Hunter, C. A.; Sanders, J. K. M. *J. Am. Chem. Soc.* **1990**, *112*, 5525.
[54]. Nishio, M.; Umezawa, Y.; Honda, K.; Tsuboyama, S.; Suezawa, H. *CrystEngComm* **2009**, *11*, 1757.
[55]. Hughes, R. M.; Waters, M. L. *J. Am. Chem. Soc.* **2005**, *127*, 6518.
[56]. Singh, N. J.; Min, S. K.; Kim, D. Y.; Kim, K. S. *J. Chem. Theory Comput.* **2009**, *5*, 515.
[57]. Rizzo, V.; Pinciroli, V. *J. Pharm. Biomed. Anal.* **2005**, *38*, 851.
[58]. Malz, F.; Jancke, H. *J. Pharm. Biomed. Anal.* **2005**, *38*, 813.

Supporting Information

1. Synthesis and characterization

1.1 General experimental

All chemicals were purchased from commercial suppliers and used as received unless otherwise noted. All reactions were carried out under a dry N_2 atmosphere in oven–dried glassware. Dry organic solvents were obtained by passing the degassed solvents through activated alumina columns. Flash chromatography was carried out using either silica gel (60 Å, 200–400 mesh) or aluminum oxide (60 Å, 20–200 mesh) as noted. Thin layer chromatography (TLC) for monitoring the reaction progress was performed using either precoated 0.25 mm silica gel 60 F254 plates or precoated 0.25 mm aluminum oxide 60 F254 plates. NMR spectra were recorded on 300 MHz, 400 MHz spectrometers. Chemical shifts are reported in ppm (**δ**) and were referenced to TMS. HRMS was recorded with a magnetic sector spectrometer using EI sources and the Q-TOF 1 spectrometer using ESI sources.

1.2 Synthesis

Balances **1** and **1'**, anhydride **11**, *N*-(2-phenyloxyl)phenyl maleimide (**17**), and *N*-(2,6-diphenoxylphenyl) maleimide were prepared utilizing our previously described routes

for the analogous parent compounds.[i] Diene **13**[ii] and *ortho*-pyridin-3-ylaniline (**10**)[iii] were obtained using literature procedures.

(9R,9aS,12aR,13S)-9,13-Dimethyl-11-(2-phenoxyphenyl)-12a,13-dihydro-9H-9,13-methanophenanthro[9,10-f]isoindole-10,12,14-(9aH,11H)-trione (**1''**). Diene **16** (0.20 g, 0.77 mmol) and *N*-(2-phenyloxylphenyl) maleimide (**17**) (0.24 g, 0.92 mmol) were dissolved in dry toluene (10 mL). The mixture was stirred and heated at reflux under N_2 for 24 h. The solvent was removed under vacuum to give a light yellow solid. Recrystallization from ethanol gave **1''** as a white crystalline solid (0.36 g, 87%). mp 310 ºC dec. ^{1}H NMR (400 MHz, $CDCl_3$) δ 8.79 (dd, *J* = 8.3 Hz, *J* = 1.2 Hz, 2H major), 8.38 (dd, *J* = 8.2 Hz, *J* = 1.3 Hz, 2H major), 8.26 (dd, *J* = 8.3 Hz, *J* = 1.0 Hz, 2H minor), 8.14 (dd, *J* = 8.4 Hz, *J* = 1.0 Hz, 2H minor), 7.61–7.72 (m, 4H major), 6.81–7.49 (m, 5H major, 12H minor), 6.65 (dd, *J* = 8.3 Hz, *J* = 1.2 Hz, 1H major), 6.44 (td, *J* = 7.7 Hz, *J* = 1.3 Hz, 1H major), 5.96 (dd, *J* = 8.4 Hz, *J* = 1.2 Hz, 1H minor), 5.73–5.78 (m, 1H major), 4.68 (dd, *J* = 7.9 Hz, *J* = 1.6 Hz, 1H major), 3.60 (s, 2H minor), 3.42 (s, 2H major), 2.31 (s, 3H major), 2.28 (s, 3H minor). ^{13}C NMR (100 MHz, $CDCl_3$): 201.1, 199.6, 174.2, 173.7, 156.2, 153.0, 133.3, 133.1, 130.9, 130.8, 130.4, 129.9, 129.3, 128.9, 128.2, 127.5, 127.4, 127.3, 126.7, 126.5, 125.3, 125.0, 124.2, 123.5, 123.4, 123.3, 121.8, 121.7, 121.6, 119.5, 118.8, 116.1, 77.5, 77.2, 77.2, 76.8, 55.2, 55.1, 48.4, 47.9, 14.8. HRMS (EI) m/z calcd for $C_{35}H_{25}NO_4$ (M^+): 523.1784; found: 523.1778.

[i] Carroll, W. R.; Pellechia, P.; Shimizu, K. D. *Org. Lett.* **2008**, *10*, 3547

[ii] Warrener, R. N.; Schultz, A. C.; Houghton, M. A.; Butler, D. N. *Tetrahedron* **1997**, *53*, 3991.

[iii] Huang, D. H.; Poon, S. F.; Chapman, D. F.; Chung, J.; Cramer, M.; Reger, T. S.; Roppe, J. R.; Tehrani, L.; Cosford, N. D. P.; Smith, N. D. *Bioorg. Med. Chem. Lett.* **2004**, *14*, 5473.

(9R,9aS,12aR,13S)-9,13-Diphenyl-11-(2-(pyridin-3-yloxy)phenyl)-12a,13-dihydro-9H-9,13-methanophenanthro[9,10-f]isoindole-10,12,14(9aH,11H)-trione (**2**). To a solution of anhydride **11** (0.29 g, 0.60 mmol) in acetic acid (25 mL), *ortho*-pyridine-3-ylaniline (**10**) (0.15 g, 0.81 mmol) was added. The mixture was stirred and heated at reflux under N_2 for 24 h. The solvent was removed under vacuum to give a brown solid. The solid was suspended in Na_2CO_3 aqueous solution (50 mL), and then extracted with CH_2Cl_2 (3 x 30 mL). The organic layer was collected, washed with brine (30 mL) and dried over MgSO4. The solvent was removed under vacuum to give a brown solid. Flash chromatography (aluminum oxide, MeOH/CH_2Cl_2 = 1/100) provided **2** as a pale white solid (0.29 g, 81%). mp 280 ºC dec. ^{1}H NMR (400 MHz, $CDCl_3$) δ 8.73 (d, *J* = 8.5 Hz, 2H minor), 8.45–8.35 (m, 2H minor, 2H major), 8.33–8.26 (m, 1H major, 2H minor), 8.16 (d, *J* = 8.5 Hz, 2H major), 6.86–7.75 (m, 19H major and 16H minor), 6.65 (dd, *J* = 8.3 Hz, *J* = 1.1 Hz, 1H minor), 6.47 (td, *J* = 7.9 Hz, *J* = 1.1 Hz, 1H minor), 6.18 (ddd, *J* = 8.3 Hz, *J* = 2.6 Hz, *J* = 1.4 Hz, 1H major), 5.93 (dd, *J* = 8.3 Hz, *J* = 1.1 Hz, 1H major), 4.68 (s, 2H major), 4.64 (dd, *J* = 7.9 Hz, *J* = 1.6 Hz, 1H minor), 4.58 (s, 2H minor). ^{13}C NMR (100 MHz, $CDCl_3$): 197.0, 195.7, 173.5, 173.0, 154.4, 152.5, 150.5, 145.7, 145.5, 143.8, 142.4, 133.9, 133.7, 133.7, 133.5, 131.3, 131.2, 131.1, 130.9, 130.7, 129.5, 129.4, 129.3, 129.2, 129.1, 128.9, 128.8, 128.6, 128.5, 128.4, 127.4, 127.0, 126.8, 126.7, 126.4, 126.3, 126.2, 126.0, 125.9, 124.4, 124.1, 123.9, 123.1, 122.9, 122.6, 122.2, 120.8, 118.4, 116.0, 77.5, 77.2, 77.1, 76.8, 63.7, 63.6, 45.6, 45.2. HRMS (EI) m/z calcd for $C_{44}H_{28}N_2O_4$ (M^+): 648.2049, found: 648.2059.

(9R,9aS,12aR,13S)-9,13-Dimethyl-11-(2-phenoxyphenyl)-12a,13-dihydro-9H-9,13-methanoisoindolo[5,6-f][1,10]phenanthroline-10,12,14(9aH,11H)-trione (**3**). Diene

13 (0.20 g, 0.77 mmol) and *N*-(2-phenyloxylphenyl) maleimide (**17**) (0.24 g, 0.92 mmol) were dissolved in CH_2Cl_2 (15 mL) and sealed in a medium pressure tube after flushing with N_2. The pressure tube was heated to 90 ºC with stirring for 24 h. After cooling, the solvent was removed under vacuum. The solid residue was washed with cold acetonitrile and acetone to give **3** as an off-white solid (0.18 g, 45%). mp 280 ºC dec. ^{1}H NMR (400 MHz, $CDCl_3$) δ 9.18 (d, *J* = 4.2 Hz, 2H major), 8.82 (d, *J* = 4.2 Hz, 2H minor), 8.67 (d, *J* = 8.4 Hz, 2H major), 8.48 (d, *J* = 8.4 Hz, 2H minor), 7.63 (dd, *J* = 8.4 Hz, *J* = 4.3 Hz, 2H major), 7.29 (dd, *J* = 8.4 Hz, *J* = 4.3 Hz, 2H minor), 6.75–7.25 (m, 5H major and 8H minor), 6.61 (d, *J* = 8.3 Hz, 1H major), 6.42 (t, *J* = 7.7 Hz, 1H major), 5.90–5.99 (m, 1H major, 1H minor), 4.68 (dd, *J* = 7.9 Hz, *J* = 1.1 Hz, 1H major), 3.56 (s, 2H minor), 3.41 (s, 2H major), 2.25 (s, 3H major), 2.21 (s, 3H minor). ^{13}C NMR (100 MHz, $CDCl_3$): 199.9, 198.6, 173.7, 173.4, 155.9, 154.8, 153.7, 152.6, 150.8, 149.9, 146.4, 146.1, 133.3, 133.1, 132.6, 132.0, 130.7, 130.5, 129.9, 129.6, 128.4, 127.8, 124.8, 124.6, 124.4, 124.2, 123.5, 122.8, 121.7, 121.5, 121.2, 119.9, 119.4, 118.7, 116.6, 77.5, 77.2, 77.1, 76.8, 55.4, 55.3, 47.9, 47.5, 14.4, 14.2. HRMS (EI) m/z calcd for $C_{33}H_{23}N_3O_4$ (M+): 525.1689; found: 525.1679.

(9R,9aS,12aR,13S)-11-(2,6-Diphenoxyphenyl)-9,13-dimethyl-12a,13-dihydro-9H-9,13-methanoisoindolo[5,6-f][1,10]phenanthroline-10,12,14(9aH,11H)-trione (**3'**). Diene **13** (0.20 g, 0.75 mmol) and *N*-(2,6-diphenoxylphenyl) maleimide (**18**) (0.32 g, 0.75 mmol) were reacted using the same procedure as described for balance **3**, the product **3'** was obtained as a pale white solid (0.28 g, 60 %). mp 280 ºC dec. ^{1}H NMR (400 MHz, $CDCl_3$) δ 8.98–9.01 (m, 2H), 8.69 (dd, *J* = 8.4 Hz, *J* = 1.3 Hz, 2H), 6.93–7.55 (m, 11H), 6.45 (d, *J* = 8.2 Hz, 1H), 6.12 (d, *J* = 7.7 Hz, 2H), 5.85 (d, *J* = 8.5 Hz, 1H), 3.63 (s, 2H), 2.37 (s, 6H). ^{13}C NMR (100 MHz, $CDCl_3$): 198.8, 173.2, 156.3, 155.8, 153.7, 149.7, 146.3,

133.1, 131.9, 130.3, 129.9, 129.5, 124.8, 124.4, 124.3, 122.6, 121.2, 119.5, 111.4, 111.0, 110.6, 77.4, 77.1, 76.8, 55.2, 47.7, 14.2. HRMS (EI) m/z calcd for $C_{39}H_{27}N_3O_5$ (M^+): 617.1951; found: 617.1939.

1-Methyl-3-(2-((9R,9aR,12aS,13S)-10,12,14-trioxo-9,13-diphenyl-9a,10,12a,13-tetrahydro-9H-9,13-methanophenanthro[9,10-f]isoindol-11(12H)-yl)phenoxy)pyridin-1-ium iodide (**6**). To a solution of balance **2** (0.20 g, 0.31 mmol) in acetone (40 mL), methyl iodide (1.0 mL, 16.1 mmol) was added. The reaction mixture was stirred at 45 ˚C for 12 h in the dark under N_2. After cooling to room temperature, a yellow precipitate was collected by filtration and washed with cold acetone to quantitatively give **6** as a yellow solid (0.25 g, 100%). mp 240 ºC. ^{1}H NMR (400 MHz, DMSO-d_6) δ 8.99–9.02 (m, 1H minor), 8.94 (d, J = 8.5 Hz, 2H minor), 8.79–8.83 (m, 1H minor), 8.73 (d, J = 6.0 Hz, 1H major), 8.51 (d, J = 8.5 Hz, 2H major), 8.31 (d, J = 7.8 Hz, 2H major), 8.20 (d, J = 7.8 Hz, 2H minor), 8.05–8.10 (m, 1H minor), 7.97–8.02 (m, 1H minor), 6.92–7.85 (m, 20H major, 17H minor), 6.63 (td, J = 7.9 Hz, J = 1.1 Hz, 1H minor), 6.31–6.36 (m, 1H major), 5.01 (s, 2H minor), 4.99 (s, 2H major), 4.44 (dd, J =7.9 Hz, J = 1.6 Hz, 1H minor), 4.34 (s, 3H minor), 4.31 (s, 3H major). ^{13}C NMR (100 MHz, DMSO-d_6): 195.6, 174.0, 152.9, 152.4, 142.2, 138.8, 137.1, 133.98, 133.6, 131.0, 130.5, 129.1, 129.1, 128.3, 128.2, 126.5, 126.0, 125.8, 125.3, 124.4, 123.2, 121.8, 63.1, 62.9, 47.9, 45.3, 40.1, 39.9, 39.7, 39.5, 39.5, 39.3, 39.1, 38.9, HRMS (ESI) m/z calcd for cation $[C_{45}H_{31}N_2O_4]$+ (M+): 663.2284; found: 663.2277.

(9S,9aR,12aS,13R)-4,9,13-Trimethyl-10,12,14-trioxo-11-(2-phenoxyphenyl)-9a,10,11,12,12a,13-hexahydro-9H-9,13-methanoisoindolo[5,6-f][1,10]phenanthrolin-4-ium iodide. (**7**). To a solution of balance **3** (80 mg, 0.15 mmol) in acetone (20 mL), methyl iodide (0.47 mL, 7.55 mmol) was added. The reaction mixture was heated at reflux for 12

h in the dark under N_2. After cooling to room temperature, a yellow precipitate was collected by filtration and washed with cold acetone to quantitatively give **7** as a yellow powder (102 mg, 100%). mp 280 ºC dec. The racemic form **7** was used without resolution. ^{1}H NMR (400 MHz, DMSO-d_6) δ 9.34 (d, J = 8.5 Hz, 1H), 9.12–9.19 (m, 2H), 8.87 (d, J = 8.6 Hz, 1H), 8.10 (dd, J = 8.4 Hz, J = 5.9 Hz, 1H), 7.98 (dd, J = 8.4 Hz, J = 4.2 Hz, 1H), 6.89–7.31 (m, 6H), 5.90 (d, J = 8.4 Hz, 1H), 5.82 (d, J = 7.5 Hz, 2H), 4.86 (s, 3H), 4.04 (s, 2H), 2.20 (s, 3H), 2.19 (s, 3H). ^{13}C NMR (100 MHz, $CDCl_3$): 198.3, 174.3, 174.1, 154.1, 153.5, 150.4, 149.1, 141.8, 140.3, 137.9, 137.4, 133.4, 132.9, 130.6, 129.9, 129.5, 127.7, 126.9, 125.3, 125.2, 124.5, 122.3, 120.6, 120.5, 115.8, 54.9, 54.9, 54.8, 47.5, 47.4, 40.2, 39.9, 39.7, 39.52, 39.5, 39.3, 39.1, 38.9, 13.9, 13.5. HRMS (ESI) m/z calcd for cation $[C_{34}H_{26}N_3O_4]^+$ (M^+): 540.1923; found: 540.1918.

1.3 Characterization

^{1}H and ^{13}C NMR spectra for all the newly synthesized molecular balances and X-crystal data (CIF) of **1''**, **2**, **3**, **3'**, **4**, **6** and **7** are available free of charge via Internet at http://pubs.acs.org/doi/abs/10.1021/jo400370e

2. Additional Figures and Tables

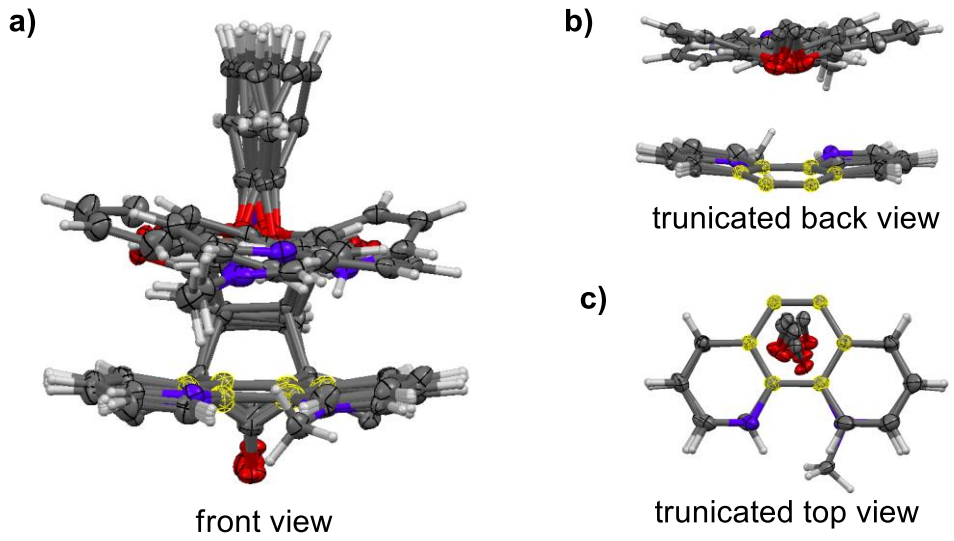

Figure 2.12 (a) Front-view of the crystal structure overlapping for **1'**, **2**, **3'**, **4**, **6** and **7** (the six atoms for overlapping operation are highlighted with yellow threads). The bridgehead groups are omitted for visual clarity; **(b)** Truncated back-view of the arm aromatic unit and shelf aromatic motifs; **(c)** Truncated top-view of the arm oxygen (with connected aromatic carbon) and the shelf aromatic motif.

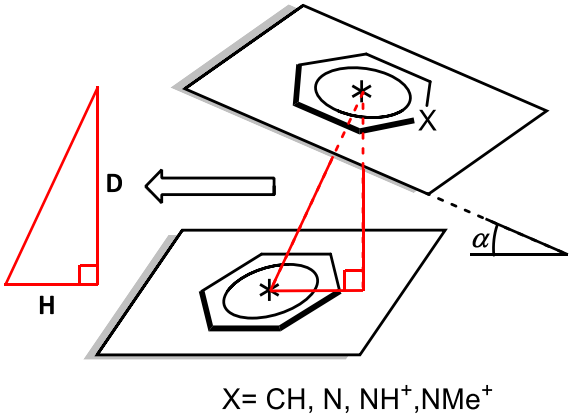

Figure 2.13 Geometric parameters defined for the characterizing the intramolecular π-stacking interactions in the *folded* conformers. (**α**: plane-to-plane angle, **D**: centroid-to-plane vertical distance, and **H**: centroid-to-centroid horizontal off-set). The top ring is aromatic ring of the arm, and the bottom is ring the outer ring of the arene shelf.

Table 2.4. The measured ΔG's [a,b] [kcal/mol] in deutrated solvents at rt.

	1	**2**	**3**	**4**[c]	**5**[c]	**6**	**7**
$CDCl_3$	0.49	-0.11	0.30	-0.40	-0.94	0.09	≤-1.74[d]
DMSO-d_6	0.32	-0.22	-0.05	-0.45	-1.43	-0.76	≤-1.74[d]
CD_3CN	0.15	-0.39	-0.06	-0.91	-1.51	-0.83	≤-1.74[d]

[a] ΔG = –R*298*ln([*folded*]/[*unfolded*]). [b] Propagation of errors gives an uncertainty less than ± 0.03 kcal/mol. [c] The ΔG's of balances **4** and **5** were obtained as the linear extrapolation to 1 equiv. of MsOH added to solutions of balances **2** and **3**, respectively (See below section). [d] Conservative estimate of the *folded/unfolded* ratio to be greater than 19/1 as only the *folded* conformer **7** was observed in the ^{1}H NMR spectra.

Table 2.5 Tabulated data for the correlation plot in the text.

	Ph–Ph	Py–Ph		PyH^+–Ph		$PyMe^+$–Ph	
Geometry	–	*distal*	*proximal*	*distal*	*proximal*	*distal*	*proximal*
E_{exp} [a,b]	-0.82	-1.36	-1.19	-1.59	-2.57	-1.90	-2.88[c]
E_{calc} [b,d]	-2.48	-3.04	–	-8.34	–	-7.88	-9.36
$E_{calc.}$ [b,e]	-2.71	-3.23	-2.36	–	–	–	–
$E_{calc.}$ [b,f]	-2.61	–	–	–	-8.91	–	-9.35

[a] Eexp = ΔΔG = ΔG[**x**] - ΔG[**1**]; **x** = **2**-**7**. ΔG's were measured in DMSO-d_6 at rt.
[b] [kcal/mol] [c] The Eexp for $PyMe^+$–Ph stacking at the *proximal* configuration was estimated to be greater than -2.88 kcal/mol. [d] CCSD(T)/CBS. Tsuzuki, S.; Mikami, M.; Yamada, S. *J. Am. Chem. Soc.* **2007**, *129*, 8656. [e] SCS-MP2/aug-cc-pVTZ. Sherrill, C. D.; Hohenstein, E. G. *J. Phys. Chem. A* **2009**, *113*, 878. [f] CCSD(T)/CBS. Singh, N. J.; Min, S. K.; Kim, D. Y.; Kim, K. S. J. *Chem. Theory and Comput.* **2009**, *5*, 515.

3. Characterizations of the O-π repulsion in crystal structures

The atom-to-centroid distance (**r**) and the horizontal displacement (**h**) between the arm ether oxygen and the interacting shelf six-membered aromatic unit were found to be 3.32–3.48 Å and 0.22–0.88 Å, respectively (Figure 2.14, Table 2.6). According to our previous study,[i] this repulsive interaction counteracts the attractive aromatic interaction

[i] Carroll, W. R.; Pellechia, P.; Shimizu, K. D. *Org. Lett.* **2008**, *10*, 3547.

and favors the open conformers. These measured parameters fit well with the reported unfavorable above-surface fashion lone pair-phenyl interaction (**r** < 5.0 Å; **h** < 4.2 Å) in the recent CSD study.[i]

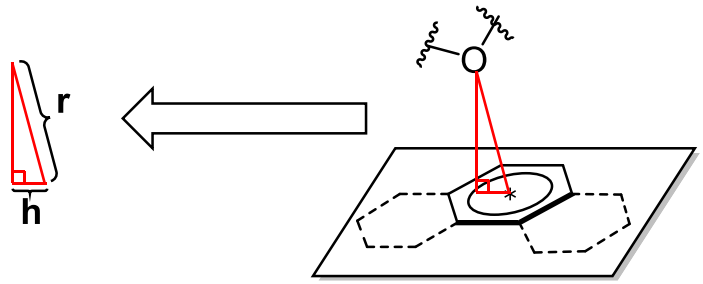

Figure 2.14. Geometric parameters defined for characterizing the O-π interaction. (**r**: the atom-to-plain distance; **h**: atom-to-centroid horizontal displacement)

Table 2.6 Measured geometric parameters (***r*** and ***h***) defined for characterizing the O-π interactions in crystal structure **1'**, **2**, **3'**, **4**, **6** and **7**.

balance	**1'**	**2**	**3'**	**4**	**6**
r [Å]	3.48	3.715	3.48	3.48	3.33-3.43[a]
h [Å]	0.57	0.44	0.22	0.53	0.37-0.48[a]

[a] Observation of the two crystallographically independent cations.

4. Quantification of the *folded* and *unfolded* conformers in solution

The quantification for the *folded* and *unfolded* conformers in solution was based on their spectral integrations of the differentially shifted succinimide methide protons in the two conformers. The signal for the *ortho* proton (**H_a**) from the aromatic pivoting unit in the *unfolded* conformer was shifted upfield off the aromatic region and distinctly appeared as a doublet of doublets, which helped to identify the **H_b** signal for the *unfolded* conformer

[i] Mooibroek, T. J.; Gamez, P. *CrystEngComm* **2012**, *14*, 1027.

The *folded/unfolded* ratios for balances **1**-**7** in the noted deuterated solvents were measured after 1 h (~ 20 half-lives) of equilibration at rt on Varian 400 MHz spectrometer. The *folded/unfolded* ratio in each case was obtained by tracking the differently shifted succinimide methide proton signals (the spectral deconvolution using VNMRJ software fitspec command was used). The corresponding folding energy (ΔG) was calculated using ΔG = –RTln([*folded*]/[*unfolded*]). The ΔG's of balances **4** and **5** were measured by adding MsOH to solutions of balances **2** and **3**, respectively. Good linear correlations were observed between the ΔG and the amount of added MsOH in both case (Figure 2.16 and 2.17). To avoid the interference from the broad water peak, the ΔG's of balances **4** and **5** were obtained by extrapolating the observed linear correlation trend to one equivalent of MsOH added (See below section for details).

5. Measuring the ΔG's for balances 4 and 5

In DMSO-d_6: The relative amount of added MsOH against the balance in each sample was calculated based on the integrated areas of the MsOH's methyl proton (**H_c**) peak (s, δ: ~2.4) and the balance's succinimide methide proton (**H_b**) peaks for the two conformers (s, δ: ~5.0) (Figure 2.15). Multiple data points were acquired within 0 to 1 equiv. range. The obtained *folded/unfolded* ratios, ΔG's and relative amount of added MsOH are shown in Table 2.7 and 2.8. The plots of ΔG's against the relative amount of added MsOH are shown in Figure 2.16 and Figure 2.17. The ΔG's were found to change linearly against the relative amount of added MsOH during the processes of |**2** + MsOH → **4**| and |**3** + MsOH → **5**|. The slopes of the linear fitting were used to extrapolate the ΔG's to 1 equiv. of MsOH to give $\Delta G_{[4]}$ and $\Delta G_{[5]}$, respectively, that is, $\Delta G_{[4]}$ = -0.23 + $\Delta G_{[2]}$ = -0.45 kcal/mol; $\Delta G_{[5]}$ = -1.38 + $\Delta G_{[3]}$ = -1.43 kcal/mol.

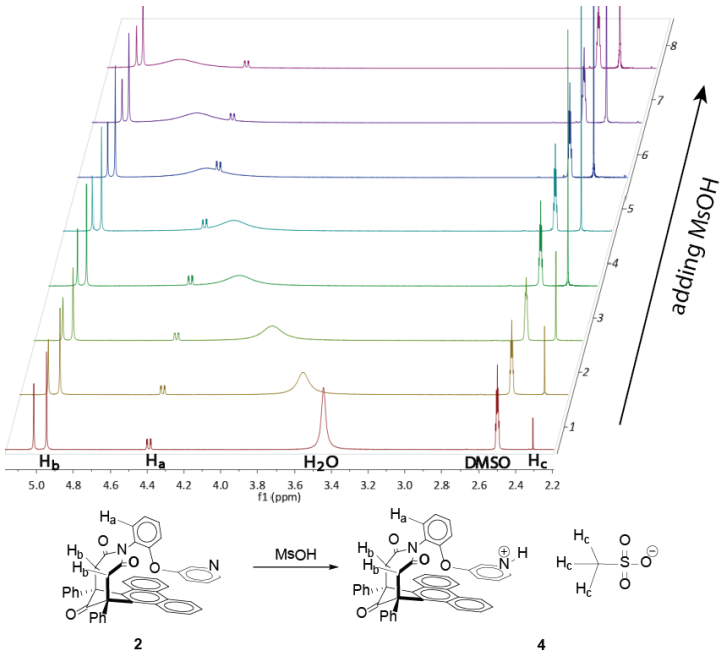

Figure 2.15 The compiled integration areas on ^{1}H-NMR spectra in the experiment process of |**2** + MsOH →**4**|.

Table 2.7 The measured relative amounts of added MsOH, *folded/unfolded* ratios and calculated ΔG's in the titration experiment of |**2** + MsOH → **4**| in DMSO-d_6

equivalent of added MsOH[a]	0.04	0.14	0.30	0.46	0.59	0.71	0.91	0.98
folded/unfolded ratio[a]	1.47	1.55	1.67	1.77	1.85	1.97	2.06	2.15
Δ*G*[kcal/mol][b]	-0.23	-0.26	-0.30	-0.34	-0.36	-0.40	-0.43	-0.45

[a] Relative error in the *folded/unfolded* ratios is less than ± 5%. [b] The error in the ΔG's is less than ± 0.03 kcal/mol.

Table 2.8. The measured relative amounts of added MsOH, *folded/unfolded* ratios and calculated ΔG's in the titration experiment of |**3** + MsOH → **5**|in DMSO-d_6

equivalent of added MsOH[a]	0.05	0.17	0.31	0.46	0.59	0.71	0.89	1.00
folded/unfolded ratio[a]	1.08	1.31	1.76	2.36	3.22	5.08	7.30	11.00
ΔG [kcal/mol][b]	-0.05	-0.16	-0.33	-0.51	-0.69	-0.96	-1.18	-1.42

[a] Relative error in the closed/open ratios is less than ± 5%. [b] The error in the ΔG's is less than ± 0.03 kcal/mol.

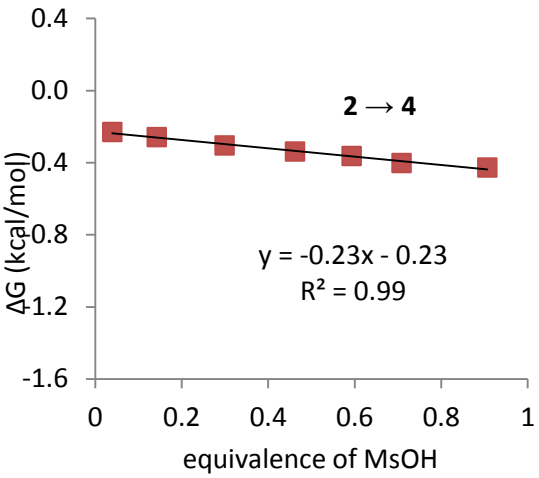

Figure 2.16 The plot of ΔG's against the relative amount of added MsOH in the titration experiment of |**2** + MsOH → **4**| in DMSO-d_6

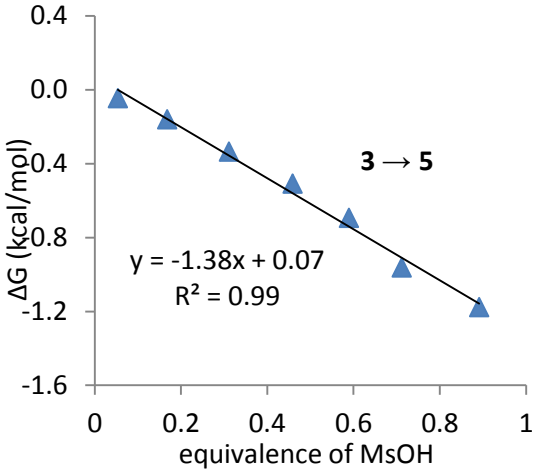

Figure 2.17 The plot of ΔG's against the relative amount of added MsOH in the titration experiment of |**3** + MsOH → **5**| in DMSO-d_6

In CD_3CN: The experiment followed the same procedure described above. The obtained *folded/unfolded* ratios, ΔG's and relative amount of added MsOH are shown in Table 2.9 and 2.10. The plots of ΔG's against the relative amount of added MsOH are shown in Figure 2.18 and 2.19. $\Delta G_{[4]}$ = -0.52 + $\Delta G_{[2]}$ = -0.91 kcal/mol; $\Delta G_{[5]}$ = -1.45 + $\Delta G_{[3]}$ = -1.51 kcal/mol.

Table 2.9 The measured relative amounts of added MsOH, *folded/unfolded* ratios and calculated ΔG's in the titration experiment of |**2** + MsOH → **4**|in CD_3CN

equivalent of added MsOH[a]	0.37	0.54	0.64	0.71	0.83
folded/unfolded ratio[a]	2.65	3.06	3.37	3.56	3.99
ΔG [kcal/mol][b]	-0.58	-0.66	-0.72	-0.75	-0.82

[a] Relative error in the closed/open ratios is less than ± 5%. [b] The error in the ΔG's is less than ± 0.03 kcal/mol.

Table 2.10 The measured relative amounts of added MsOH, *folded/unfolded* ratios and calculated ΔG's in the titration experiment of |**3** + MsOH → **5**|in CD_3CN

equivalent of added MsOH[a]	0.26	0.39	0.59	0.75	0.84
folded/unfolded ratio[a]	1.72	2.22	3.57	5.63	7.27
ΔG [kcal/mol][b]	-0.32	-0.47	-0.75	-1.02	-1.17

[a] Relative error in the closed/open ratios is less than ± 5%. [b] The error in the ΔG's is less than ± 0.03 kcal/mol.

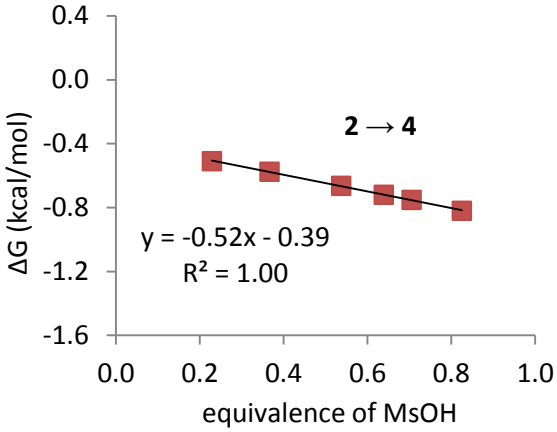

Figure 2.18 The plot of ΔG's against the relative amount of added MsOH in the titration experiment of |**2** + MsOH → **4**| in CD_3CN

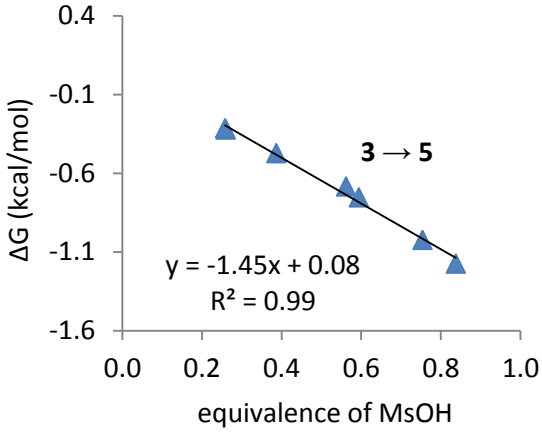

Figure 2.19 The plot of ΔG's against the relative amount of added MsOH in the titration experiment of |**3** + MsOH → **5**| in CD_3CN

In $CDCl_3$: The experiment followed the same procedure described above. The obtained *folded/unfolded* ratios, ΔG's and relative amount of added MsOH are shown in Table 2.13 and 2.14. The plots of ΔG's against the relative amount of added MsOH are shown in Figure 2.20 and Figure 2.21. $\Delta G_{[4]}$ = -0.29 + $\Delta G_{[2]}$ = -0.40 kcal/mol; $\Delta G_{[5]}$ = -1.24 + $\Delta G_{[3]}$ = -0.94 kcal/mol

Table 2.11 The measured relative amounts of added MsOH, *folded/unfolded* ratios and calculated ΔG's in the titration experiment of |**2** + MsOH → **4**| in $CDCl_3$

equivalent of added MsOH[a]	0.04	0.14	0.33	0.48	0.64	0.79	0.84	0.99
folded/unfolded ratio[a]	1.25	1.31	1.44	1.56	1.69	1.81	1.83	1.98
ΔG [kcal/mol][b]	-0.13	-0.16	-0.22	-0.26	-0.31	-0.35	-0.36	-0.40

[a] Relative error in the closed/open ratios is less than ± 5%. [b] The error in the ΔG's is less than ± 0.03 kcal/mol.

Table 2.12 The measured relative amounts of added MsOH, *folded/unfolded* ratios and calculated ΔG's in the titration experiment of |**3** + MsOH → **5**| in $CDCl_3$

equivalent of added MsOH[a]	0.09	0.15	0.33	0.44	0.59	0.73	0.88	0.96
folded/unfolded ratio[a]	0.64	0.78	1.04	1.33	1.72	2.36	3.34	4.32
ΔG [kcal/mol][b]	0.27	0.14	-0.02	-0.17	-0.32	-0.51	-0.71	-0.87

[a] Relative error in the closed/open ratios is less than ± 5%. [b] The error in the ΔG's is less than ± 0.03 kcal/mol.

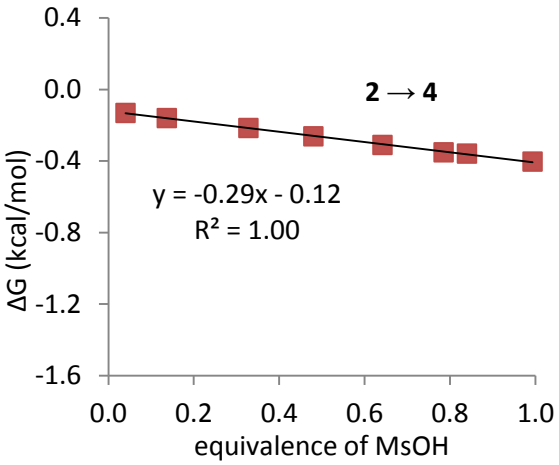

Figure 2.20 The plot of ΔG's against the relative amount of added MsOH in the titration experiment of |**2** + MsOH → **4**| in $CDCl_3$

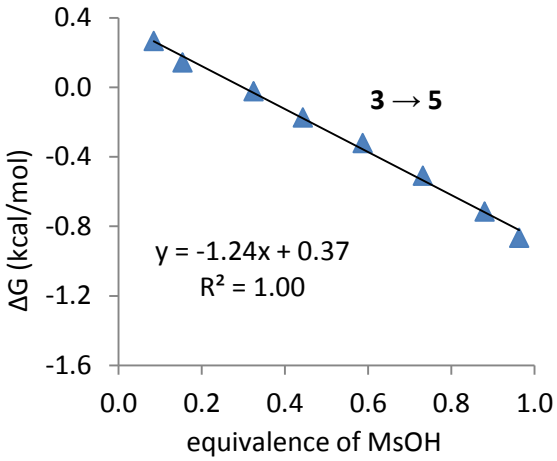

Figure 2.21 The plot of ΔG's against the relative amount of added MsOH in the titration experiment of |**3** + MsOH → **5**| in $CDCl_3$

6. Error analysis and maximum *folded/unfolded* ratios

The NMR samples in this work were prepared by dissolving ~10 mg of the purified balance in 0.7 mL of the deuterated solvent of choice, giving a total concentration of ~22 mM (assuming an average molecular weight of 650). NMR peak areas were measured using peak-fitting software, which greatly reduces the error of the integration analysis. Using peak-fitting methods, NMR integration error is less than 1% for concentrations above 10 mM.[i]

Therefore, the error for a 1:1 *folded/unfolded* ratio is very small as peaks for both conformers correspond to concentrations greater than 10 mM. This error is equal to the square root of the sum of the squares of 1% and 1%, which is only 1.4% (Equation 2.1).

$$Error_{\frac{[folded]}{[unfolded]}} = \sqrt{Error^2_{[folded]} + Error^2_{[unfolded]}} \qquad \text{(Equation 2.1)}$$

[i] Rizzo, V.; Pinciroli, V. *J. Pharmaceut. Biomed.* **2005**, *38*, 851

However, for non-unity ratios, integration error will depend mostly on the concentration of the minor conformer as the integration error. Precise measurements of error at different concentrations could not be found. However, Rizzo et al. states that,[viii] "*In our experience with 400–500 MHz instruments and non-refrigerated ^{1}H-probes, qNMR may be applied to solutions with concentration as low as 1 mM if a precision of 5% is acceptable.*" This observation is consistent our own observations of integration errors at 1 mM. Below 1 mM the error percentages increase rapidly above 5%, therefore, the 1 mM concentration was used as a limiting value.

Thus, for a 22 mM sample, the highest ratio that we can accurately measure is 19:1, where the minor conformer concentration is at the limiting concentration of 1 mM. This ratio will also have the highest percent error. Using equation 1 and plugging in a 1% error for the major conformer and 5% error for the minor conformer, the error in the *folded/unfolded* ratio will be 5.1%.

The highest error in ΔG for the *unfolded-folded* conformational equilibrium is calculated using Equations 2.2 and 2.3 for the maximum ratio of 19:1. Therefore, the propagated error in ΔG ($Error_{\Delta G}$) is dependent on $Error_{\frac{[folded]}{[unfolded]}}$. When the folding ratio is 19/1, $Error_{\frac{[folded]}{[unfolded]}}$ is ±5.1% which is 0.0026. Plugging into equation 3 provides a maximum $Error_{\Delta G}$ of ±0.03 kcal/mol.

$$\Delta G = RTln\left(\frac{[folded]}{[unfolded]}\right) \quad \text{(Equation 2.2)}$$

$$Error_{\Delta G} = R \times T \times Error_{\frac{[folded]}{[unfolded]}} \quad \text{(Equation 2.3)}$$

$$Error_{\Delta\Delta G} = \sqrt{Error_{\Delta G}^2 + Error_{\Delta G}^2} \quad \text{(Equation 2.4)}$$

CHAPTER 3

THE CH-π INTERACTION OF METHYL ETHERS AS A MODEL FOR CARBOHYDRATE-*N*-HETEROARENE INTERACTIONS[i]

[i] Reproduced with permission from Li, P.; Parker, T. M.; Hwang, J.; Deng, F.; Smith, M. D.; Pellechia, P. J.; Sherrill, C. D.; Shimizu, K. D. *Org. Lett.* **2014**, *16*, 5064. Copyright 2014 American Chemical Society.

1. Introduction

Carbohydrate recognition plays a key role in many biological processes[1] such as fertilization,[2] immune response,[3] and inflammation.[4] Thus, the study of factors that enhance carbo-hydrate affinity and selectivity has been the focus of extensive research efforts.[5] While hydrogen bonding is generally considered the primary interaction,[6] CH-π interactions[7] have also been cited as key contributors to carbohydrate binding.[8] Interestingly, a high percentage of the CH-π interactions of carbohydrates involve heterocyclic aromatic surfaces.[9] For example, the protein-sugar complex between *Urtica dioica* agglutinin and the triose NAG3 contains four CH-π interactions each involving a different heterocyclic aromatic residue (Trp21, Trp23, His67 and Trp69) (Figure 3.1A).[10] Thus, the goal of this work was to determine whether carbohydrates form stronger CH-π interactions with heterocyclic versus non-heterocyclic aromatic surfaces. Our strategy was to employ a small molecule model system in conjunction with computational studies to address this question. In this study, methyl ether groups were used as minimalistic models of carbohydrates. Methyl ethers can form similar CH-π interactions as those in carbohydrates as they have alkyl groups directly attached to polar oxygens (Figure 3.1B). In addition, the methyl ether groups lack hydrogen bond donating OH groups that would complicate the analysis. We found that the presence of the ether oxygen plays a key role in modulating the interaction energies and geometries of this moiety.

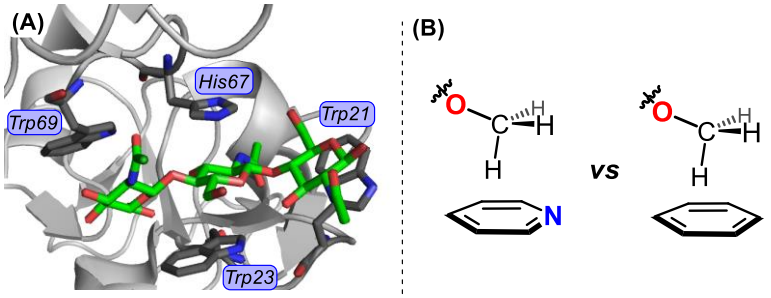

Figure 3.1 (A) Crystal structure of the active site of the *Urtica dioica* agglutinin with a bound tri-*N*-acetylchitotriose (NAG3).[9] The heterocyclic residues that form CH-π interactions (Trp69, Trp23, His67 and Trp21) are highlighted (PDB entry 1EHH); **(B)** Schematic representation of the CH-π interactions of a methyl ether group with an *N*-heterocyclic and non-heterocyclic aromatic ring.

Molecular torsional balances are small molecule model systems designed to measure the strength of intramolecular non-covalent interactions via shifts in a conformational equilibrium.[11] Utilizing this strategy, we have recently developed a rigid bicyclic molecular balance that has been successfully applied to study a number of weak non-covalent interactions including π-π,[12] CH-π,[13] deuterium-π,[14] and heterocyclic-π interactions.[15] For this study, these balances were modified to study the CH-π interactions of heterocyclic and non-heterocyclic aromatic surfaces (Figure 3.2). Balances **1**-**6** were designed with a methyl arm (OCH_3 or CH_2CH_3) and an aromatic surface containing two, one, or zero N-heterocyclic units that could form an intramolecular CH-π interaction. The balances were synthesized via the same modular route.[11-14]

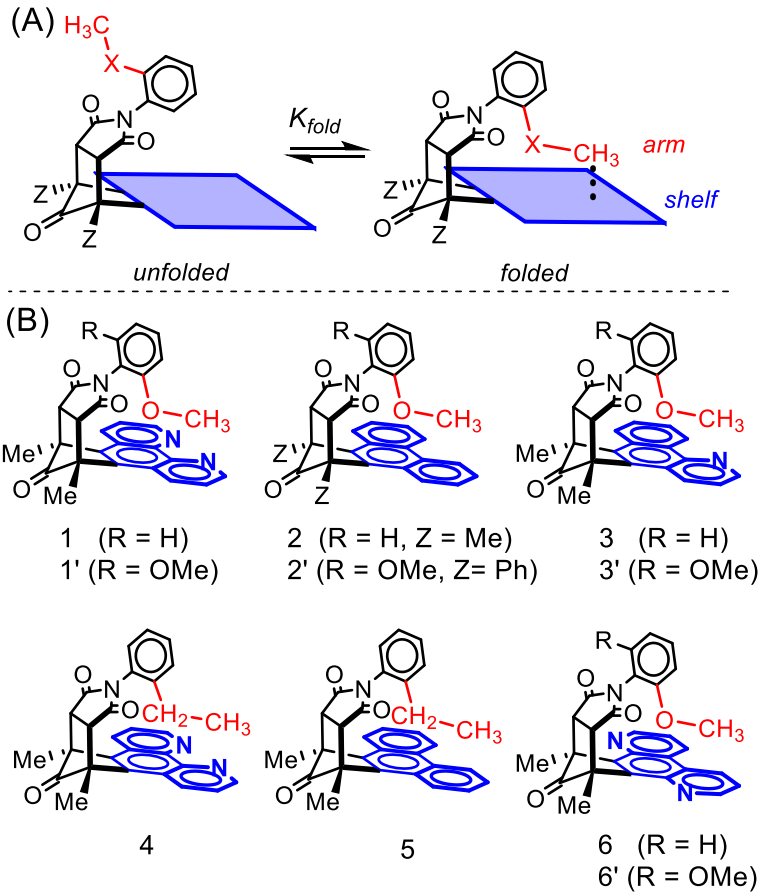

Figure 3.2 (A) Schematic representation of the *unfolded–folded* conformational equilibrium of molecular balances **1-3** for measuring the CH-π interactions of the methyl ether group; **(B)** Structures of the *folded* conformers of molecular balances with methyl ether (**1, 2, 3,** and **6**) and with ethyl arms (**4** and **5**) and their two-armed analogues (**1'**, **2'**, **3'** and **6'**) for X-crystallographic analysis.

2. Results and Discussion

First, the ability of balances **1-6** to form an intramolecular CH-π interaction in the *folded* conformer between the methyl arm and the aromatic shelf was assessed in solution and in the solid-state. In solution (CD_2Cl_2), large upfield chemical shifts were observed for the *folded* versus *unfolded* methyl arm protons in the ^1H NMR spectra (Table 3.1). These upfield shifts ($\Delta\delta$ = 1.3 to 1.5 ppm) were consistent with the methyl groups being in contact with the aromatic shelf in the *folded* conformers and forming the desired

intramolecular CH-π interactions. The differences in the chemical shifts of the methyl protons were readily measured at rt, as the *unfolded* and *folded* conformers were in slow exchange in the ^{1}H NMR spectra.[11-14]

Table 3.1 ^{1}H NMR solution measurements of balances **1-6** in CD_2Cl_2 at 25 °C.

balance	CH-π interaction	$\Delta\delta_{CH3}$ [a]	$\frac{[folded]}{[unfolded]}$ [b]	ΔG [c]
1	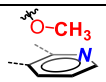	1.42	1.04	-0.02
2	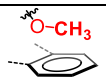	1.48	0.59	+0.31
3	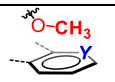 ***Y*** = N & CH	1.45	0.79	+0.14
4	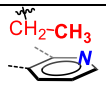	1.20	1.33	-0.17
5	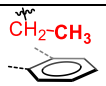	1.15	1.41	-0.20
6	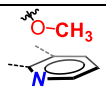	1.31	0.66	+0.25

[a] Difference in ^{1}H chemical shift (ppm) of the CH_3 protons between the *unfolded* and *folded* conformers. [b] Measured from the integration areas of the CH_3 peaks in the ^{1}H NMR spectra (error < ± 5%). [c] Folding energies in kcal/mol (±0.03 kcal/mol).

The intramolecular CH-π interactions were also characterized in the solid-state by X-ray crystallography. To ensure the formation of the *folded* conformers in the solid-state, 'two-armed' balances (**1'**, **2'**, **3'** and **6'**) were prepared and crystallized. The two-armed balances have the same arm at both *ortho*-positions of the pivot ring, and thus, one arm is always in the *folded* conformation, and the other arm is in the *unfolded* conformation. X-ray crystallographic analysis of **1'-3'** and **6'** showed the expected intramolecular CH-π

interactions (Figure 3.3). In each structure, a proton on the methyl group of the *folded* arm was within the proper atom-to-plane distance (2.56 - 2.61 Å) to form a CH-π interaction with the aromatic shelf.[16]

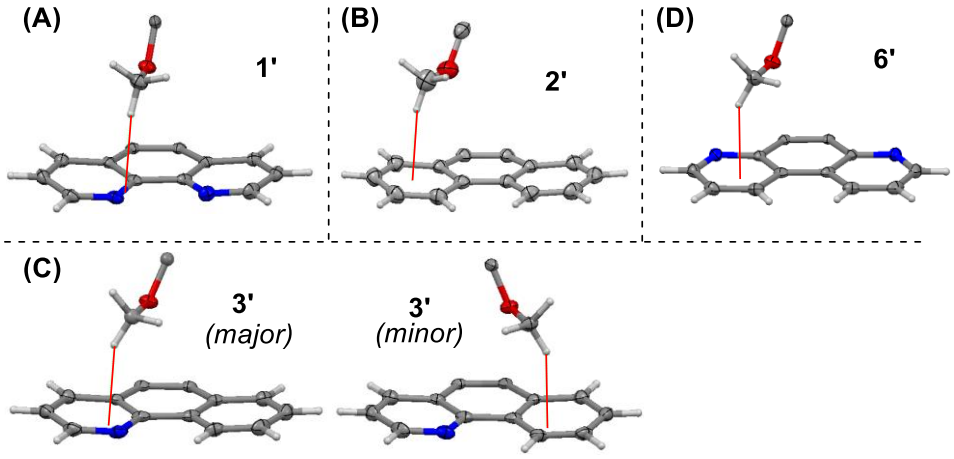

Figure 3.3 Truncated front views of the X-ray crystal structures of balances **1' (A)**, **2' (B)**, **3' (C)** and **6' (D)**, highlighting the intramolecular CH-π interactions. In the structure for **3'**, both the **3'** major and **3'** minor configurations were observed with a ratio of 62:38. The atom-to-plane distances for the intramolecular CH-π interactions are highlighted as red lines.

Next, the strengths of the CH-π interactions were measured in solution (Table 3.1). The folding ratios were measured in solution (CD_2Cl_2) by integration of the corresponding peaks in the ^1H NMR spectra and converted into folding energies [$\Delta G = -RT \ln([folded]/[unfolded])$]. First, the folding energies of balances **1** and **2** were compared to test whether the methyl ether arm formed stronger interactions with heterocyclic or non-heterocyclic aromatic surfaces. Balances **1** and **2** had folding energies of -0.02 and +0.31 kcal/mol, respectively. Thus, the intramolecular interactions in heterocyclic **1** were more stabilizing by -0.33 kcal/mol than in non-heterocyclic **2**. Analysis of hybrid balance **3**, which contained a heterocyclic and a non-heterocyclic ring, provided further evidence that

the heterocyclic surface formed stronger intramolecular interactions. The OCH_3 group in **3** can flip back and forth between the heterocyclic and non-heterocyclic outer ring of the benzoquinoline surface.[17] Indeed, both intramolecular CH-π configurations were observed in the crystal structure of **3'** (Figure 3.3C). The populations of the two configurations were unequal in the crystal structure, as the OCH_3-heterocyclic interaction was favored by approximately 2:1 (62:38). Analyses of the folding ratios of **3** in solution were also consistent with the heterocyclic ring forming stronger intramolecular interactions. The folding energy of **3** (+0.14 kcal/mol) fell almost halfway between the folding energies of the purely heterocyclic and non-heterocyclic balances **1** and **2** (-0.02 and +0.31 kcal/mol).

In assessing the reason for the above stability trends, we arrived at the conclusion that they probably did not arise from differences in the strengths of the CH-π interactions. Our reasoning was that CH-π interactions are generally considered to be dispersion dominated interactions.[18] The dispersion interactions for an *N*-heterocyclic and an isosteric non-heterocyclic ring should be very similar as the difference in polarizability of a nitrogen to a CH group is minor.[19] Furthermore, the dipole of the *N*-heterocycle should have little effect on the CH-π interaction. To confirm that heterocyclic and non-heterocyclic surfaces form similar strength CH-π interactions, we conducted *ab initio* calculations (estimated complete-basis-set-coupled-cluster, CCSD(T)/CBS) comparing the CH-π interactions of methane with benzene and pyridine, respectively. Although differences in geometry were observed, the intermolecular interactions in the two systems were isoenergetic (-1.39 versus -1.41 kcal/mol).

Thus, an alternative hypothesis was developed based on the role of the oxygen linkers in balances **1-3**. To isolate the influence of the oxygen linker, we synthesized two

analogous heterocyclic and non-heterocyclic balances **4** and **5** without oxygen linkers where the OCH_3 groups were replaced by CH_2CH_3 groups. Balances **4** and **5** formed similar intramolecular CH-π interactions as balances **1**-**3**. This was evident from the similarly large upfield chemical shifts (~1.2 ppm) of their terminal methyl protons in the *folded* conformers (Table 3.1).

In contrast to methyl ether balances **1**-**3**, balances **4** and **5** had very similar interaction energies for the heterocyclic and non-heterocyclic surfaces. Balances **4** and **5** had folding energies of -0.17 and -0.20 kcal/mol, respectively, which were within experimental error (±0.03 kcal/mol). Thus, both computational and experimental studies concurred that the differences in the interactions between the heterocyclic and non-heterocyclic aromatic surfaces appeared to be due to the oxygen linker.

Two hypotheses were formulated to explain the influence of the oxygen linker on the intramolecular interactions. The first hypothesis was that the oxygen linker was polarizing the C-H bond of the methyl ether. This polarization hypothesis was consistent with theoretical[20] and experimental[21] studies that found that more polarized or acidic C–H bonds form stronger CH-π interactions. The second hypothesis was that the C-O bond dipole was interacting with the heterocyclic dipole. The two hypotheses were tested computationally and experimentally by positioning the OCH_3 group at different angles over the *N*-heterocyclic ring (Figure 3.4). The dihedral angle (**α**) of the C-O bond dipole with respect to the heterocycle dipole was systematically varied and the corresponding interaction energies were measured (Figure 3.4). For the C-H bond polarization hypothesis, the interaction energy should not vary substantially and would only be weakened when the electronegative oxygen and nitrogen atoms were in close proximity. However, for the

dipole hypothesis, there should be a strong stabilizing as well as a destabilizing effect, depending upon the orientation of the dipoles.

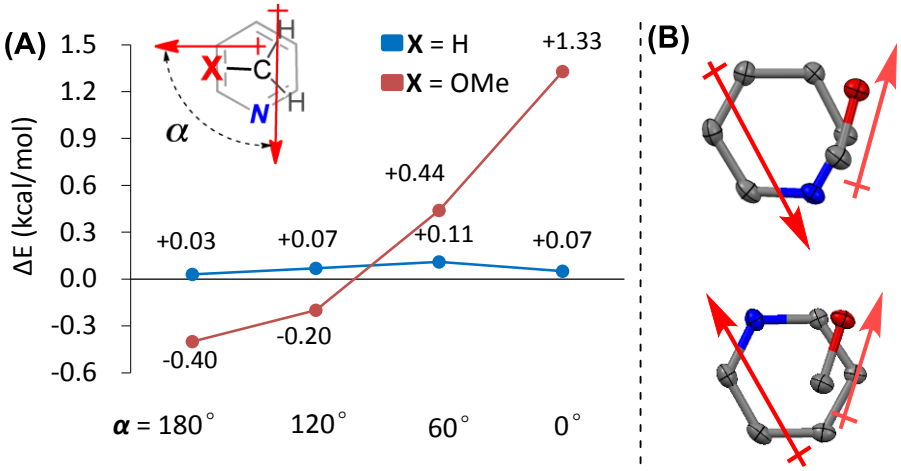

Figure 3.4 (A) Calculated CCSD(T)/CBS [i.e., MP2/CBS from aug-cc-pVQZ/aug-cc-pV5Z extrapolation + (CCSD(T)/aug-cc-pVTZ – MP2/aug-cc-pVTZ)] interaction energy differences (**ΔE**) between the heterocyclic and non-heterocyclic CH-π complexes [ΔE = E (CH_3**X**/Py) - E (CH_3**X**/Bz); **X** = H or OMe] at four different orientations of the dipoles (**α** = 180˚, 120˚, 60˚ and 0˚);[i] **(B)** Partial top-views of the CH-π interaction regions in crystal structures **1'** (top) and **6'** (bottom) highlighting the orientations of the C-O bond and heterocycle dipoles.

The results from our computational and experimental studies were consistent with the dipole hypothesis. First, the computational study estimated the complexation energy of dimethyl ether with pyridine or benzene. The CH_3 group of dimethyl ether was positioned over the aromatic ring with a single C–H bond forming a CH-π interaction. Intermolecular interaction energies were computed for a series of dihedral angles **α**. The difference in interaction energies when pyridine was replaced by benzene, ΔE, was plotted as a function of **α** in Figure 3.4 (red curve). When the C-O and pyridine dipoles were antiparallel (**α** = 180°), the interaction between dimethyl ether and pyridine was stabilized

[i] Details and Results of Theoretical Calculations are available free of charge via Internet at http://pubs.acs.org/doi/abs/10.1021/ol502418k

compared to the interaction energy between dimethyl ether and benzene (ΔE = -0.40 kcal/mol). When the C-O and pyridine dipoles were parallel (**α** = 0°), the interaction energy was strongly destabilizing for pyridine versus benzene (ΔE = 1.33 kcal/mol). To confirm that these geometric effects were indeed due to interactions between the C-O dipole and the heterocycle dipole, a control study was performed in which dimethyl ether was replaced in the computations by methane (blue curve in Figure 3.4). Consistent with our hypothesis, the removal of the C-O dipole by replacing dimethyl ether with methane resulted in very small values for ΔE (the difference between methane/pyridine and methane/benzene) that are nearly constant with respect to **α**.

A similar experiment was carried out using our molecular balances. The precise positioning of the OCH_3 and heterocycle dipoles was more difficult using model system. However, we were able to synthesize and test a new balance **6** which had the heterocyclic nitrogens at the 4- and 7-positions. This places the *N*-heterocyclic nitrogens on opposite edge of the aromatic shelf in comparison to the original 1,10-phenanthroline shelf. Comparison of balances **1** and **6** provided a means to study two different geometries of the interaction. The orientation of the heterocycle dipole of the outer ring on the shelf and the C-O bond from the crystal structures of **1'** and **6'** (Figure 3.4B) most closely correlates to **α** = 120° and 60°, respectively. Thus, the dipoles in **1** point in opposite directions and the dipoles in **6** point in the same direction. The measured folding energies for **1** and **6** (-0.02 and +0.25 kcal/mol) revealed the same stability trend predicted by the computational study. When the dipoles were antiparallel as in balance **1**, the OCH_3-heterocyclic interaction was more stabilizing (lower in energy). When the dipoles were aligned in the same direction as in **6**, the OCH_3-heterocyclic interaction was destabilized (higher in energy).

3. Conclusion

In conclusion, we have utilized a combination of theory and model systems to study the CH-π interactions of N-heterocyclic and non-heterocyclic surfaces. There was excellent agreement between the two approaches. The -OCH_3 group was found to be capable of forming stronger non-covalent interactions with *N*-heterocyclic surfaces. In contrast, the -CH_2CH_3 group showed similar interaction energies for the two types of surfaces. Thus, the methyl ether oxygen appears to play a key role in modifying the interaction energies with heterocyclic surfaces. The oxygen atom does not appear to enhance the CH-π interaction directly. Instead, the C-O dipole is interacting with the heterocycle dipole, which can strengthen or weaken the OCH_3-aromatic interaction. These stability trends may have bearing on many biologically important carbohydrate-aromatic interactions. The attraction between C-O and heterocycle dipoles explain the prevalence of carbohydrate-*N*-heteroarene interactions. This dipole-dipole interaction could also be used to optimize carbohydrate binding in synthetic and bioengineered carbohydrate receptors. New molecular balances containing other biologically relevant heterocyclic motifs, such as tryptophane, pyrimidine and purines, are currently being developed in our laboratory to further investigate this phenomenon.

Reference

[1]. (a) Dwek, R. A. *Chem. Rev.* **1996**, *96*, 683. (b) Bertozzi, C. R.; Kiessling, L. L. *Science* **2001**, *291*, 2357. (c) Gabius, H. J.; Siebert, H. C.; Andre, S.; Jimenez-Barbero, J.; Rudiger, H. *ChemBioChem* **2004**, *5*, 740; (d) Garg, H. G.; Cowman, M. K.; Hales, C. A.; *Carbohydrate Chemistry, Biological and Medical Applications,* 1st ed.; Elsevier: Amsterdam; Boston, 2008. (e) Walter, F.; Vicens, Q.; Westhof, E. *Curr. Opin. Chem. Biol.* **1999**, *3*, 694. (f) Vicens, Q.; Westhof, E. *ChemBioChem* **2003**, *4*, 1018. (g) Willis, B.; Arya, D. P. *Adv. Carbohydr. Chem. Biochem.* **2006**, *60*, 251. (h) Lis, H.; Sharon, N. *Chem. Rev.* **1998**, *98*, 637.

[2]. Benoff, S. *Mol. Hum. Reprod*. **1997**, *3*, 599.

[3]. Holmskov, U.; Thiel, S.; Jensenius, J. C. *Annu. Rev. Immunol.* **2003**, *21*, 547.

[4]. Lasky, L. A. *Annu. Rev. Biochem.* **1995**, *64*, 113.

[5]. (a) James, T. D.; Shinkai, S., Artificial receptors as chemosensors for carbohydrates. In *Topics Current Chemistry*, Penades, S., Ed. Springer: Heidelberg, 2002; Vol. *218*, pp 159-200. (b) Striegler, S. *Curr. Org. Chem.* **2003**, *7*, 81. (c) James, T. D.; Phillips, M. D.; Shinkai, S. *Boronic acids in saccharide recognition*; RSC Publishing: Cambridge, 2006. (d) Davis, A. P.; Wareham, R. S. *Angew. Chem., Int. Ed.* **1999**, *38*, 2978. (e) Mazik, M. *Chem. Soc. Rev.* **2009**, *38*, 935. (f) Mazik, M. *RSC Adv.* **2012**, *2*, 2630. (f) Boraston, A. B.; Bolam, D. N.; Gilbert, H. J.; Davies, G. *J. Biochem. J.* **2004**, 382, 769. (g) Arnaud, J.; Audfray, A.; Imberty, A. *Chem. Soc. Rev.* **2013**, *42*, 4798.

[6]. (a) Weis, W. I.; Drickamer, K. *Annu. Rev. Biochem.* **1996**, *65*, 441. (b) Lis, H.; Sharon, N. *Chem. Rev.* **1998**, *98*, 637. (c) Davis, A. P.; Wareham, R. S. *Angew. Chem., Int. Ed.* **1999**, *38*, 2978. (d) Mazik, M. *Chem. Soc. Rev.* **2009**, *38*, 935.

[7]. (a) Nishio, M. *Phys. Chem. Chem. Phys.* **2011**, *13*, 13873. (b) Takahashi, O.; Kohno, Y.; Nishio, M. *Chem. Rev.* **2010**, *110*, 6049. (c) Zhang, Z. B.; Xia, B. Y.; Han, C. Y.; Yu, Y. H.; Huang, F. H. *Org. Lett.* **2010**, *12*, 3285. (d) Zhang, Z. B.; Luo, Y.; Chen, J. Z.; Dong, S. Y.; Yu, Y. H.; Ma, Z.; Huang, F. H. *Angew. Chem., Int. Ed.* **2011**, *50*, 1397. (e) Zhang, Z. B.; Yu, G. C.; Han, C. Y.; Liu, J. Y.; Ding, X.; Yu, Y. H.; Huang, F. H. *Org. Lett.* **2011**, *13*, 4818. (f) Xue, M.; Yang, Y.; Chi, X. D.; Zhang, Z. B.; Huang, F. H. *Acc. Chem. Res.* **2012**, *45*, 1294.

[8]. (a) Fernandez, M. D.; Canada, F. J.; Jimenez-Barbero, J.; Cuevas, G. *J. Am. Chem. Soc.* **2005**, *127*, 7379. (b) Terraneo, G.; Potenza, D.; Canales, A.; Jimenez-Barbero, J.; Baldridge, K. K.; Bernardi, A. *J. Am. Chem. Soc.* **2007**, *129*, 2890. (c) Laughrey, Z. R.; Kiehna, S. E.; Riemen, A. J.; Waters, M. L. *J. Am. Chem. Soc.* **2008**, *130*, 14625. (d) Ramirez-Gualito, K.; Alonso-Rios, R.; Quiroz-Garcia, B.; Rojas-Aguilar, A.; Diaz, D.; Jimenez-Barbero, J.; Cuevas, G. *J. Am. Chem. Soc.* **2009**, *131*, 18129. (e) Barwell, N. P.; Davis, A. P. *J. Org. Chem.* **2011**, *76*, 6548. (f) Santana, A. G.; Jimenez-Moreno, E.; Gomez, A. M.; Corzana, F.; Gonzalez, C.; Jimenez-Oses, G.; Jimenez-Barbero, J.; Asensio, J. L. *J. Am. Chem. Soc.* **2013**, *135*, 3347. (g) Chen, W. T.; Enck, S.; Price, J. L.; Powers, D. L.; Powers, E. T.; Wong, C. H.; Dyson, H. J.; Kelly, J. W. *J. Am. Chem.*

Soc. **2013**, *135*, 9877. (h) Asensio, J. L.; Arda, A.; Canada, F. J.; Jimenez-Barbero, J. *Acc. Chem. Res.* **2013**, *46*, 946. (i) Spiwok, V.; Lipovova, P.; Skalova, T.; Buchtelova, E.; Hasek, J.; Kralova, B. *Carbohydr. Res.* **2004**, *339*, 2275.

[9]. (a) Asensio, J. L.; Arda, A.; Canada, F. J.; Jimenez-Barbero, J. *Acc. Chem. Res.* **2013**, *46*, 946. (b) Nishio, M.; Umezawa, Y.; Fantini, J.; Weiss, M. S.; Chakrabarti, P. *Phys. Chem. Chem. Phys.* **2014**, *16*, 12648.

[10]. Harata, K.; Muraki, M. *J. Mol. Biol.* **2000**, *297*, 673.

[11]. (a) Paliwal, S.; Geib, S.; Wilcox, C. S. *J. Am. Chem. Soc.* **1994**, *116*, 4497. (b) Mati, I. K.; Cockroft, S. L. *Chem. Soc. Rev.* **2010**, *39*, 4195.

[12]. Carroll, W. R.; Pellechia, P.; Shimizu, K. D. *Org. Lett.* **2008**, *10*, 3547.

[13]. (a) Carroll, W. R.; Zhao, C.; Smith, M. D.; Pellechia, P. J.; Shimizu, K. D. *Org. Lett.* **2011**, *13*, 4320. (b) Zhao, C.; Li, P.; Smith, M. D.; Pellechia, P. J.; Shimizu, K. D. *Org. Lett.* **2014**, *16*, 3520.

[14]. Zhao, C.; Parrish, R. M.; Smith, M. D.; Pellechia, P. J.; Sherrill, C. D.; Shimizu, K. D. *J. Am. Chem. Soc.* **2012**, *134*, 14306.

[15]. Li, P.; Zhao, C.; Smith, M. D.; Shimizu, K. D. *J. Org. Chem.* **2013**, *78*, 5303.

[16]. Nishio, M.; Umezawa, Y.; Honda, K.; Tsuboyama, S.; Suezawa, H. *CrystEngComm* **2009**, *11*, 1757.

[16]. Nijamudheen, A.; Jose, D.; Shine, A.; Datta, A. *J. Phys. Chem. Lett.* **2012**, *3*, 1493

[17]. (a) Tsuzuki, S.; Honda, K.; Uchimaru, T.; Mikami, M.; Tanabe, K. *J. Am. Chem. Soc.* **2000**, *122*, 3746. (b) Shibasaki, K.; Fujii, A.; Mikami, N.; Tsuzuki, S. *J. Phys. Chem. A* **2006**, *110*, 4397. (c) Tsuzuki, S.; Hon-da, K.; Uchimaru, T.; Mikami, M.; Fujii, A. *J. Phys. Chem. A* **2006**, *110*, 10163. (d) Morita, S.; Fujii, A.; Mikami, N.; Tsuzuki, S. *J. Phys. Chem. A* **2006**, *110*, 10583. (e) Tsuzuki, S.; Honda, K.; Fujii, A.; Uchimaru, T.; Mikami, M. *Phys. Chem. Chem. Phys.* **2008**, *10*, 2860. (f) Tsuzuki, S.; Fujii, A. *Phys. Chem. Chem. Phys.* **2008**, *10*, 2584. (g) Fujii, A.; Hayashi, H.; Park, J. W.; Kazama, T.; Mikami, N.; Tsuzuki, S. *Phys. Chem. Chem. Phys.* **2011**, *13*, 14131. (h) Fujii, A.; Hayashi, H.; Tsuzuki, S. *Chem. Phys. Lett.* **2012**, *537*, 11.

[18]. (a) Hunter, C. A. *Angew. Chem., Int. Ed.* **2004**, *43*, 5310. (b) Sherrill, C. D. *Acc. Chem. Res.* **2013**, *46*, 1020.

[19]. (a) Ugozzoli, F.; Arduini, A.; Massera, C.; Pochini, A.; Secchi, A. *New J. Chem.* **2002**, *26*, 1718. (b) Ribas, J.; Cubero, E.; Luque, F. J.; Orozco, M. *J. Org. Chem.* **2002**, *67*, 7057. (c) Takahashi, O.; Kohno, Y.; Saito, K. *Chem. Phys. Lett.* **2003**, *378*, 509. (d) Amicangelo, J. C.; Gung, B. W.; Irwin, D. G.; Romano, N. C. *Phys. Chem. Chem. Phys.* **2008**, *10*, 2695. (e) Gung, B. W.; Emenike, B. U.; Lewis, M.; Kirschbaum, K. *Chem—Eur. J.* **2010**, *16*, 12357.

[20]. (a) Thomas, K. M.; Naduthambi, D.; Zondlo, N. J. *J. Am. Chem. Soc.* **2006**, *128*, 2216. (b) Pandey, A. K.; Naduthambi, D.; Thomas, K. M.; Zondlo, N. J. *J. Am. Chem. Soc.* **2013**, *135*, 4333. (c) Zondlo, N. J. *Acc. Chem. Res.* **2013**, *46*, 1039.

Supporting Information

1. Synthesis and characterization

1.1 Synthesis

Diones **7** and **8** were purchased from commercial suppliers. Diones **9**[i], **10**[ii] were obtained according to the literature procedures without modification. Dienes **11**[iii], **12**[iv], **13** and **14** were synthesized according to a modified two-steps procedure from diones **7**, **8**, **9** and **10**, respectively. These crude dienes **11**-**14** were obtained as a mixture of monomer and dimer forms [v] and used directly in the next step without purification. [vi] *N*-arylmaleimides **15**, **16**, and **17** were obtained according to literature procedure using maleic anhydride and a substituted aniline. [vii] The one-armed balances **1**-**6** and two-armed balances **1'**, **3'** and **6'** were synthesized following the previously reported Diels-Alder reaction between the corresponding diene and maleimide.[viii] Balances **1**-**6**, **1'**, **3'** and, **6'**

[i] Chen, Y. M.; Liu, Y. J.; Li, Q.; Wang, K. Z. *J. Inorg. Biochem.* **2009**, *103*, 1395.
[ii] Bonhote, P.; Wrighton, M. S. *Synlett* **1997**, 897.
[iii] Warrener, R. N.; Schultz, A. C.; Houghton, M. A.; Butler, D. N. *Tetrahedron* **1997**, *53*, 3991
[iv] a) Jones, D. W. *J. Chem. Soc. Perk. Trans. I* **1977**, 980; b)Fuchs, B.; Pasternak, M. *Tetrahedron* **1981**, *37*, 2501; c) Plater, M. J.; Schmidt, D. M.; Howie, R. A. *J. Chem. Res-S* **1997**, 390
[v] Fuchs, B.; Pasternak, M.; Scharf, G. *J. Chem. Soc. Chem. Comm.* **1976**, 53
[vi] The dimerized dienes can dissociate to the monor form during the thermal Dials-Alder reaction. The NMR spectra of dimerized dienes were less clear due to the [3,3] Cope rearrangement which occurs rapidly on an NMR timescale at rt in solution. (see note iii for detail explanation). The HRMS data were given for verification purpose.
[vii] Matuszak, N.; Muccioli, G. G.; Labar, G.; Lambert, D. M. *J. Med. Chem.* **2009**, *52*, 7410.
[viii] Li, P.; Zhao, C.; Smith, M. D.; Shimizu, K. D. *J. Org. Chem.* **2013**, *78*, 5303.

are newly reported compounds. Balance **2'** was obtained as previously described.[i] The synthesis of balance **2** is detailed below as an example for the modular synthetic route for assembling these balances.

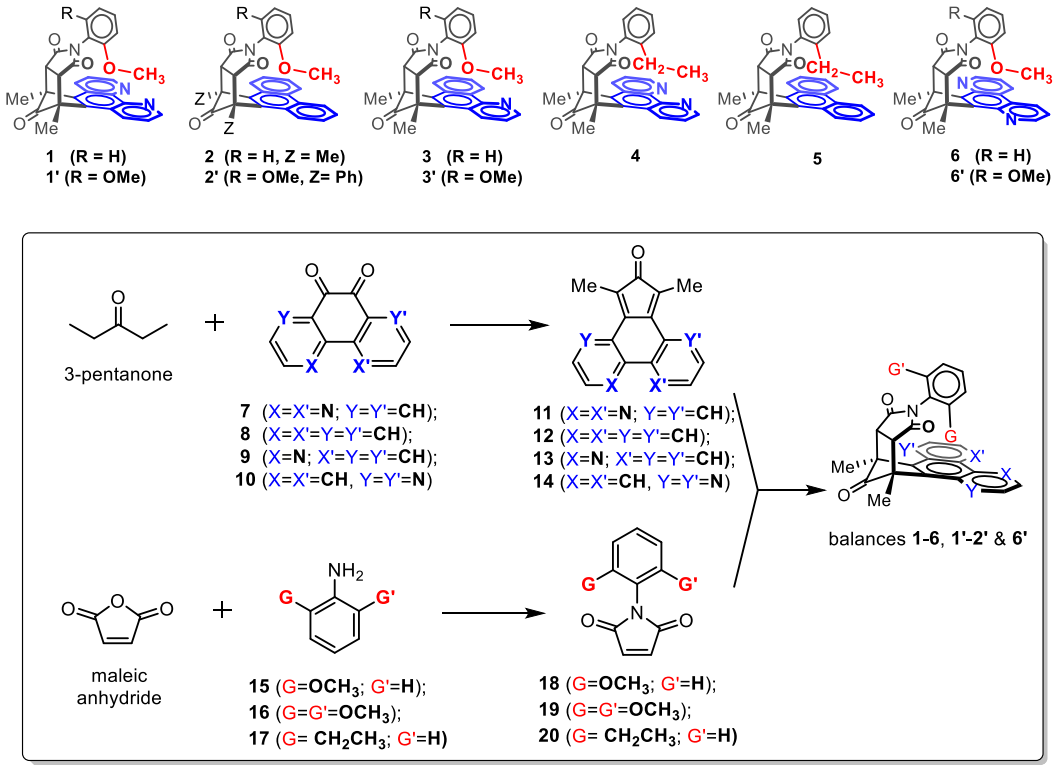

Figure 3.5 List of molecular balances **1-6** (shown in their *folded* conformers) and precursors used in this study and the general synthetic route

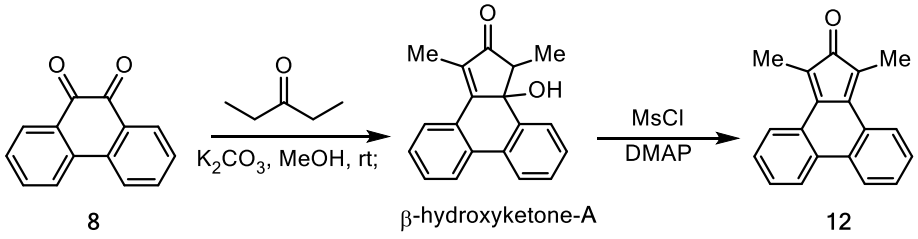

Diene 12. Potassium carbonate (1.32 g, 9.55 mmol) and pentan-3-one (0.82 g, 9.52 mmol) were suspended in dry methanol (30 mL). To the above suspension, phenanthrene-

[i] Carroll, W. R.; Zhao, C.; Smith, M. D.; Pellechia, P. J.; Shimizu, K. D. *Org. Lett.* **2011**, *13*, 4320.

9,10-dione (**8**) (1.00 g 4.81 mmol) was added portion-wise over 10 min, and the mixture was stirred at rt for 12 h. The reaction mixture was then concentrated to 5 mL under vacuum and suspended in water. The insoluble solid was collected and dried under vacuum to give the β-hydroxyketone-A as a solid (1.20 g, 90 %), which was used in the next step without further purification. ^{1}H NMR (400 MHz, $CDCl_3$) δ 8.02-7.96 (m, 1H), 7.95-7.90 (m, 1H), 7.73 (dd, *J* = 7.6 Hz, *J* = 1.3 Hz, 1H), 7.35-7.58 (m, 5H), 3.08 (q, *J* = 7.5 Hz, 1H), 2.10 (s, 3H), 1.57 (d, *J* = 7.5 Hz, 3H). ^{13}C NMR (100 MHz, $CDCl_3$): 208.7, 161.6, 139.4, 135.2, 133.4, 132.6, 131.0, 129.6, 129.4, 129.3, 128.5, 128.4, 126.5, 125.1, 124.5, 75.5, 47.9, 11.4, 9.9. HRMS (ESI) *m*/*z* calcd. for $[C_{19}H_{16}O_2]^+$ (M^+): 276.1150; found: 276.1149. β-hydroxyketone-A (1.20 g, 4.34 mmol) and 4-dimethylaminopyridine (1.50 g, 12.3 mmol) were dissolved in dry CH_2Cl_2 (40 mL) and cooled to 0 ºC. To the above solution, methanesulfonyl chloride (0.84 mL, 10.9 mmol) was added under N_2, and the solution was stirred at rt for 12 h. The reaction mixture was washed with water (3 x 50 mL) and brine (50 mL) before it was dried with $MgSO_4$, and the solvent was removed under vacuum. The solid residue was washed with cold methanol (~ 10 mL) to give diene **12** as a white solid (0.70 g, 62 %). ^{1}H NMR (400 MHz, $CDCl_3$) δ 8.50–8.22 (m, 2H), 7.84 (bs, 1H), 7.68–7.44 (m, 3H), 7.22–7.15 (m, 1H), 6.93 (bs, 1H), 1.88 (s, 3H), 1.22 (s, 3H). HRMS *m*/*z* calcd. for $[(C_{19}H_{14}O)_2]^+$ ($2M^+$): 516.2089; found: 516.2078.

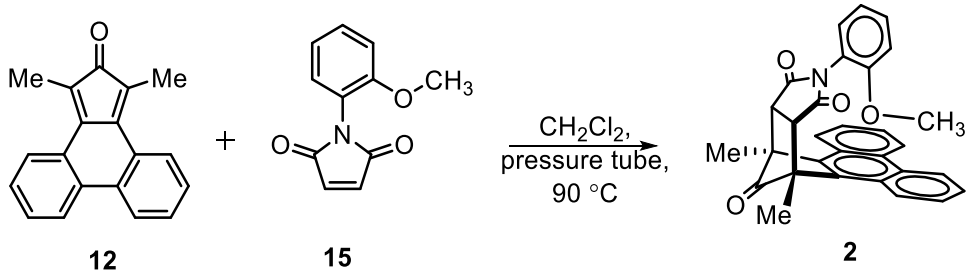

11-(2-methoxyphenyl)-9,13-dimethyl-12a,13-dihydro-9H-9,13-methanophenanthro[9,10-f]iso-indole-10,12, 14(9aH,11H)-trione. (**2**) Diene **12** (80 mg, 0.31 mmol) and *N*-(2-methoxylphenyl) maleimide (**15**) (76 mg, 0.37 mmol) were dissolved in dry CH_2Cl_2 (10 mL) and sealed in a medium pressure tube after flushing with N_2. The pressure tube was heated to 90 ºC with stirring for 24 h. After cooling, the solvent was removed under vacuum. The solid residue was washed with cold methanol (~10 mL) and then cold acetonitrile (~ 2 mL) to give **2** as an off-white solid (122 mg, 84 %). ^{1}H NMR (400 MHz, $CDCl_3$) δ 8.82-8.72 (m, 2H major, 2H minor), 8.41-8.32 (m, 2H major, 2H minor), 7.74-7.55 (m, 4H major, 4H minor), 7.10 (ddd, *J* = 8.4 Hz, *J* = 7.6 Hz, *J* = 1.7 Hz, 1H minor), 7.03 (ddd, *J* = 8.4 Hz, *J* = 7.6 Hz, *J* = 1.7 Hz, 1H major), 6.84 (dd, *J* = 7.8 Hz, *J* = 1.7 Hz, 1H minor), 6.81–6.76 (m, 1H minor), 6.71 (dd, *J* = 8.4 Hz, *J* = 1.2 Hz, 1H major), 6.43 (dd, *J* = 8.4 Hz, *J* = 1.2 Hz, 1 minor), 6.29 (ddd, *J* = 7.8 Hz, *J* = 7.6 Hz, *J* = 1.2 Hz, 1H major), 4.59 (dd, *J* = 7.8 Hz, *J* = 1.7 Hz, 1H major), 3.64 (s, 3H major), 3.55 (s, 2H major), 3.54 (s, 2H minor), 2.33 (s, 6H major), 2.29 (s, 6H minor), 2.15 (s, 1H minor). ^{13}C NMR (100 MHz, $CDCl_3$) δ 201.3, 173.9, 154.3, 133.4, 133.3, 131.1, 130.8, 130.6, 130.5, 128.6, 127.8, 127.5, 127.4, 127.3, 127.2, 126.9, 125.6, 125.3, 123.4, 123.2, 120.6, 120.2, 119.7, 111.9, 111.7, 55.7, 55.2, 55.1, 53.9, 48.2, 48.0, 15.0, 14.9. HRMS (ESI) *m/z* calcd. for $[C_{30}H_{23}NO_4]^+$ (M^+): 461.1627; found: 461.1630.

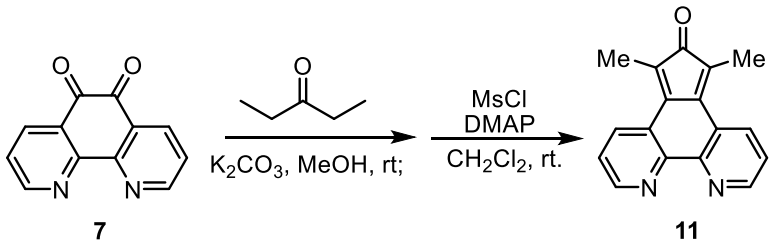

Diene 11 was synthesized using the same procedure described for diene **12** using 1,10-phenanthroline-5,6-dione (**7**) (1.00 g 4.76 mmol) and pentan-3-one (0.82 g, 9.52 mmol). Diene **11** was obtained as an off-white solid (0.75 g, 61 % for the two steps). The ^{1}H-NMR spectrum was compared with literature.[i] HRMS (ESI) *m/z* calcd. for $[C_{17}H_{12}N_2O]^+$ (M^+): 260.0950; found: 260.0959

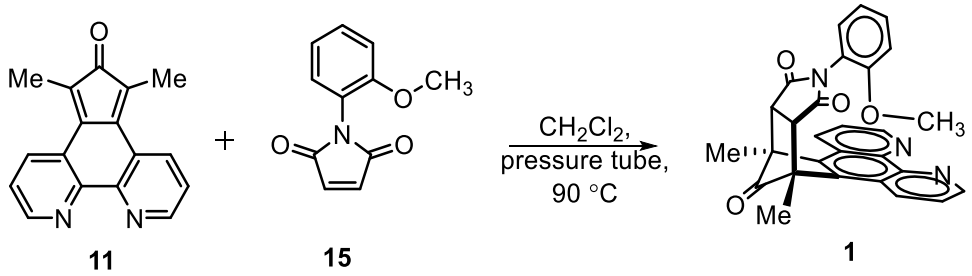

11-(2-methoxyphenyl)-9,13-dimethyl-12a,13-dihydro-9H-9,13-methanoiso-indolo[5,6-f][1,10] phenanthroline-10,12,14(9aH,11H)-trione. (**1**) Diene **11** (80 mg, 0.31 mmol) and *N*-(2-methoxylphenyl) maleimide (**15**) (76 mg, 0.37 mmol) were reacted using the same procedure as described for balance **2**. Balance **1** was obtained as a white solid (109 mg, 76%). ^{1}H NMR (400 MHz, $CDCl_3$) δ 9.24 (dd, *J* = 4.8 Hz, *J* = 1.5 Hz, 2H major, 2H minor), 8.73 (dd, *J* = 8.5 Hz, *J* = 1.5 Hz, 2H major, 2H minor), 7.68 (dd, *J* = 8.5 Hz, *J* = 4.3 Hz, 2H major, 2H minor), 7.15-7.09 (m, 1H minor), 7.06 (ddd, *J* = 8.3 Hz, *J* = 7.6 Hz, *J* = 1.7 Hz, 1H major), 6.81-6.79 (m, 2H minor), 6.74 (dd, *J* = 8.4 Hz, *J* = 1.0 Hz, 1H major), 6.45 (dd, *J* = 8.4 Hz, *J* = 1.0 Hz, 1H minor), 6.33 (ddd, *J* = 7.7 Hz, *J* = 7.6 Hz, *J*

[i] Warrener, R. N.; Schultz, A. C.; Houghton, M. A.; Butler, D. N. *Tetrahedron* **1997**, *53*, 3991

= 1.0 Hz, 1H major), 4.64 (dd, *J* = 7.8 Hz, *J* = 1.7 Hz, 1H major), 3.65 (s, 3H major), 3.61 (s, 2H major), 3.58 (s, 2H minor), 2.33 (s, 6H major), 2.31 (s, 6H minor), 2.24 (s, 3H minor). ^{13}C NMR (100 MHz, $CDCl_3$) δ 200.2, 199.1, 173.7, 154.4, 154.0, 150.8, 150.3, 146.1, 133.6, 133.5, 132.8, 132.7, 131.0, 130.8, 128.6, 127.5, 125.1, 124.7, 123.6, 123.4, 121.0, 120.5, 119.3, 119.1, 112.1, 111.8, 77.5, 55.7, 55.5, 55.4, 54.4, 47.8, 47.7, 29.9, 14.5, 14.3. HRMS (ESI) *m/z* calcd. for $[C_{28}H_{21}N_3O_4]^+$ (M^+): 463.1532, found; 463.1521.

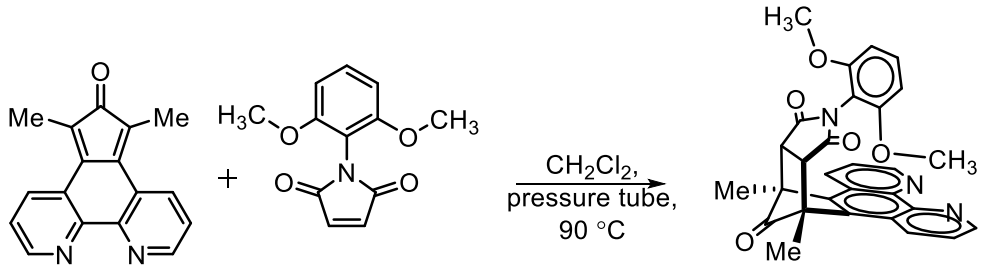

11-(2,6-dimethoxyphenyl)-9,13-dimethyl-12a,13-dihydro-9H-9,13-methanoiso-indolo[5,6-f] [1,10]phenanthroline-10,12,14(9aH,11H)-trione. (**1'**) Diene **11** (80 mg, 0.31 mmol) and *N*-(2,2'-dimethoxylphenyl) maleimide (**16**) (108 mg, 0.46 mmol) were reacted using the same procedure as described for balance **2**. Balance **1'** was obtained as a white solid (130 mg, 85%). ^{1}H NMR (400 MHz, $CDCl_3$) δ 9.23 (dd, *J* = 4.3 Hz, *J* = 1.2 Hz, 2H), 8.73 (dd, *J* = 8.4 Hz, *J* = 1.2 Hz, 2H), 7.67 (dd, *J* = 8.4 Hz, *J* = 4.3 Hz, 2H), 7.05 (t, *J* = 8.5 Hz, 1H), 6.38 (dd, *J* = 8.5 Hz, *J* = 1.0 Hz, 1H), 6.06 (dd, *J* = 8.5 Hz, *J* = 1.0 Hz, 1H), 3.67 (s, 3H), 3.61 (s, 2H), 2.31 (s, 6H), 2.27 (s, 3H). ^{13}C NMR (100 MHz, $CDCl_3$) δ 199.4, 173.5, 155.7, 155.1, 149.9, 133.9, 133.5, 131.0, 125.3, 123.7, 107.8, 104.3, 103.7, 56.1, 55.4, 54.8, 47.7, 14.4. HRMS (ESI) *m/z* calcd. for $[C_{29}H_{23}N_3O_5]^+$ (M^+): 493.1638 found: 493.1635.

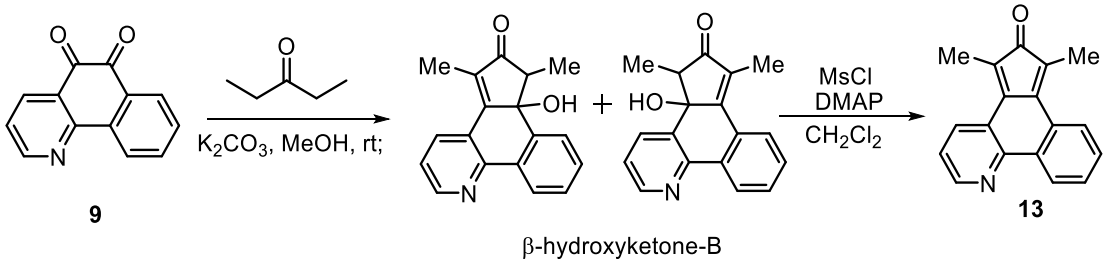

Diene 13. Potassium carbonate (1.32 g, 9.55 mmol) and pentan-3-one (0.82 g, 9.52 mmol) were suspended in dry methanol (30 mL). To the above suspension, benzo[*h*]quinoline-5,6-dione (**9**)[xi] (1.00 g 4.78 mmol) was added in portion-wise over 10 min, and the mixture was stirred at rt for 12 h. The solvent was then removed under vacuum. The residue was washed with water and dried under vacuum to give the β-hydroxyketone-B (two constitutional isomers with a ratio of ~1:2.3) as a greyish white solid (1.05 g, 79 %). ^{1}H NMR (400 MHz, $CDCl_3$) δ 8.65 (dd, *J* = 4.8 Hz, *J* = 1.7 Hz, 1H major), 8.63 (dd, *J* = 4.8 Hz, *J* = 1.7 Hz, 1H major), 8.57-8.54 (m, 1H minor), 8.49-8.43 (m, 1H major), 8.01 (dd, *J* = 7.8 Hz, *J* = 1.7 Hz, 1H major), 7.80 (dd, *J* = 7.8 Hz, *J* = 1.7 Hz, 1H minor), 7.75-7.71 (m, 1H minor), 7.62-7.41 (m, 3H major and 2H minor), 7.32 (dd, *J* = 7.8 Hz, *J* = 4.8 Hz, 1H major), 7.27 (dd, *J* = 7.8 Hz, *J* = 4.8 Hz, 1H minor), 3.10 (q, *J* = 7.4 Hz, 1H major), 3.04 (q, *J* = 7.4 Hz, 1H minor), 2.11 (s, 3H minor), 2.09 (s, 3H major), 1.60 (d, *J* = 7.4 Hz, 3H major), 1.57 (d, *J* = 7.4 Hz, 3H minor). ^{13}C NMR (100 MHz, $CDCl_3$) δ 208.3, 208.1, 160.3, 159.6, 151.0, 150.8, 150.4, 150.0, 140.4, 136.9, 136.2, 135.8, 134.9, 134.1, 133.7, 132.7, 131.2, 130.9, 130.0, 129.7, 129.4, 128.9, 126.9, 126.3, 125.8, 124.3, 123.6, 122.9, 75.7, 75.2, 48.07, 47.9, 11.4, 11.3, 10.0, 9.7. HRMS (ESI) *m/z* calcd. for $[C_{18}H_{15}NO_2]^+$ (M^+): 277.1103; found: 277.1100. The β-hydroxyketone-B (1.05 g, 3.79 mmol) and 4-dimethylaminopyridine (1.50 g, 12.3 mmol) was dissolved in dry CH_2Cl_2 (40 mL) and cooled to at 0 ºC. To the above solution, methanesulfonyl chloride (0.84 mL, 10.9 mmol) was added under nitrogen and kept stirring at rt for 12 h. The reaction mixture was

then washed with water (3 x 50 mL) and brine (50 mL) before it was dried with $MgSO_4$, and the solvent was removed under vacuum. The solid residue was washed with cold methanol to give diene **13** as a white solid (0.75 g, 76 %). ^{1}H-NMR (400 MHz, $CDCl_3$) δ 9.25-8.72 (m, 2H), 8.26-6.78 (m, 5H), 2.03-1.73 (m, 3H), 1.25-1.14 (m, 3H). HRMS (ESI) *m/z* calcd. for $[C_{18}H_{13}NO]^+$ (M^+): 259.0997; found: 259.1004.

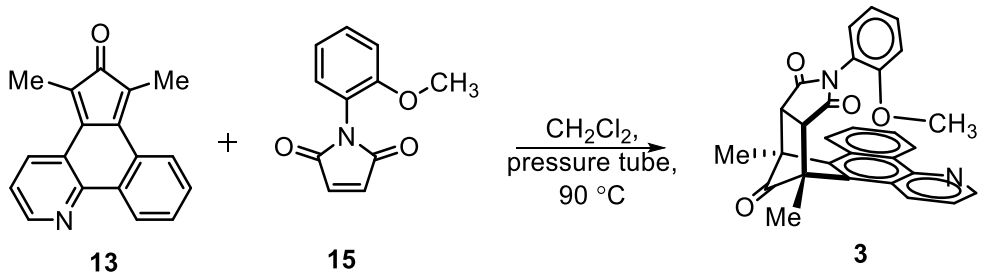

11-(2-methoxyphenyl)-9,13-dimethyl-12a,13-dihydro-9H-9,13-methanobenzo-[h]isoindolo[5,6-f]quinoline-10,12,14(9aH,11H)-trione. (**3**) Diene **13** (80 mg, 0.31 mmol) and *N*-(2-methoxylphenyl) maleimide (**15**) (76 mg, 0.37 mmol) were reacted using the same procedure as described for balance **2**. Balance **3** was obtained as a beige-white solid (97 mg, 68 %). ^{1}H NMR (400 MHz, CD_2Cl_2) δ 9.50-9.43 (m, 1H major, 1H minor), 8.99 (td, *J* = 4.5 Hz, *J* = 1.7 Hz, 1H major), 8.98 (dd, *J* = 4.5 Hz, *J* = 1.7 Hz, 1H minor), 8.65 (dd, *J* = 8.4 Hz, *J* = 1.7 Hz, 1H major), 8.64 (dd, *J* = 8.4 Hz, *J* = 1.7 Hz, 1H minor), 8.40-8.33 (m, 1H major, 1H minor), 7.81-7.70 (m, 2H major, 2H minor), 7.56 (dd, *J* = 8.4 Hz, *J* = 4.3 Hz, 1H minor), 7.55 (dd, *J* = 8.4 Hz, *J* = 4.3 Hz, 1H major), 7.18-7.04 (m, 1H major, 1H minor), 6.86-6.73 (m, 1H major, 2H minor), 6.47 (d, *J* = 8.2 Hz, 1H minor), 6.31 (td, *J* = 7.8 Hz, *J* = 1.2 Hz, 1H major), 4.51 (dd, *J* = 7.8 Hz, *J* = 1.6 Hz, 1H major), 3.64 (s, 3H major), 3.58 (s, 2H major, 2H minor), 2.32 (s, 3H major), 2.30 (s, 3H, minor), 2.28 (s, 3H major), 2.26 (s, 3H minor), 2.19 (s, 3H minor). ^{13}C NMR (100 MHz, $CDCl_3$) δ 200.8, 199.4, 174.1, 173.9, 173.7, 173.6, 154.7, 154.5, 154.3, 154.2, 149.3, 148.8, 146.9,

146.5, 140.1, 134.4, 134.2, 132.7, 132.5, 132.5, 132.4, 132.3, 132.1, 130.8, 130.6, 129.5, 129.2, 129.1, 128.9, 128.6, 127.7, 127.6, 127.3, 125.7, 125.6, 124.7, 124.5, 122.6, 122.3, 122.1, 120.8, 120.3, 119.6, 119.5, 112.0, 111.8, 55.7, 55.5, 55.4, 55.3, 55.1, 48.1, 48.0, 47.9, 47.8, 14.8, 14.6, 14.5. HRMS (ESI) *m/z* calcd. for $[C_{29}H_{22}N_2O_4]^+$ (M^+): 462.1580; found: 462.1575.

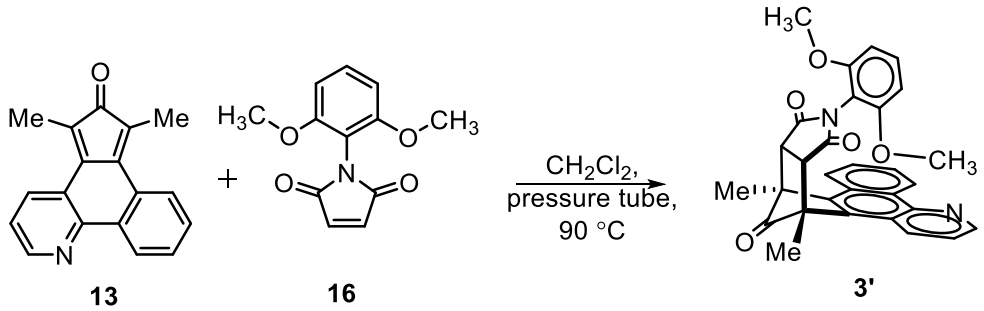

11-(2,6-dimethoxyphenyl)-9,13-dimethyl-12a,13-dihydro-9H-9,13-methano-benzo[h]isoindolo [5,6-f]quinolone-10,12,14(9aH,11H)-trione. (**3'**) Diene **13** (80 mg, 0.31 mmol) and *N*-(2,2'-dimethoxylphenyl) maleimide (**16**) (108 mg, 0.46 mmol) were reacted using the same procedure as described for balance **2**. Balance **3'** was obtained as a white crystalline solid (110 mg, 72 %). ^{1}H NMR (400 MHz, CD_2Cl_2) δ 9.48-9.43 (m, 1H), 8.98 (dd, *J* = 4.3 Hz, *J* = 1.7 Hz, 1H), 8.64 (dd, *J* = 8.4 Hz, *J* = 1.7 Hz, 1H), 8.40 – 8.33 (m, 1H), 7.77 – 7.71 (m, 2H), 7.56 (dd, *J* = 8.4 Hz, *J* = 4.3 Hz, 1H), 7.08 (t, *J* = 8.5 Hz, 1H), 6.42 (dd, *J* = 8.5 Hz, *J* = 1.0 Hz, 1H), 6.08 (dd, *J* = 8.5 Hz, *J* = 1.0 Hz, 1H), 3.67 (s, 3H), 3.59 (s, 2H), 2.29 (s, 3H), 2.25 (s, 3H), 2.20 (s, 3H). ^{13}C NMR (100 MHz, CD_2Cl_2) δ 200.1, 174.3, 174.0, 156.3, 155.8, 149.2, 147.2, 134.9, 133.1, 133.0, 132.9, 131.0, 130.0, 129.0, 127.6, 125.9, 125.1, 123.1, 122.4, 104.4, 104.1, 56.5, 55.7, 55.5, 48.5, 48.4, 15.90, 14.7. HRMS (ESI) *m/z* calcd. for $[C_{30}H_{24}N_2O_5]^+$ (M^+): 492.1685; found: 492.1680.

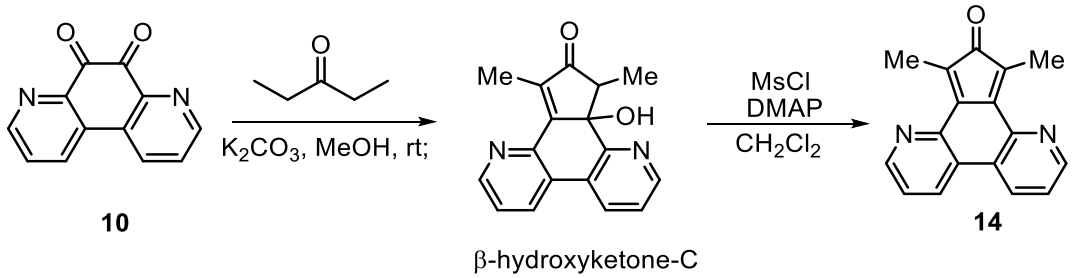

Diene 14. Potassium carbonate (1.32 g, 9.55 mmol) and pentan-3-one (0.82 g, 9.52 mmol) were suspended in dry methanol (30 mL). To the above suspension, 4,7-phenanthroline-5,6-dione (**10**)[xii] (1.00 g, 4.76 mmol) was added in portion-wise over 10 min, and the mixture was stirred at rt for 12 h. The solvent was then removed under vacuum. The residue was washed with water and dried under vacuum to give the β-hydroxyketone-C as an off-white solid (0.93 g, 70 %). ^{1}H NMR (400 MHz, DMSO-d_6) δ 8.75 (dd, J = 4.7 Hz, J = 1.6 Hz, 1H), 8.61-8.56 (m, 2H), 8.48 (dd, J = 8.2 Hz, J = 1.6 Hz, 1H), 7.58 (dd, J = 8.2 Hz, J = 4.7 Hz, 1H), 7.51 (dd, J = 8.2 Hz, J = 4.7 Hz, 1H), 3.17 (t, J = 7.4 Hz, 1H), 2.15 (s, 3H), 1.40 (d, J = 7.3 Hz, 3H). ^{13}C NMR (100 MHz, DMSO-d_6) δ 209.2, 158.8, 157.2, 149.6, 149.1, 148.1, 137.9, 132.8, 132.0, 128.3, 125.9, 124.7, 124.0, 76.5, 47.0, 10.7, 9.6. HRMS (ESI) *m/z* calcd. for $[C_{17}H_{14}N_2O_2]^+$ (M^+): 278.1055; found: 278.1053. The β-hydroxyketone-C (0.93 g, 3.34 mmol) and 4-dimethylaminopyridine (1.50 g, 12.3 mmol) was dissolved in dry CH_2Cl_2 (40 mL) and cooled to at 0 ºC. To the above solution, methanesulfonyl chloride (0.84 mL, 10.9 mmol) was added under nitrogen and kept stirring at rt for 12 h. The reaction mixture was then washed with water (3 x 50 mL) and brine (50 mL) before it was dried with $MgSO_4$, and the solvent was removed under vacuum. The solid residue was washed with cold methanol to give diene **14** as a white solid (0.60 g, 69 %) ^{1}H NMR (400 MHz, $CDCl_3$) δ 8.90 (bs, 1H), 8.50 (m, 3H), 7.53-

7.38 (m, 2H), 2.00 (bs, 3H), 1.37-1.23 (s, 3H). HRMS (ESI) *m/z* calcd. for $[C_{17}H_{12}N_2O]^+$ (M^+): 260.0950; found: 260.0948.

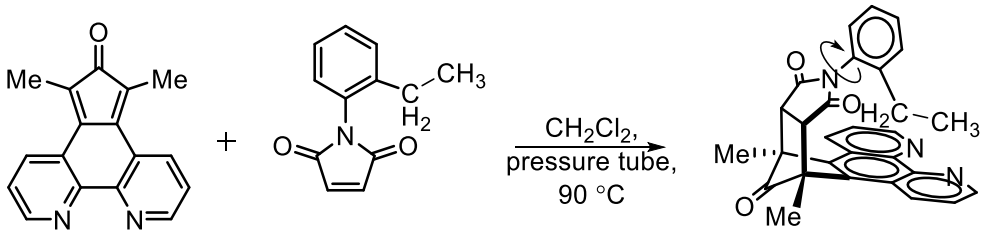

11 **17** **4**

11-(2-ethylphenyl)-9,13-dimethyl-12a,13-dihydro-9H-9,13-methanoisoindolo [5,6-f][1,10]phen-anthroline-10,12,14(9aH,11H)-trione. (**4**) Diene **11** (80 mg, 0.31 mmol) and *N*-(2-ethylphenyl) maleimide (**17**) (92 mg, 0.46 mmol) were reacted using the same procedure as described for balance **2**. Balance **4** was obtained as a white solid (124 mg, 87 %). ^{1}H NMR (400 MHz, CD_2Cl_2) δ 9.20-9.12 (m, 2H major, 2H minor), 8.76-8.65 (m, 2H major, 2H minor), 7.73-7.58 (m, 2H major, 2H minor), 7.23-7.03 (m, 2H major, 2H minor), 6.91-6.74 (m, 2H major), 6.54 (td, *J* = 7.6 Hz, *J* = 1.6 Hz, 1H minor), 4.25 (dd, *J* = 7.9 Hz, *J* = 1.2 Hz, 1H minor), 3.66 (s, 2H major), 3.65 (s, 2H minor), 2.32 (s, 6H minor), 2.30 (s, 6H major), 2.22 (q, *J* = 7.6 Hz, 2H minor), 0.99 (t, *J* = 7.6 Hz, 3H minor), 0.05 (q, *J* = 7.6 Hz, 2H major), -0.21 (t, *J* = 7.6 Hz, 3H major). ^{13}C NMR (100 MHz, CD_2Cl_2) δ 200.4, 199.3, 174.8, 174.7, 151.1, 150.9, 147.3, 146.8, 141.8, 141.6, 134.3, 133.9, 132.9, 130.6, 130.2, 130.1, 130.0, 129.5, 128.8, 128.1, 127.2, 127.1, 126.9, 125.3, 125.1, 123.7, 123.7, 55.9, 55.8, 48.5, 48.1, 24.4, 22.1, 14.7, 14.5, 12.7. HRMS (ESI) *m/z* calcd. for $[C_{29}H_{23}N_3O_3]^+$ (M^+): 461.1739; found: 461.1736.

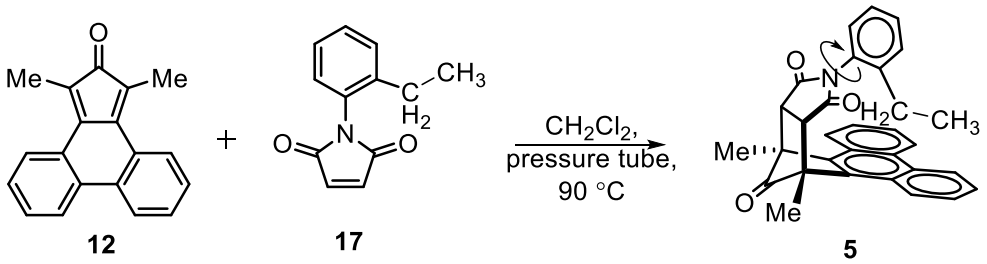

11-(2-ethylphenyl)-9,13-dimethyl-12a,13-dihydro-9H-9,13-methanophenanthro-[9,10-f]isoindole-10,12,14(9aH,11H)-trione. (**5**) Diene **12** (80 mg, 0.31 mmol) and *N*-(2-ethylphenyl) maleimide (**17**) (92 mg, 0.46 mmol) were reacted using the same procedure as described for balance **2**. Balance **5** was obtained as a white solid (104 mg, 73%). ^{1}H NMR (400 MHz, CD_2Cl_2) δ 8.90-8.73 (m, 2H major, 2H minor), 8.46-8.31 (m, 2H major, 2H minor), 7.76-7.60 (m, 4H major, 4H minor), 7.20-7.07 (m, 2H major, 1H minor), 7.03 (td, *J* = 7.5 Hz, *J* = 1.2 Hz, 1H minor), 6.90-6.74 (m, 2H major), 6.47 (ddd, *J* = 7.8 Hz, *J* = 7.4 Hz, *J* = 1.6 Hz, 1H minor), 4.25 (dd, *J* = 7.8 Hz, *J* = 1.2 Hz, 1H minor), 3.61 (s, 2H major), 3.59 (s, 2H minor), 2.32 (s, 6H minor), 2.29 (s, 6H major), 2.23 (q, *J* = 7.6 Hz, 2H minor), 0.99 (t, *J* = 7.5 Hz, 3H minor), 0.20-0.04 (m, 2H major), -0.16 (t, *J* = 7.5 Hz, 3H major). ^{13}C NMR (100 MHz, CD_2Cl_2) δ 201.4, 200.1, 175.0, 174.9, 142.0, 141.8, 134.1, 133.8, 131.6, 131.2, 130.9, 130.0, 129.8, 129.3, 128.6, 128.3, 128.2, 128.1, 128.0, 127.9, 127.8, 127.7, 127.2, 126.9, 126.8, 125.7, 124.0, 55.6, 55.5, 48.9, 48.4, 24.4, 21.9, 15.2, 15.1, 14.5, 12.5. HRMS (ESI) *m/z* calcd. for $[C_{31}H_{25}NO_3]^+$ (M^+): 459.1834; found: 459.1837.

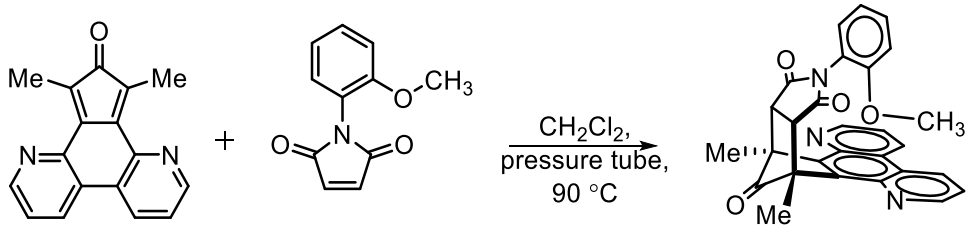

14 **15** **6**

11-(2-methoxyphenyl)-9,13-dimethyl-12a,13-dihydro-9H-9,13-methanoisoindolo-[5,6-f][4,7]phe-nanthroline-10,12,14(9aH,11H)-trione. (**6**) Diene **14** (80 mg, 0.31 mmol) and *N*-(2-methoxylphenyl) maleimide (**15**) (76 mg, 0.37 mmol) were reacted using the same procedure as described for balance **2**. Balance **6** was obtained as a white solid (100 mg, 69 %) ^{1}H NMR (400 MHz, CD_2Cl_2) δ 9.05 (dd, *J* = 4.3 Hz, *J* = 1.7 Hz, 2H minor), 9.03 (dd, *J* = 4.3 Hz, *J* = 1.7 Hz, 2H major), 8.99 (dd, *J* = 8.6 Hz, *J* = 1.7 Hz, 2H major), 8.97 (dd, *J* = 8.6 Hz, *J* = 1.7 Hz, 2H minor), 7.64 (dd, *J* = 8.5 Hz, *J* = 4.3 Hz, 2H major), 7.64 (dd, *J* = 8.5 Hz, *J* = 4.3 Hz, 2H minor), 7.14 (ddd, *J* = 8.4 Hz, *J* = 7.0 Hz, *J* = 2.2 Hz, 1H minor), 7.09 (ddd, *J* = 8.4 Hz, *J* = 7.6 Hz, *J* = 1.7 Hz, 1H major), 6.88-6.80 (m, 2H minor), 6.78 (dd, *J* = 8.4 Hz, *J* = 1.2 Hz, 1H major), 6.50 (dd, *J* = 8.4 Hz, *J* = 1.1 Hz, 1H minor), 6.35 (td, *J* = 7.7 Hz, *J* = 1.2 Hz, 1H major), 4.57 (dd, *J* = 7.7 Hz, *J* = 1.7 Hz, 1H major), 3.64 (s, 3H major), 3.58 (s, 2H minor), 3.58 (s, 2H major), 2.39 (s, 6H major), 2.37 (s, 6H minor), 2.33 (s, 3H minor). ^{13}C NMR (100 MHz, CD_2Cl_2) δ 203.0, 201.5, 173.6, 173.6, 155.0, 154.9, 151,0 150.7, 144.9, 144.5, 138.6, 138.4, 131.3, 131.2, 130.9, 130.8, 129.1, 128.0, 125.8, 125.4, 122.5, 122.3, 120.8, 120.7, 120.7, 120.6, 112.5, 112.5, 56.5, 56.5, 56.2, 55.0, 49.0, 48.8, 30.3, 14.6, 14.3. HRMS (ESI) *m/z* calcd. for $[C_{28}H_{21}N_3O_4]^+$ (M^+): 463.1532; found: 463.1531.

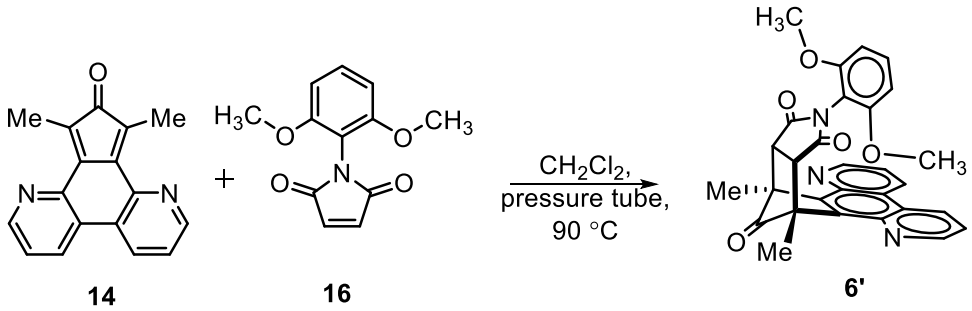

11-(2,6-dimethoxyphenyl)-9,13-dimethyl-12a,13-dihydro-9H-9,13-methanoiso-indolo[5,6-f][4,7] phenanthroline-10,12,14(9aH,11H)-trione. (**6'**) Diene **14** (80 mg, 0.31 mmol) and *N*-(2,2'-dimethoxylphenyl) maleimide (**16**) (108 mg, 0.46 mmol) were reacted using the same procedure as described for balance **2**. Balance **6'** was obtained as a white solid (120 mg, 78 %) ^{1}H NMR (400 MHz, CD_2Cl_2) δ 9.05 (dd, *J* = 4.3 Hz, *J* = 1.7 Hz, 1H), 8.98 (dd, *J* = 8.5 Hz, *J* = 1.7 Hz, 1H), 7.63 (dd, *J* = 8.5 Hz, *J* = 4.3 Hz, 1H), 7.09 (t, *J* = 8.5 Hz, 1H), 6.44 (dd, *J* = 8.5 Hz, *J* = 1.0 Hz, 1H), 6.11 (dd, *J* = 8.6 Hz, *J* = 1.0 Hz, 1H), 3.67 (s, 3H), 3.59 (s, 2H), 2.36 (s, 6H), 2.34 (s, 3H). ^{13}C NMR (100 MHz, CD_2Cl_2**)** δ 201.9, 173.5, 156.3, 155.9, 150.6, 144.9, 138.6, 131.1, 130.9, 125.7, 122.2, 104.5, 104.3, 56.5, 56.4, 55.2, 49.0, 14.6. HRMS (ESI) *m/z* calcd. for $[C_{29}H_{23}N_3O_5]^+$ (M^+): 493.1638; found: 493.1641.

1.2 Characterization

^{1}H and ^{13}C NMR spectra for all newly reported compounds and crystal data (cif) of **1'**, **2'** and **6'** are available free of charge via Internet at http://pubs.acs.org/doi/abs/10.1021/ol502418k

2. Characterization of the CH-π interactions in crystal structures 1'-3'and 6'

Formation of the intramolecular CH-π interactions was confirmed in the X-ray crystal structures of two-armed balances **1'-3'** and **6'**. It was found in all *four* crystal structures that the arm (O)CH_3 in the *folded* conformation stayed close above the one outer six-membered ring on the shelf (Figure 3.6a). Characterization of the CH-π interactions between the arm (O)CH_3 and opposing six-membered ring was carried out using a set of parameters as demonstrated in Figure 3.6b. The interacting CH proton was found to point toward the opposing six-membered ring with an atom-to-plane distance (***H***) of 2.56 to 2.61 Å, and a C-H-plane accessing angle (***α***) of 147˚ to 154 (Table 3.2). The projection of CH proton on the ring reside plane was found to be off the ring centroid by a displacement (d_1) of 0.25 to 1.30 Å, These observations are in well agreement with the reported geometry for aliphatic CH-π interactions (***H*** = ~2.75 Å, $d_1 \leq 1.47$ Å, and ***α*** = ~157˚).[i]

[i] Nishio, M.; Umezawa, Y.; Honda, K.; Tsuboyama, S.; Suezawa, H. *CrystEngComm* **2009**, *11*, 1757

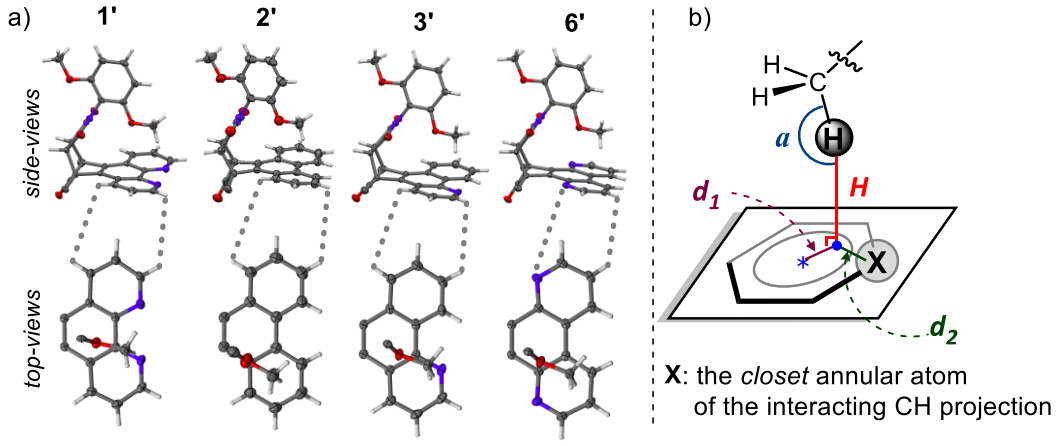

Figure 3.6 (a) Side views (top row) and truncated top views (bottom row) of the X-ray crystal structures **1'-3'** and **6'** highlighting the relative position between the interacting arm OCH_3 and shelf arene. The bridgehead functional groups are omitted for viewing clarity. The major structure observed in **3'** is shown here. (b) Definition of the geometric parameters for characterizing the intramolecular CH-π interactions in these crystal structures: the hydrogen-to-plane distance (***H***); the C-H-plane accessing angle (***α***); the hydrogen projection-to-centroid displacement (***d₁***), the closet annular sp^2 atom of the interacting CH projection (**X**), the hydrogen projection-to-X displacement (***d₂***).

Table 3.2 Measured geometric parameters for characterizing CH-π interactions in crystal structures **1'-3'** and **6'**: the atom-to-plane distance (***D***), CH-to-plane accessing angle (**α**) and the hydrogen projection-to-centroid displacement (***d₁***), the closest annular sp^2 atom (***X***), and the hydrogen projection-to-X displacement (***d₂***).

Balance.	D [Å]	α	d_1[Å]	d_2[Å]	X
1'	2.61	154.02°	1.30	0.47	N
2'	2.57	154.56°	0.25	1.20	C
3'	2.57	148.21°	0.85	0.56	C/N[a]
6'	2.56	147.32°	0.47	0.96	C

[a]Two different but highly superimposable structures were observed for **3'**. X atom was nitrogen in the major structure (62%) and carbon in the minor structure (38%)

The above crystal structures of two-armed balances were considered to adequately reproduce the geometry of the intramolecular CH-π interactions occurred to the one-armed balances **1**-**3** and **6**. Crystal packing and other intermolecular interactions were found to impact little these crystal structures. This is supported by the similarity between the

calculated optimal geometry for the *folded* conformers and the *folded* part of these crystal structures. The *folded* conformers of balances **1**-**3** and **6** were optimized at the DFT-M06/6-31G** level of theory[i] using Spartan 10 (Figure 3.7). The methoxyl arms in these optimized conformations adopted similar positions as compared with the *folded* arms in the two-armed crystal structures.

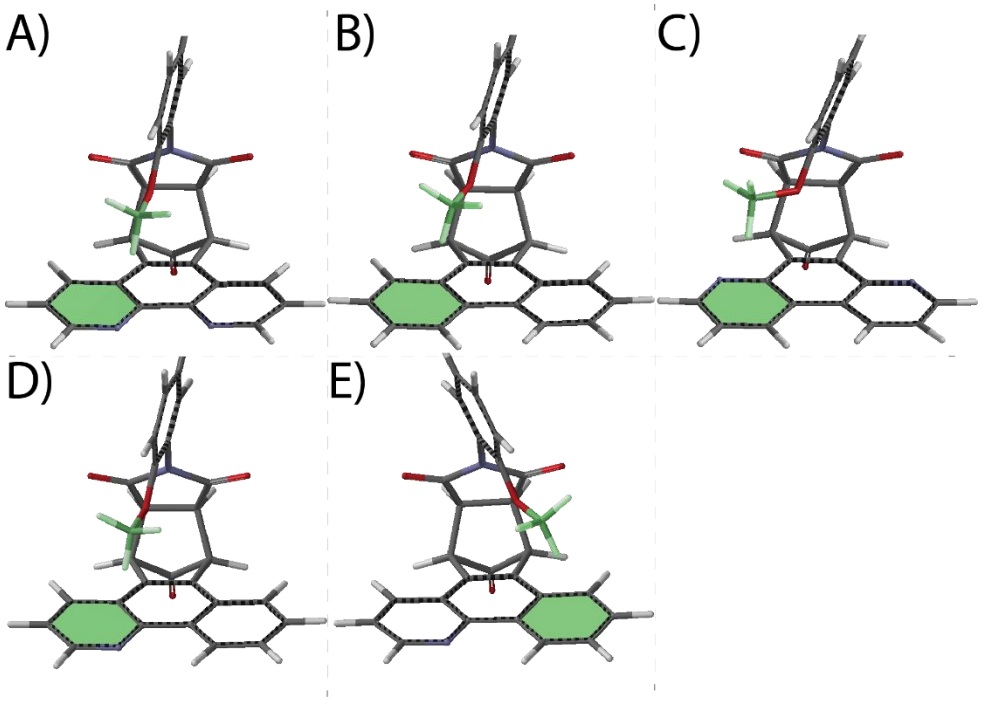

Figure 3.7 Front views of the optimized geometry (DFT-M06/6-31G**, *in vacuum*) for the *folded* balances **1** (**A**), **2** (**B**), **3** (**D** and **E**) and **6** (**C**). To lower the computational cost, the bridgehead groups were eliminated. The interacting methyl groups and six-membered aromatic units are highlighted in green.

3. In-Solution Conformational Analysis for Balances 1-6.

A series of 2D NMR spectroscopic analyses were carried out to study the geometry of the intramolecular CH-π interactions in balances **1-6** in solution. ^{1}H-NMR spectral assignment for balances **1-6** , **1'**, **3'** and **6'** (Figure 3.8 to 3.16) were done with aid from

[i] Nijamudheen, A.; Jose, D.; Shine, A.; Datta, A. *J. Phys. Chem. Lett.* **2012**, *3*, 1493.

^{1}H-^{13}C HSQC and ^{1}H-^{1}H COSY experiments. Next, ^{1}H-^{1}H NOESY experiments were carried out to probe the spatial relationship between the arm (O)CH_3 and shelf arene in balances **1-3**, **6**, **1'-3'**, and **6'** in solution (Figure 3.17 to 3.23).

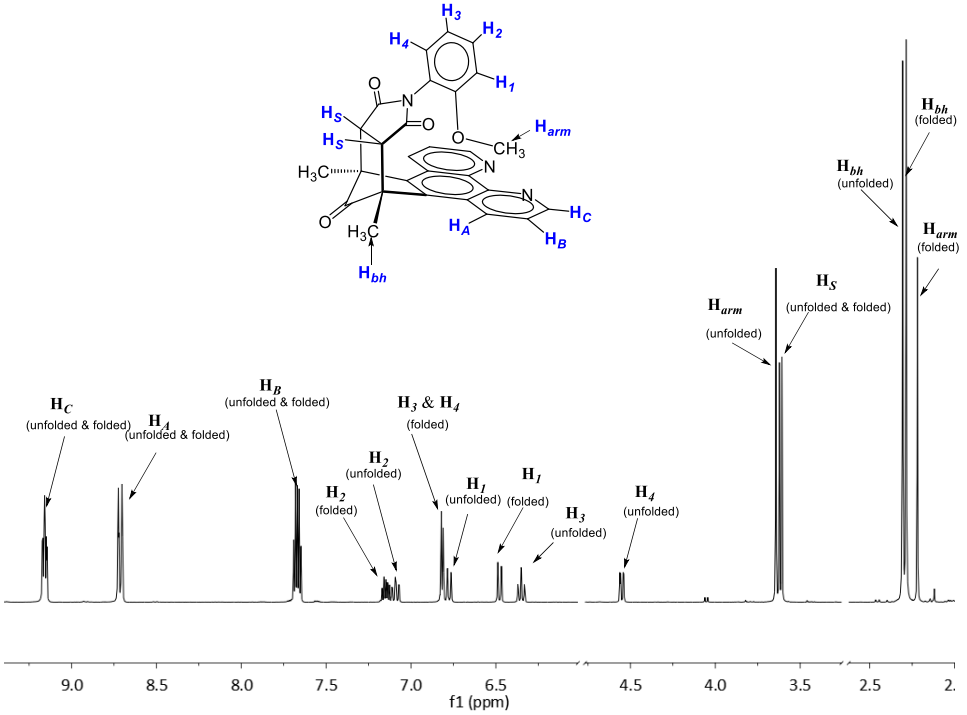

Figure 3.8 Assignment of the ^{1}H NMR spectrum for balance **1** in CD_2Cl_2. The indexing of protons in balances is provided. The *unfolded* and *folded* conformers are indicated in parenthesis.

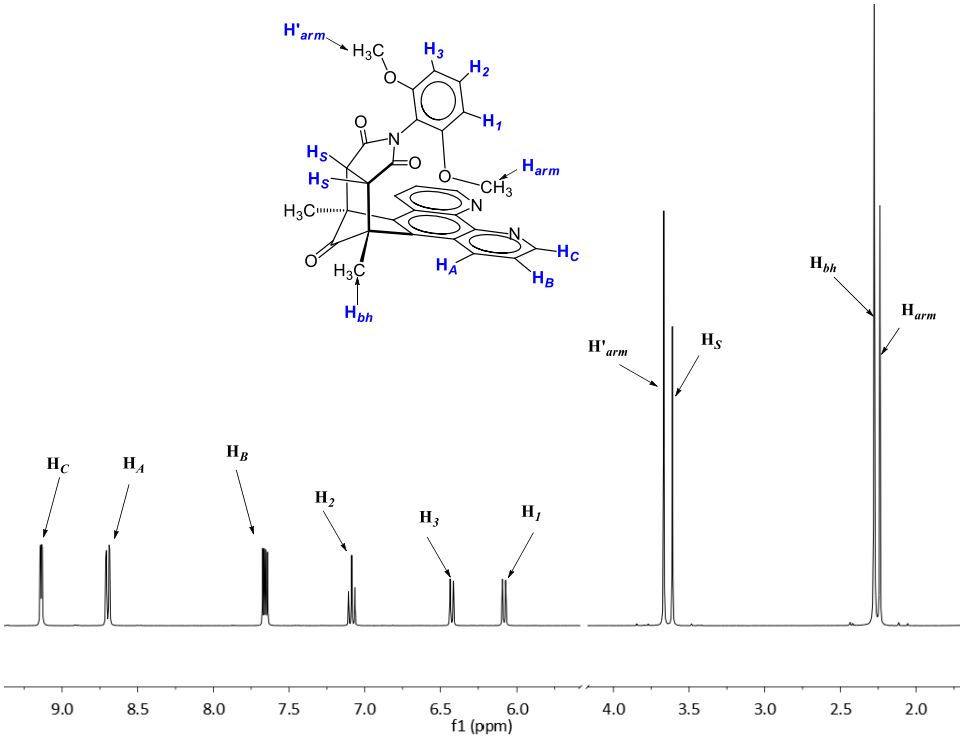

Figure 3.9 Assignment of the ^{1}H NMR spectrum for balance **1'** in CD_2Cl_2. The indexing of protons in balances is provided.

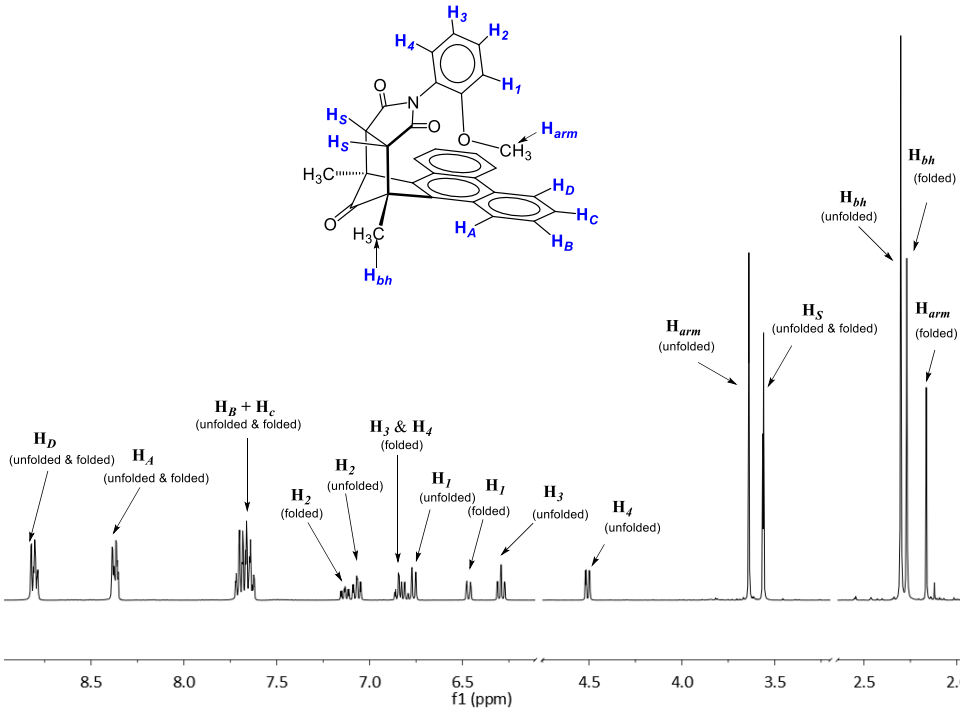

Figure 3.10 Assignment of the ^{1}H NMR spectrum for balance **2** in CD_2Cl_2. The indexing of protons in balances is provided. The *unfolded* and *folded* conformers are indicated in parenthesis.

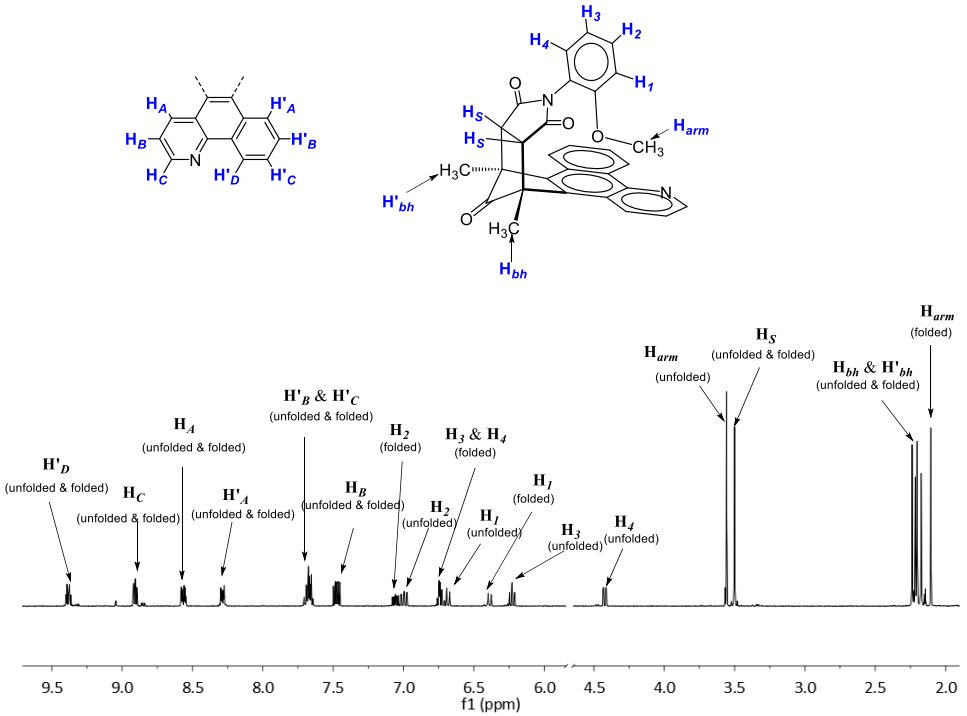

Figure 3.11 Assignment of the ^{1}H NMR spectrum for balance **3** in CD_2Cl_2. The indexing of protons in balances is provided. The *unfolded* and *folded* conformers are indicated in parenthesis.

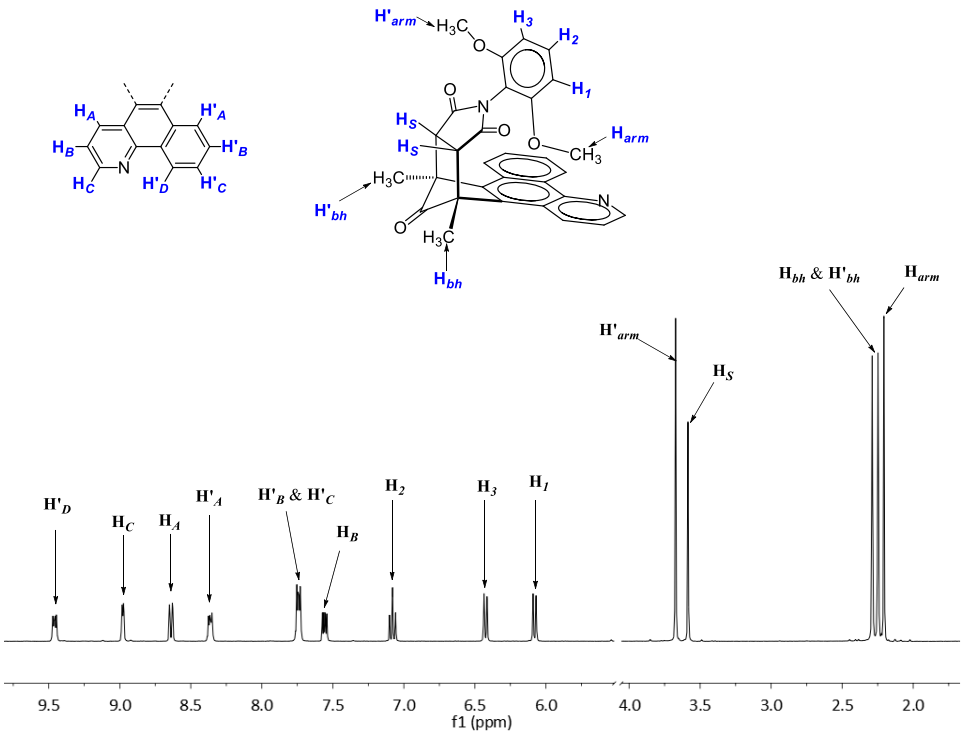

Figure.3.12 Assignment of the ^{1}H NMR spectrum for balance **3'** in CD_2Cl_2. The indexing of protons in balances is provided.

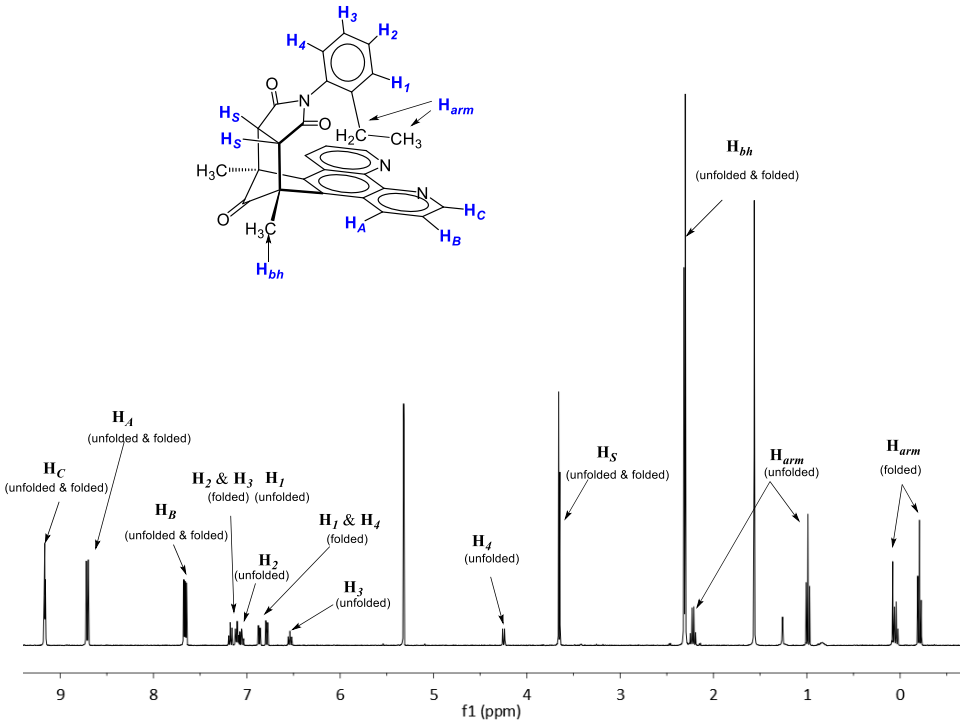

Figure 3.13 Assignment of the ^{1}H NMR spectrum for balance **4** in CD_2Cl_2. The indexing of protons in balances is provided. The *unfolded* and *folded* conformers are indicated in parenthesis

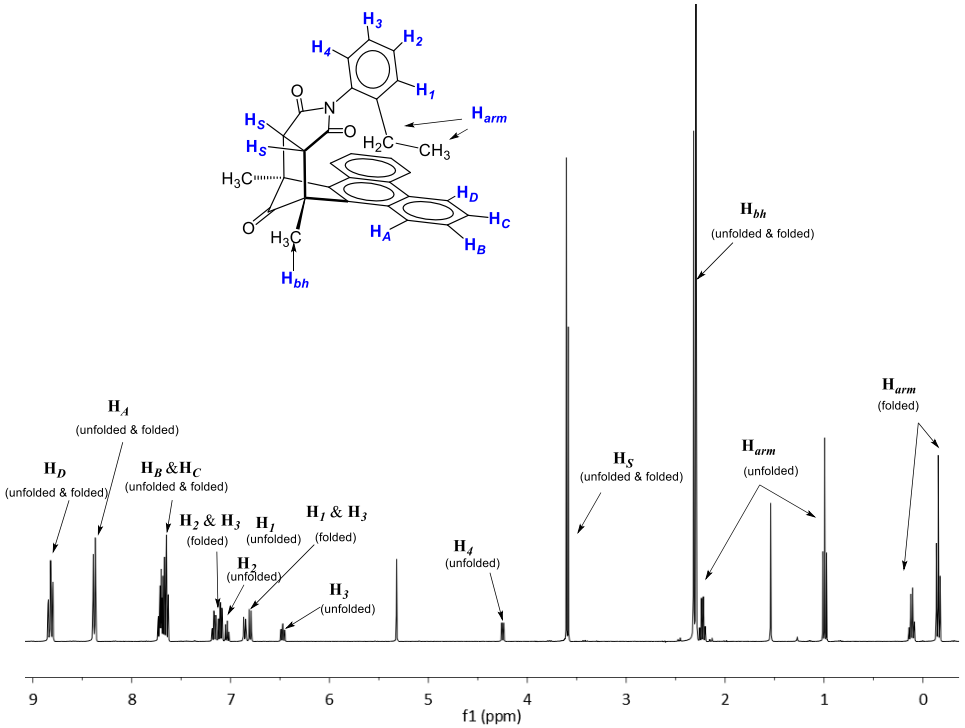

Figure 3.14 Assignment of the ^{1}H NMR spectrum for balance **5** in CD_2Cl_2. The indexing of protons in balances is provided. The *unfolded* and *folded* conformers are indicated in parenthesis.

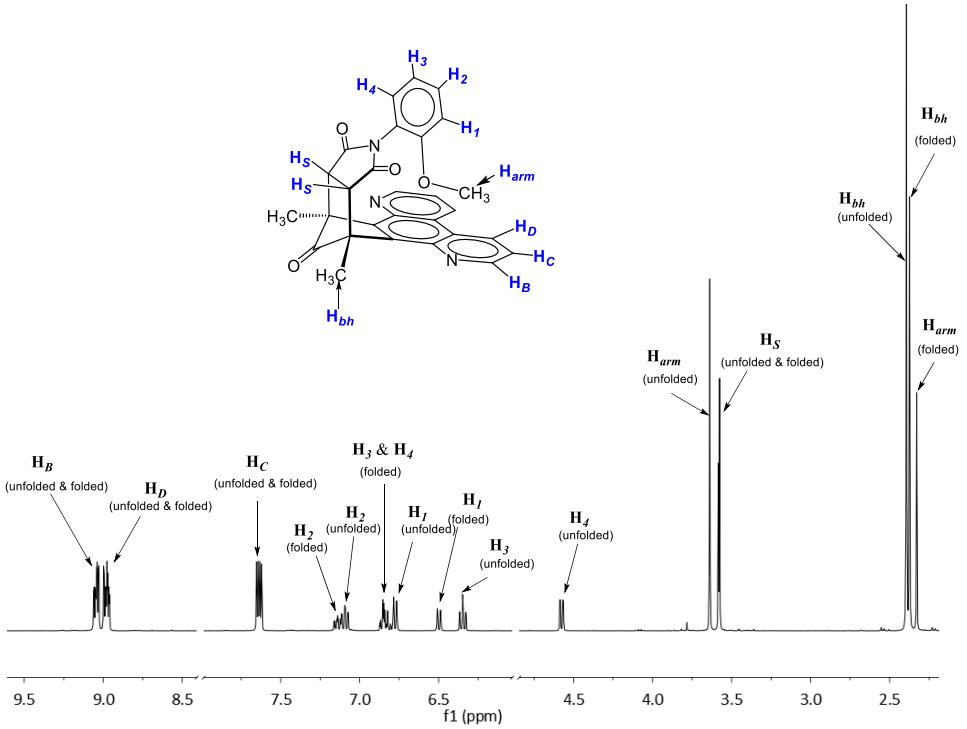

Figure 3.15 Assignment of the ^{1}H NMR spectrum for balance **6** in CD_2Cl_2. The indexing of protons in balances is provided. The *unfolded* and *folded* conformers are indicated in parenthesis

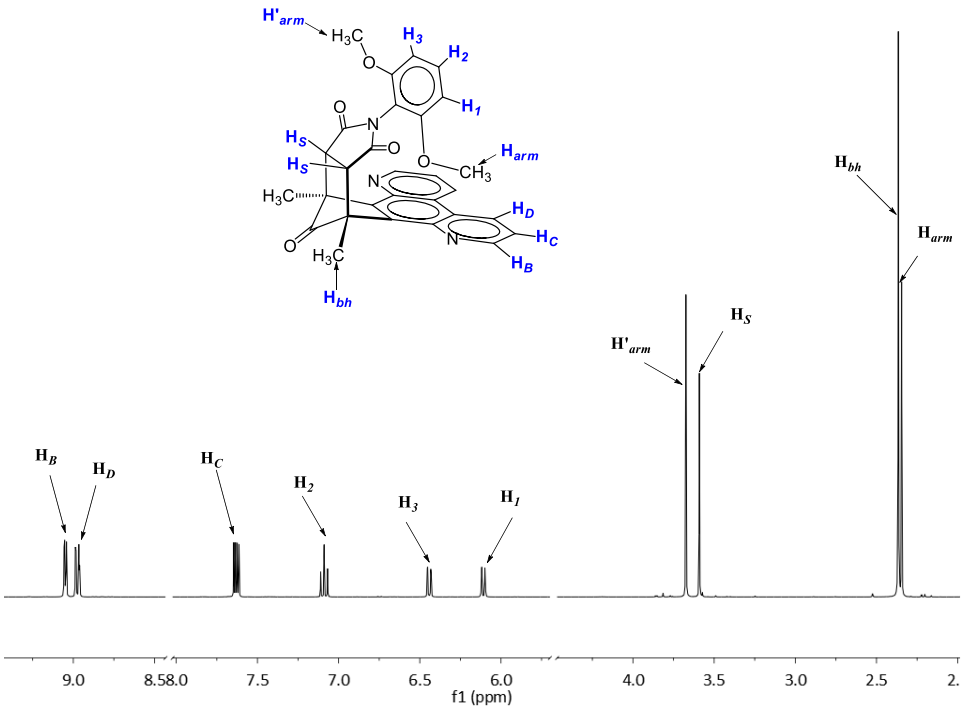

Figure 3.16 Assignment of the ^{1}H NMR spectrum for balance **6'** in CD_2Cl_2. The indexing of protons in balances is provided.

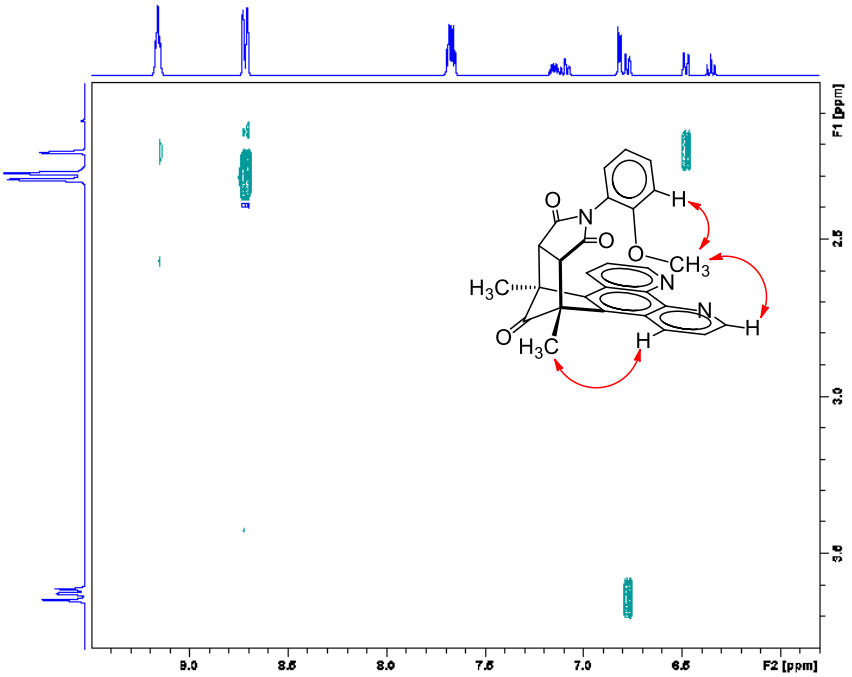

Figure 3.17 Partial ^{1}H-^{1}H NOESY spectrum of balance **1** highlighting the spatial proximity between the arm OCH_3 with the shelf aromatic surface in the *folded* conformer.

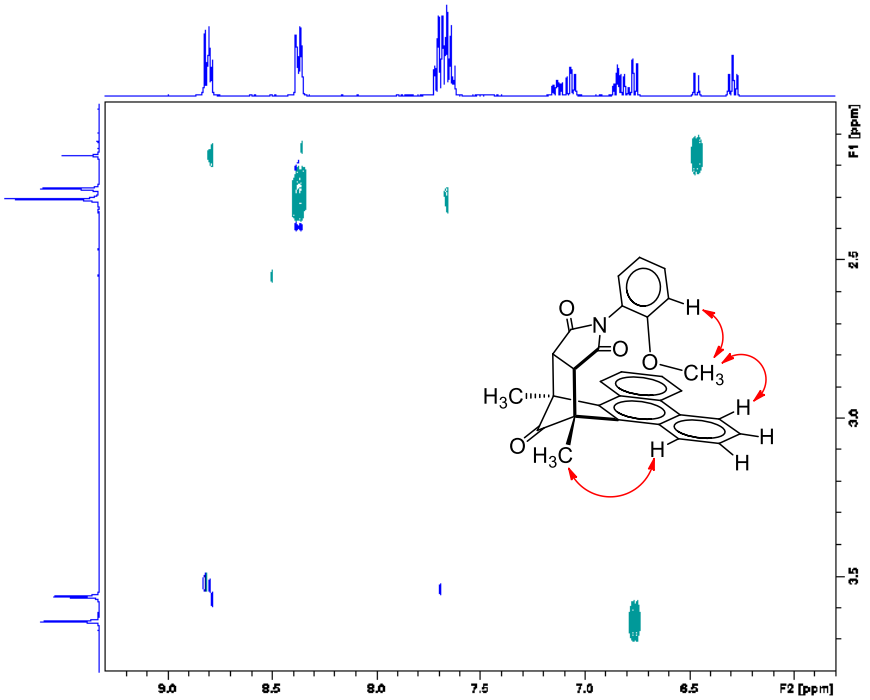

Figure 3.18 Partial ^{1}H-^{1}H NOESY spectrum of balance **2** highlighting the spatial proximity between the arm OCH_3 with the shelf aromatic surface in the *folded* conformer.

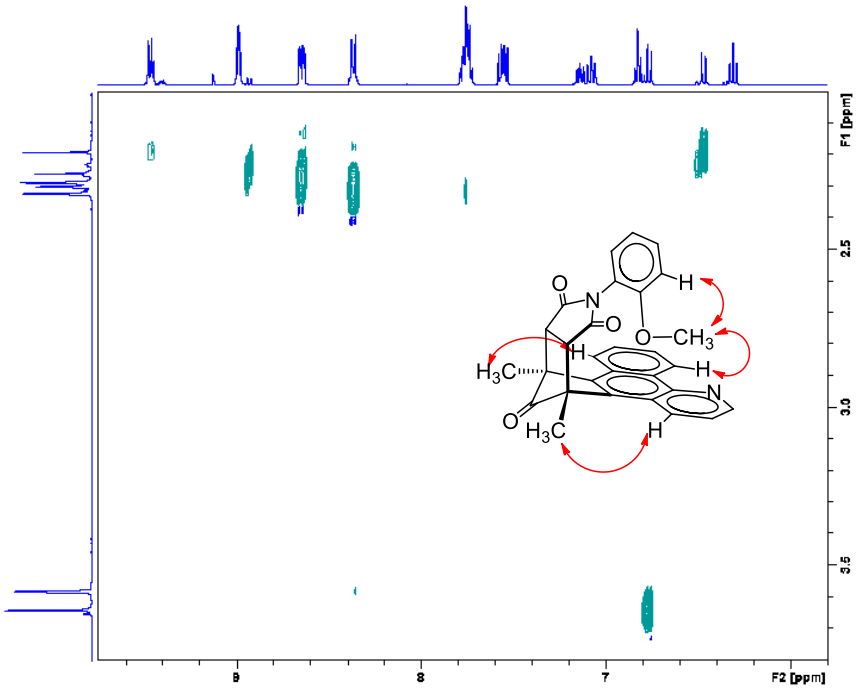

Figure 3.19 Partial ^{1}H-^{1}H NOESY spectrum of balance **3** highlighting the spatial proximity between the arm OCH_3 with the shelf aromatic surface in the *folded* conformer.

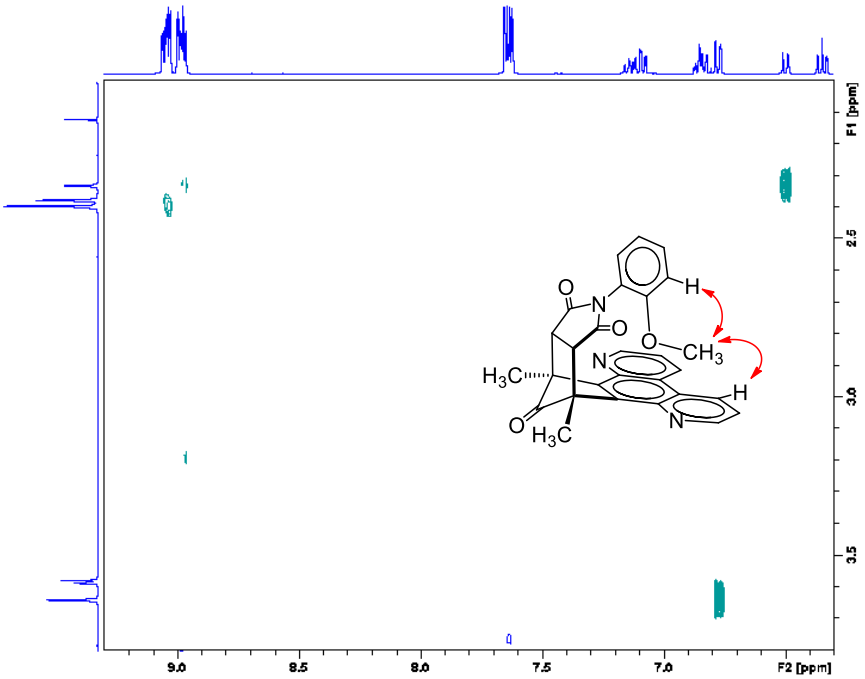

Figure 3.20 Partial ^{1}H-^{1}H NOESY spectrum of balance **6** highlighting the spatial proximity between the arm OCH_3 with the shelf aromatic surface in the *folded* conformer

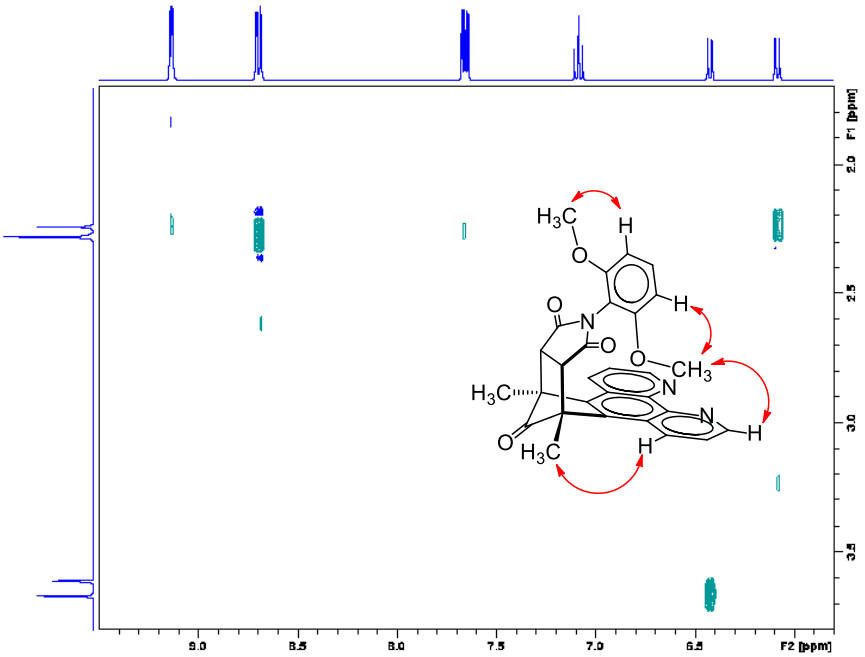

Figure 3.21 Partial ^{1}H-^{1}H NOESY spectrum of balance **1'** highlighting the spatial proximity between the arm OCH_3 with the shelf aromatic surface in the *folded* conformer.

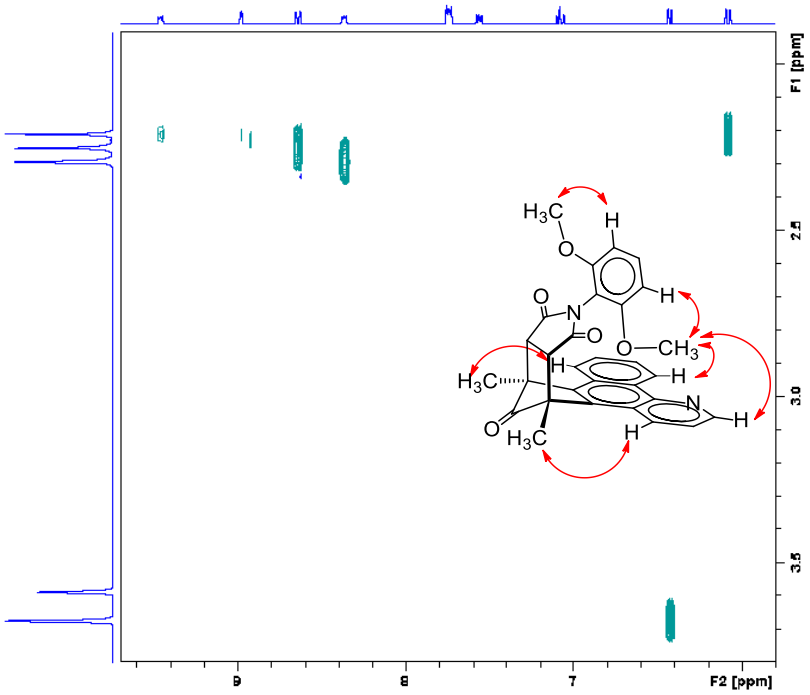

Figure 3.22 Partial ^{1}H-^{1}H NOESY spectrum of balance **3'** highlighting the spatial proximity between the arm OCH_3 with the shelf aromatic surface in the *folded* conformer

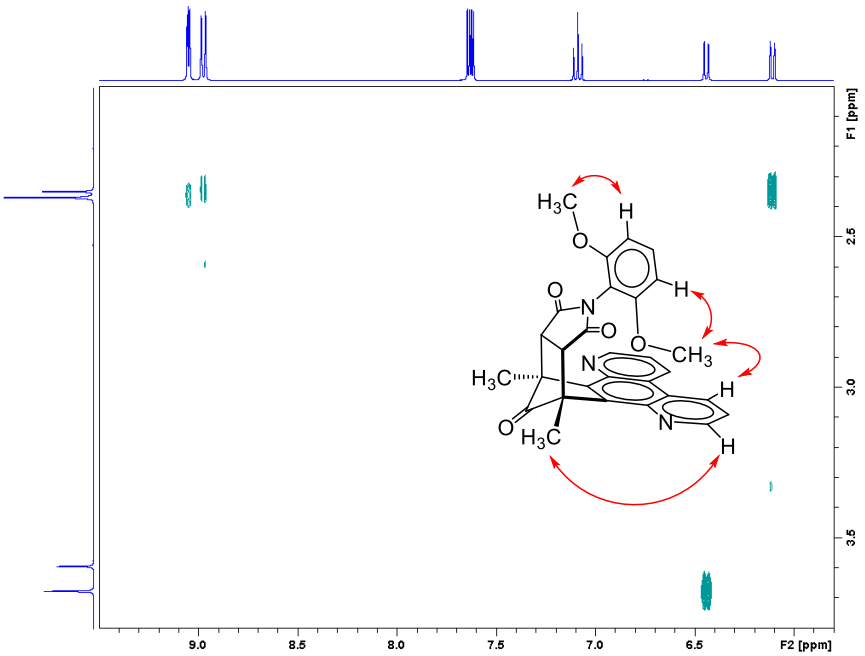

Figure 3.23 Partial ^{1}H-^{1}H NOESY spectrum of balance **6'** highlighting the spatial proximity between the arm OCH_3 with the shelf aromatic surface in the *folded* conformer

3 Quantification of the *folded* and *unfolded* conformers in solution

Quantification of the *folded* and *unfolded* conformers for balances **1**, **2**, **3** and **6** in solution was based on the spectral integrations of the differently shifted arm OCH_3 proton signals on the ^{1}H NMR spectra. As shown in the above section, the arm OCH_3 proton (**H*arm*** in Figure 3.24) in the *folded* conformer was significantly upfield shifted (s, δ: ~2.2 to 2.3 ppm) due to its proximity to the arene shelf than in the *unfolded* conformer (s, δ: ~3.6 ppm). Identification of the two singlets was done by analyzing the ^{1}H-^{13}C HSQC spectra where the two H_{arm} singlets correlate to the two slightly differently shifted ^{13}C signals between 55 and 60 ppm. For the accuracy concern, the spectral deconvolution using Mnova NMR software multiplet line fitting was applied to the corresponding region on the spectra. The measured *folded*/*unfolded* ratios were converted to the folding energies

(ΔG's) [ΔG = –*R*Tln([*folded*]/[*unfolded*])]. Similar quantitative analysis was also carried out in other six common organic solvents of different polarity (Table 3.3).

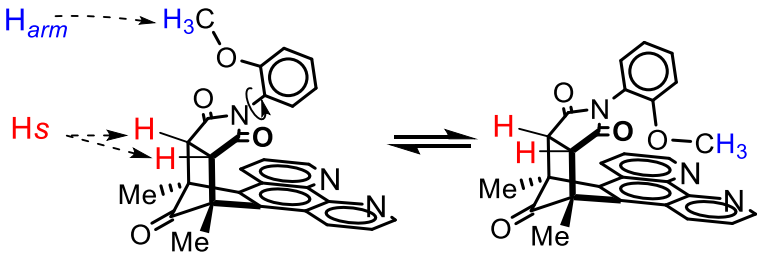

unfolded *folded*

Figure 3.24 The *unfolded* ⇌ *folded* conformational equilibrium of balance **1** highlighting the protons (**H*arm*** and **H*s***) for quantifying the two conformers in solution on the ^{1}H-NMR spectra.

Table 3.3 Measured folding energies (ΔG, kcal/mol)[a] for balances **1**, **2**, **3** and **6** in six common organic solvents at 25 ˚C

	C_6D_6	C_6D_5Br	$CDCl_3$	CD_2Cl_2	CD_3CN	DMSO-d_6
$E_T(30)$[b]	34.3	36.6	39.1	40.7	45.6	45.1
1	+0.09	+0.06	+0.21	-0.02	-0.33	-0.31
2	+0.45	+0.28	+0.41	+0.31	+0.04	+0.05
3	+0.31	+0.13	+0.27	+0.14	-0.11	-0.15
6	+0.56	+0.36	+0.49	+0.25	-0.09	-0.05

[a]. Uncertainty less than ± 0.03 kcal/mol. [b] Matyushov, D. V.; Schmid, R.; Ladanyi, B. M. *J. Phys. Chem. B* **1997**, *101*, 1035.

The arm OCH_3 protons' (H_{arm}) signals were chose to quantify the conformers in this study rather than the succinimide protons' (H_S) signals which were used previously.[i] This was due to the fact that the H_{arm}'s displayed a consistent significant chemical shift change (Δδ) between the *unfolded* and *folded* conformers. In contrast, H_S signal displayed a relatively smaller even, in some cases, non-identifiable Δδ among two conformers, which can compromise the accuracy of quantification. The consistency between these two ways

[i] Carroll, W. R.; Zhao, C.; Smith, M. D.; Pellechia, P. J.; Shimizu, K. D. *Org. Lett.* **2011**, *13*, 4320

of quantification was verified. The [*folded*]/[*unfolded*] ratios were measured by tracking both sets of peaks and compared. As shown in Table 3.4, the [*folded*]/[*unfolded*] ratios measured by tracking the H_{arm} and H_S signals are essentially identical (within the error of experiments), suggesting high consistency.

Table 3.4 Measured [*folded*]/[*unfolded*] ratios using two different sets of peaks, i.e., the arm OCH_3 protons (H_{arm}) and the succinimide methide protons (H_S) in six solvents at 25 ˚C.

		C_6D_6	C_6D_5Br	$CDCl_3$	CD_2Cl_2	CD_3CN	DMSO-d_6
1	by H_{arm}	0.86	1.10	0.70	1.04	1.73	1.69
	by H_S	0.88	1.10	0.71	1.04	1.73	1.67
2	by H_{arm}	0.47	0.62	0.50	0.59	0.93	0.92
	by H_S	0.48	0.62	0.54[a]	0.60	0.92	0.92
3	by H_{arm}	0.59	0.81	0.64	0.79	1.21	1.30
	by H_S	0.57	NA[a]	0.65	NA[a]	1.24	1.27
6	by H_{arm}	0.39	0.54	0.44	0.66	1.17	1.09
	by H_S	0.40	0.55	NA[a]	0.65	1.21	1.07

[a]. Observable overlap between the two singlets. [b] Non-observable chemical shift difference.

Quantification of the *folded* and *unfolded* conformers for balances **4-5** in solution was done by tracking the terminal CH_3 signals (triplets) in the two conformers on the ^{1}H-NMR spectra. The ^{1}H-NMR spectral assignments are provided in Figure 3.12 and 3.13. The ΔG's were measured in three solvents of different polarity (C_6D_6, CD_2Cl_2 and DMSO-d_6) (Table 3.5).

Table 3.5 Measured ΔG's (kcal/mol)[a] for balances **4** and **5** in C_6D_6, CD_2Cl_2 and DMSO-d_6 at 25 ˚C

	C_6D_6	CD_2Cl_2	DMSO-d_6
$E_T(30)$	34.3	40.7	45.1
4	-0.18	-0.17	-0.67
6	-0.26	-0.20	-0.61

[a]. Uncertainty less than ± 0.03 kcal/mol

CHAPTER 4

CORRELATION BETWEEN SOLID-STATE AND SOLUTION CONFORMATIONAL RATIOS IN A SERIES OF *N*-(*O*-TOLYL)SUCCINIMIDE MOLECULAR ROTORS[i]

[i] Reproduced with permission from: Li, P.; Hwang, J.; Maier, J. M.; Zhao, C.; Kaborda, D. V.; Smith, M. D.; Pellechia, P. J.; Shimizu, K. D. *Cryst. Growth Des.* **2015**, *15*, 3561. Copyright 2015 American Chemical Society.

1. Introduction

X-ray crystallography is a powerful tool in modern chemistry and biochemistry for the determination of the three-dimensional structure of natural products,[1,2] rational drug design,[3,4] the study of non-covalent interactions,[5-7] and solid-form pharmaceuticals.[8,9] An important question in these studies is whether an X-ray crystal structure accurately reflects the conformation in solution.[10-12] Conversely, can the conformation in solution be used to predict the conformation in a crystal structure? To address these questions, the X-ray crystal structure and solution conformational ratios for a series of 30 molecular rotors based on an atropisomeric bicyclic *N*-(*o*-tolyl)succinimide framework were measured and compared (Figure 4.1).

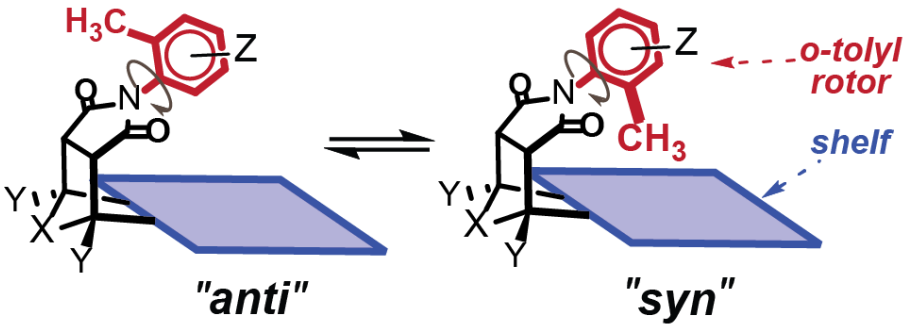

Figure 4.1 Schematic representation of the *anti-syn* conformational equilibrium of a bicyclic *N*-(*o*-tolyl)succinimide molecular rotor.

The suitability of atropisomeric *N*-arylsuccinimides for studying the correlation between solid-state and solution structures was previously recognized by Verma,[13] Kishikawa,[14] and Grossmann.[15] The rigid bicyclic framework fixes the position of most of the atoms, which greatly simplifies its conformational analysis. The only major degree of rotational freedom is the C-N single bond connecting the *o*-tolyl rotor to the succinimide ring. Due to steric repulsion between the *ortho*-methyl group of the rotor and the imide carbonyls, the *N*-tolyl and succinimide rings avoid the co-planar geometry. This leads to

anti- and *syn*- atropisomers that are conformationally distinct due to the asymmetry of the succinimide ring arising from the fused bicyclic framework.

In the course of our studies using molecular balances to measure weak non-covalent interactions,[16-23] we realized that we had access to a library of 30 *N*-(*o*-tolyl)succinimide rotors that displayed a wide range of *anti*-/*syn*- conformational ratios (Figure 4.2). This provided a unique opportunity to examine the correlation or lack of correlation between their solid-state and solution structures. By comparison, the scope of previous studies utilizing this framework[18,20,23] was based on a small number of structures (**12**-**14**) limiting the certainty and generality of the observed trends.

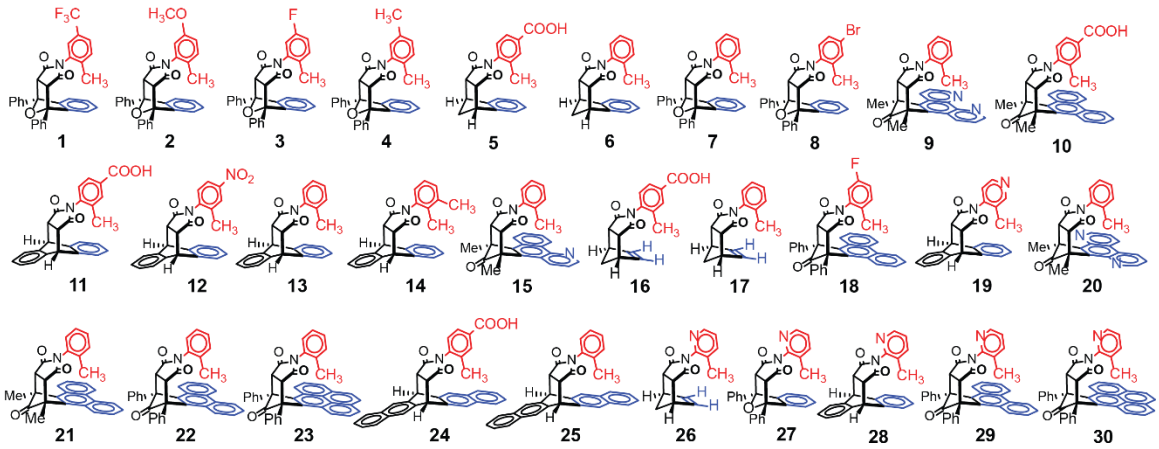

Figure 4.2 Structures of molecular rotors **1-30** used in the solid-state versus solution correlation study. The *o*-tolyl rotor is highlighted in red, and the shelf surface is highlighted in blue

We specifically focused on bicyclic *N*-(*o*-tolyl)succinimides with *ortho*-methyl groups because their atropisomers are generally bereft of the common factors that lead to differences in solid-state and solution structures.[24,25] First, the *ortho*-methyl group is non-polar and does not form strong intermolecular interactions such as hydrogen bonds or

dipole-dipole interactions.[26,27] Second, the methyl group is relatively small, which minimizes the differences in the packing forces between the *syn*- and *anti*-conformers.

This study was enabled by the ability to rapidly assemble a large library of *o*-tolyl rotors containing different shelves, bicyclic frameworks, and rotor substituents. The modular rotors were typically synthesized in one to two steps via previously described synthetic routes.[18,20] The library included twenty new rotors (**1-6**, **8-11**, **15-21**, **24**, **25**, **29**, and **30**), seven previously described rotors from our group (**7**, **17**, **22**, **23**, and **26-28**),[18,23] and three from the literature (**12-14**).[14,15]

2. Results and discussion

First, the mole fraction of the *syn*-conformers (χ_{syn}) were measured in solution via ^{1}H NMR (Table 4.1 in SI). Due to restricted rotation around the C_{tolyl}-N_{imide} bond, the *syn*- and *anti*-conformers were in slow exchange at room temperature leading to distinct sets of peaks for each conformer. Integration of the *syn*- and *anti*-methyl singlets yielded the equilibrium $\chi_{syn\ values}$ with an accuracy from ±1.4% (χ_{syn} = 0.41) to ±5.2% (χ_{syn} = 0.97) (See SI for details). The solution χ_{syn} values for the rotors spanned the entire range from 0.13 to 0.97. These variations were attributed to: 1) the absence or presence of an intramolecular CH-π interaction between the *o*-tolyl methyl group and the aromatic shelves[18,20] 2) repulsive steric interactions between the *o*-tolyl methyl group and the aromatic shelf,[28] and 3) differences in the 'bite-angle' of the bicyclic framework due to the different steric and geometric constraints of the bicyclic bridge (X-groups in Figure 4.1).[29]

The χ_{syn} values were also measured in the solid-state via X-ray crystallographic analysis. Single crystals for 27 rotors were obtained through slow evaporation from

organic solutions, yielding 28 structures (two crystal forms for rotor **7**, see Figure 4.1 in SI). The structures of the three rotors (**12**, **13** and **14**) in literature were obtained from the CSD (refcodes: RIZCOS; UJULUG; IHUBOC). As in the solution studies, the crystal structures displayed a range of χ_{syn} values from 0 to 1. More interestingly, approximately a third of the structures (13 out of 31) contained a mixture of *syn*- and *anti*-conformers, introducing the possibility that we might observe quantitative correlations between the crystal and solution χ_{syn} values.

Closer examination of these structures confirmed that the crystallization process did not appear to impose a strong bias toward one conformer, as the two conformers appeared to have very similar packing energies. This conclusion was reached based on the following observations. First, there were almost an equal number of crystals favoring each conformer. Strong packing forces would have most likely favored one conformer over the other. Second, the two conformers had similar shapes and volumes (Figure 4.3).[30-32] Although the *anti*-conformer with its protruding *ortho*-methyl group appears to be the larger conformer, the imide nitrogen can readily pyramidalize[33,34] reducing the size of the *anti*-conformer and allowing it to fit in the same space as the *syn*-conformer. For example, the *syn*- and *anti*-conformers occupied the same crystallographic space in the majority of the mixed conformer crystals. Third, no strong intermolecular interactions were observed such as hydrogen bonding or dipole-dipole interactions in the extended structures.[35] The only exceptions were the hydrogen bonds formed by the carboxylic acid groups of **16** and **24**. However, these carboxylic groups were positioned on the rotating axis of the *o*-tolyl rotors, and thus these hydrogen bonding interactions act equally on the *syn*- and *anti*-conformers.

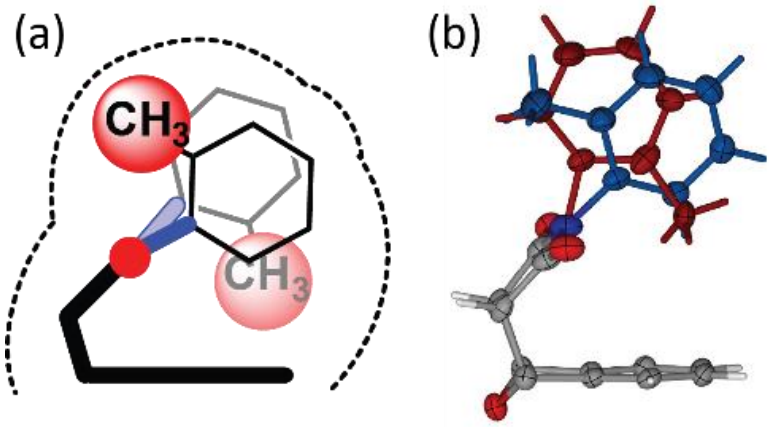

Figure 4.3 (a) Schematic representation for the *anti*- and *syn*-conformers of *o*-tolyl rotor 7 occupying the same crystallographic site in crystal. **(b)** Partial side-view of crystal structures **7** highlighting the partial disorder at the *o*-tolyl rotor motif; the *syn*-conformer is highlighted in red and the *anti*-conformer is highlighted in blue.

Next, a comparison of the solution and crystal χ_{syn} values was performed (Figure 4.4). This analysis revealed a strong qualitative correlation between the solution and crystal χ_{syn} values. For every rotor, the favored conformer in solution was also the favored conformer in the crystal. For example, there are no "mismatched" data points in the upper left or lower right quadrants of the plot in Figure 4.4 where the solution χ_{syn} was > 0.5 and crystal χ_{syn} was < 0.5 or *vice versa*. However, the correlation was not a 1:1 linear correlation as depicted by the broken line in Figure 4.4. The correlation was better described as a step-function (Figure 4.4, solid line) or steep sigmoidal function. Thus, the rotors fell into two distinct groups based on their solution χ_{syn} values. Group 1 were rotors (**1**-**8** and **23**-**30**) that displayed a conformational preference in solution (solution χ_{syn} > 0.56 or < 0.44). The corresponding crystal structures all displayed the same conformational preference but usually with a stronger bias as the crystal χ_{syn} values of 1.0 and 0.0 were the most common. Group 2 were rotors (**9**-**22**) that did not show a clear conformational preference in solution (solution χ_{syn} = 0.50 ±0.06). Their corresponding crystal structure

χ_{syn} values likewise showed no clear preference but with a very wide variation from 0.0 to 1.0 with an average χ_{syn} of 0.64 ±0.11.

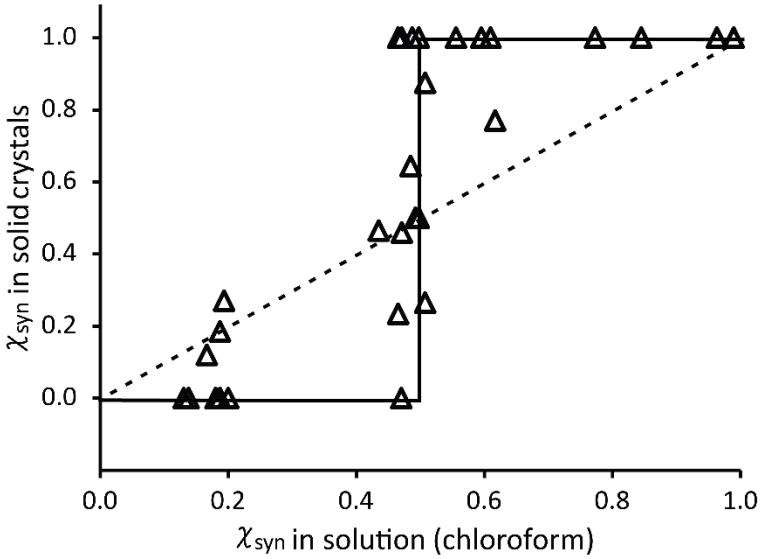

Figure 4.4 A correlation plot of the measured solution and crystal χ_{syn} values for a library of 30 *o*-tolyl molecular rotors

Rotors that deviated from the step-function correlation curve were examined to see if they possessed unusual packing or structural features. These included the 4 crystal structures (**3**, **5**, **7**, and **25**) in Group 1 (solution χ_{syn} values > 0.5 or < 0.5) that did not form pure *syn*- or *anti*-crystals and the 5 crystal structures (**11**, **12**, **14**, **16**, and **18**) in Group 2 (solution χ_{syn} values ≈ 0.5) that formed pure *syn*- or *anti*-crystals. Analysis of these structures showed no significant difference in their crystallographic parameters from the other structures in their group such as space group, presence or absence of solvent, or specific intermolecular interactions (Table 4.1 in SI).

One possibility was that the conformational χ_{syn} values observed in the crystals were due to the rotation and equilibration of the rotamers in the solid-state. However, a number of observations suggested that the rotors could not rotate and interconvert within

the crystals. This was also consistent with previous studies by Kishikawa[14] and Grossmann[15] that did not report any signs of interconversion of crystalline *N*-(*o*-tolyl) succinimides at room temperature. First, two crystals (**17** and **19**) contained crystallographically independent *syn*- and *anti*-conformers suggesting that the conformers were kinetically locked in the crystals. If the conformers were able to interconvert then these crystals should have been conformationally disordered[36,37] Second, the χ_{syn} values for a single crystal of **7** (non-solvate) were measured at two different temperatures and were exactly the same (χ_{syn} = 0.07). This provided further evidence for the lack of interconversion in the crystals because, in solution where the conformers can interconvert, the χ_{syn} values vary with temperature due to the entropy term. Finally, the rotational barriers of the *N*-(*o*-tolyl) succinimides rotors in solution are (20-21 kcal/mol)[14] which is near the upper limit for rotation at room temperature. Rotational barriers in the crystalline-state are typically significantly higher,[38] which would raise the barriers above the threshold to allow rotation in the crystals.

Although the main goal of this study was to empirically test the correlation between X-ray crystal and solution-state conformational preferences, it is interesting to hypothesize on the origins of the observed trends. Overall, the trends appear to be consistent with the current theories of the crystallization process[39-42] and the relative rates of interconversion in crystals versus solution. For rotors in Group 1, the preferred conformer has a higher concentration in solution providing a driving force for its selective crystallization. This conformational preference in solution is maintained throughout the crystallization process because the preferred conformer concentration is continually being replenished, as the rate of interconversion in solution is much faster than the rate of crystallization.[14] For rotors in

Group 2, there is an equal concentration of the two conformers in solution and thus there is a similar driving force for the crystallization of the *syn*- and *anti*-conformers. This explains the higher prevalence of mixed conformer crystals within this group. Also, these rotors would be more sensitive to any small differences in the packing energies and thus, there were also a significant percentage of crystals that were all *syn* or *anti*.

Another possible origin of the step-function correlation of the χ_{syn} values was the formation of stable homo-dimers (*syn*-*syn* or *anti*-*anti*) in the crystallization process. This would explain the predominance of all *syn*- or all *anti*- crystals in Group 1. However, the majority of crystals in Group 2 contained mixtures of *syn*- and *anti*-conformers, which suggests that formation of stable homo-dimers was not the origin of the step-function correlation.

3. Conclusion

In summary, we have carried out a correlation study between the solution and crystal structures for a library of bicyclic *N*-(*o*-tolyl) succinimide molecular rotors. A strong qualitatively correlation was found between the atropisomeric χ_{syn} values in solution and in crystal structures. The dominant conformer in solution was consistently found to be the dominant conformer in the crystal structures. However, the correlation was not linear and was better characterized as a step-function. Hopefully, this study will provide empirical guidance in the applications of X-ray structure analysis in the design of functional solid-state crystalline materials, and the development of stable solid-form pharmaceuticals.

Broader conclusions drawn from this study should be constrained to the subset of molecules, which 1) have conformers that are rapidly interconverting at room temperature and 2) have minimal differences in packing energy and intermolecular interactions. For this subset of molecules, the crystalline conformational preferences can be accurately predicted based on the solution conformational preferences. The only caveats are conformers in Group 2, which have very similar energies in solution ($\Delta\Delta G \leq 0.15$ kcal/mol, based on the solution χ_{syn} ranges of ±0.06). The crystalline conformational preferences in Group 2 are difficult to predict because they vary widely. Fortunately, it is easy to identify the rotors in Group 2 based on their solution χ_{syn} values.

Conversely, prediction of solution conformational preferences using crystal structures is less certain. The crystalline conformational preferences generally matched those in solution. In particular, it is unlikely that a molecule that displays a strong conformational preference in the crystal structure will have the opposite conformational preference in solution. However, due to the poor correlation for rotors in Group 2 and the lack of a 1:1 quantitative correlation, it is possible for a crystal structure to have a strong conformational preference but no clear conformational preference in solution. Fortunately, Group 2 spans a very narrow energy range of conformers, and thus, even a small difference in energy ($\Delta\Delta G > 0.15$ kcal/mol) would place the conformers in the more predictable Group 1.

Reference

[1]. Jones, N. *Nature* **2014**, *505*, 602.
[2]. Rissanen, K. *Advanced X-ray crystallography*; Springer: Heidelberg ; New York, 2012.
[3]. Blundell, T. L.; Jhoti, H.; Abell, C. *Nat. Rev. Drug Discovery* **2002**, *1*, 45.
[4]. Davis, A. M.; Teague, S. J.; Kleywegt, G. J. *Angew. Chem., Int. Ed.* **2003**, *42*, 2718.
[5]. Dunitz, J. D.; Gavezzotti, A. *Angew. Chem., Int. Ed.* **2005**, *44*, 1766.
[6]. Spackman, M. A.; McKinnon, J. J. *CrystEngComm* **2002**, *4*, 378.
[7]. Dunitz, J. D.; Gavezzotti, A. *Acc. Chem. Res.* **1999**, *32*, 677.
[8]. Fleischman, S. G.; Kuduva, S. S.; McMahon, J. A.; Moulton, B.; Walsh, R. D. B.; Rodriguez-Hornedo, N.; Zaworotko, M. J. *Cryst. Growth Des.* **2003**, *3*, 909.
[9]. Blagden, N.; de Matas, M.; Gavan, P. T. P.; York, P. *Adv. Drug Deliver. Rev.* **2007**, *59*, 617.
[10]. Nangia, A. *Acc. Chem. Res.* **2008**, *41*, 595.
[11]. Cruz-Cabeza, A. J.; Bernstein, J. *Chem. Rev.* **2014**, *114*, 2170.
[12]. Derdour, L.; Skliar, D. *Chem. Eng. Sci.* **2014**, *106*, 275.
[13]. Srivastava, V.; Srivastava, V.; Verma, S. M. *J. Org. Chem.* **1994**, *59*, 3560.
[14]. Kishikawa, K.; Yoshizaki, K.; Kohmoto, S.; Yamamoto, M.; Yamaguchi, K.; Yamada, K. *J. Chem. Soc., Perkin Trans. 1* **1997**, 1233.
[15]. Grossmann, G.; Potrzebowski, M. J.; Olejniczak, S.; Ziolkowska, N. E.; Bujacz, G. D.; Ciesielski, W.; Prezdo, W.; Nazarov, V.; Golovko, V. *New J. Chem.* **2003**, *27*, 1095.
[16]. Carroll, W. R.; Pellechia, P. J.; Shimizu, K. D. *Org. Lett.* **2008**, *10*, 3547.
[17]. Carroll, W. R.; Zhao, C.; Smith, M. D.; Pellechia, P. J.; Shimizu, K. D. *Org. Lett.* **2011**, *13*, 4320
[18]. Zhao, C.; Parrish, R. M.; Smith, M. D.; Pellechia, P. J.; Sherrill, C. D.; Shimizu, K. D. *J. Am. Chem. Soc.* **2012**, *134*, 14306.
[19]. Li, P.; Zhao, C.; Smith, M. D.; Shimizu, K. D. *J. Org. Chem.* **2013**, *78*, 5303.
[20]. Zhao, C.; Li, P.; Smith, M. D.; Pellechia, P. J.; Shimizu, K. D. *Org. Lett.* **2014**, *16*, 3520.
[21]. Li, P.; Parker, T. M.; Hwang, J.; Deng, F.; Smith, M. D.; Pellechia, P. J.; Sherrill, C. D.; Shimizu, K. D. *Org. Lett.* **2014**, *16*, 5064.
[22]. Hwang, J.; Li, P.; Carroll, W. R.; Smith, M. D.; Pellechia, P. J.; Shimizu, K. D.; J. Am. Chem. Soc. 2014, 136, 14060-14067.
[23]. Maier, J. M.; Li, P.; Hwang, J.; Smith, M. D.; Shimizu, K. D. *J. Am. Chem. Soc.* **2015**, *137*, 8014.
[24]. Kessler, H.; Zimmermann, G.; Forster, H.; Engel, J.; Oepen, G.; Sheldrick, W. S. *Angew. Chem., Int. Ed. Engl.* **1981**, *20*, 1053.
[25]. Loosli, H. R.; Kessler, H.; Oschkinat, H.; Weber, H. P.; Petcher, T. J.; Widmer, A. *Helv. Chim. Acta.* **1985**, *68*, 682.
[26]. Nishio, M. *CrystEngComm* **2004**, *6*, 130.
[27]. Takahashi, O.; Kohno, Y.; Nishio, M. *Chem. Rev.* **2010**, *110*, 6049.

[28]. Nijamudheen, A.; Jose, D.; Shine, A.; Datta, A. *J. Phys. Chem. Lett.*, **2012**, *3*, 1493.
[29]. Bhayana, B.; Ams, M. R. *J. Org. Chem.*, **2011**, *76*, 3594.
[30]. Brock, C. P.; Dunitz, J. D. *Chem. Mater.* **1994**, *6*, 1118.
[31]. Dunitz, J. D.; Filippini, G.; Gavezzotti, A. *Tetrahedron* **2000**, *56*, 6595.
[32]. Dunitz, J. D.; Gavezzotti, A. *Cryst. Growth Des.* **2005**, *5*, 2180.
[33]. Langowski, B. A.; Rothchild, R.; Sapse, A. M. *Spectrosc. Lett.* **2001**, *34*, 235.
[34]. Marshall, K.; Rosmarion, K.; Sklyut, O.; Azar, N.; Callahan, R.; Rothchild, R. *J. Fluorine Chem.* **2004**, *125*, 1893.
[35]. Dunitz, J. D.; Gavezzotti, A. *Cryst. Growth Des.* **2012**, *12*, 5873.
[36]. Godinez, C. E.; Zepeda, G.; Garcia-Garibay, M. A. *J. Am. Chem. Soc.* **2002**, *124*, 4701.
[37]. Garcia-Garibay, M. A. *Proc. Natl. Acad. Sci. U. S. A.* **2005**, *102*, 10771.
[38]. Derdour, L.; Skliar, D. *Chem. Eng. Sci.* **2014**, *106*, 275.
[39]. De Yoreo, J. J.; Vekilov, P. G. *Biomineralization* **2003**, *54*, 57.
[40]. Davey, R. J.; Schroeder, S. L. M.; ter Horst, J. H. *Angew. Chem., Int. Ed.* **2013**, *52*, 2166.
[41]. Davey, R. J.; Allen, K.; Blagden, N.; Cross, W. I.; Lieberman, H. F.; Quayle, M. J.; Righini, S.; Seton, L.; Tiddy, G. J. T. *CrystEngComm* **2002**, *4*, 257.
[42]. Volmer, M. *Kinetik der phasenbildung*; Theodor Steinkopff: Dresden und Leipzig, 1939.

Supporting Information

1. Additional tables and figures

Table 4.1 Measured mole fraction of *syn*-conformer (χ_{syn}) in solution[a] and in solid-state crystals and relevant information of crystal structure.

	χ_{syn}		Inclusion solvent molecule	Space group	Z	Z'	Kitaigorodskii coefficiency (C_k)[b]	Conformer in crystal	Crystallization solvents
	In solution	In crystal							
1	0.13	0.00	-	P-1	4	2	67.5%	anti-[c]	C_6H_6
2	0.14	0.00	-	$P2_1/n$	4	1	66.1%	anti-	$CHCl_3$
3	0.17	0.12[k]	-	$Pca2_1$	4	1	66.6%	both[d]	$CHCl_3$
4	0.18	0.00	-	$P2_1/n$	4	1	65.7%	anti-	CH_2Cl_2
5	0.19	0.19[k]	-	$P2_1/n$	4	1	74.2%	both[d]	CH_3OH-CH_3CN
6	0.19	0.00	-	$P2_1/n$	4	1	67.9%	anti-	$CHCl_3$
7	0.19	0.27[f]	CH_3CN	$P2_1/c$	4	1	68.8%	both[c,d]	CH_3CN
		0.07[k]	-	$Pca2_1$	4	1	68.72	both[d]	$CHCl_3$
8	0.20	0.00	$CHCl_3$	P-1	2	1	64.4%	anti-[c]	$CHCl_3$
9	0.43	0.47	CH_2Cl_2	P-1	2	1	70.1%	both[d]	CH_2Cl_2
10	0.47	0.23	CH_3CN	P-1	2	1	71.4%	both[d]	$CHCl_3$/CH_3CN
11	0.47	1.00	unknown[e]	R-3	18	1	n/a	syn-	$CHCl_3$
12	0.47[h]	1.00[h]	-	$P2_1/n$	4	1	64.6%	syn-	C_6H_6
13	0.47	0.46[g]	-	R-3r	6	1	69.0%	both[d]	CH_3Ph or $CHCl_3$
14	0.47	1.00[i]	CH_3NO_2	$P2_1/n$	4	1	65.5%	syn-	CH_3NO_2
15	0.48	0.64	$CHCl_3$	P-1	2	1	74.9%	both[d]	$CHCl_3$-CH_3COCH_3

16	0.49	1.00	-	$P2_1/n$	4	1	71.3%	syn-	CH_3OH-CH_3COCH_3
17	0.49	0.50 [f]	-	$P2_1/c$	8	2	66.9%	both[c]	$CHCl_3$-CH_3CN
18	0.50	1.00	-	$P2_12_12_1$	4	1	67.8%	syn-	$CHCl_3$
19	0.50	0.50	-	$P2_1/c$	8	2	65.9%	both[c]	$CHCl_3$-CH_3COCH_3
20	0.51	0.26	-	C2/c	8	1	71.1%	both[d]	CH_2Cl_2-CH_3CN
21	0.51	0.88	CH_3Ph	P-1	2	1	60.0%	both[d]	$CHCl_3$
22	0.56	1.00 [f]	-	P-1	2	1	68.0%	syn-	EtOAc-CH_3CN
23	0.60	1.00 [f]	CH_2Cl_2	$P2_1/c$	8	4	67.3%	syn-[c]	CH_2Cl_2-CH_3CN
24	0.61	1.00	$CHCl_3$	P-1	2	1	66.2%	syn-	$CHCl_3$
25	0.62	0.77 [k]	-	R-3	18	1	68.3%	both[d]	$CHCl_3$
26	0.77	1.00	-	$P2_1/n$	4	1	69.4%	syn-	$CHCl_3$
27	0.84	1.00	-	P-1	2	1	67.0%	syn-	$CHCl_3$
28	0.96	1.00	-	$P2_1/c$	4	1	66.1%	syn-	CH_3OH
29	0.97[j]	1.00	-	P-1	2	1	68.8%	syn-	$CHCl_3$
30	0.97 [j]	1.00	-	$P2_1/c$	8	2	68.9%	syn-[c]	$CHCl_3$

[a] Measured in $CDCl_3$; Error is within 7.1% (see Error Analysis section). [b] Kitaigorodski, A. I. Organic Chemical Crystallography, Consultants Bureau: New York, 1961; Packing coefficient is calculated by using the following equation: $C_k = Z*V_{mol}/V_{cell}$, where V_{mol} is the molecular volume of the *formula unit* (A^3), V_{cell} is the volume of the unit cell (A^3), and Z is the number of formula unit in the unit cell. [c] More than one crystallographically independent molecules were observed. [d] Co-existence of the *syn*- and *anti*-conformers was identified as partial disorder as the o-tolyl rotor motif. [e] Large amount of unknown/unidentifiable solvent exist. [f] Ref. Zhao, C.; Parrish, R. M.; Smith, M. D.; Pellechia, P. J.; Sherrill, C. D.; Shimizu, K. D. *J. Am. Chem. Soc.* **2012**, *134*, 14306. [g] Ref. Grossmann, G.; Potrzebowski, M. J.; Olejniczak, S.; Ziolkowska, N. E.; Bujacz, G. D.; Ciesielski, W.; Prezdo, W.; Nazarov, V.; Golovko, V. *New J. Chem.* **2003**, *27*, 1095. [h] Ref. Kishikawa, K.; Yoshizaki, K.; Kohmoto, S.; Yamamoto, M.; Yamaguchi, K.; Yamada, K. *J. Chem. Soc., Perkin Trans. 1* **1997**, 1233. [i] Ref. Csoregh, I.; Finge, S.; Weber, E. *Struct. Chem.* **2003**, *14*, 241. [j] The detection limit for χ_{syn} in solution was set to be 0.03 to 0.97. (See Error Analysis section) [k.] Repeating crystallization gave the same result.

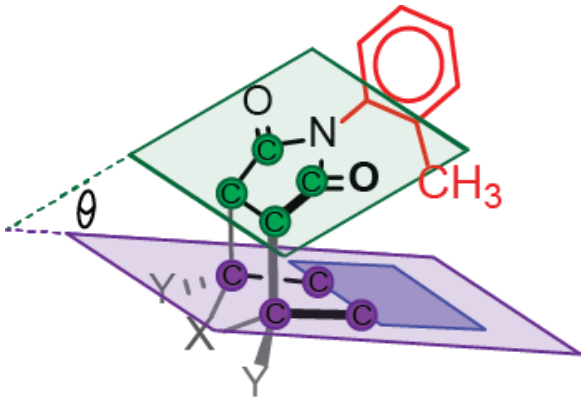

Figure 4.5 Schematic representation for the bite angle (**θ**) in the bicyclic framework: the green and purple planes were defined using the eight carbon atoms highlighted in color.

Table 4.2 Measured bite angle (**θ**) for 30 rotors in their crystal structures.

No.	**θ**	No.	**θ**	No.	**θ**	No.	**θ**	No.	**θ**
1	52.8[a]	**7**	52.7[a]	**13**	58.8	**19**	59.2[a]	**25**	62.0
2	52.6	**8**	52.0	**14**	60.6	**20**	52.9	**26**	53.4
3	51.6	**9**	53.5	**15**	55.4	**21**	56.1	**27**	55.8
4	51.8	**10**	55.4	**16**	52.8	**22**	56.0	**28**	60.7
5	55.3	**11**	62.8	**17**	52.9[a]	**23**	56.1[a]	**29**	55.7
6	55.0	**12**	59.0	**18**	56.7	**24**	60.3	**30**	57.3[a]

[a] Average of multiple crystal structures or crystallographically independent molecules.

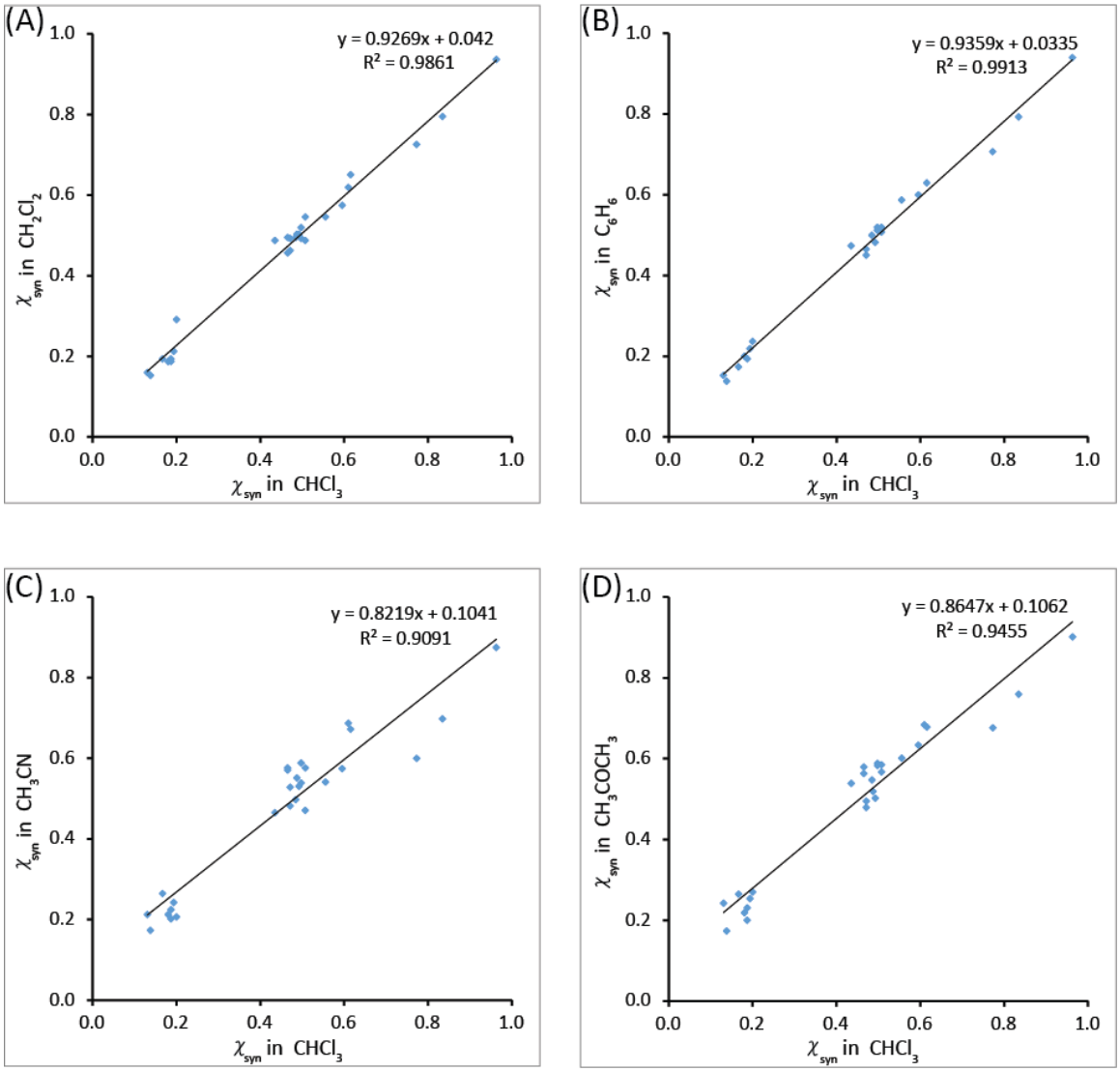

Figure 4.6 Correlation between the measure χ_{syn} in $CHCl_3$ and in *four* other common solvents: CH_2Cl_2(**A**), C_6H_6(**B**), CH_3CN(**C**), and CH_3COCH_3(**D**), highlighting the minimal solvent impact over χ_{syn} in solution. Numerical data are tabulated in Table 4.3

Table 4.3 The measured in-solution χ_{syn} for 30 rotors in this study.[a]

No	$CDCl_3$	CD_2Cl_2	C_6D_6	CD_3CN	CD_3COCD_3
1	0.13	0.16	0.15	0.21	0.24
2	0.14	0.15	0.14	0.17	0.17
3	0.17	0.19	0.17	0.27	0.27
4	0.18	0.19	0.20	0.21	0.22
5	0.18	0.19	n/a[b]	0.20	0.20
6	0.19	0.19	0.19	0.23	0.23
7	0.19	0.21	0.22	0.24	0.25
8	0.20	0.29	0.24	0.21	0.27
9	0.44	0.49	0.47	0.47	0.54
10	0.47	0.46	n/a[b]	0.58	0.58
11	0.47	0.50	n/a[b]	0.57	0.56
12	0.47[c]	n/a[d]	n/a[d]	n/a[d]	n/a[d]
13	0.47	0.49	0.45	0.53	0.48
14	0.47	0.46	0.47	0.48	0.50
15	0.49	0.50	0.50	0.50	0.55
16	0.49	0.50	n/a[b]	0.55	0.52
17	0.50	0.52	0.51	0.59	0.58
18	0.50	0.49	0.52	0.54	0.59
19	0.50	0.52	0.51	0.59	0.58
20	0.51	0.55	0.51	0.58	0.59
21	0.51	0.49	0.52	0.47	0.57
22	0.56	0.55	0.59	0.54	0.60
23	0.60	0.57	0.60	0.57	0.63
24	0.61	0.62	n/a[b]	0.69	0.68
25	0.62	0.65	0.63	0.67	0.68
26	0.77	0.73	0.71	0.60	0.68
27	0.83	0.80	0.79	0.70	0.76
28	0.96	0.94	0.94	0.88	0.90
29	0.97	0.97	n/a[b]	n/a[b]	n/a[b]
30	0.97	0.97	n/a[b]	n/a[b]	n/a[b]

[a] Error is within 5.4% (see Error Analysis section). [b] Insoluble [c] Ref. Kishikawa, K.; Yoshizaki, K.; Kohmoto, S.; Yamamoto, M.; Yamaguchi, K.; Yamada, K. *J. Chem. Soc., Perkin Trans. 1* **1997**. [d] Unavailable in literature.

2. Synthesis and characterization

2.1 Synthesis

All rotors in this study except for **12** were synthesized via one of the two previously reported synthetic routes (Figure 4.7).[i,ii] In ***Route I*** the final rotor was obtained via a thermal condensation of an *endo*-bicyclic anhydride containing the shelf-unit and an *o*-methyl aniline derivative.[xxv] In ***Route II*** the rotor was obtained via a Diels-Alder reaction between the diene bearing the shelf-unit and a maleimide bearing the *o*-tolyl rotor.[ii] The *o*-methyl aniline and bicyclic anhydride derivatives in *Route I* and the diene and maleimide derivatives in *Route II* (Figure 4.8) were either purchased from commercial suppliers or obtained following the literature procedures without modifications (*vide infra*). For the sake of brevity, the anhydride and diene derivatives were indexed arbitrarily as shown in Figure 4.7 and referred to accordingly throughout the text. The syntheses for rotors **6** and **9** were provided in detail to illustrate the two synthetic routes, respectively.

[i] Carroll, W. R.; Pellechia, P.; Shimizu, K. D. *Org. Lett.* **2008**, *10*, 3547.; Carroll, W. R.; Zhao, C.; Smith, M. D.; Pellechia, P. J.; Shimizu, K. D. *Org. Lett.* **2011**, *13*, 4320.; Zhao, C.; Parrish, R. M.; Smith, M. D.; Pellechia, P. J.; Sherrill, C. D.; Shimizu, K. D. *J. Am. Chem. Soc.* **2012**, *134*, 14306.; Zhao, C.; Li, P.; Smith, M. D.; Pellechia, P. J.; Shimizu, K. D. *Org. Lett.* **2014**, *16*, 3520. Hwang, J.; Li, P.; Carroll, W. R.; Smith, M. D.; Pellechia, P. J.; Shimizu, K. D. *J. Am. Chem. Soc.* **2014**, *136*, 14060.

[ii] Li, P.; Zhao, C.; Smith, M. D.; Shimizu, K. D. *J. Org. Chem.* **2013**, *78*, 5303.; Li, P.; Parker, T. M.; Hwang, J.; Deng, F.; Smith, M. D.; Pellechia, P. J.; Sherrill, C. D.; Shimizu, K. D. *Org. Lett.* **2014**, *16*, 5064

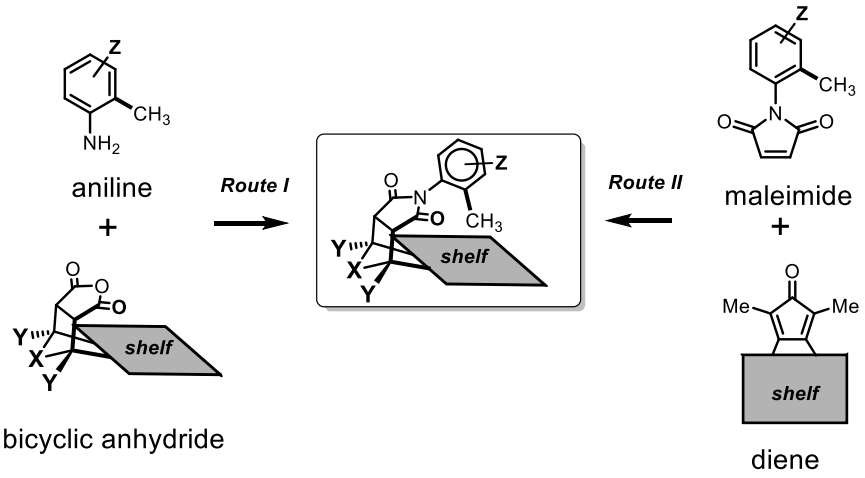

Figure 4.7 Two modular synthetic routes for assembling the *o*-tolyl rotors: (left) Diels-Alder reaction between a diene derivative containing the aromatic shelf and a maleimide derivative containing the *o*-tolyl rotor and thermal imide formation (right) between a bicyclic anhydride bearing the aromatic shelf and an *o*-methyl aniline derivative.

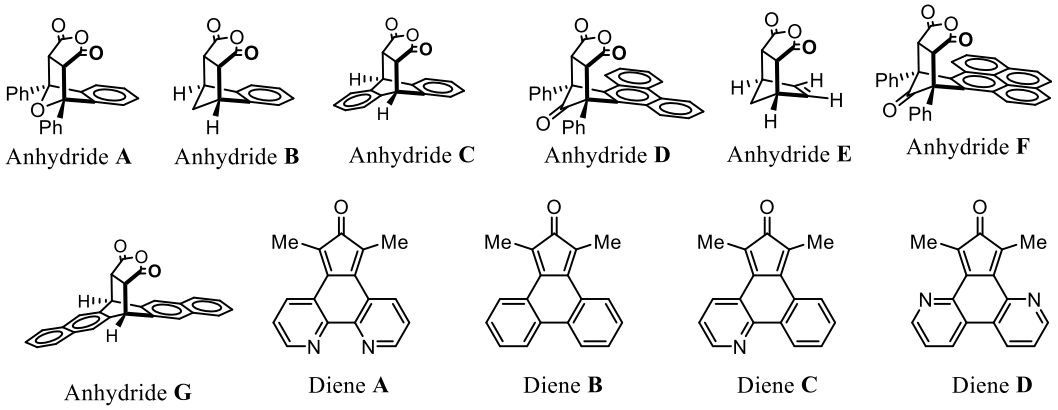

Figure 4.8 The anhydride and diene derivatives (with arbitrary indexes) used in the syntheses.

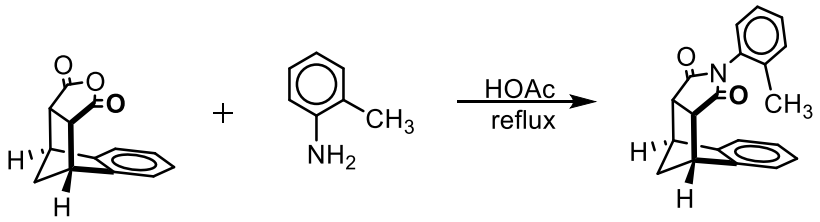

Anhydride **B**

(3aR,4R,9S,9aS)-2-(o-tolyl)-3a,4,9,9a-tetrahydro-1H-4,9-methanobenzo[f]iso-indole-1,3(2H)-dione.(**6**) Rotor **6** was synthesized using ***Route I*** from anhydride **B**[i] and *o*-methyl aniline. Anhydride **B** (100 mg, 0.47 mmol) and *o*-toluidine (54 mg, 0.50 mmol) were dissolved in 10 mL acetic acid. The mixture was heated at reflux with stirring for 24 h. The solvent was then removed under vacuum. The residue was dissolved in 25 mL of EtOAc, washed twice with 50 mL of water. The organic layer was collected and dried under vacuum. The crude product was washed with cold methanol (~10 mL) and then cold acetonitrile (~ 2 mL) to give **6** as an off-white solid (109 mg, 77 %). mp: 214 °C ^{1}H NMR (400 MHz, $CDCl_3$) δ 7.31-6.82 (m, 7H syn and anti), 6.76 (dd, *J* = 7.6 Hz, *J* = 1.4 Hz, 1H syn), 5.34 (d, *J* = 7.8 Hz, 1H anti), 3.88-3.81 (m, 2H syn), 3.63 (dd, *J* = 3.0 Hz, *J* = 1.8 Hz, 2H syn), 3.61 (dd, *J* = 3.1 Hz, *J* = 1.8 Hz, 1H anti), 2.14-1.85 (m, 5H anti and 2H syn), 0.94 (s, 3H syn). ^{13}C NMR (100 MHz, $CDCl_3$) δ 176.06, 143.14, 142.77, 136.41, 135.51, 130.91, 130.68, 130.57, 129.32, 129.29, 127.97, 127.54, 127.36, 126.73, 126.53, 123.28, 54.44, 52.31, 48.10, 48.00, 46.74, 46.29, 17.71, 16.96. HRMS (EI) (m/z) calcd for $[C_{20}H_{17}NO_2]^+$ (M+): 303.1259; found: 303.1259.

[i] Fotins, J.; Smithrud, D. B. *J. Org. Chem.* **2005**, *70*, 4452.

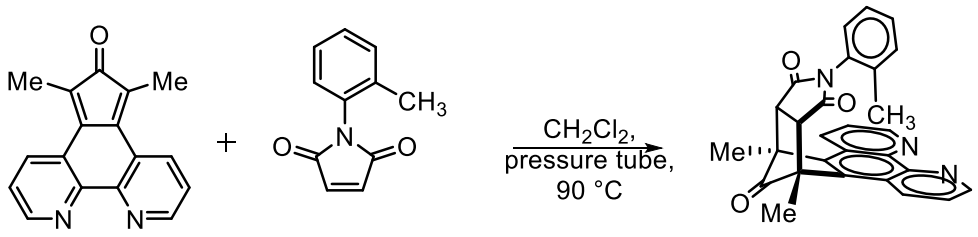

Diene **A**

(9R,9aS,12aS,13S)-9,13-dimethyl-11-(o-tolyl)-9,9a,12a,13-tetrahydro-10H-9,13-methano-isoindolo[5,6-f][1,10]phenanthroline-10,12,14(11H)-trione. (**9**) Rotor **9** was synthesized using ***Route II*** from diene **A**,[i] and *N*-(*o*-tolyl) maleimide.[ii] Diene **A** (80 mg, 0.31 mmol) and *N*-(*o*-tolyl) maleimide (70 mg, 0.37 mmol) were dissolved in dry CH_2Cl_2 (10 mL) in a pressure tube. The vessel was flushed with N_2, sealed and heated to 90 ºC with stirring for 24 h. After cooling, the solvent was removed under vacuum. The solid residue was washed with cold methanol (~10 mL) and then cold acetonitrile (~ 2 mL) to give **9** as an off-white solid (110 mg, 79 %). mp: 290 °C (dec) ^{1}H NMR (400 MHz, CD_2Cl_2) δ 9.18-9.13 (m, 2H syn and anti), 8.75-8.69 (m, 2H *syn* and anti), 7.72-7.62 (m, 2H syn and anti), 7.17-6.70 (m, 4H syn and 2H anti), 6.59-6.51 (m, 1H anti), 4.35 (dd, *J* = 7.9 Hz, *J* = 1.2 Hz, 1H anti), 3.65 (s, 2H syn), 3.64 (s, 2H anti), 2.32 (s, 6H anti), 2.31 (s, 6H syn), 1.93 (s, 3H anti), -0.07 (s, 3H syn). ^{13}C NMR (100 MHz, CD_2Cl_2) δ 200.39, 199.50, 174.47, 174.28, 151.06, 150.92, 147.28, 146.81, 136.16, 135.77, 134.18, 133.90, 132.91, 132.88, 131.25, 131.18, 130.56, 129.98, 129.79, 128.58, 128.34, 128.10, 127.19, 126.68, 125.42, 125.14, 123.73, 123.68, 55.93, 55.81, 48.44, 48.09, 17.79, 15.74, 14.70, 14.54. HRMS (EI) *m/z* calcd. for $[C_{28}H_{21}N_3O_3]^+$ (M^+): 447.1583; found: 447.1591.

[i] Warrener, R. N.; Schultz, A. C.; Houghton, M. A.; Butler, D. N. *Tetrahedron* **1997**, *53*, 3991

[ii] Matuszak, N.; Muccioli, G. G.; Labar, G.; Lambert, D. M. *J. Med. Chem.* **2009**, *52*, 7410.

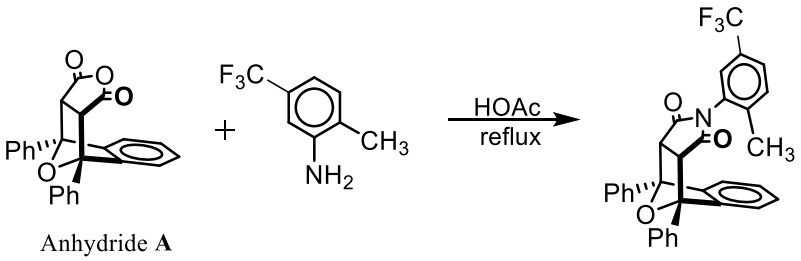

Anhydride **A**

(3aS,4R,9S,9aS)-2-(2-methyl-5-(trifluoromethyl)phenyl)-4,9-diphenyl-3a,4,9,9a-tetrahydro-1H-4,9-epoxybenzo[f]isoindole-1,3(2H)-dione. (**1)** Anhydride **A**[i] (100 mg, 0.27 mmol) and 2-methyl-5-(trifluoromethyl) aniline[ii] (52 mg, 0.30 mmol) were reacted using *Route I* to give **1** as an off-white solid (117 mg, 83 %) mp: 242 °C ^{1}H NMR (300 MHz, $CDCl_3$) δ 8.15-7.92 (m, 4H syn and anti), 7.65-6.98 (m, 13H syn and 12H anti), 5.69 (s, 1H anti), 4.38 (s, 2H syn), 4.33 (s, 2H anti), 2.16 (s, 3H anti), 1.15 (s, 3H syn). ^{13}C NMR (75 MHz, $CDCl_3$) δ 173.15, 144.32, 140.30, 136.29, 131.47, 130.98, 128.97, 128.82, 128.63, 128.41, 128.39, 127.26, 126.39, 125.08, 121.28, 90.89, 54.83, 17.92. HRMS (EI) (m/z) calcd for $[C_{32}H_{22}F_3NO_3]^+(M^+)$: 525.1552; found: 525.1554.

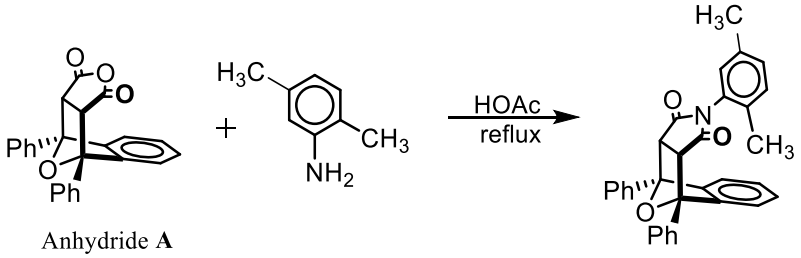

Anhydride **A**

(3aR,4R,9S,9aS)-2-(2,5-dimethylphenyl)-4,9-diphenyl-3a,4,9,9a-tetrahydro-1H-4,9-epoxy-benzo[f]isoindole-1,3(2H)-dione. (**4**). Anhydride **A**[i] (100 mg, 0.27 mmol) and 2,5-dimethyl-aniline[ii] (36 mg, 0.30 mmol) were reacted using *Route I* to give **4** as an off-white solid (122 mg, 96 %). mp: 254 °C ^{1}H NMR (300 MHz, $CDCl_3$) δ 8.16-6.83 (m, 17H

[i] Carroll, W. R.; Pellechia, P.; Shimizu, K. D. *Org. Lett.* **2008**, *10*, 3547.;
[ii] Commercially available.

syn and 15H anti), 6.76 (s, 1H syn), 5.26 (s, 1H anti), 4.32 (s, 2H syn), 4.29 (s, 2H anti), 2.27 (s, 3H syn), 2.14 (m, 3H anti), 2.04 (s, 3H anti), 1.04 (s, 3H syn). ^{13}C NMR (75 MHz, $CDCl_3$) δ 173.54, 144.55, 136.59, 136.53, 132.44, 130.68, 130.44, 130.24, 128.83, 128.75, 128.46, 128.31, 127.84, 127.27, 121.32, 121.25, 90.72, 54.79, 20.73, 17.29. HRMS (EI) (m/z) calcd for $[C_{32}H_{25}NO_3]^+(M^+)$: 471.1834; found: 471.1838.

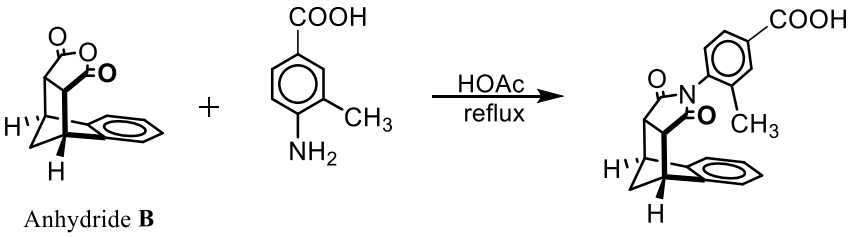

Anhydride **B**

4-((3aR,4R,9S,9aS)-1,3-dioxo-1,3,3a,4,9,9a-hexahydro-2H-4,9-methanobenzo-[f]iso-indol-2-yl)-3-methylbenzoic acid. (**5**) Anhydride **B**[i] (100 mg, 0.47 mmol) and 4-amino-3-methylbenzoic acid[ii] (40 mg, 0.30 mmol) were reacted using *Route I* to give **5** as an off-white solid (130 mg, 80 %). mp: 284 °C ^{1}H NMR (400 MHz, $CDCl_3$) δ 7.99-7.63 (m, 2H syn and anti), 7.38-7.06 (m, 4H syn and anti), 6.97 (d, *J* = 8.2 Hz, 1H syn), 5.52 (d, *J* = 8.2 Hz, 1H anti), 3.99-3.88 (m, 2H syn and anti), 3.82-3.68 (m, 2H syn and anti), 2.22-2.13 (m, 1H syn and anti), 2.08 (s, 3H anti), 2.07-1.98 (m, 1H syn and anti), 1.10 (s, 3H syn). ^{13}C NMR (101 MHz, $CDCl_3$) δ 175.70, 175.64, 170.69, 143.09, 142.75, 137.17, 136.32, 135.96, 135.58, 132.85, 132.58, 130.02, 129.97, 128.66, 128.48, 128.37, 128.06, 127.73, 127.55, 123.41, 123.37, 54.52, 52.39, 48.35, 48.24, 46.91, 46.45, 17.85, 17.14. HRMS (EI) (m/z) calcd for $[C_{21}H_{17}NO_4]^+$ (M^+): 347.1158; found: 347.1159.

[i] Fotins, J.; Smithrud, D. B. *J. Org. Chem.* **2005**, *70*, 4452.
[ii] Commercially available.

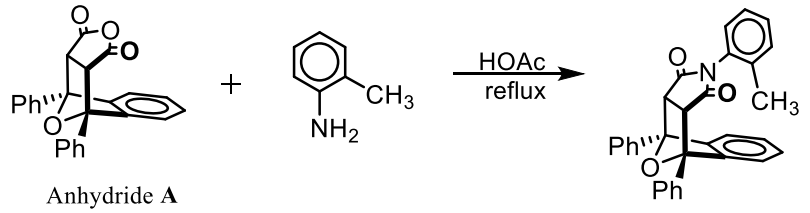

Anhydride **A**

(3aR,4R,9S,9aS)-4,9-diphenyl-2-(o-tolyl)-3a,4,9,9a-tetrahydro-1H-4,9-epoxy-benzo[f] isoindole-1,3(2H)-dione.[i] (**7**) Anhydride **A**[ii] (100 mg, 0.27 mmol) and 2-methyl aniline[iii] (32 mg, 0.30 mmol) were reacted using *Route I* to give **7** as an off-white solid (102 mg, 83 %). ^{1}H NMR (400 MHz, $CDCl_3$) δ 8.12-8.00 (m, 2H anti and syn), 7.60-6.92 (m, 15H anti and 16H syn), 5.51 (d, *J* = 7.8 Hz, 1H anti), 4.34 (s, 2H syn), 4.30 (s, 2H anti), 2.09 (s, 3H anti), 1.08 (s, 3H syn). The spectral data were in agreement with the literature reported.

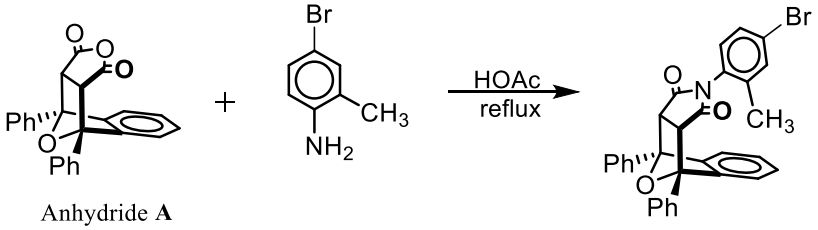

Anhydride **A**

(3aR,4R,9S,9aS)-2-(4-bromo-2-methylphenyl)-4,9-diphenyl-3a,4,9,9a-tetrahydro-1H-4,9-epoxybenzo[f]isoindole-1,3(2H)-dione. (**8**) Anhydride **A**[ii] (100 mg, 0.27 mmol) and 4-bromo-2-methylaniline[iii] (55 mg, 0.30 mmol) were reacted using *Route I* to give **8** as an off-white solid (107 mg, 74 %). mp: 214 °C ^{1}H NMR (300 MHz, $CDCl_3$) δ 8.17-7.95 (m, 4H syn and anti), 7.68-6.95 (m, 13H syn and 12H anti), 6.83 (d, *J* = 8.4 Hz, 1H syn), 5.39 (d, *J* = 8.4 Hz, 1H anti), 4.34 (s, 2H syn), 4.31 (s, 2H anti), 2.08 (s, 3H anti), 1.07 (s, 3H syn). ^{13}C NMR (75 MHz, $CDCl_3$) δ 173.10, 172.89, 144.99, 144.40, 138.00,

[i] Zhao, C.; Parrish, R. M.; Smith, M. D.; Pellechia, P. J.; Sherrill, C. D.; Shimizu, K. D. *J. Am. Chem. Soc.* **2012**, *134*, 14306.
[ii] Carroll, W. R.; Pellechia, P.; Shimizu, K. D. *Org. Lett.* **2008**, *10*, 3547.
[iii] Commercially available.

136.57, 136.33, 133.85, 129.99, 129.58, 128.99, 128.91, 128.86, 128.78, 128.49, 128.37, 127.24, 127.20, 123.53, 121.33, 121.17, 90.72, 90.35, 54.73, 17.73, 17.03. HRMS (EI) (m/z) calcd for $[C_{31}H_{22}BrNO_3]^+$ (M^+): 535.0783; found: 535.0787.

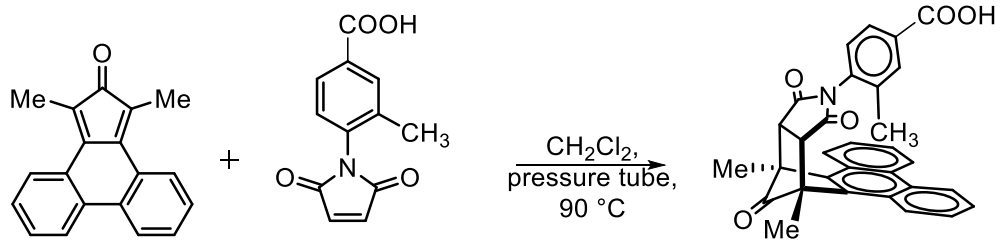

Diene **B**

4-((9R,9aS,12aR,13S)-9,13-dimethyl-10,12,14-trioxo-9,9a,10,12,12a,13-hexa-hydro-11H-9,13-methanophenanthro[9,10-f]isoindol-11-yl)-3-methylbenzoic acid. (**10**) Diene **B**[i], (80 mg, 0.31 mmol) and *N*-(*p*-carboxy-*o*-tolyl) maleimide[ii] (72 mg, 0.37 mmol) were reacted using *Route II* to give **10** as an off-white solid (106 mg, 70 %). mp: 294 °C (dec) ^{1}H NMR (400 MHz, CD_2Cl_2) δ 8.93-8.62 (m, 2H syn and anti), 8.37 (dd, *J* = 8.2 Hz, *J* = 1.0 Hz, 2H syn and anti), 7.86-7.55 (m, 5H syn and anti), 7.44 (d, *J* = 1.7 Hz, 1H syn), 7.15 (dd, *J* = 8.2 Hz, *J* = 1.7 Hz, 1H anti), 6.93 (d, *J* = 8.2 Hz, 1H syn), 4.40 (d, *J* = 8.2 Hz, 1H anti), 3.63 (s, 2H syn), 3.61 (s, 2H anti), 2.32 (s, 6H anti), 2.30 (s, 6H syn), 1.99 (s, 3H anti), 0.03 (s, 3H syn). ^{13}C NMR (100 MHz, $CDCl_3$) δ 200.76, 199.60, 173.90, 173.69, 170.21, 136.76, 135.80, 135.54, 135.04, 133.36, 133.07, 132.68, 132.53, 131.31, 130.85, 130.05, 129.75, 128.39, 128.06, 127.62, 127.53, 127.42, 127.29, 126.87, 125.26, 125.16, 123.56, 123.48, 55.34, 55.18, 53.88, 48.44, 48.05, 31.87, 31.13, 31.08, 29.37, 17.74, 15.44, 14.96, 14.84. HRMS (EI) (m/z) calcd for $[C_{31}H_{23}NO_5]^+$ (M^+): 489.1576; found: 489.1591

[i] Fuchs, B.; Pasternak, M.; Scharf, G. *J. Chem. Soc. Chem. Comm.* **1976**, 53; Li, P.; Zhao, C.; Smith, M. D.; Shimizu, K. D. *J. Org. Chem.* **2013**, *78*, 5303.

[ii] Matuszak, N.; Muccioli, G. G.; Labar, G.; Lambert, D. M. *J. Med. Chem.* **2009**, *52*, 7410.

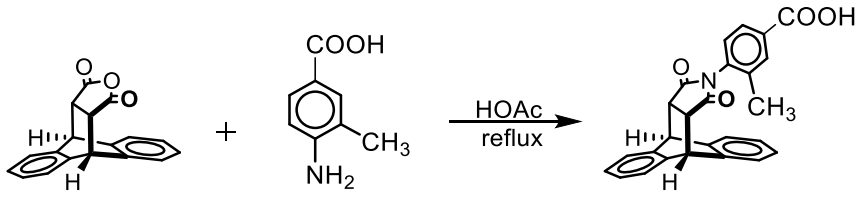

Anhydride **C**

4-((9R,10S,11R,15S)-12,14-dioxo-9,10-dihydro-9,10-[3,4]epipyrroloanthracen-13-yl)-3-methylbenzoic acid. (**11**) Anhydride **C**[i] (100 mg, 0.36 mmol) and 4-amino-3-methylbenzoic acid[ii] (60 mg, 0.40 mmol) were reacted using *Route I* to give **11** as an off-white solid (103 mg, 70 %). mp: 274 °C (dec) ^{1}H NMR (400 MHz, $CDCl_3$) δ 8.15-7.12 (m, 10H syn and anti), 7.05 (d, *J* = 8.2 Hz, 1H syn), 5.61 (d, *J* = 8.2 Hz, 1H anti), 4.92 (s, 2H syn), 4.90 (s, 2H anti), 3.48-3.41 (m, 2H syn and anti), 2.13 (s, 3H anti), 1.12 (s, 3H syn). ^{13}C NMR (100 MHz, $CDCl_3$) δ 175.76, 175.62, 170.91, 170.80, 141.91, 141.26, 139.34, 138.94, 137.21, 137.00, 136.31, 135.77, 135.72, 135.13, 134.76, 133.19, 132.94, 132.73, 130.19, 129.18, 129.09, 128.84, 128.55, 128.38, 127.92, 127.61, 127.43, 127.09, 126.99, 125.66, 125.42, 124.53, 124.40, 47.48, 46.01, 45.49, 17.85, 16.63. HRMS (EI) (m/z) calcd for $[C_{26}H_{19}NO_4]^+$ (M^+): 409.1314; found: 409.1318.

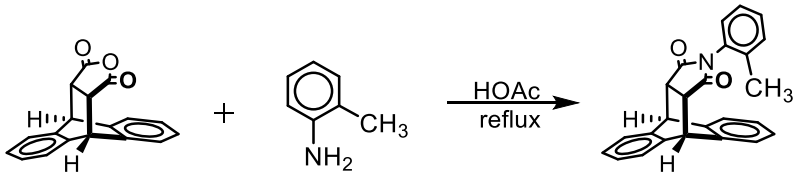

Anhydride **C**

(9R,10S,11R,15S)-13-(o-tolyl)-9,10-dihydro-9,10-[3,4]epipyrroloanthracene-12,14 -dione.[i] (**13**) Anhydride **C**[i] (100 mg, 0.36 mmol) and 2-methylaniline[ii] (41 mg, 0.39 mmol) were reacted using *Route I* to give **13** as an off-white solid (105 mg, 80 %). ^{1}H

[i] Zhao, C.; Parrish, R. M.; Smith, M. D.; Pellechia, P. J.; Sherrill, C. D.; Shimizu, K. D. *J. Am. Chem. Soc.* **2012**, *134*, 14306.

[ii] Commercially available

NMR (400 MHz, $CDCl_3$) δ 6.79-7.43 (m, 12H syn and 11H anti), 5.43 (d, *J* = 7.6 Hz, 1H anti), 4.76-4.88 (m, 2H syn and anti), 3.29-3.41 (m, 2H syn and anti), 1.98 (s, 3H anti), 0.97 (s, 3H syn). The spectral data were in agreement with the literature reported.

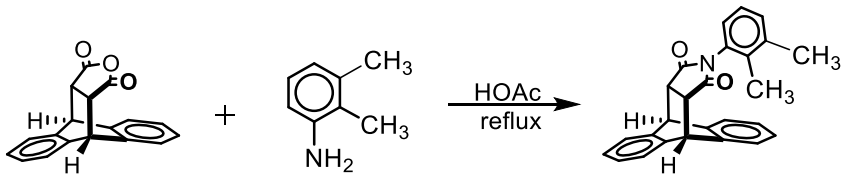

Anhydride **C**

(9R,10S,11R,15S)-13-(2,3-dimethylphenyl)-9,10-dihydro-9,10-[3,4]epipyrrolo-anthracene-12,14-dione. [i] (**14**). Anhydride **C** [ii] (100 mg, 0.36 mmol) and 2,3-dimethylaniline[iiixxxi] (48 mg, 0.40 mmol) were reacted using *Route I* to give **14** as an off-white solid (109 mg, 80 %). ^{1}H NMR (400 MHz, $CDCl_3$) δ 7.48-6.94 (m, 10H syn and anti), 6.84 (t, *J* = 7.7 Hz, 1H anti), 6.70 (dd, *J* = 7.5 Hz, *J* = 1.1 Hz, 1H syn), 5.27 (d, *J* = 7.8 Hz, 1H anti), 4.85 (s, 2H syn), 4.83 (s, 2H anti), 3.38-3.29 (m, 2H syn and anti), 2.16 (s, 3H anti), 2.09 (s, 3H syn), 1.86 (s, 3H anti), 0.81 (s, 3H syn). ^{13}C NMR (100 MHz, $CDCl_3$) δ 176.31, 176.22, 142.09, 141.48, 139.46, 138.99, 138.31, 138.12, 134.71, 133.98, 131.06, 131.03, 130.87, 130.68, 128.17, 127.93, 127.69, 127.52, 127.30, 126.95, 126.87, 126.36, 126.18, 125.62, 125.39, 125.35, 124.91, 124.46, 124.34, 47.34, 47.27, 45.97, 45.47, 20.34, 14.38, 12.88.

[i] Csoregh, I.; Finge, S.; Weber, E. *Struct. Chem.* **2003**, *14*, 241.; Weber, E.; Finge, S.; Csoregh, I. *J. Org. Chem.* **1991**, *56*, 7281.

[ii] Zhao, C.; Parrish, R. M.; Smith, M. D.; Pellechia, P. J.; Sherrill, C. D.; Shimizu, K. D. *J. Am. Chem. Soc.* **2012**, *134*, 14306.

[iii] Commercially available

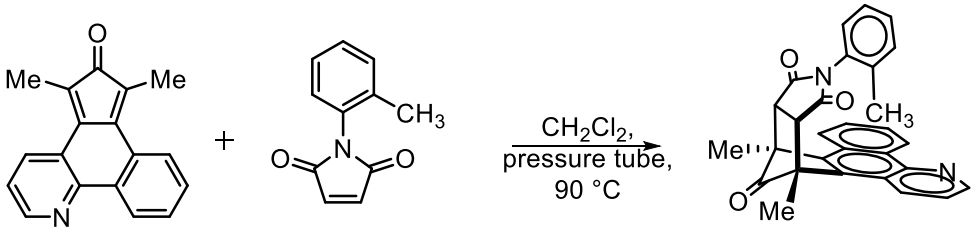

Diene **C**

(9R,9aS,12aR,13S)-9,13-dimethyl-11-(o-tolyl)-9,9a,12a,13-tetrahydro-10H-9,13-methanobenzo[h]isoindolo[5,6-f]quinoline-10,12,14(11H)-trione. (**15**). Diene **C**[i] (80 mg, 0.31 mmol) and *N*-(*o*-tolyl) maleimide[ii] (70 mg, 0.37 mmol) were reacted using *Route II* to give **15** as an off-white solid (110 mg, 80 %). mp: 238 °C (dec) ^{1}H NMR (400 MHz, CD_2Cl_2) δ 9.52-9.38 (m, 1H syn and anti), 9.02-8.97 (m, 1H syn and anti), 8.69-8.63 (m, 1H syn and anti), 8.42-8.33 (m, 1H syn and anti), 7.82-7.69 (m, 2H syn and anti), 7.60-7.50 (m, 1H syn and anti), 7.14-6.94 (m, 2H syn and anti), 6.83-6.73 (m, 1H syn and anti), 6.55-6.46 (m, 1H anti), 4.33 (dd, *J* = 7.9 Hz, *J* = 1.3 Hz, 1H anti), 3.61 (s, 2H syn), 3.60 (s, 2H anti), 2.34 (s, 3H anti), 2.33 (s, 3H syn), 2.30 (s, 3H anti), 2.29 (s, 3H syn), 1.93 (s, 3H anti), -0.06 (s, 3H syn). ^{13}C NMR (100 MHz, $CDCl_3$) δ 200.48, 199.49, 174.30, 174.03, 173.95, 173.89, 149.25, 149.14, 135.80, 134.93, 134.54, 134.17, 132.61, 132.35, 132.13, 130.91, 130.78, 130.58, 129.94, 129.60, 129.38, 129.34, 129.29, 129.22, 129.03, 127.84, 127.76, 127.56, 126.84, 126.73, 126.33, 125.75, 125.72, 124.52, 124.47, 122.49, 122.32, 122.25, 122.19, 55.57, 55.41, 55.29, 55.15, 48.09, 48.05, 47.79, 47.60, 17.63, 15.38, 14.78, 14.61, 14.59, 14.50. HRMS (EI) (m/z) calcd for $[C_{29}H_{22}N_2O_3]^+$ (M^+): 446.1630; found: 446.1622.

[i] Li, P.; Parker, T. M.; Hwang, J.; Deng, F.; Smith, M. D.; Pellechia, P. J.; Sherrill, C. D.; Shimizu, K. D. *Org. Lett.* **2014**, *16*, 5064.

[ii][ii] Matuszak, N.; Muccioli, G. G.; Labar, G.; Lambert, D. M. *J. Med. Chem.* **2009**, *52*, 7410.

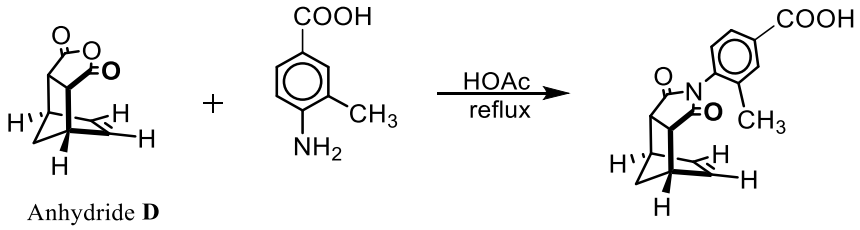

Anhydride **D**

4-((3aR,4S,7R,7aS)-1,3-dioxo-1,3,3a,4,7,7a-hexahydro-2H-4,7-methanoisoindol-2-yl)-3-methylbenzoic acid. (**16**) Anhydride **D**[i] (100 mg, 0.61 mmol) and 4-amino-3-methylbenzoic acid[i] (101 mg, 0.67 mmol) were reacted using *Route I* to give **15** as an off-white solid (150 mg, 83 %) mp: 245 °C ^{1}H NMR (400 MHz, $CDCl_3$) δ 7.99-7.63 (m, 2H syn and anti), 7.38-7.06 (m, 4H syn and anti), 6.97 (d, *J* = 8.2 Hz, 1H syn), 5.52 (d, *J* = 8.2 Hz, 1H anti), 3.99-3.88 (m, 2H syn and anti), 3.82-3.68 (m, 2H syn and anti), 2.22-2.13 (m, 1H syn and anti), 2.08 (s, 3H anti), 2.07-1.98 (m, 1H syn and anti), 1.10 (s, 3H syn). ^{13}C NMR (100 MHz, $CDCl_3$) δ 175.70, 175.64, 170.69, 143.09, 142.75, 137.17, 136.32, 135.96, 135.58, 132.85, 132.58, 130.02, 129.97, 128.66, 128.48, 128.37, 128.06, 127.73, 127.55, 123.41, 123.37, 54.52, 52.39, 48.35, 48.24, 46.91, 46.45, 17.85, 17.14. HRMS (EI) (m/z) calcd for $[C_{21}H_{17}NO_4]^+$ (M^+): 347.1158; found: 347.1159.

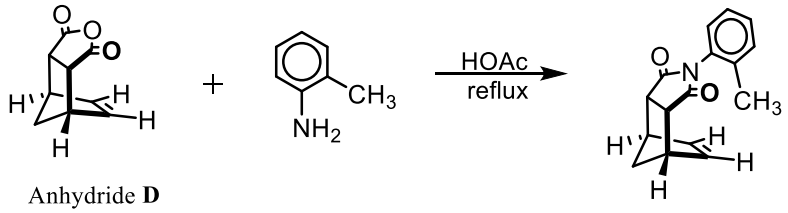

Anhydride **D**

(3aR,4S,7R,7aS)-2-(o-tolyl)-3a,4,7,7a-tetrahydro-1H-4,7-methanoisoindole-1,3(2H)-dione.[ii] (**17**) Anhydride **D**[i] (100 mg, 0.61 mmol) and and 2-methylaniline[i] (71 mg, 0.67 mmol) were reacted using *Route I* to give **17** as an off-white solid (100 mg, 65 %).

[i] Commercially available

[ii] Zhao, C.; Parrish, R. M.; Smith, M. D.; Pellechia, P. J.; Sherrill, C. D.; Shimizu, K. D. *J. Am. Chem. Soc.* **2012**, *134*, 14306.

^{1}H NMR (400 MHz, $CDCl_3$) δ 7.38-7.20 (m, 3H syn and anti), 7.03 (d, *J* = 7.5 Hz, 1H syn), 6.91 (d, *J* = 7.5 Hz, 1H anti), 6.35 (t, *J* = 1.6 Hz, 2H anti), 6.32 (t, *J* = 1.6 Hz, 2H syn), 3.56-3.44 (m, 4H syn and anti), 2.18 (s, 3H anti), 2.15 (s, 3H syn), 1.80-1.88 (m, 1H syn and anti), 1.60-1.69 (m, 1H syn and anti). The spectral data were in agreement with the literature reported.

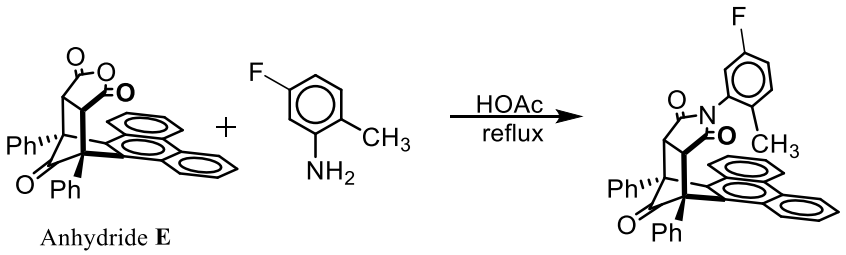

Anhydride **E**

(9R,9aR,12aS,13S)-11-(5-fluoro-2-methylphenyl)-9,13-diphenyl-9,9a,12a,13-tetra hydro-10H-9,13-methanophenanthro[9,10-f]isoindole-10,12,14(11H)-trione. (**18**) Anhy-dride **E**[i] (200 mg, 0.42 mmol) and 5-fluoro-2-methylaniline[ii] (57 mg, 0.46 mmol) were reacted using *Route I* to give **18** as an off-white solid (204 mg, 85 %). mp: 290 °C (dec) ^{1}H NMR (400 MHz, CD_2Cl_2) δ 8.77 (d, *J* = 8.4 Hz, 2H syn and anti), 8.70 (d, *J* = 8.4 Hz, 2H syn and anti), 8.45-8.27 (m, 2H syn and anti), 7.86-6.66 (m, 17H syn and 16H anti), 4.70 (s, 2H syn), 4.69 (s, 2H anti), 3.96 (dd, *J* = 9.0 Hz, *J* = 2.7 Hz, 1H anti), 2.12 (s, 3H anti), -0.11 (s, 3H syn). ^{13}C NMR (100 MHz, $CDCl_3$) δ 197.05, 195.86, 173.33, 173.05, 161.66, 159.55, 159.22, 133.76, 133.74, 133.54, 131.85, 131.79, 131.68, 131.60, 131.37, 131.11, 131.05, 130.97, 129.57, 129.54, 129.28, 129.16, 128.88, 128.76, 128.69, 128.65, 127.62, 127.38, 127.15, 126.92, 126.55, 126.37, 126.15, 125.92, 123.33, 123.10, 116.69,

[i] Carroll, W. R.; Pellechia, P.; Shimizu, K. D. *Org. Lett.* **2008**, *10*, 3547.
[ii] Commercially available

116.54, 116.33, 114.98, 114.75, 113.94, 113.70, 63.73, 45.54, 45.11, 17.13, 14.68. HRMS (EI) (m/z) calcd for $[C_{31}H_{22}FNO_3]^+$ (M^+): 587.1897; found: 587.1895.

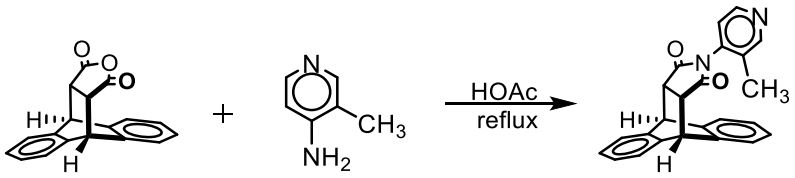

Anhydride **C**

(9R,10S,11R,15S)-13-(3-methylpyridin-4-yl)-9,10-dihydro-9,10-[3,4]epipyrrolo-anthracene-12,14-dione. (**19**). Anhydride **C**[i] (100 mg, 0.36 mmol) and 3-methylpyridin-4-amine[ii] (43 mg, 0.40 mmol) were reacted using *Route I*[iii] to give **19** as an off-white solid (85 mg, 65 %). mp: 248 °C ^{1}H NMR (400 MHz, $CDCl_3$) δ 8.53-8.22 (m, 2H syn and anti), 7.51-7.09 (m, 5H syn and anti), 6.94 (d, *J* = 5.2 Hz, 1H syn), 5.57 (d, *J* = 5.2 Hz, 1H anti), 4.89 (t, *J* = 7.0 Hz, 2H syn and anti), 3.46-3.43 (m, 2H syn and anti), 2.08 (s, 3H anti), 1.12 (s, 3H syn). ^{13}C NMR (101 MHz, $CDCl_3$) δ 175.12, 174.92, 151.99, 151.85, 148.09, 147.73, 141.70, 141.07, 139.23, 139.06, 139.00, 138.83, 131.82, 131.29, 127.61, 127.45, 127.14, 127.04, 125.62, 125.38, 124.54, 124.42, 122.50, 121.94, 100.10, 47.54, 47.51, 45.97, 45.47, 15.02, 13.95. HRMS (EI) (m/z) calcd for $[C_{24}H_{18}N_2O_2]^+$ (M^+): 366.1368; found: 366.1370.

[i] Zhao, C.; Parrish, R. M.; Smith, M. D.; Pellechia, P. J.; Sherrill, C. D.; Shimizu, K. D. *J. Am. Chem. Soc.* **2012**, *134*, 14306.

[ii] Commercially available

[iii] The crude product was washed with saturated sodium bicarbonate solution before drying up under vacuum.

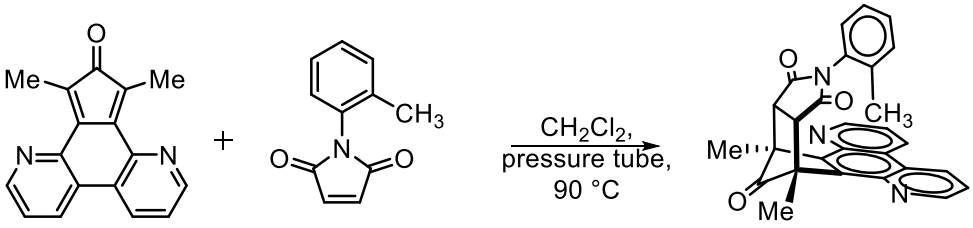

Diene **D**

(9R,9aS,12aR,13S)-9,13-dimethyl-11-(o-tolyl)-9,9a,12a,13-tetrahydro-10H-9,13-methano-isoindolo[5,6-f][4,7]phenanthroline-10,12,14(11H)-trione. (**20**) Diene **D**[i] (80 mg, 0.31 mmol) and *N*-(*o*-tolyl) maleimide[ii] (70 mg, 0.37 mmol) were reacted using *Route II* to give **20** as an off-white solid (110 mg, 80 %). mp: 296 °C (dec) ^{1}H NMR (400 MHz, CD_2Cl_2) δ 9.12-8.87 (m, 4H syn and anit), 7.74-7.54 (m, 2H syn and anti), 7.15-6.68 (m, 4H syn and 2H anti), 6.58-6.50 (m, 1H anti), 4.39 (dd, *J* = 7.9 Hz, *J* =1.3 Hz, 1H anti), 3.62 (s, 2H syn), 3.60 (s, 2H anti), 2.41 (s, 6H anti), 2.40 (s, 6H syn), 1.92 (s, 3H anti), 0.03 (s, 3H syn). ^{13}C NMR (100 MHz, CD_2Cl_2) δ 202.68, 201.64, 174.07, 173.75, 151.04, 150.94, 144.70, 144.49, 138.61, 138.32, 136.10, 136.05, 131.61, 131.34, 131.27, 131.24, 131.05, 130.96, 129.67, 129.50, 128.57, 128.16, 128.09, 127.10, 126.72, 125.98, 125.48, 122.59, 122.52, 56.58, 56.54, 49.08, 48.65, 30.25, 17.85, 15.85, 14.56, 14.34. HRMS (EI) (m/z) calcd for $[C_{28}H_{21}N_3O_3]^+$ (M^+): 447.1583; found: 447.1585.

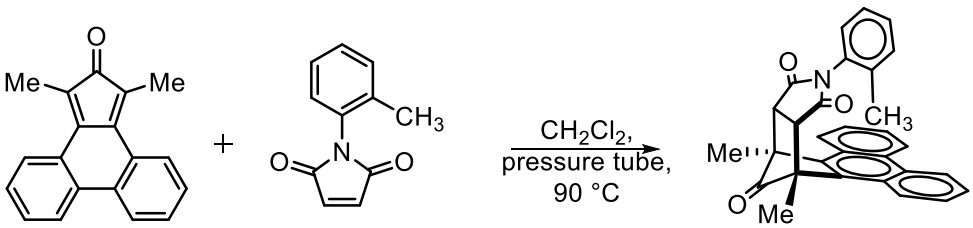

Diene **B**

[i] Li, P.; Parker, T. M.; Hwang, J.; Deng, F.; Smith, M. D.; Pellechia, P. J.; Sherrill, C. D.; Shimizu, K. D. *Org. Lett.* **2014**, *16*, 5064.

[ii] Matuszak, N.; Muccioli, G. G.; Labar, G.; Lambert, D. M. *J. Med. Chem.* **2009**, *52*, 7410.

(9R,9aS,12aR,13S)-9,13-dimethyl-11-(o-tolyl)-9,9a,12a,13-tetrahydro-10H-9,13-methano-phenanthro[9,10-f]isoindole-10,12,14(11H)-trione. (**21**) Diene **B**[i] (80 mg, 0.31 mmol) and *N*-(*o*-tolyl) maleimide[ii] (70 mg, 0.37 mmol) were reacted using *Route II* to give **21** as an off-white solid (124 mg, 90 %). mp: 240 °C ^{1}H NMR (400 MHz, $CDCl_3$) δ 8.83-8.68 (m, 2H syn and anti), 8.41-8.34 (m, 2H syn and anti), 7.74-7.58 (m, 4H syn and anti), 7.08-6.64 (m, 4H syn and 2H anti), 6.51-6.41 (m, 1H anti), 4.40 (dd, *J* = 7.9 Hz, *J* = 1.1 Hz, 1H anti), 3.57 (s, 2H syn), 3.56 (s, 2H anti), 2.34 (s, 3H anti), 2.32 (s, 3H syn), 1.94 (s, 3H anti), -0.01 (s, 3H syn). ^{13}C NMR (100 MHz, CD_2Cl_2) δ 201.37, 200.28, 174.74, 174.46, 136.60, 135.94, 134.97, 134.05, 133.80, 131.74, 131.62, 131.51, 131.23, 131.08, 130.96, 129.78, 129.54, 129.35, 128.58, 128.34, 128.13, 128.10, 127.90, 127.75, 127.69, 127.66, 127.33, 127.03, 126.89, 126.83, 125.74, 125.68, 123.99, 123.91, 55.66, 55.50, 48.78, 48.42, 17.80, 15.59, 15.21, 15.08. HRMS (EI) (m/z) calcd for $[C_{30}H_{23}NO_3]^+$ (M^+): 445.1678; found: 445.1677.

[i] Li, P.; Zhao, C.; Smith, M. D.; Shimizu, K. D. *J. Org. Chem.* **2013**, *78*, 5303.;
[ii] Matuszak, N.; Muccioli, G. G.; Labar, G.; Lambert, D. M. *J. Med. Chem.* **2009**, *52*, 7410

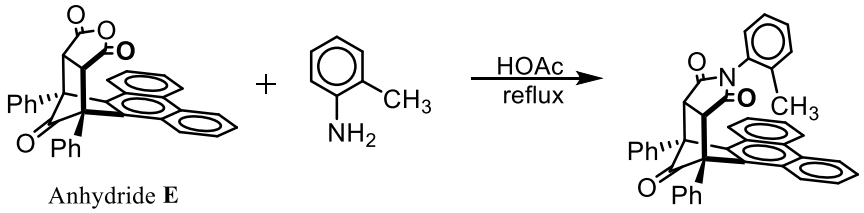

Anhydride **E**

(9R,9aR,12aS,13S)-9,13-diphenyl-11-(o-tolyl)-9,9a,12a,13-tetrahydro-10H-9,13-methanophenanthro[9,10-f]isoindole-10,12,14(11H)-trione.[i] (**22**) Anhydride **E**[ii] (200 mg, 0.42 mmol) and 2-methylaniline[iii] (50 mg, 0.46 mmol) were reacted using *Route II* to give **22** as an off-white solid (196 mg, 82 %). ^{1}H NMR (400 MHz, $CDCl_3$) δ 8.73 (d, *J* = 8.5 Hz, 2H syn), 8.67 (d, *J* = 7.6 Hz, *J* = 1.2 Hz, 2H anti), 8.38 (td, *J* = 7.6 Hz, *J* =1.2 Hz, 2H syn and anti), 7.72 (td, *J* = 7.6 Hz, *J* =1.2 Hz, 2H syn and anti), 7.63-6.86 (m, 17H syn and 16H anti), 6.74 (d, *J* = 7.4 Hz, 1H syn), 6.46 (t, *J* = 7.4 Hz, 1H anti), 4.65 (s, 2H syn), 4.64 (s, 2H anti), 4.35 (dd, *J* = 7.9 Hz, *J* = 1.3 Hz, 1H anti), 2.06 (s, 3H anti), -0.02 (s, 3H syn). The spectral data were in agreement with the literature reported.

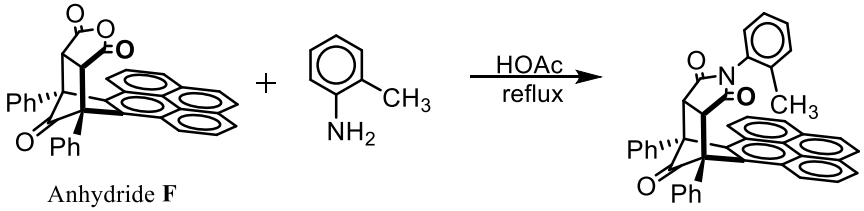

Anhydride **F**

(9R,9aR,12aS,13S)-9,13-diphenyl-11-(o-tolyl)-9,9a,12a,13-tetrahydro-10H-9,13-methano-pyreno[4,5-f]isoindole-10,12,14(11H)-trione.[i] (**23**) Anhydride **F**[ii] (200 mg, 0.40 mmol) and 2-methylaniline[iii] (50 mg, 0.46 mmol) were reacted using *Route I* to give **23** as an off-white solid (206 mg, 87 %). ^{1}H NMR (400 MHz, $CDCl_3$) δ 8.52-8.40 (m, 2H syn and anti), 8,14-8.05 (m, 2H syn and anti), 8.04 (s, 2H anti), 8.03 (s, 2H syn), 7.77 (td, *J* =

[i] Zhao, C.; Parrish, R. M.; Smith, M. D.; Pellechia, P. J.; Sherrill, C. D.; Shimizu, K. D. *J. Am. Chem. Soc.* **2012**, *134*, 14306.
[ii] Carroll, W. R.; Pellechia, P.; Shimizu, K. D. *Org. Lett.* **2008**, *10*, 3547.
[iii] Commercially available

7.6 Hz, *J* = 1.1 Hz, 2H syn and anti), 7.68-6.76 (m, 15H syn and 14H anti), 6.54 (d, *J* = 7.6 Hz, 1H syn), 6.06 (t, *J* = 7.6 Hz, 1H anti), 4.72 (s, 2H anti), 4.70 (s, 2H syn), 3.78 (dd, *J* = 7.9 Hz, *J* =1.2 Hz, 1H anti), 2.02 (s, 3H anti), -0.58 (s, 3H syn). The spectral data were in agreement with the literature reported.

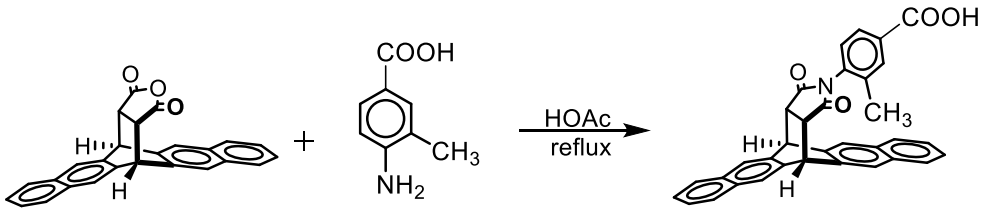

Anhydride **G**

4-((6R,13S,15R,19S)-16,18-dioxo-6,13-dihydro-6,13-[3,4]epipyrrolopentacen-17-yl)-3-methylbenzoic acid. (**24**) Anhydride **G**[i] (150 mg, 0.40 mmol) and 4-amino-3-methylbenzoic acid[ii] (66 mg, 0.44 mmol) were reacted using *Route I* to give **24** as an off-white solid (152 mg, 75 %) mp: 300 °C (dec) ^{1}H NMR (400 MHz, $CDCl_3$) δ 8.02-7.14 (m, 12H), 7.03 (d, *J* = 8.3 Hz, 1H syn), 5.15 (s, 2H, syn), 5.13 (s, 2H anti), 5.03 (d, *J* = 8.2 Hz, 1H anti), 3.68-3.53 (m, 2H syn and anti), 2.12 (s, 3H anti), 0.55 (s, 3H syn). ^{13}C NMR (100 MHz, $CDCl_3$) δ 175.82, 175.68, 169.69, 138.57, 138.12, 136.83, 136.25, 136.02, 135.69, 133.06, 132.83, 132.77, 132.71, 132.63, 130.01, 129.91, 128.68, 128.50, 128.34, 128.21, 127.92, 127.78, 127.60, 126.63, 126.49, 126.45, 124.44, 124.12, 123.21, 123.08, 47.47, 47.41, 45.88, 45.38, 17.84, 15.77. HRMS (EI) (m/z) calcd for $[C_{34}H_{23}NO_4]^+$ (M^+): 509.1622; found: 509.1627.

[i] Jia, Z. Y.; Li, S.; Nakajima, K.; Kanno, K.; Takahashi, T. *J. Org. Chem.* **2011**, *76*, 293.
[ii] Commercially available

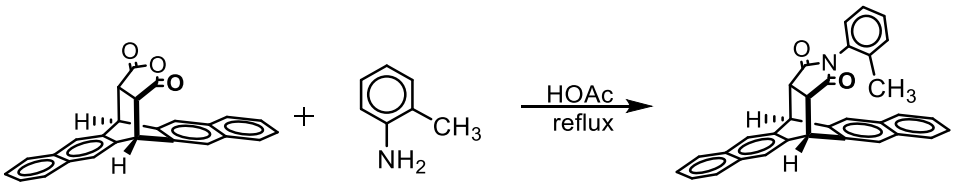

Anhydride **G**

(6R,13S,15R,19S)-17-(o-tolyl)-6,13-dihydro-6,13-[3,4]epipyrrolopentacene-16,18-dione. (**25**) Anhydride **G**[i] (150 mg, 0.40 mmol) and 2-methylaniline[ii] (47 mg, 0.44 mmol) were reacted using *Route I* to give **25** as an off-white solid (130 mg, 70 %). mp: 282 °C ^{1}H NMR (400 MHz, $CDCl_3$) δ 7.98-7.67 (m, 8H syn and anit), 7.55-7.39 (m, 4H syn and anti), 7.22-6.87 (m, 4H syn and 2H anti), 6.62 (t, *J* = 7.6 Hz, 1H anti), 5.16 (s, 2H syn), 5.13 (s, 2H anti), 4.97 (d, *J* = 7.7 Hz, 1H anti), 3.57 (s, 2H syn and anti), 2.06 (s, 3H anti), 0.49 (s, 3H syn). ^{13}C NMR (75 MHz, $CDCl_3$) δ 176.28, 175.99, 146.62, 144.28, 144.19, 135.49, 134.89, 132.26, 132.08, 132.01, 131.91, 124.27, 124.22, 124.12, 123.71, 53.01, 52.62, 47.06, 46.13, 45.71, 45.39, 19.42, 18.34. HRMS (EI) (m/z) calcd for $[C_{33}H_{23}NO_2]^+$ (M^+): 465.1729; found: 465.1731.

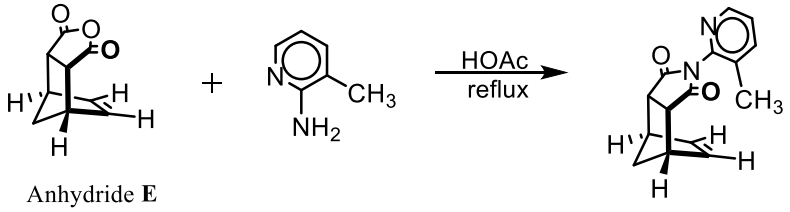

Anhydride **E**

(3aR,4S,7R,7aS)-2-(3-methylpyridin-2-yl)-3a,4,7,7a-tetrahydro-1H-4,7-methano-isoindole-1,3(2H)-dione.[iii] (**26**). Anhydride **E**[ii] (100 mg, 0.61 mmol) and 3-methylpyridin-2-amine[ii] (72 mg, 0.67 mmol) were reacted using *Route I*[iv] to give **26** as an off-white solid

[i] Jia, Z. Y.; Li, S.; Nakajima, K.; Kanno, K.; Takahashi, T. *J. Org. Chem.* **2011**, *76*, 293.
[ii] Commercially available
[iii]. Maier, J. M.; Li, P.; Hwang, J.; Smith, M. D.; Shimizu, K. D. *J. Am. Chem. Soc.* **2015**, *137*, 8014
[iv] The crude product was washed with saturated sodium bicarbonate solution before drying up under vacuum.

(108 mg, 70 %). ^{1}H NMR (400 MHz, CD_2Cl_2) δ 8.41-8.36 (m, 1H syn and anti), 7.68-7.63 (m, 1H syn and anti), 7.33-7.25 (m, 1H syn and anti), 6.33 (t, *J* = 1.8 Hz, 2H syn) 6.29 (t, *J* = 1.8 Hz, 2H anti), 3.53-3.44 (m, 4H syn and anti), 2.14 (s, 3H anti), 2.11 (s, 3H syn), 1.84-1.58 (m, 2H syn and anti). ^{13}C NMR (100 MHz, $CDCl_3$) δ 176.40, 176.16, 147.60, 147.55, 145.57, 145.48, 140.13, 139.80, 135.45, 134.66, 131.98, 131.56, 124.67, 124.62, 52.87, 52.44, 47.28, 46.26, 45.54, 45.21, 18.01, 17.27. Copies of ^{1}H and ^{13}C NMR spectra were provided. HRMS (EI) (m/z) calcd for ($C_{14}H_{14}N_2O_2$) (M^+): 254.1055; found: 254.1053.

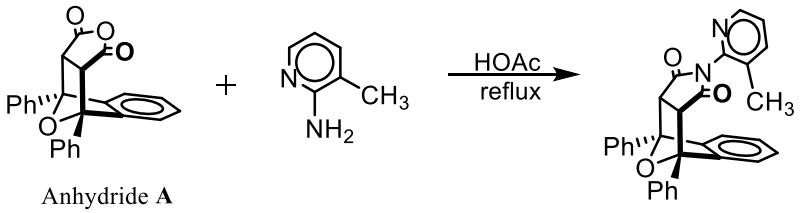

Anhydride **A**

(3a*R*,4*R*,9S,9aS)-2-(3-methylpyridin-2-yl)-4,9-diphenyl-3a,4,9,9a-tetrahydro-1*H*-4,9-epoxy-benzo[*f*]isoindole-1,3(2*H*)-dione.[i] (**27**). Anhydride **A**[ii] (100 mg, 0.27 mmol) and 3-methylpyridin-2-amine[iii] (32 mg, 0.30 mmol) were reacted using *Route II*[iv] to give **27** as an off-white solid (93 mg, 75 %). ^{1}H NMR (400 MHz, CD_2Cl_2) δ 8.42-7.97 (m, 5H syn and anit), 7.62-7.44 (m, 7H syn and anti), 7.33-6.97 (m, 5H syn and anti), 4.40 (s, 2H syn), 4.32 (s, 2H anti), 2.11 (s, 3H anti), 1.13 (s, 3H syn). ^{13}C NMR (100 MHz, CD_2Cl_2) δ 173.20, 147.74, 147.63, 145.71, 145.69, 144.36, 140.21, 139.98, 137.30, 137.21, 132.71, 131.98, 129.26, 129.15, 129.12, 128.95, 128.92, 127.73, 127.70, 125.26, 125.09, 121.69,

[i] Maier, J. M.; Li, P.; Hwang, J.; Smith, M. D.; Shimizu, K. D. *J. Am. Chem. Soc.* **2015**, *137*, 8014

[ii] Carroll, W. R.; Pellechia, P.; Shimizu, K. D. *Org. Lett.* **2008**, *10*, 3547

[iii] Commercially available

[iv] The crude product was washed with saturated sodium bicarbonate solution before drying up under vacuum.

121.20, 91.06, 90.70, 55.44, 55.31, 20.05, 17.43, 16.49. Copies of ^{1}H and ^{13}C NMR spectra were provided. HRMS (EI) (m/z) calcd for $[C_{30}H_{22}N_2O_3]^+$ (M^+): 458.1630; found: 458.1623

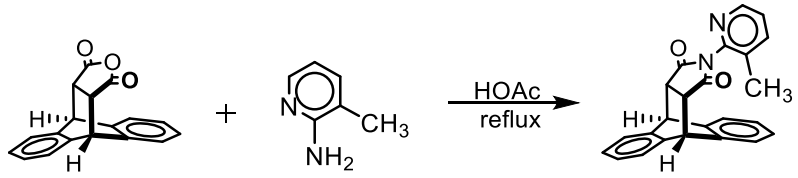

Anhydride **C**

(9R,10S,11R,15S)-13-(3-methylpyridin-2-yl)-9,10-dihydro-9,10-[3,4]epipyrrolo-anthracene-12,14-dione.[i] (**28**) Anhydride **C**[ii] (100 mg, 0.36 mmol) and 3-methylpyridin-2-amine[iii] (43 mg, 0.40 mmol) were reacted using *Route I*[iv] to give **28** as an off-white solid (101 mg, 77 %). ^{1}H NMR (400 MHz, $CDCl_3$) δ 8.38-8.32 (m, 1H syn), 8.22-8.17 (m, 1H anti), 7.55-6.99 (m, 10H syn and anti), 5.01-4.82 (m, 2H syn and anti), 3.50-3.41 (m, 2H syn and anti), 2.09 (s, 3H anti), 1.12 (s, 3H syn). ^{13}C NMR (100 MHz, $CDCl_3$) δ 175.50, 147.28, 145.05, 141.85, 139.97, 139.52, 132.33, 127.39, 126.89, 125.57, 124.82, 124.35, 47.61, 45.40, 15.67. Copies of ^{1}H and ^{13}C NMR spectra were provided. HRMS (EI) (m/z) calcd for $[C_{24}H_{18}N_2O_2]^+$ (M^+): 366.1368; found: 366.1368.

[i] Maier, J. M.; Li, P.; Hwang, J.; Smith, M. D.; Shimizu, K. D. *J. Am. Chem. Soc.* **2015**, *137*, 8014

[ii] Zhao, C.; Parrish, R. M.; Smith, M. D.; Pellechia, P. J.; Sherrill, C. D.; Shimizu, K. D. *J. Am. Chem. Soc.* **2012**, *134*, 14306.

[iii] Commercially available

[iv] The crude product was washed with saturated sodium bicarbonate solution before drying up under vacuum.

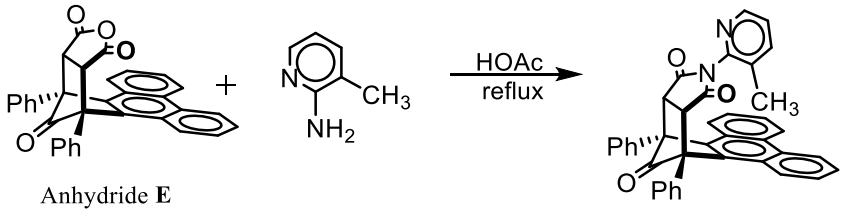

Anhydride **E**

(9R,9aR,12aS,13S)-11-(3-methylpyridin-2-yl)-9,13-diphenyl-9,9a,12a,13-tetrahydro-10H-9,13-methanophenanthro[9,10-f]isoindole-10,12,14(11H)-trione. (**29**). Anhydride **D** [i] (200 mg, 0.42 mmol) and 3-methylpyridin-2-amine[xxxi] (50 mg, 0.46 mmol) were reacted using *Route I*[ii] to give **29** as an off-white solid (196 mg, 84 %). mp: 298 °C (dec) *Only the syn conformer was observed in the NMR spectra.* ^{1}H NMR (400 MHz, $CDCl_3$) δ 8.67 (d, *J* = 8.5 Hz, 2H), 8.36 (d, *J* = 7.8 Hz, 2H), 8.28 (d, *J* = 3.7 Hz, 1H), 7.83-6.97 (m, 16H), 4.69 (s, 2H), 0.06 (s, 3H). ^{13}C NMR (100 MHz, $CDCl_3$) δ 196.12, 173.19, 133.96, 133.78, 131.76, 131.08, 129.61, 129.37, 128.72, 128.61, 127.35, 126.92, 126.61, 126.23, 124.84, 123.07, 63.70, 45.89, 14.54. . HRMS (m/z) calcd for $[C_{39}H_{26}N_2O_3]^+$ (M^+) 570.1943; found: 570.1946.

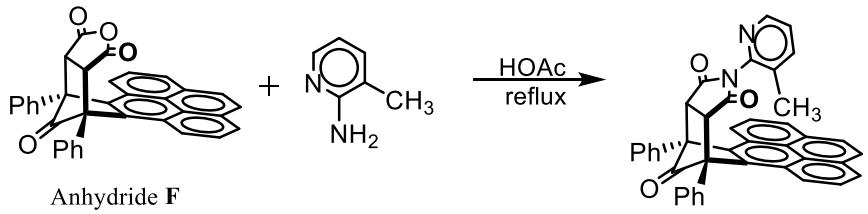

Anhydride **F**

(9R,9aR,12aS,13S)-11-(3-methylpyridin-2-yl)-9,13-diphenyl-9,9a,12a,13-tetrahydro-10H-9,13-methanopyreno[4,5-f]isoindole-10,12,14(11H)-trione. (**10**) Anhydride **F**[i] (200 mg, 0.40 mmol) and 3-methylpyridin-2-amine[ii] (49 mg, 0.45 mmol) were reacted using *Route I*[iii] to give **30** as an off-white solid (202 mg, 85 %). mp: 300 °C (dec) *Only the syn conformer was observed in the NMR spectra.* ^{1}H NMR (400 MHz, $CDCl_3$) δ 8.45

[i] Carroll, W. R.; Pellechia, P.; Shimizu, K. D. *Org. Lett.* **2008**, *10*, 3547

[ii] The crude product was washed with saturated sodium bicarbonate solution before drying up under vacuum.

(d, *J* = 7.9 Hz, 2H syn), 8.24 (dd, *J* = 4.7 Hz, *J* = 0.8 Hz, 1H syn), 8.08 (dd, *J* = 7.6 Hz, *J* = 0.8 Hz, 2H syn), 8.01 (s, 2H syn), 7.82-7.24 (m, 12H syn), 7.00 (dd, *J* = 7.6 Hz, *J* = 4.7 Hz, 1H syn), 6.95 (dd, *J* = 7.6 Hz, *J* = 0.8 Hz, 1H syn), 4.78 (s, 2H), -0.50 (s, 3H). ^{13}C NMR (100 MHz, $CDCl_3$) δ 196.60, 173.18, 134.83, 133.74, 131.50, 131.25, 129.67, 129.56, 128.75, 128.71, 127.67, 126.23, 126.17, 125.68, 125.63, 124.81, 123.73, 63.94, 46.08, 13.83. HRMS (m/z) calcd for $[C_{41}H_{26}N_2O_3]^+$ (M^+): 594.1943; found: 594.1955.

2.2 Characterization

^{1}H and ^{13}C NMR spectra for all newly reported compounds and crystal data (cif) of rotors **1**−**11**, **15**, **16**, **18**−**21**, **24**, **25**, **29**, **30** are available free of charge via Internet at http://pubs.acs.org/doi/abs/10.1021/acs.cgd.5b00906

3. Measurement of the Mole Fraction of *syn*-Conformer (χ_{syn}) In Solution.

Quantification of the *syn*- and *anti*-conformers in solution was carried out by comparing the integration of the corresponding peaks in ^{1}H NMR spectra.[i] The separate signals for the *ortho*-methyl protons of the rotor motif were used to measure the *syn*-*anti* conformational equilibrium. The *ortho*-methyl group in the *syn*-conformer is positioned close to the aromatic, and thus the singlet for the *syn*-conformer of the *ortho*-methyl group displays an upfield shift of 0.02~2.50 ppm in the ^{1}H NMR spectra in comparison to the singlet for the *anti*-conformer. For rotors with small alkene shelves, the chemical shift difference for the *ortho*-methyl group between *syn*- and *anti*- conformers was often too small to accurately integrate the ratio. In those cases, other protons on the *o*-tolyl rotor

[i] Zhao, C.; Parrish, R. M.; Smith, M. D.; Pellechia, P. J.; Sherrill, C. D.; Shimizu, K. D. *J. Am. Chem. Soc.* **2012**, *134*, 14306; Zhao, C.; Li, P.; Smith, M. D.; Pellechia, P. J.; Shimizu, K. D. *Org. Lett.* **2014**, *16*, 3520.

motif were used to measure the *syn-/anti-* ratios.[i] The mole fraction of *syn*-conformer (χ_{syn}) in solution was then calculated from the *syn/anti* ratio (Equation 4.1). The solution χ_{syn} values for the 30 rotors were measured in chloroform and four other common crystallization solvents (Table 4.3)

$$c_{syn} = \frac{[syn]}{[syn]+[anti]} \qquad \text{(Equation 4.1)}$$

Error Analysis for Solution χ_{syn}

The NMR samples in this work were prepared by dissolving ~10 mg of the purified molecular rotors in 0.7 mL of the deuterated solvent of choice, giving a total concentration of ~ 33 mM (assuming an average molecular weight of 440). NMR peak areas were measured using the MestRenova line-fitting function to reduce the error in integration. The error of quantitative NMR analysis was considered to be 1% for concentrations above 10 mM as appropriate line-fitting methods were adopted.[ii] Therefore, the error for χ_{syn} ($Error_{\chi syn}$) would reach the minimum at $\chi_{syn} = \frac{1}{1+\sqrt{2}} = 0.41$ (assuming the integration error proportionally relates to the isomer concentration) and was estimated to be 1.7% (Equation 4.2) as both conformers had a concentration above 10 mM.

$$\begin{aligned} Error_{\chi_{syn}} &= \sqrt{Error_{[syn]}^2 + Error_{([syn]+[anti])}^2} \\ &= \sqrt{Error_{[syn]}^2 + Error_{[syn]}^2 + Error_{[anti]}^2} \\ &= \sqrt{2 * Error_{[syn]}^2 + Error_{[anti]}^2} \end{aligned} \qquad \text{(Equation 4.2)}$$

[i] Zhao, C.; Parrish, R. M.; Smith, M. D.; Pellechia, P. J.; Sherrill, C. D.; Shimizu, K. D. *J. Am. Chem. Soc.* **2012**, *134*, 14306; Zhao, C.; Li, P.; Smith, M. D.; Pellechia, P. J.; Shimizu, K. D. *Org. Lett.* **2014**, *16*, 3520.

[ii] See references in: Rizzo, V.; Pinciroli, V. *J. Pharmaceut. Biomed.* **2005**, *38*, 851.

However the integration error in χ_{syn} values near the extreme values (χ_{syn} = 0 or 1) is larger due to the lower concentration and larger error of the minor conformer. Precise measurements of error at different concentrations were not performed. However, Rizzo *et al*. found that,[i] "*In our experience with 400–500 MHz instruments and non-refrigerated* ^{1}*H-probes, qNMR* (quantitative NMR) *may be applied to solutions with concentration as low as 1 mM if a precision of 5% is acceptable*" We, thus, set our detection limit conservatively at 1 mM in order to keep error in integration no higher than 5%. The measurable limit for χ_{syn} were estimated to be 0.03 to 0.97 based the smaller peak being 5% of the larger peak. $Error_{\chi syn}$ at these χ_{syn} limits was estimated to be 7.1% (χ_{syn} = 0.03) and 5.2% (χ_{syn} = 0.97).

[i] Rizzo, V.; Pinciroli, V. *J. Pharmaceut. Biomed.* **2005**, *38*, 851.

CHAPTER 5

SOLVENT-INDUCED REVERSIBLE SOLID-STATE COLOR CHANGE OF AN INTRAMOLECULAR CHARGE-TRANSFER COMPLEX[i]

[i] Reproduced with permission from: Li, P.; Maier, J. M.; Hwang, J.; Smith, M. D.; Krause, J. A.; Mullis, B. T.; Strickland, S. M. S.; Shimizu, K. D. *Chem. Comm.* **2015**, *51*, 14809. Copyright 2015 Royal Society of Chemistry.

1. Introduction

Aromatic CT complexes[1] have found applications in host-guest complexes,[2,3] supramolecular assemblies,[4-6] self-healing,[7-9] and responsive materials,[10-12] and organic electronics.[13,14] Interestingly, aromatic CT interactions have not been as widely utilized in sensing applications, which is probably due to their low extinction coefficients and/or low association constants.[15-17] However, CT interactions have a number of unique characteristics that are advantageous for sensing, molecular switches, and dynamic supramolecular systems. First, CT complexes typically absorb in the visible region of the UV-vis spectrum, and thus CT sensors can be monitored by the naked-eye. Second, the colors of CT complexes are highly sensitive to the electronic properties of the donor and acceptor units[18] and to the relative geometry of the donor and acceptor units.[19-21] Thus, binding effects that induce changes in the CT complex geometry can be easily monitored by variations in their colours.[15-17,22,23]

The goal of this study was to develop a responsive colorimetric system based on an intramolecular CT interaction. Unlike the majority of CT sensors,[24] CT molecule **1** contains both the donor and acceptor units. The two pyrene (PYR) donor units are linked to a central 1,4,5,8-naphthalenedimide (NDI) acceptor unit (Figure 5.1a) forming a sandwich-type 2:1 aromatic stacking complex. Thus, the guest .molecule does not need to contain a donor or acceptor unit, which greatly expands the number of potential guests and the general utility of this design. The sensing mechanism is the guest-induced changes in geometry of the intramolecular CT interaction, which could be monitored by changes in color of the CT complex.

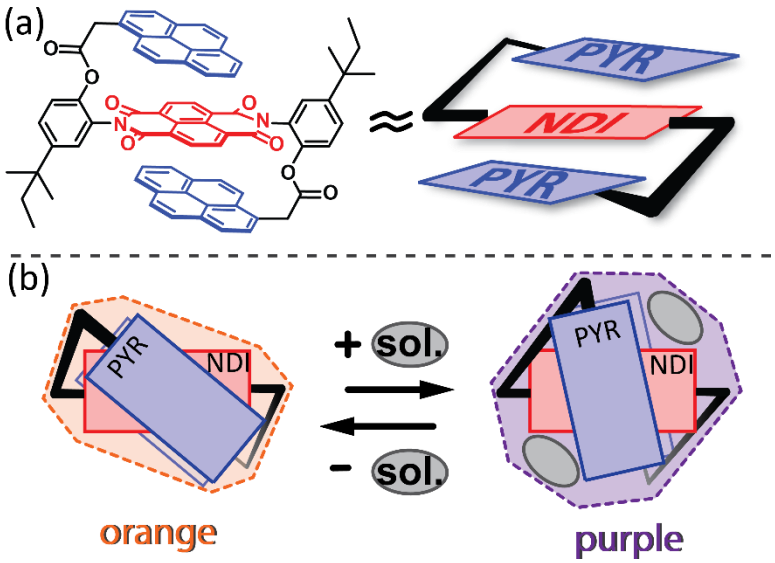

Figure 5.1 (a) Molecular CT platform **1** highlighting the intramolecular donor-acceptor-donor sandwich complex; and **(b)** a schematic representation of the solvation-desolvation induced complexation change in color and geometry in **1**

2. Results and Discussion

The CT molecule **1** was readily prepared in three steps from commercially available 1-pyreneacetic acid, 2-amino-4-tert-amylphenol, and 1,4,5,8-naphthalenedianhydride (Scheme 5.1).[i] The two PYR donor units were connected to the central NDI acceptor unit via two short but flexible linkers, which ensured the formation of the intramolecular aromatic stacking complex but also allowed sufficient conformational freedom to allow the donor and acceptor units to adopt different geometries. The 5-atom linker (-C=C-O-C-C) was designed based on a similar 5-atom linker that was previously used to form a similar sandwich aromatic stacking complex around a NDI core.[25] Since **1** did not contain recognition groups that form strong directional interactions, the guest-induced colorimetric properties of **1** were initially studied in the solid-state where the confined condensed-phase

[i] For synthesis details see Supporting Information..

environment could allow guest molecules to sterically influence the relative geometry of the donor and acceptor units. Thus, the 2:1 PYR to NDI stoichiometry of the sandwich complex[25,26] was important to ensure that both surfaces of the NDI would be occupied and could not form additional interactions with adjacent molecules of **1**.[i]

Scheme 5.1 Synthesis of the molecular CT model **1** and control **2**.

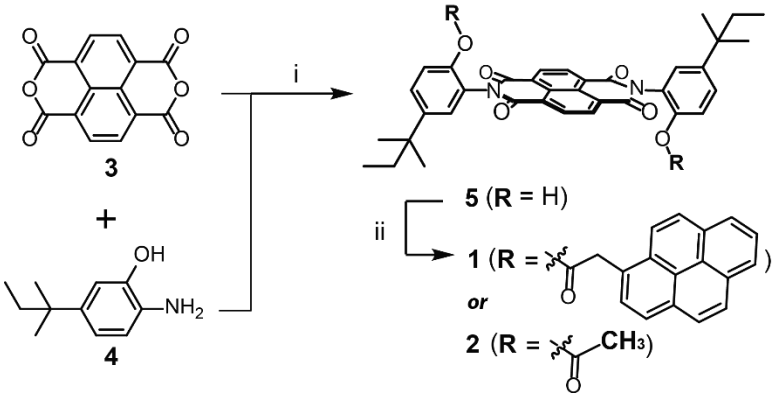

The ability of **1** to form an intramolecular CT complex was first confirmed in solution by the observation of the distinctive CT band in the visible region of the absorption spectrum. The λ_{max} at 505 nm was consistent with previous reports of PYR-NDI CT complexes.[3,6,9,11,27-29] The effectiveness of the linker in forming and maintaining the intramolecular PYR-NDI complexation was also demonstrated by comparison with an intermolecular PYR-NDI complex formed between pyrene and control **2**, a structural analogue containing the same symmetrically substituted NDI core but lacking of the two pyrene donor groups. The intermolecular **2**•pyrene complex displayed a similar CT band (λ_{max} at 510 nm) but only at higher concentrations (> 10 mM).

[i] CT molecule **1** appears to be locked in the *anti*-conformation due to restricted rotation with the PYR groups on opposite sides of the NDI surface (See Ref. 25). The rotational barrier for these *N*-arylimide rotor was previously measured to be 27 kcal/mol (Ref. 26), which is too high for isomerization to the *syn*-conformer at the room temperature. Furthermore, heating *anti*-**1** in solution and the solid-state at the elevated temperature (80 °C) for 24 h showed no indications of the *syn*-conformer when monitored by ^{1}H NMR.

Next, the observation of different colored solid samples of **1** upon treatment with different solvents provided the first indications that the geometry and color of the intramolecular CT complex in **1** were sensitive to solvent inclusion. When **1** was precipitated from dichloromethane, a purple solid was obtained, which was similar to the color of **1** in solution. However, when **1** was precipitated from acetone, a distinctly different orange colored solid was obtained. The purple and orange solids of **1** were further characterized by diffuse reflectance UV-vis spectroscopy (Figure 5.2). The purple solid of **1** showed a well-resolved CT absorption band with a λ_{max} at 530 nm. In comparison, the orange solid of **1** showed a similar but blue-shifted CT band with a λ_{max} at 500 nm. By comparison, control **2**, which only contained an NDI unit showed no CT band in the visible region of the diffuse reflectance UV-vis spectrum.

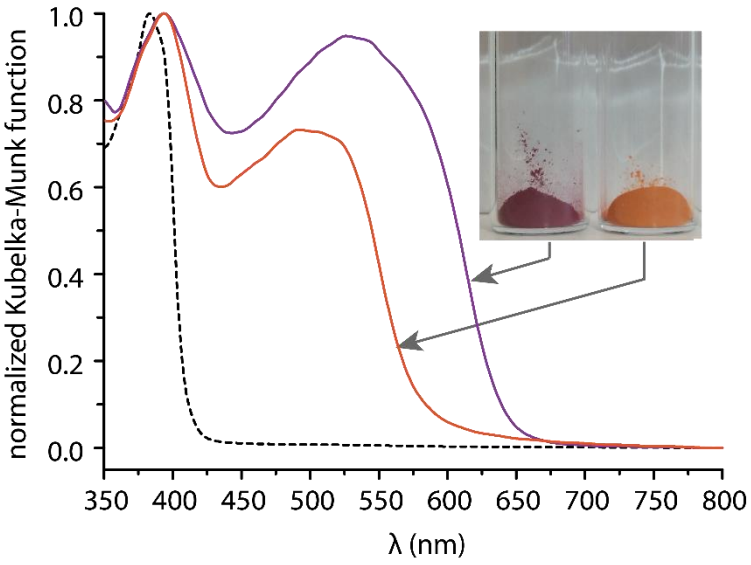

Figure 5.2 Normalized diffuse reflectance UV-vis spectra of the purple CH_2Cl_2-solvate solid of **1** (purple line), the orange non-solvate solid of **1** (orange line), and the white solid of control **2** (dotted black line).

^{1}H NMR and HRMS analysis confirmed that both the purple and orange solids contained pure samples of **1**. The only differences were that the purple solid was a solvate

of **1** containing two equivalents of dichloromethane; whereas, the orange solid was a non-solvate of **1**. Thermogravimetric analysis (TGA) of the purple solid further confirmed the presence of two CH_2Cl_2 molecules. A clear weight loss of 13%was observed when the purple solid was heated to 180 °C, which was consistent with the loss of two equivalents of CH_2Cl_2. After heating in the TGA, the purple solid became red-orange.[i] In contrast, the orange solid showed no observable weight loss on heating in the TGA to 200 °C. Interestingly, the purple CH_2Cl_2-solvate of **1** was stable as the stoichiometry and coloration did not change after a month at room temperature as monitored by ^{1}H NMR and UV-vis spectrometry.

The purple and orange solids of **1** could be easily and repeatedly interconverted by precipitation from the appropriate solvent. First, the purple CH_2Cl_2-solvate could be readily regenerated from the orange non-solvate by precipitation from dichloromethane (Figure 5.3a). Conversely, the orange non-solvate solid of **1** could be regenerated from purple **1** by precipitation from acetone. Acetone is a poor solvent for **1** and efficiently extracts any included solvent from solid samples of **1**. The ease with which **1** can uptake or lose included solvent molecules was demonstrated by simply wetting samples of **1** with a minimum amount of the CH_2Cl_2 or acetone, which yielded the corresponding color change for the CH_2Cl_2 solvate or non-solvate forms, respectively (Figure 5.9 in SI).[ii]

[i] The post-TGA sample of the purple solvate was a low crystalline solid form and displayed a red coloration (Figure 5.8 in SI).

[ii] Exposing the purple and orange solid samples of **1** to solvent vapors for 5 h showed no noticeable color change.

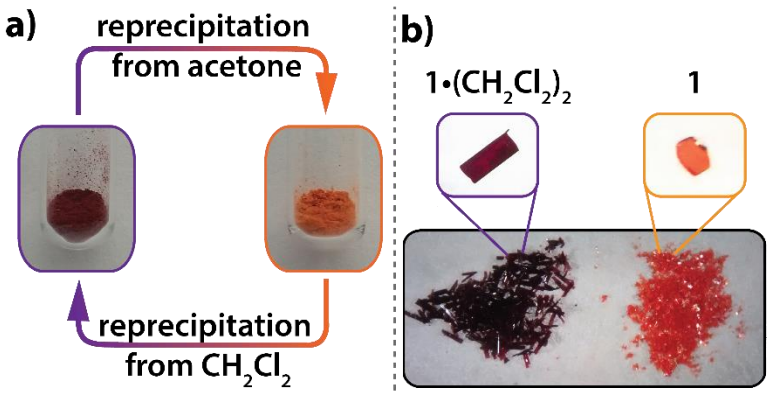

Figure 5.3 (a) The reversible color switching of solid **1** between purple CH_2Cl_2-solvate and orange non-solvate solid forms by precipitation from dichloromethane and acetone, respectively. **(b)** The CH_2Cl_2-solvate (left) and non-solvate (right) crystals of **1**, highlighting the distinct difference in color.

To test the hypothesis that the different colored solid forms of **1** were due to variations in the orientation of the PYR donor and NDI acceptor units in the intramolecular CT complex, X-ray quality single crystals of **1** from CH_2Cl_2 and acetone were obtained and analyzed by X-ray crystallography (Figure 5.3b). Dark purple plate crystals were obtained from CH_2Cl_2 containing two equivalents of CH_2Cl_2 per **1** molecule. Conversely, orange thin plate crystals were obtained from acetone, which do not contain any trapped solvent molecules.[i] The colors of the crystals formed from each solvent were similar to the purple and orange solids formed in the earlier precipitation studies in the same two solvents. This suggested that the single crystals were the same structural forms as the colored precipitated solids, which was confirmed in the matching XRD patterns for the precipitated solids with the simulated XRD patterns from the X-ray crystal structures (Figure 5.10 in SI).

[i] The similarity in color between single crystals and precipitates were further confirmed quantitatively by diffuse reflectance UV-vis spectroscopy of the single crystals (Figure 5.9 in SI).

Despite the differences in color and solvation, the structures of the sandwich CT complexes in the purple and orange crystals of **1** were surprisingly similar (Figure 5.4). The folded conformations of **1** in both structures adopted the desired sandwich complex with the PYR donor units forming centrosymmetric aromatic stacking interactions on both faces of the central NDI unit (Figure 5.4). The PYR-center to NDI-plane distances (3.5 and 3.6 Å) for the solvate and non-solvate structures were very similar and were consistent with an intramolecular aromatic stacking interaction.

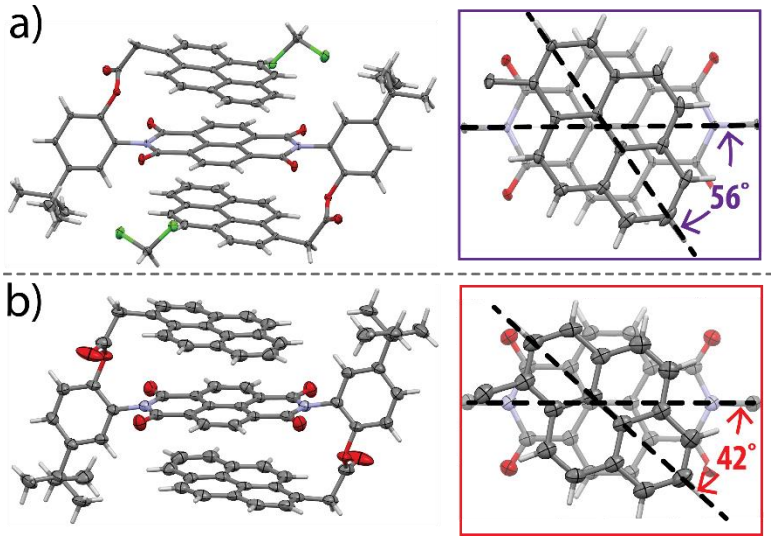

Figure 5.4 Side views of the X-ray structures of **(a)** the dark purple **1**•$(CH_2Cl_2)_2$ and **(b)** the orange non-solvate **1** crystals. Insets are top views of the PYR and NDI surfaces (with linkers, frameworks, and bottom PYR surface omitted for viewing clarity). The pyrene surfaces in both crystals were disordered and only the major conformers (76% and 72%) are shown.

To help identify the geometric variations that lead to the dramatic differences in color of the solids, additional four crystal structures of **1** containing different solvent molecules (CH_2Cl_2/CH_3CN, CH_3NO_2, $EtNO_2$, and dioxane) were obtained and analyzed. In each case, the solvate structure displayed a similar centrosymmetric aromatic stacking complex in **1** with two included solvent molecules. These solvate crystals were all purple

or purple-red in contrast with the orange color of non-solvate crystal of **1**. This confirmed that the solvent molecules themselves were not participating directly in the CT complex as the solvents varied widely in their atomic and electronic structures and yet all of the solvates of **1** had a similar purple color. The only consistent difference between the solvate and non-solvate was in the orientation of the PYR and NDI surfaces as defined by the dihedral angle (**θ**) between the long axes of the two surfaces (Figure 5.4).[i] The purple solvate crystals consistently had **θ** angles greater than 50° (57°, 53°, 64-66°,[ii] and 52°) and the orange non-solvate had **θ** values less than 50° (33 and 42°).[iii] This same structural parameter (**θ**) has recently been identified by a recent computational study by Lin to help explain the orientations of PYR and NDI units in previous reported CT crystal structures.[30]

The computational study by Lin predicted that **θ** angles from 50° to 75° would be the most thermodynamically stable for aromatic stacked PYR and NDI surfaces due to more favorable attractive electrostatic interactions.[30] This prediction is consistent with the observed geometries of the crystal structures of the **1** solvates. In the presence of included solvent, the PYR and NDI units of 1 have sufficient room and freedom to adopt the more stable stacking geometries (**θ** > 50°). The solvent molecules are able to fill the voids created by the more perpendicular X-shaped arrangement of the PYR and NDI units (Fig 5.1b). In contrast, in the absence of included solvent molecules, the PYR and NDI units adopt a more compact and aligned geometry (**θ** < 50°) to avoid forming voids. Thus the

[i] The distances between the PYR and NDI units were also examined (See Table 5.1 in SI) but no correlation of these distances with the color of the crystals was observed.

[ii] Two crystallographically independent molecules were observed in the **1**•$(EtNO_2)_2$ crystal structure.

[iii] The two **θ** angles are both for the same orange non-solvate crystal of **1**. The pyrene arms are disordered with two distinct populations leading to two separate **θ** angles.

packing forces in the non-solvate structure prevent the PYR and NDI units from adopting the more stable X-shaped geometry.

3. Conclusion

In conclusion, we have developed an intramolecular CT molecule **1** which can reversibly change color from purple to orange in the presence and absence of solvent in the solid-state. The color switching abilities were attributed to solvent-induced changes in the intramolecular stacking geometry. The presence of solvent in the crystalline matrix allows the PYR and NDI units to form the more stable purple CT complex. In the absence of included solvent molecules, the PYR and NDI units are forced into a less stable orange CT complex. What is striking from the comparison of the crystal structures of **1** is how sensitive the CT band is to these subtle variations in the PYR-NDI dihedral angles. Small variations in **θ** angles (~10°) are readily observable by the naked-eye from the different colors of the resulting solids. Rathore and Kochi have previously shown that the intensity of the CT band and transition energies are highly sensitive to very small differences in the distances between aromatic donor and acceptor units.[21] However, we have not come across a similar example demonstrating the sensitivity of the CT band to the orientations (angles) of the aromatic donor and acceptor units. This sensitivity could form the basis for a new type of intramolecular CT sensor, which can be read out by the naked-eye or inexpensive visible spectrometers. Further studies on the impact of the donor-acceptor orientation on the CT transition energy are currently underway in our laboratories.

Reference

[1]. Briegleb, G. *Elektronen-Donator-Acceptor-Complexes*. Springer-Verlag, Berlin and New York, 1961.

[2]. Zhu, Z. X.; Cardin, C. J.; Gan, Y.; Colquhoun, H. M. *Nat. Chem.* **2010**, *2*, 653.

[3]. Colquhoun, H. M.; Williams, D. J.; Zhu, Z. *J. Am. Chem. Soc.* **2002**, *124*, 13346.

[4]. Kumar, M.; Rao, K. V.; George, S. J. *Phys. Chem. Chem. Phys.* **2014**, *16*, 1300.

[5]. Das, A.; Ghosh, S. *Angew. Chem., Int. Ed.* **2014**, *53*, 2038.

[6]. Jalani, K.; Kumar, M.; George, S. J. *Chem. Comm.* **2013**, *49*, 5174.

[7]. Burattini, S.; Greenland, B. W.; Merino, D. H.; Weng, W. G.; Seppala, J.; Colquhoun, H. M.; Hayes, W.; Mackay, M. E.; Hamley, I. W.; Rowan, S. J. *J. Am. Chem. Soc.* **2010**, *132*, 12051.

[8]. Fox, J.; Wie, J. J.; Greenland, B. W.; Burattini, S.; Hayes, W.; Colquhoun, H. M.; Mackay, M. E.; Rowan, S. J. *J. Am. Chem. Soc.* **2012**, *134*, 5362.

[9]. Burattini, S.; Colquhoun, H. M.; Fox, J. D.; Friedmann, D.; Greenland, B. W.; Harris, P. J. F.; Hayes, W.; Mackay, M. E.; Rowan, S. J. *Chem. Comm.* **2009**, 6717.

[10]. Haino, T.; Watanabe, A.; Hirao, T.; Ikeda, T. *Angew. Chem., Int. Ed.* **2012**, *51*, 1473.

[11]. (a) Das, A.; Ghosh, S. *Angew. Chem., Int. Ed.* **2014**, *53*, 1092; (b) Das, A.; Ghosh, S. *Chem. Comm.* **2014**, *50*, 11657.

[12]. Tian, Y. K.; Shi, Y. G.; Yang, Z. S.; Wang, F. *Angew. Chem., Int. Ed.* **2014**, *53*, 6090.

[13]. Tayi, A. S.; Shveyd, A. K.; Sue, A. C. H.; Szarko, J. M.; Rolczynski, B. S.; Cao, D.; Kennedy, T. J.; Sarjeant, A. A.; Stern, C. L.; Paxton, W. F.; Wu, W.; Dey, S. K.; Fahrenbach, A. C.; Guest, J. R.; Mohseni, H.; Chen, L. X.; Wang, K. L.; Stoddart, J. F.; Stupp, S. I. *Nature* **2012**, *488*, 485.

[14]. Sagade, A. A.; Rao, K. V.; Mogera, U.; George, S. J.; Datta, A.; Kulkarni, G. U. *Adv. Mater.* **2013**, *25*, 559.

[15]. Mukhopadhyay, P.; Iwashita, Y.; Shirakawa, M.; Kawano, S.; Fujita, N.; Shinkai, S. *Angew. Chem., Int. Ed.* **2006**, *45*, 1592.

[16]. Rasberry, R. D.; Smith, M. D.; Shimizu, K. D.; *Org. Lett.* **2008**, *10*, 2889.

[17]. Trivedi, D. R.; Fujiki, Y.; Goto, Y.; Fujita, N.; Shinkai, S.; Sada, K. *Chem. Lett.* **2008**, *37*, 550.

[18]. Mulliken, R. S.; Person, W. B.; *Annu. Rev. Phys. Chem.* **1962**, *13*, 107.

[19]. (a) Staab, H. A.; Herz, C. P.; Krieger, C.; Rentea, M. *Chem. Ber.* **1983**, *116*, 3813; (b) Staab, H. A.; Knaus, G. H.; Henke, H. E.; Krieger, C. *Chem. Ber.* **1983**, *116*, 2785; (c) Reimann, R.; Staab, H. A. *Angew. Chem., Int. Ed. Engl.* **1978**, *17*, 374; (d) Staab, H. A.; Reimannhaas, R.; Ulrich, P.; Krieger, C. *Chem. Ber.* **1983**, *116*, 2808.; (e) Staab, H. A.; Gabel, G.; Krieger, C. *Chem. Ber.* **1983**, *116*, 2827.

[20]. Schroff, L. G.; Zsom, R. L. J.; Vanderweerdt, A. J. A.; Schrier, P. I.; Geerts, J. P.; Nibbering, N. M. M.; Verhoeven, J. W.; Deboer, T. J. *Recl. Trav. Chim. Pays-Bas*, **1976**, *95*, 89.

[21]. Rathore, R.; Lindeman, S. V.; Kochi, J. K. *J. Am. Chem. Soc.* **1997**, *119*, 9393.

[22]. Leight, K. R.; Esarey, B. E.; Murray, A. E.; Reczek, J. J.; *Chem. Mater.* **2012**, *24*, 3318.
[23]. (a) B. K. Kaletas, R. Dobrawa, A. Sautter, F. Wurthner, M. Zimine, L. De Cola, R. M. Williams, *J. Phys. Chem. A* **2004**, *108*, 1900.; (b) N. Van Anh, F. Schlosser, M. M. Groeneveld, I. H. M.; van Stokkum, F. Wurthner, R. M. Williams, *J. Phys, Chem. C* **2009**, *113*, 18358.
[24]. B. Wang, E. V. Anslyn, *Chemosensors principles, strategies, and applications*. In Wiley Series in Drug Discovery and Development; John Wiley & Sons: Hoboken, N.J., 2011
[25]. Y. S. Chong, W. R. Carroll, W. G. Burns, M. D. Smith, K. D. Shimizu, *Chem.–Eur. J.* **2009**, *15*, 9117.
[26]. R. D. Rasberry, K. D. Shimizu, *Org. Biomol. Chem.* **2009**, *7*, 3899.
[27]. Q. Jiang, H. Y. Zhang, M. Han, Z. J. Ding, Y. Liu, *Org. Lett.* **2010**, *12*, 1728.
[28]. H. A. Staab, D. Q. Zhang, C. Krieger, *Liebigs Ann-Recl.* **1997**, 1551.
[29]. M. R. Molla, S. Ghosh, *Chem.–Eur. J.* **2012**, *18*, 9860.
[30]. M. Y. Yeh, H. C. Lin, *Phys. Chem. Chem. Phys.* **2014**, *16*, 24216.

Supporting Information

1. Additional Figures and Tables

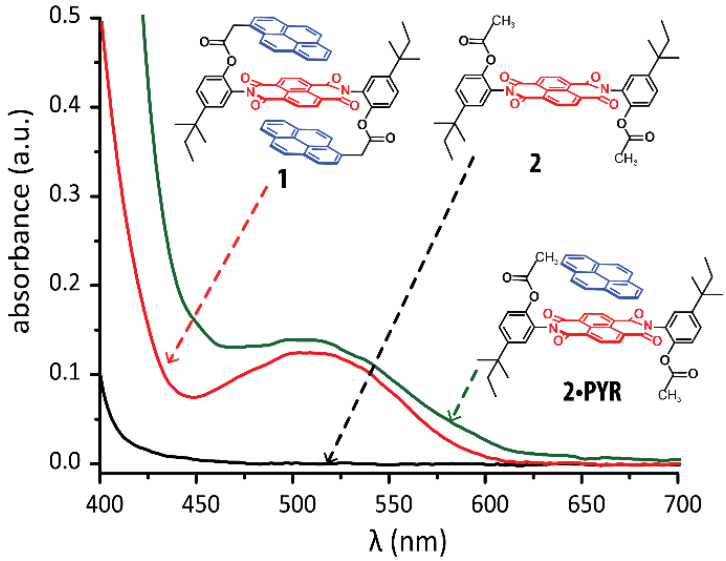

Figure 5.5 UV-vis spectra of molecular CT model **1** (red trace) and control **2** (black trace) at 0.25 mM in chloroform and the intermolecular **2**•PYR complex (green trace) at 6.55 mM in chloroform.

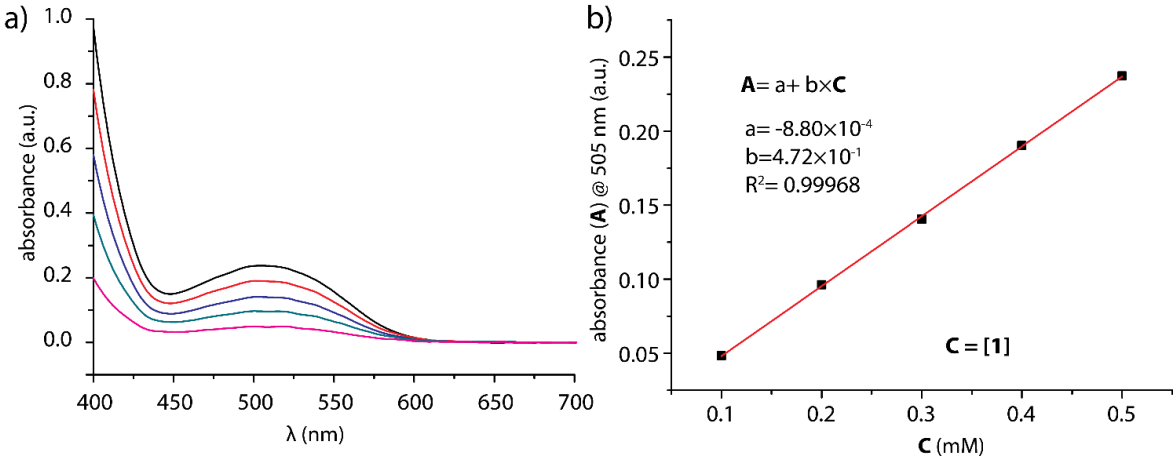

Figure 5.6 Partial UV/vis spectra of **1** in chloroform from 0.1 to 0.5 mM highlighting the charge-transfer absorption band (left), and the linear fitting of absorption (**A**) at λ_{max} = 505 nm against the concentration of **1** (right).

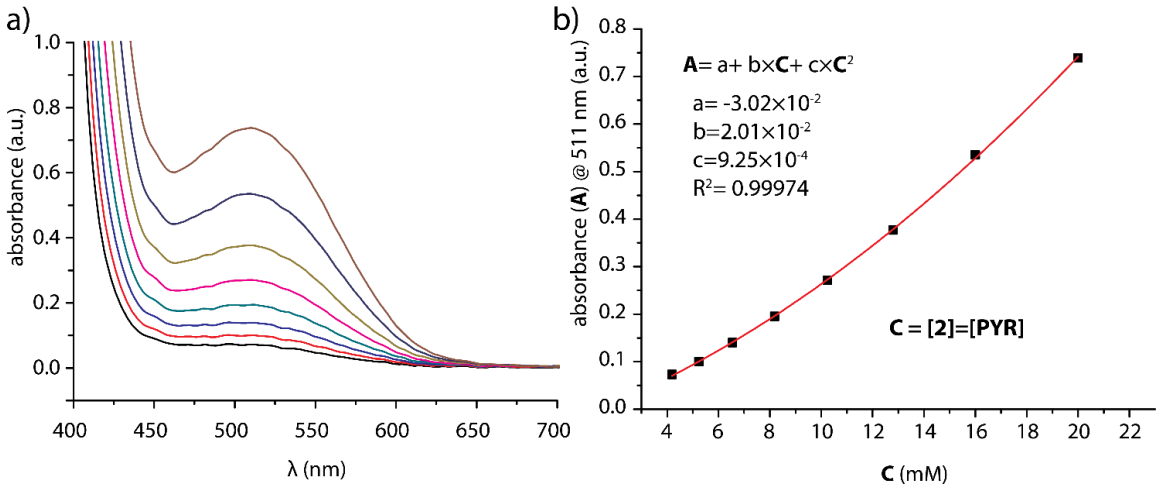

Figure 5.7 Partial UV/vis spectra of **2**·PYR in chloroform from 4.2 to 20 mM highlighting the charge-transfer absorption band (left), and the polynomial fitting of absorption (A) at λ_{max} = 511 nm against the concentration of **[2]** (right).

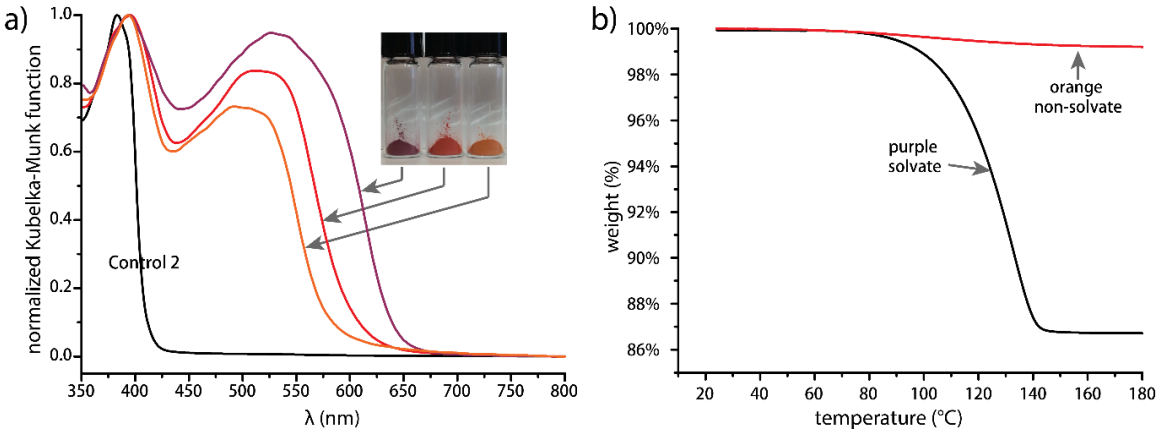

Figure 5.8 (a) Normalized solid-state diffuse reflectance UV-vis spectra for purple and red solid of **1** (inlet) and white solid of control **2**; (b) TGA traces of the purple (black) and orange (red) powders of **1**.

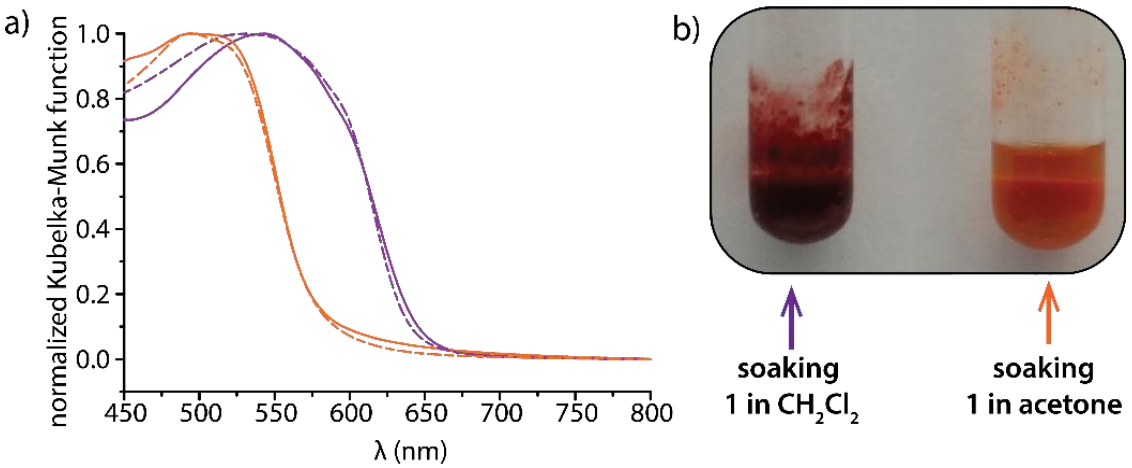

Figure 5.9 (a) Solid-state diffuse reflectance UV-vis spectra of purple and orange solids (colored solid traces) and dichloromethane-solvate and non-solvate crystals (colored dashed traces) of **1**, highlighting the similarity in color between the solid and crystal samples. (b) Soaking **1** in a minimum amount of dichloromethane and acetone, highlighting the sensitivity of color change.

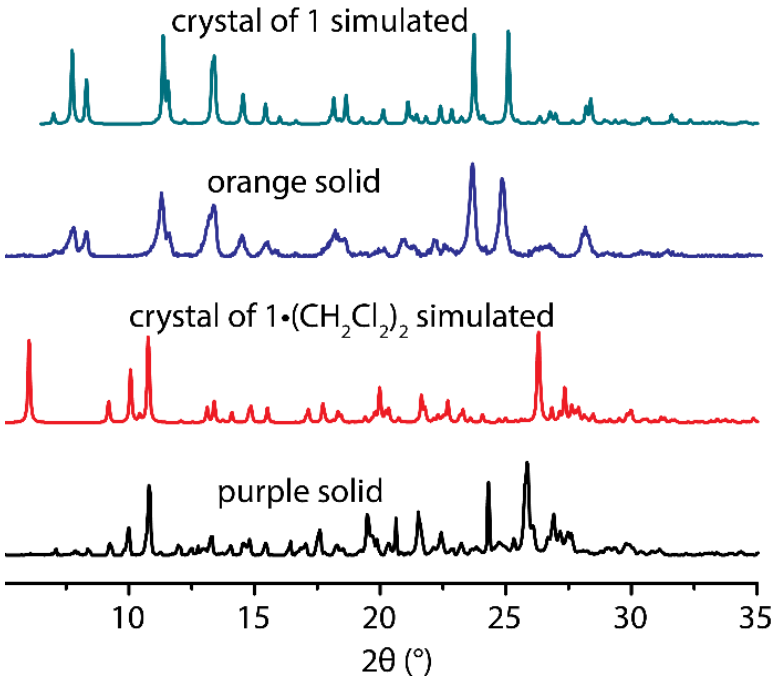

Figure 5.10 Powder X-ray diffraction data for the orange and purple solids of **1** together with the simulated powder patterns from the crystal structures **1** and **1**•$(CH_2Cl_2)_2$.

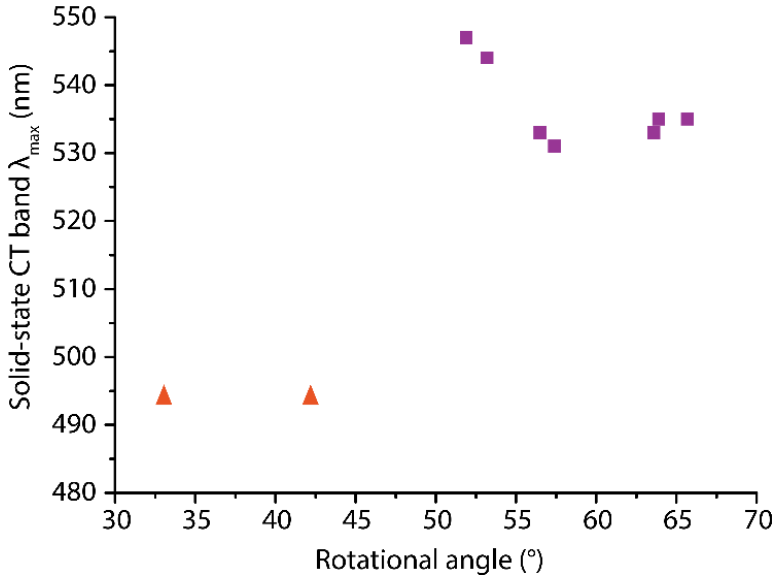

Figure 5.11 Scatter plot of the CT band λ_{max} against the rotational angle (**θ**) between PYR and NDI units of the intramolecular CT complexes in the six crystal structures of **1**, highlighting the **θ** angle difference between the solvate (■) and non-solvate structures (▲).

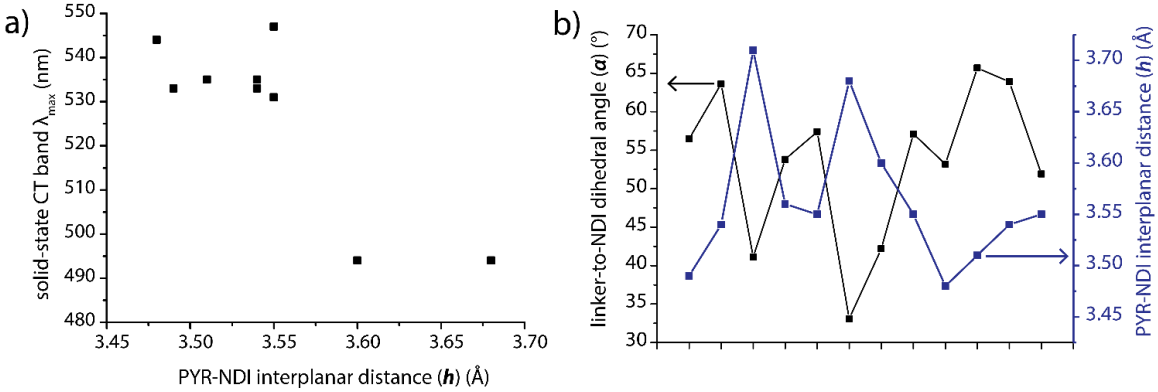

Figure 5.12 (a) Scatter plot of the CT band λ_{max} against the PYR-NDI interplanar distance (**h**) of the intramolecular CT complexes in the six crystal structures of **1**, highlighting their insignificant correlation due to the small difference in **h** (~0.05 Å) between the solvate and non-solvate structures. (b) Double-Y plot of the linker-to-NDI dihedral angle (**α**) and PYR-NDI interplanar distance (**h**) of the intramolecular CT complexes in the six crystal structures, highlighting that variations in the PYR-NDI interplanar distance were tightly related to the linker rotation. All observed conformations were included. Definitions of geometric parameters **α** and **h** are illustrated in Figure 5.13

2. Synthesis and Characterization

Bisphenol **5** was obtained as previous reported;[i] thermal condensation of 1,4,5,8-naphthalenetetracarboxylic dianhydride (**3**) and 2-amino-4-*tert*-amylphenol (**4**). The esterification of 1-pyreneacetic acid and bisphenol **5** using 1-ethyl-3-(3-dimethylaminopropyl)carbodiimide (EDCI) and *N, N*-dimethylaminopyridine (DMAP) in acetonitrile at room temperature gave the crude product **1** that consisted of both *anti* and *syn* conformers. The crude **1** was then thermally equilibrated at 80 ºC for 10 h in 1,1,2,2-tetrachloroethane (TCE) and precipitated in CH_2Cl_2/acetonitrile giving the pure *anti* conformer of **1** as purple color powder. Control **2** was obtained similarly from bisphenol **5** and acetic acid as a white powder. Thermal equilibration of **2** gave a mixture of approximately 1:1 *anti*- and *syn*- conformers. Molecular models **1** and control **2** are newly reported compounds, and their ^1H and ^{13}C spectra are provided.[ii]

(1,3,6,8-tetraoxo-1,3,6,8-tetrahydrobenzo[lmn][3,8]phenanthroline-2,7-diyl)bis-(4-(tert-pentyl)-2,1-phenylene) bis(2-(pyren-1-yl)acetate). (**1**) Bisphenol **5** (100 mg, 0.17 mmol) was dissolved in 5 mL of dried acetonitrile. To the above solution, 1-pyreneacetic acid (130 mg, 0.51 mmol), DMAP (10 mg, 0.09 mmol) and EDCI (80 mg, 0.51 mmol) were added. The reaction mixture was stirred at room temperature for 12 h, and the solvent was then removed under vacuum. The residue was dissolved in dichloromethane (40 mL), washed with water (2×40 mL), sodium carbonate solution (2×40 mL), and brine (40 mL), and dried with $MgSO_4$. The solvent was removed in vacuum, and solid residue was

[i] Chong, Y. S.; Carroll, W. R.; Burns, W. G.; Smith, M. D.; Shimizu, K. D. *Chem.-Eur. J.* **2009**, *15*, 9117.

[ii] Available free of charge via Internet at http://pubs.rsc.org/en/Content/ArticleLanding/2015/CC/c5cc06140g

suspended in acetone. The orange insoluble was collected by filtration as crude **1** (130 mg, 71 %). Crude **1** was dissolved in TCE (5 mL) and heated at 80 °C under N_2 for 10 h to equilibrate. The solvent was removed under vacuum giving a purple solid residue, which upon recrystallization in CH_2Cl_2/AcCN gave pure anti conformer of **1** as a purple solid. ^{1}H NMR (400 MHz, $CDCl_3$) δ 8.04 (d, *J* = 9.2 Hz, 2H), 7.76 – 7.27 (m, 20H), 6.95 (s, 4H), 4.22 (s, 4H), 1.84 (q, *J* = 7.5 Hz, 4H), 1.50 (s, 12H), 0.93 (t, *J* = 7.4 Hz, 6H). ^{13}C NMR (100 MHz, TCE-d_2) δ 167.95, 160.83, 148.37, 143.95, 129.74, 129.35, 129.16, 128.22, 128.06, 127.77, 127.38, 126.95, 126.79, 126.60, 125.87, 125.66, 125.54, 125.09, 124.75, 124.25, 123.30, 123.21, 123.14, 123.13, 122.73, 122.62, 77.43, 77.31, 77.11, 76.79, 39.80, 37.91, 36.94, 29.60, 28.43, 9.27. HRMS (ESI) m/z calcd for $[C_{72}H_{54}N_2O_8]^+$ (M^+): 1075.3958; found 1075.3925.

(1,3,6,8-tetraoxo-1,3,6,8-tetrahydrobenzo[lmn][3,8]phenanthroline-2,7-diyl)bis-(4-(tert-pentyl)-2,1-phenylene) diacetate. (**2**) Control **2** was synthesized using the same procedure described for **1** using bisphenol **5** (0.30 g, 0.51 mmol), acetic acid (87 µL, 1.52 mmol), DMAP (30 mg, 0.25 mmol) and EDCI (0.24 g, 1.52 mmol). Crude **2** was obtained as a white powder (0.25 g, 73%). Thermal equilibration in TCE at 80 ºC under N_2 for 10 h gave a mixture of *anti* and *syn* conformers (1.2:1). ^{1}H NMR (400 MHz, $CDCl_3$) δ 8.87 (s, 4H syn and anti), 7.51 (dd, *J* = 8.7 Hz, *J* = 2.3 Hz, 2H syn and anti), 7.38 (d, *J* = 8.7 Hz, 2H anti), 7.37 (d, *J* = 8.7 Hz, 2H syn), 7.32 (d, *J* = 2.3 Hz, 2H anti), 7.29 (d, *J* = 2.3 Hz, 2H syn), 2.06 (s, 4H syn), 2.04 (s, 4H anti), 1.68 (q, *J* = 7.1 Hz, 4H syn), 1.67 (q, *J* = 7.1 Hz, 4H anti), 1.33 (s, 12H syn), 1.33 (s, 12H anti), 0.78 (t, *J* = 7.4 Hz, 6H syn and anti). ^{13}C NMR (100 MHz, TCE-d_2) δ 167.99, 167.94, 161.96, 148.11, 143.88, 131.44, 127.66, 127.34, 127.16, 127.08, 126.61, 126.58, 125.27, 125.17, 122.65, 37.72, 36.78, 28.14,

20.96, 20.81, 9.11. HRMS (ESI) m/z calcd for $[C_{40}H_{38}N_2O_8]^+$ (M^+): 674.2628; found: 674.2618.

3. Solvate and Non-Solvate Single Crystals of 1.

Five solvate and one non-solvate forms of single crystals of **1** were obtained through slow evaporation from organic solvents. Their resolved crystal structures were summarized as below. [i]

One solvate single crystal was obtained from CH_2Cl_2 solution, and was found to have an empirical formula of $C_{74}H_{54}N_2O_8$•$2CH_2Cl_2$. Solvate **1**•$2CH_2Cl_2$ was an intense red plate crystal, in which $C_{74}H_{54}N_2O_8$ molecule (**1**) crystallized in the monoclinic space group $P2_1/n$. The asymmetric unit consist of half of $C_{74}H_{54}N_2O_8$ molecule and one dichloromethane molecule. The pyrene unit was found to disorder over two closely spaced, co-planar orientations via a *ca.* 12.5° 'pivot' around the ipso carbon. The population was refined to two conformations of 0.76/0.24 ratio. Disorder was also found for the inclusion dichloromethane over two positions. Repeating crystallization in CH_2Cl_2 gave the same crystal.

One solvate single crystal was obtained from the CH_2Cl_2/AcCN system, and was found to have an empirical formula of $C_{74}H_{54}N_2O_8$•$1.36(CH_3CN)0.64(CH_2Cl_2)$. Solvate **1**•$2(CH_3CN/CH_2Cl_2)$ was a dark red blocklike crystal in which $C_{74}H_{54}N_2O_8$ (**1**) crystallized in the monoclinic space group $P2_1/n$. The asymmetric unit consists of half of $C_{74}H_{54}N_2O_8$ molecule, which is located on an inversion center, and a volume of disordered solvent, which are CH_3CN and CH_2Cl_2. The solvent disorder was modeled with three independent

[i] Detail X-ray crystallographic data and cif files are available free of charge via Internet at http://pubs.rsc.org/en/Content/ArticleLanding/2015/CC/c5cc06140g

groups: one acetonitrile and two dichloromethane groups. A slight positional disorder exist at the far end of pyrene units as suggested by the elongated displacement ellipsoids. A reasonable refinement, however, was achieved giving an average position for the pyrene unit. Disorder was also found at the *tert*-amyl group.

One non-solvate form of small crystal[i] was obtained from the $CHCl_3/CH_3CN$ system, and was found to have an empirical formula of $C_{74}H_{54}N_2O_8$. Non-solvate **1** was a *thin yellow-orange plate* in which $C_{74}H_{54}N_2O_8$ (**1**) crystallized in the triclinic space group *P*-1. The asymmetric unit consists of half of $C_{74}H_{54}N_2O_8$ molecule, which is located on an inversion center. The disorder primarily takes the form of differently orientated but essentially co-planar pyrene motifs. The population fraction of each orientation was refined to be 0.72/0.28. The *tert*-amyl groups were also found to be disordered. No inclusion solvent molecules were found. Repeating crystallization in the $CHCl_3/CH_3CN$ system failed in obtaining good quality single crystals. Recrystallization in acetone, however, gave quality single crystals of the same non-sovlate **1** but with greater dimensions.

One solvate form of crystal was obtained from the CH_3NO_2, and was found to have an empirical formula of $C_{74}H_{54}N_2O_8 \bullet 2(CH_3NO_2)$. Solvate $\mathbf{1} \bullet 2(CH_3NO_2)$ was a red plate crystal in which $C_{74}H_{54}N_2O_8$ (**1**) crystallized in the triclinic space group *P*-1. The asymmetric unit consists of half of $C_{74}H_{54}N_2O_8$ molecule, which is located on an inversion center, and one CH_3NO_2. No disorder was found. Repeating crystallization in CH_3NO_2 gave the same crystal.

[i] The data for structure resolution was instead collected using synchrotron at the X-ray crystallography facility at the Department of Chemistry, University of Cincinnati, Cincinnati, OH.

One solvate form of crystal was obtained from the nitroethane, and was found to have an empirical formula of $C_{74}H_{54}N_2O_8$•2($CH_3CH_2NO_2$). Solvate **1**•2($CH_3CH_2NO_2$) was a dark red tablet crystal in which $C_{74}H_{54}N_2O_8$ (**1**) crystallized in the triclinic space group *P*-1. The asymmetric unit consists of half each of two crystallographically independent $C_{74}H_{54}N_2O_8$ molecules, each of which is located on an inversion center, and two independent nitroethane molecules. The *tert*-amyl groups of each $C_{74}H_{54}N_2O_8$ molecule were found to be rotationally disordered. Repeating crystallization in the $EtNO_2$ system gave the same crystal.

One solvate form of crystal was obtained from the dioxane, and was found to have an empirical formula of $C_{74}H_{54}N_2O_8$•2($C_4H_8O_2$). Solvate **1**•2($C_4H_8O_2$) was a thin red plate crystal in which $C_{74}H_{54}N_2O_8$ (**1**) crystallized in the monoclinic space group $P2_1/c$. The asymmetric unit consists of half of $C_{74}H_{54}N_2O_8$ molecule, which is located on an inversion centers, and one dioxane molecule. No disorder was found. Repeating crystallization in the dioxane system gave the same crystal.

One non-solvate crystal of **2** was obtain from chloroform, and was found to have an empirical formula of $C_{40}H_{38}N_2O_8$. Non-solvate **2** was a colourless tablet in which $C_{40}H_{38}N_2O_8$ (**2**) crystallized in the monoclinic space group $P2_1/c$. The asymmetric unit consists of half of $C_{40}H_{38}N_2O_8$ molecule, which is located on a crystallographic inversion center. No disorder was found. Repeating crystallization in chloroform gave the same crystal.

To effectively characterize and analyze these crystal structures and intramolecular PYR-NDI CT complex therein, several parameters were defined and measured (Figure 5.13). To characterize the length of the five-atom covalent linker, the distance (***l***) between

carbonyl α-C and C_{aryl}-N_{imide} bond was measured. To characterize the conformational flexibility of the covalent linker, the dihedral angle ($\boldsymbol{\alpha}$) between phenyl ring and naphthalenediimide residing planes was measured. To characterize the rotational displacement between PYR and NDI units in the intramolecular CT complex, the rotational angle ($\boldsymbol{\theta}$) between their long axes was measured. To characterize the intramolecular aromatic stacking interaction between PYR and NDI units, the stacking angle ($\boldsymbol{\beta}$) as defined by the dihedral angle of the PYR and NDI residing planes, the interplanar distance (***h***) as defined by the PYR centroid to NDI residing plane distance, and the horizontal displacement (***d***) as defined by the distance between the PYR centroid project and NDI centroid were measured. The measured values are provided in Table 5.1.

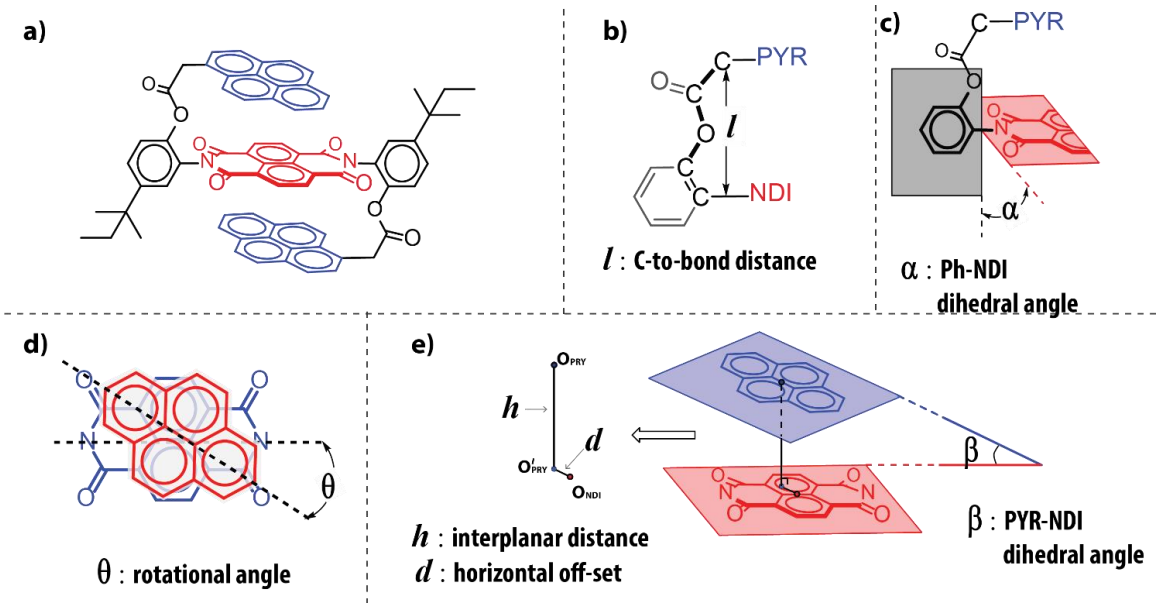

Figure 5.13 Geometric parameters defined to characterize the intramolecular PYR-NDI CT complex in **1**: (a) Chemdraw representation of **1** in side view; (b) the C-to-CN bond distance (**l**) for characterizing linker length; (c) the dihedral angle (**α**) between the N-Ph and NDI residing planes for characterizing the conformational flexibility of linker motif; (d) the twist angle (**θ**) defined by the long axes of PYR and NDI units; (e) the interplanar distance (**h**) between the PYR and NDI residing planes, the horizontal off-set (**d**) between the centroids of PYR and NDI units, and PYR-NDI stacking angle (**β**) for characterizing the intramolecular aromatic stacking interaction

Table 5.1. Measured geometric parameters in crystal structures of **1** and **2**

	inclusion solvent	solvent-to-**1** ratios	relative population[a]	rotation angle (***θ***)	dihedral angle (***α***)	interplanar distance (***h***)	linker length (***l***)	horizontal offset (***d***)	stacking angle (***β***)	CT profile[e]		
										λ_{max} (nm)	$\lambda_{half\text{-}height}$ (nm)	$\lambda_{on\text{-}set}$ (nm)
1	CH_2Cl_2	2:1	76%[b]	56.5	78.4	3.49	4.48	0.17	6.3	533	613	638
			24%[b]	63.6	78.4	3.54	4.48	0.57	7.1			
	CH_2Cl_2 & CH_3CN[d]	2:1	100%	57.4	76.9	3.55	4.48	0.25	6.4	531	620	646
	none	0	28%[b]	33.1	75.4	3.68	4.41	0.58	5.1	494	553	578
			72%[b]	42.2	75.4	3.60	4.36	0.35	5.7			
	CH_3NO_2	2:1	100%	53.2	83.5	3.48	4.43	0.19	5.6	544	629	658
	$EtNO_2$	2:1	50%[c]	65.7	74.6	3.51	4.49	0.80	7.4	535	612	643
			50%[c]	63.9	72.2	3.54	4.51	0.55	7.4			
	dioxane	2:1	100%	51.9	73.8	3.55	4.50	0.38	4.7	547	591	612
2	none	0	100%	n/a	89.5	n/a	4.64	n/a	n/a	n/a	n/a	n/a

[a] Relative population of multiple PYR-NDI geometries from partial disorder or multiple crystallographically independent molecules. (See later structure analysis section for details); [b] Partial disorder at the pyrene motif was resolved into two slightly differently CT interaction geometries; [c] Two crystallographically independent molecules of **1** were observed; [d] A volume of disordered solvent was modeled into three independent groups: one acetonitrile and two dichloromethane groups. [e] The UV-vis spectra were provided in Figure S10.

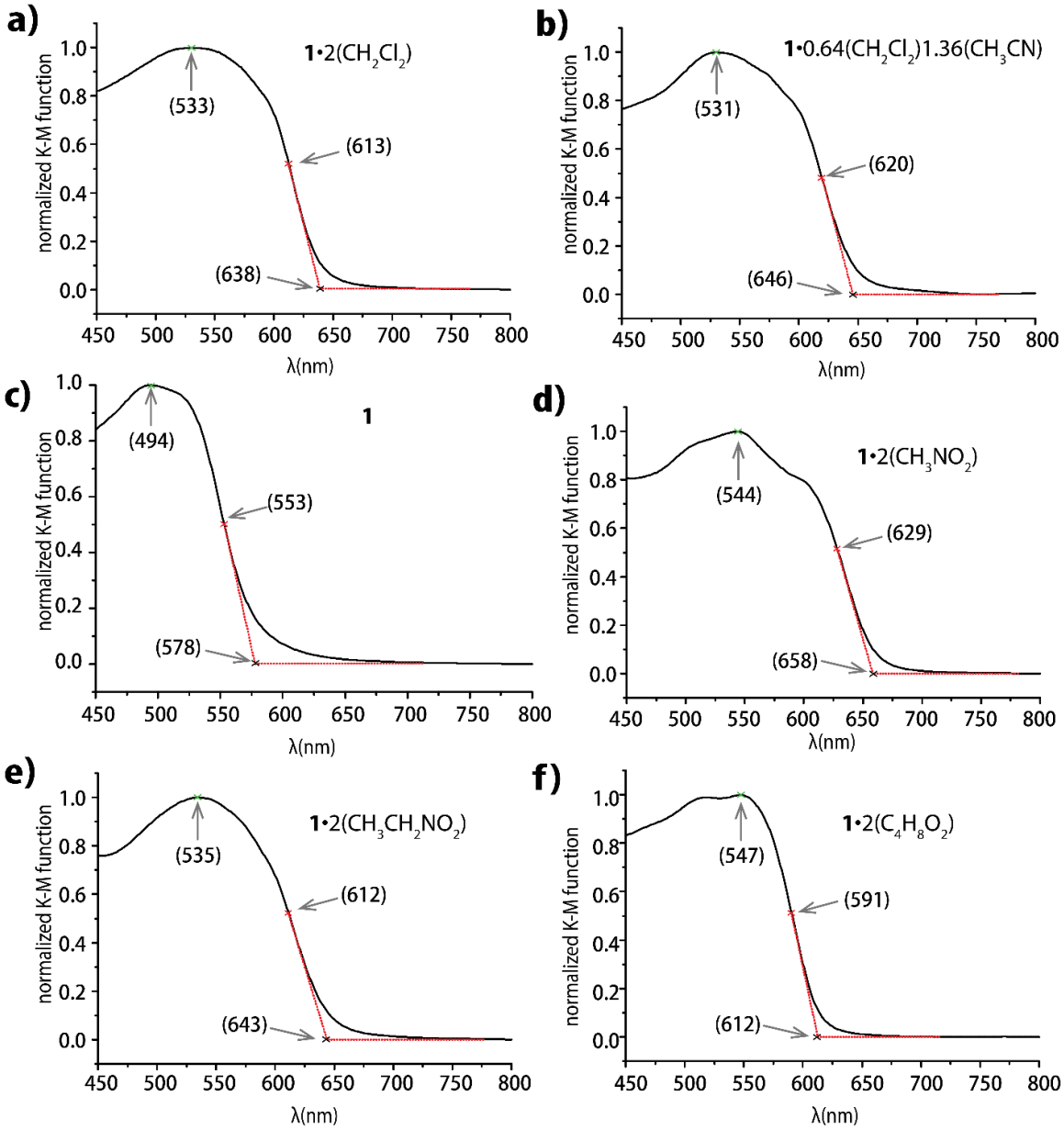

Figure 5.14 Solid-state diffuse reflectance UV-vis spectra of six-single crystals of **1** highlighting the λ_{max}, $\lambda_{half\text{-}height}$, and $\lambda_{on\text{-}set}$ of the CT absorption band.

CHAPTER 6

FUTURE WORK

1. Introduction

We have demonstrated that the C-shape *N*-arylimide molecular balances are indeed excellent tools to investigate weak aromatic interactions in solution and solid-state environments. However, this system still has the potential to be used in many other physical organic studies. Some ideas for future work have already been mentioned in Section 7 in Chapter 1. In this chapter, we briefly discussed *two* other on-going projects in our laboratory with the aim of highlighting the ability of these molecular balances to further contribute to the study of aromatic interactions. The primary focus will be on the necessary molecular designs for these applications.

2. Water-soluble molecular balance

Aqueous solvent systems have been a "holy grail" in the experimental studies of non-covalent interactions due to their biological relevance.[1-4] Moreover, the unique polar and cohesive nature of aqueous environment may exert dramatic impacts on various dispersion-driven aromatic interactions.[5-7] One interesting research topic in this regard thus has been to isolate the solvophobic contributions to the interaction energy for various aromatic interactions in water.[3,7,8] Unfortunately, our current molecular balances do not dissolve in protic solvents due to their predominant hydrophobic. Therefore, modifications of this versatile model system that would lead to solubility in aqueous solvent systems are particularly desirable (Figure 6.1).

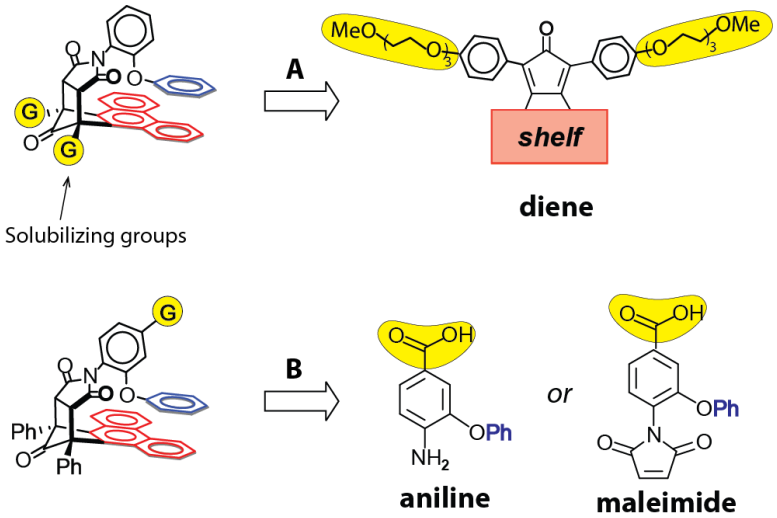

Figure 6.1 Schematic representation of two retro-synthetic strategies to prepare water-soluble molecular balances together with their corresponding starting materials. The solubilizing groups or their precursors are highlighted in yellow.

Figure 6.1 highlights two general strategies to water-soluble π-stacking molecular balances. The common underlying idea is to incorporate solubilizing groups (highlighted in yellow) to counterbalance the predominant hydrophobic domain. To effectively solubilize the molecular balance in solvents with high water content, however, the water-solubilizing groups should contain multiple strong ionic hydrophilic sites, such as ammonium, carboxylate, phosphonate and sulfonate. For example, strategy **A** that installs two tri-glycol methyl ether groups at the bridgehead of the bicyclic framework yielded a balance that dissolved in methanol but not in water. In this regard, the strategy **B** is more promising since the carboxylic group could either turned into an ionic group as the salt form or serve as a "handle" to attach additional solubilizing groups. Moreover, the carboxylic group can be masked into a less hydrophilic precursor, such as a methyl ester, during the synthesis and then unmasked in the last step, greatly relieving the complication of handling polar hydrophilic intermediates during the synthesis and purification.

3. Orthogonal multipolar interaction of N-heteroarenes

Since the pioneering study on weak attractive C-F···C=O interactions by Diederich and co-workers,[9] more attention has been focused on the dipolar interactions between polar function groups in orthogonal alignments.[10,11] The nature of multipolar interactions has been still under debate. For example, the observed orthogonal C-F···C=O interactions have been argued to come from an "n→π*" bond instead of a dipole-dipole interaction.[12] The dipolar interactions of *N*-heteroarenes, however, have been rarely studied despite of their abundance in biological processes and pharmaceuticals. Therefore, one interesting question is "*do C-F and N-heteroarene form the unique multipolar interaction*?" Fluorine has been profoundly utilized in medicinal research to modulate the activity, selectivity, and stability of biologically active compounds.[13] The unique ring dipole of *N*-heteroarenes may help better probe the nature of orthogonal multipolar interaction of C-F bonds.

The ability of our C-shape *N*-arylimide molecular balances to enforce the designed intramolecular interaction geometry offers a means to experimentally investigate the orthogonal interactions between a C-F bond and pyridine ring (Figure 6.2 A). Preliminary results suggest the existence of these favorable interaction. The orthogonal C-F···pyridine interaction (the dipole-dipole angle: 92°) observed in our molecular balance was clearly much more stabilizing in comparison with the C-F···benzene interaction (Figure 6.2 B). Study of heterocyclic balance with the pyridine ring fixed in the opposite direction could help to test the "n→π*" hypothesis for the orthogonal interactions of C-F bonds. This approach is currently being carried out in our laboratory.

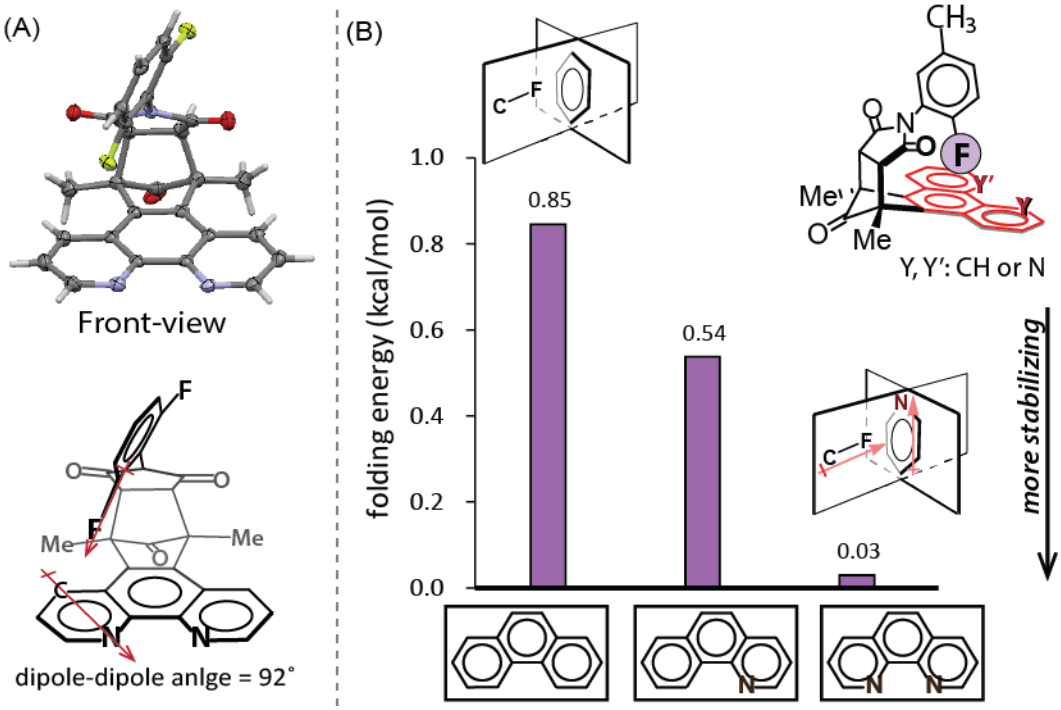

Figure 6.2 (A) Front view of the X-ray crystal structure of a two-arm fluorine-heteroarene balance (top) together with the ChemDraw representation (bottom), highlighting the orthogonal alignment between the C-F bond dipole and opposing pyridine ring dipole; (B) Measured folding energies for a series of F-arm balances with zero, one, and two heterocyclic nitrogens on the tricyclic shelf arene, highlighting the stabilizing orthogonal C-F···pyridine interaction.

4. Concluding Remark

We briefly looked at two on-going projects utilizing the C-shape *N*-arylimide balances. Future work will surely expand beyond those mentioned in this dissertation. We hope this short chapter served to highlight the greater potential and bright future of this versatile balance model in exploring and assessing aromatic interactions.

Reference

[1]. Guckian, K. M.; Schweitzer, B. A.; Ren, R. X. F.; Sheils, C. J.; Paris, P. L.; Tahmassebi, D. C.; Kool, E. T. *J. Am. Chem. Soc.* **1996**, *118*, 8182.

[2]. Guckian, K. M.; Schweitzer, B. A.; Ren, R. X. F.; Sheils, C. J.; Tahmassebi, D. C.; Kool, E. T. *J. Am. Chem. Soc.* **2000**, *122*, 2213.

[3]. Wilcox, C. S.; Bhayana, B. *Angew. Chem., Int. Ed.* **2007**, *46*, 6833.

[4]. Rashkin, M. J.; Waters, M. L. *J. Am. Chem. Soc.* **2002**, *124*, 1860.

[5]. Yang, L. X.; Adam, C.; Nichol, G. S.; Cockroft, S. L. *Nat. Chem.* **2013**, *5*, 1006.

[6]. Hwang, J. W.; Dial, B. E.; Li, P.; Kozik, M. E.; Smith, M. D.; Shimizu, K. D. *Chem. Sci.* **2015**, *6*, 4358.

[7]. Adam, C.; Yang, L.; Cockroft, S. L. *Angew. Chem., Int. Ed.* **2015**, *54*, 1164.

[8]. Yang, L.; Adam, C.; Cockroft, S. L. *J. Am. Chem. Soc.* **2015**, *137*, 10084.

[9]. Hof, F.; Scofield, D. M.; Schweizer, W. B.; Diederich, F. *Angew. Chem., Int. Ed.* **2004**, *43*, 5056.

[10]. Fischer, F. R.; Wood, P. A.; Allen, F. H.; Diederich, F. *Proc. Natl. Acad. Sci. U. S. A.* **2008**, *105*, 17290.

[11]. Paulini, R.; Muller, K.; Diederich, F. *Angew. Chem., Int. Ed.* **2005**, *44*, 1788.

[12]. Kamer, K. J.; Choudhary, A.; Raines, R. T. *J. Org. Chem.* **2013**, *78*, 2099.

[13]. Muller, K.; Faeh, C.; Diederich, F. *Science* **2007**, *317*, 1881.

APPENDIX A
COPYRIGHT PERMISSIONS

For chapter 2:

Copyright Clearance Center RightsLink®

Home | Create Account | Help | Live Chat

ACS Publications
Most Trusted. Most Cited. Most Read.

Title: Comprehensive Experimental Study of N-Heterocyclic π-Stacking Interactions of Neutral and Cationic Pyridines

Author: Ping Li, Chen Zhao, Mark D. Smith, et al

Publication: The Journal of Organic Chemistry

Publisher: American Chemical Society

Date: Jun 1, 2013

Copyright © 2013, American Chemical Society

LOGIN

If you're a copyright.com user, you can login to RightsLink using your copyright.com credentials. Already **a RightsLink user** or want to learn more?

PERMISSION/LICENSE IS GRANTED FOR YOUR ORDER AT NO CHARGE

This type of permission/license, instead of the standard Terms & Conditions, is sent to you because no fee is being charged for your order. Please note the following:

- Permission is granted for your request in both print and electronic formats, and translations.
- If figures and/or tables were requested, they may be adapted or used in part.
- Please print this page for your records and send a copy of it to your publisher/graduate school.
- Appropriate credit for the requested material should be given as follows: "Reprinted (adapted) with permission from (COMPLETE REFERENCE CITATION). Copyright (YEAR) American Chemical Society." Insert appropriate information in place of the capitalized words.
- One-time permission is granted only for the use specified in your request. No additional uses are granted (such as derivative works or other editions). For any other uses, please submit a new request.

For chapter 3:

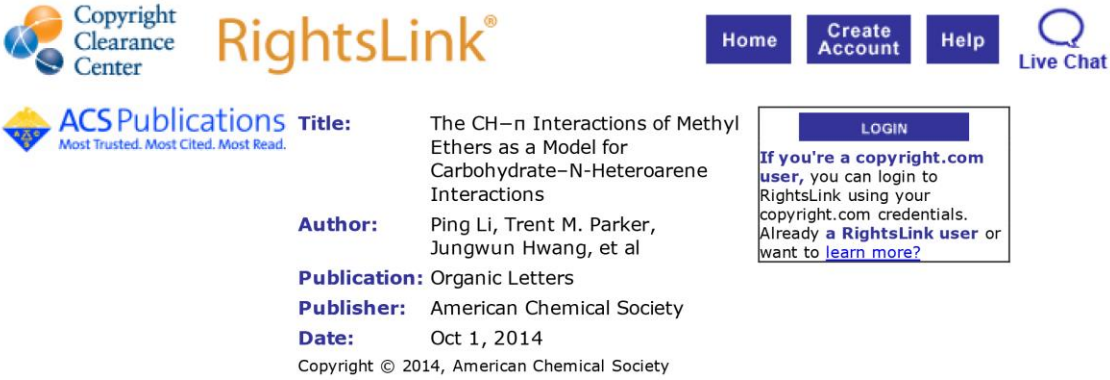

Copyright Clearance Center RightsLink®

Home | Create Account | Help | Live Chat

ACS Publications
Most Trusted. Most Cited. Most Read.

Title: The CH−π Interactions of Methyl Ethers as a Model for Carbohydrate–N-Heteroarene Interactions

Author: Ping Li, Trent M. Parker, Jungwun Hwang, et al

Publication: Organic Letters

Publisher: American Chemical Society

Date: Oct 1, 2014

Copyright © 2014, American Chemical Society

LOGIN

If you're a copyright.com user, you can login to RightsLink using your copyright.com credentials. Already **a RightsLink user** or want to learn more?

PERMISSION/LICENSE IS GRANTED FOR YOUR ORDER AT NO CHARGE

This type of permission/license, instead of the standard Terms & Conditions, is sent to you because no fee is being charged for your order. Please note the following:

- Permission is granted for your request in both print and electronic formats, and translations.
- If figures and/or tables were requested, they may be adapted or used in part.
- Please print this page for your records and send a copy of it to your publisher/graduate school.
- Appropriate credit for the requested material should be given as follows: "Reprinted (adapted) with permission from (COMPLETE REFERENCE CITATION). Copyright (YEAR) American Chemical Society." Insert appropriate information in place of the capitalized words.
- One-time permission is granted only for the use specified in your request. No additional uses are granted (such as derivative works or other editions). For any other uses, please submit a new request.

For chapter 4:

PERMISSION/LICENSE IS GRANTED FOR YOUR ORDER AT NO CHARGE

This type of permission/license, instead of the standard Terms & Conditions, is sent to you because no fee is being charged for your order. Please note the following:

- Permission is granted for your request in both print and electronic formats, and translations.
- If figures and/or tables were requested, they may be adapted or used in part.
- Please print this page for your records and send a copy of it to your publisher/graduate school.
- Appropriate credit for the requested material should be given as follows: "Reprinted (adapted) with permission from (COMPLETE REFERENCE CITATION). Copyright (YEAR) American Chemical Society." Insert appropriate information in place of the capitalized words.
- One-time permission is granted only for the use specified in your request. No additional uses are granted (such as derivative works or other editions). For any other uses, please submit a new request.

For chapter 5:

Solvent-induced reversible solid-state colour change of an intramolecular charge-transfer complex

P. Li, J. M. Maier, J. Hwang, M. D. Smith, J. A. Krause, B. T. Mullis, S. M. S. Strickland and K. D.Shimizu, *Chem. Commun.*, 2015, 51, 14809. DOI: 10.1039/C5CC06140G

Dear Ping Li

The Royal Society of Chemistry (RSC) hereby grants permission for the use of your paper(s) specified below in the printed and microfilm version of your thesis. You may also make available the PDF version of your paper(s) that the RSC sent to the corresponding author(s) of your paper(s) upon publication of the paper(s) in the following ways: in your thesis via any website that your university may have for the deposition of theses, via your university's Intranet or via your own personal website. We are however unable to grant you permission to include the PDF version of the paper(s) on its own in your institutional repository. The Royal Society of Chemistry is a signatory to the STM Guidelines on Permissions (available on request).

Please note that if the material specified below or any part of it appears with credit or acknowledgement to a third party then you must also secure permission from that third party before reproducing that material.

Please ensure that the thesis states the following:

Reproduced by permission of The Royal Society of Chemistry

and include a link to the paper on the Royal Society of Chemistry's website.

Please ensure that your co-authors are aware that you are including the paper in your thesis.

Regards

Gill Cockhead
Publishing Contracts & Copyright Executive

Gill Cockhead
Publishing Contracts & Copyright Executive
Royal Society of Chemistry,
Thomas Graham House,
Science Park, Milton Road,
Cambridge, CB4 0WF, UK
Tel +44 (0) 1223 432134